Nanoscale imaging and characterisation of Amyloid-β

Claire Louisa Tinker-Mill

M.Sc. B.Sc. (Hons)

May 2015

This thesis is submitted in partial fulfilment of the requirements for the degree of Doctor of Philosophy.

No part of this thesis has been or is being submitted to any other university or academic institution.

Abstract

In this work several novel Scanning Probe Microscopy (SPM) methods have been applied to the study of the amyloid peptide implicated in the pathogenesis of Alzheimer’s disease (AD). Amyloid-β (Aβ) undergoes a hierarchy of aggregation following a structural transition making it an ideal subject of studying with SPM.

The application of SPM based techniques to biological samples has become increasingly common place. However, these techniques are not always immediately suitable for imaging delicate samples of proteins and adaptions must be made before imaging can be considered successful. AD is the most common form of dementia worldwide, and a growing concern for health authorities. As a result it has attracted the attention of a wide range of disciplines. There has been much work conducted which combines the main pathogenic peptide, Aβ , with Atomic Force Microscopy (AFM) in order to elucidate more about its aggregation behaviour, however these techniques offer little more than structural comments, with only the most advanced forms of cryo-Electron Microscopy (EM) providing more details on the nanoscale. Presented here is a method for reliably and robustly producing samples of Aβ by capturing them at various stages of aggregation, as well as the results of subsequent imaging by various methods of AFM. Each of the AFM techniques studied provides additional “added value” to the data which can typically be collected by AFM; either nanomechanical, elastic, thermal or spectroscopical.

By imaging samples of Aβ with Ultrasonic Force Microscopy, a detailed substructure to the morphology could be seen, which correlates well with the most advanced cryo-EM work. In addition this technique was ideal for detecting the most toxic from of Aβ, early aggregates, in a sensitive and non-destructive fashion robustly differentiating them from the underlying layer of another peptide (poly-L-Lysine) that was designed to reliably capture the Aβ aggregates. Early work investigating the potential for combining an established method of thermal AFM with a mid-IR laser system also shows promise for detecting the response of the protein.

It was also the focus of this work to study the aggregation of Aβ using Dynamic Light Scattering (DLS), in order to confirm whether the technique could identify differences between populations throughout the aggregation process. This was applied in conjunction with potential therapeutics which target the early aggregates to prevent their accumulation, as well as block formation of fibrils.

Ultimately this work aims to shows with care to the initial protocols used, physical techniques such as AFM and DLS can be added to the existing methods of monitoring aggregation. Synergistic use of these techniques can generate a clearer overall picture of the effect of metal ions/developing therapeutics on Aβ aggregation and provide more detail than classical biological techniques alone.

Acknowledgments and dedications

Acknowledgments

I would first like to thank Prof. David Allsop and Dr. Oleg Kolosov for their patience and guidance throughout the completion of this work. I would also like to extend my eternal gratitude to my colleagues in both the Department of Physics and Biomedical Life Sciences for their help and advice.

I am blessed to have made so many friends throughout this PhD; both within the university and elsewhere. Jenny Mayes and Alex Robson, thank you for brightening my morning with many a cup of coffee and chatter, in addition to all your support with my research. Riccardo Mazzocco, who will always be “my favourite Italian”. Kylie O’Shea and Ben Shreeve, without whom I would not have enjoyed nearly as much cake as I have currently. The wonderful Taylor Lura, Emily Smith and Christie Herd, who have made me laugh so hard I have cried. My “Bookend” Louise Walker for fostering my madness and creating the candyfloss world with me. I would like to thank Dr. Christine Shirras for her guidance and support as my teaching mentor. Lastly, my friends in Canada; Ronnie and Liz Drolle, who I would never have had the joy of meeting if it were not for this PhD. All of these people, and more, have made this experience the happiest of my life. You’ve brought so much joy, sparkle and laughter as we’ve journeyed together. I’m so lucky to have you in my life.

My family’s support and belief in me has been paramount throughout my studies, and I thank them from the bottom of my heart of believing in me, comforting me and giving me the strength I have.

Most importantly I want to thank my long-suffering husband, Richard. Without you I would not be me, and this would not have happened. We share this achievement as we do everything. I love you now, forever and always and cannot thank you enough for your support and love.

Dedications

The work in this thesis is dedicated to those that sadly did not get the opportunity to see me finish this journey, but offered their unconditional support and love throughout my life.

Vera Pennington, who sadly lost her own battle with Alzheimer’s disease inspired with her tireless work as a daughter, mother and grandmother.

Rex Pennington, who went long before this journey began. Thank you for the memories.

Marjorie and Ernest Tinker, without whom I would not have been able to begin this journey. I love and miss you both so much and am eternally grateful for all that you did for me. It breaks my heart you will not see me graduate.

Detailed content list

Summary of contents

Introduction

A brief introduction to the work in this thesis, including the rationale behind the work and the challenges faced. The reasoning behind the focus on Alzheimer's disease and the application of SPM and other physical techniques to this disease are given, in addition to an overview of these techniques.

Chapter One: Literature review and theoretical concepts

This first chapter is separated into two distinct parts. Part A details the physical theoretical concepts and relevant background knowledge for the SPM techniques, alongside others such as DLS. Current understanding of the nanostructure of the amyloid peptide which has been the focus of this work, Aβ, is also detailed, gathering together information from a variety of experimental techniques. The second half of the literature specifically focuses on Alzheimer's disease, which is caused by the accumulation and aggregation of Aβ. The neuropathology and biochemical processes behind the disease are discussed along with therapeutic strategies. It is the aim of this chapter as a whole to provide a solid understanding of the work conducted within this thesis, and its relevance to Alzheimer's disease and the aggregation of Aβ.

Chapter Two: Experimental Methodology

Within this chapter are detailed descriptions of all techniques used during the work in this thesis are described. The chapter begins by discussing the SPM techniques used in this chapter as multiple modes have been used. Care is given to describe and highlight the differences in data collection from these different systems. Details of the sample preparation and any biological experimental design are noted in the latter part of the chapter. Where work was conducted by another researcher, or a contribution has been made in some manner, it is also noted here.

Chapter Three: Substrate development of the imaging of amyloid proteins with SPM methods

It was essential to the work in this thesis to design a stable and reliable method of generating samples of Aβ for imaging with SPM techniques. This first body of work details this development. The approach taken was either to modify the substrate or the buffer system used to incubate the peptide for aggregation. The outcomes of these experiments are discussed, along with the final methodology for substrate attachment. A detailed analysis of the effect and interaction of this substrate and Aβ is also discussed. This chapter laid the foundation for subsequent work with SPM, and adaption of this system to other techniques.

Chapter Four: Scanning Probe Microscopy methods of imaging Amyloid Peptides during the aggregation process

Following on from the initial work to design a reliable substrate work was conducted comparing the traditional mode of SPM used for imaging biological samples, TM, with an adaption of Contact mode (CM) known as UFM. This technique allows for frictionless work, which is ideal of biological samples, while allowing details of the samples nanomechanical structure to be mapped. A comparison between UFM and a similar method of detecting nanomechanical data via AFM (HFM) is also made.

Chapter Five: Spectroscopy and Thermal SPM Methods of studying Aβ1:42

Advancing on the SPM techniques studied in the previous chapter, here work is focused on the application of thermal AFM techniques, and later, the development of new spectroscopical techniques. The use of mid-IR to detect structural features of the sample under investigation, by using its photothermal excitement is a new promising field. However it is currently limited by resolution (~100 nm) and complications with sample behaviour. It was the goal of this work to begin the development of a technique to study biological molecules in a mid-IR setting with the resolution typically seen with an AFM.

Chapter Six: The application of biophysical techniques to the study of the inhibition of aggregation of Aβ using PINPs liposomes

Over the last 5 years the RI-OR2-TAT inhibitor has been developed to prevent the aggregation of Aβ via the accumulation of early toxic aggregates. More recently it has been attached by “click chemistry” to a liposome, which acts a carrier to enhance the peptide inhibitors potency. DLS has been used in numerous studies to track the aggregation and involvement of new liposome based inhibitors, and the work in this chapter seeks to combine DLS, SPM and classical aggregation monitoring methods to shed light on the action and effect of the Peptide-Inhibitor NanoParticles (PINPs).

Chapter Seven: Conclusion and Future Perspectives

This chapter summarises the key conclusions from each chapter of results, while also positioning these in the context of future work to be conducted.

List of figures

List of Abbreviations

Aβ1:40/1:42 (Amyloid beta 1:40/1:42)

AD (Alzheimer's Disease)

ADAM (A Disintegrin And Metalloproteinase)

ADDLs (Aβ-derived diffusible ligands)

AFM (Atomic Force Microscopy)

ALICE (Accelerators and Lasers in Combined Experiments)

Alzheimer's Disease (AD)

APP (Amyloid Precursor Protein)

ATR (Attenuated Total Reflectance)

ATR−FTIR (Attenuated total reflectance Fourier transform infrared spectroscopy)

BACE1 (beta-site amyloid precursor protein cleaving enzyme 1)

BBB (blood-brain-barrier)

CLIO (Centre Laser Infrarouge d'Orsay)

CNS (Central Nervous System

DLS (Dynamic Light Scattering)

ERS (Electron Spin Resonance)

fAD (Familial Alzheimer's Disease)

Free Electron Laser (FEL)

HOPG (Highly Ordered Pyrolytic Graphene)

JKR model (Johnson-Kendal-Roberts)

lock-in amplifier (LIA)

MCI (Mild Cognitive Impairment)

MND (motor neurons disease)

nm (nanometers)

PINPs (Peptide Inhibitor NanoParticles)

QCL (Quantum Cascade Laser)

RIP (Regulated Intramembrane Proteolysis)

ROS (Reactive Oxygen Species)

SNIM (Scanning Near-field IR Microscopy)

SPM (Scanning Probe Microscopy)

SThM (Scanning Thermal Microscopy)

STM (Scanning Tunnelling Microscopy)

ThT (Thioflavin T)

van der Waals (VDW)

ε4 (Apolipoprotein E4)

Introduction

The most common techniques used to elucidate structural or morphological details of samples on the nanoscale are SPM or electron microscopy (EM) based methods. Both offer significant advantages and disadvantages over one another. While the most advanced EM systems can provide visualisation up to the atomic level, the necessary sample preparation is complicated, time-consuming and often destructive. Typically it requires heavy metal staining or coating of the sample surface with a conductive layer, such as carbon. However when this is applied to biological samples it can have disastrous consequences; cross-linking of aldehyde groups, disruption of molecular bonds, and obscuring fine nanoscale features. EM also has one key disadvantage for biological samples; it fails to provide any details beyond that of the sample structure. In contrast, while AFM based methods can offer topographical details via the standard feedback mechanisms they employ during scanning, most also offer varying levels of additional qualitative, (and in some cases), quantitative, analysis of the samples material properties. TM AFM is the most common technique for imaging biological samples, as it provides the least friction and most gentle scanning conditions for samples which are often delicate and easily destroyed or disrupted. In addition to topographical detail, information about the samples "phase" response can also be collected, thus offering an indication of variations in the samples elasticity, adhesion or hardness.

Before any scanning probe imaging could take place, it was essential to create a substrate which biological samples could attach to that was anatomically flat, robust and lacking in background contrast, either topographical or nanomechanical. It was essential to create a simple, cheap and reliable protocol which could be used to capture moieties of all sizes and charges. Significant developments of the standard AFM substrate, muscovite mica, were needed before a protocol could be used repeatedly. However this process presented an opportunity to understand the factors needed when selecting a protocol and mica was not suitable for all the work conducted within this thesis.

Recent developments in the field of AFM have led to the creation of exciting new modes of operation, many of which utilise CM to detect more advanced details of the samples properties. The work reported in this thesis seeks to apply some of these new techniques; either from commercial or in-house systems to biological samples and offer conclusions about their suitability for this purpose. One such technique is Ultrasonic Force Microscopy (UFM), an already established technique for studying the elastic and contact stiffness properties of samples with nanoscale resolution. UFM offers a distinct advantage for a contact based AFM technique as it is uniquely frictionless. By oscillating the sample above the cantilevers resonance frequency (or the probe in waveguide-UFM) the cantilever can be seen to be infinitely rigid, and its indentation into the sample surface is brief. Using a force jump curve to study the interaction of the tip and sample surface shows that the elastic properties and stiffness affect the response of the cantilever during this indentation. It was one aim of the work reported here to transfer this technique to a variety of biological samples, and determine whether it posed an advantage over the standard Tapping Mode imaging and whether any additional nanomechnical data could be gathered.

In addition to the application of UFM to new samples there is increased interest in the area of SPM to combine techniques such as Raman spectroscopy and Fourier transform infrared spectroscopy (FTIR) with AFM to provide nanoscale resolution. Surface enhanced Raman spectroscopy already offers the possibility to gather spectra detailing samples chemical properties but on the non-local level i.e. it is not linked to simultaneous morphological mapping. Recently this has been shown to be possible; Scanning Near-field Optical Microscopy and AFM have been combined with Raman spectroscopy or a mid-IR laser source to offer a resolution ~100 nm and local mapping of a sample chemical properties across a relevant vibrational spectra. Each of these systems shows promise at the potential for mapping chemical changes alongside structural ones as samples such as cancer cells at different stages of disease progression undergo changes. These techniques also offer exciting possibilities for samples on an even smaller scale. Proteins frequently require a scale of investigation <100 nm, and it was the aim of work here to elucidate whether it was possible to combine and adapt and existing AFM technique with a mid-IR laser source to detect differences in chemical composition across a sample. Two approaches were taken, one involving preliminary work using an established commercial system, the Nano-IR (Anasys Instruments, USA), and the other combining thermal AFM with the mid-IR laser from the ALICE accelerator – similar to the Photo-Thermal Micro Spectroscopy (PTMS). Both techniques showed promising results and have laid an extensive foundation for future work.

All forms of AFM being investigated in this work were applied to samples of peptide considered to be the main pathogenic factor in AD. A growing worldwide concern, this disorder is one of many amyloidoses disorders. This particular disorder is defined by the extracellular deposits of an amyloid protein, Amyloid-β (Aβ), known as amyloid plaques. In conjunction with intracellular deposits of phosphorylated tau, this peptide is thought to cause increased inflammation via numerous oxidative stress responses, (among other theories), leading to gradual and ultimately extensive neuronal death in the cerebral cortex and hippocampus. From a clinical perspective AD results in a loss of cognitive function, with dramatic effects on memory, object recognition and speech. The main protein of interest in this work, Aβ, like all amyloid proteins, undergoes a distinct hierarchy of aggregation. This begins when the monomeric form is released from a cleavage pathway and undergoes a conformational change to become predominantly β-sheeted. This conformation triggers the aggregation of the monomer through a variety of species levels until it becomes a mature fibre (MF), which is then deposited into the amyloid plaques detected at post-mortem. While the initial focus on disease prevention lay around the clearance of this amyloid plaque burden from the brain it is now becoming clear that the early aggregates are more toxic in nature. Therapeutics targeting Aβ therefore increasingly target this aggregation stage.

Over several years Prof. Allsop’s team (Lancaster University, UK) have been working to develop an Aβ inhibitor which targets the early aggregates. Initially this took the form of a small peptide, which was then retro-inverted to prevent its degradation within the body. Further modifications have been made to increase its stability, potency and allow it to cross the blood-brain-barrier (BBB). The most current form of this inhibitor is attached by click-chemistry to a liposome to further enhance these features (RI-OR2-TAT-PINPs). In addition to studying the general aggregation stages of Aβ using multiple AFM techniques, it was also necessary to test an additional physical method of studying the aggregation process. Dynamic Light Scattering (DLS) is becoming increasingly common as a method of analysing pharmaceuticals, and was applied here in conjunction with AFM to study the effects of RI-OR2-TAT-PINPs on Aβ aggregation.

While combining the fields of Physics and Biology, and the techniques typically found in each, it was essential to set aims for the work reported in this thesis. These are summarised below:

- Develop a reliable, robust and reproducible method of depositing and attaching Aβ onto a substrate for subsequent nanoscale resolution imaging.
- Beginning with TM AFM, to image the aggregation stages of Aβ by taking time points during incubation. Following confirmation that this was possible the nanomechanical properties of Aβ could then be studied using UFM.
- Apply a variety of SPM based spectroscopical, nanomechanical and thermal techniques to samples of Aβ, with substrate and sample preparation development as necessary.
- Attempt to develop the application of underliquid-AFM.
- Study the interactions of additional features on Aβ aggregation, including developing therapeutics and effects of metal ions.
- Develop the concept of AFM-IR, a combination of thermal AFM and a mid-IR laser applicable to Aβ studies to detect changes in the chemical properties of a sample.
- Apply DLS to the aggregation process, and its prevention.
- To develop the concept that physical techniques such as AFM and DLS are highly applicable for studying biological samples on the nanoscale, and offer a complimentary set of experiments alongside the traditional methods used in biology, (ThT assay, immunoassays).

This thesis initially discusses the theoretical concepts which surround the methodology of physics techniques used in this work, followed by a discussion of AD and the peptide Aβ. Following this the results of substrate development experiments, AFM data collected using a variety of techniques, and experiments conducted using peptide inhibitors are discussed. Finally, conclusions are drawn from this body of work, and future developments and experiments are proposed.

Chapter One: Theoretical concepts and Literature review

Part A: Theoretical concepts of Scanning Probe Microscopy and Dynamic Light Scattering and their relation to the study of peptide nanostructures

1.1 Introduction

In order to study any biological material on the nanoscale one requires the correct tool to do so. There are several methods which can allow the study of protein morphology at this level but perhaps the most common and versatile is Scanning Probe Microscopy (SPM). Originally developed in 1982 as Scanning Tunnelling Microscopy (STM) the technique quickly evolved into the type of SPM focused on in this work, Atomic Force Microscopy[13-15]. The use of AFM for the high resolution imaging of materials surfaces has become increasingly common place in a wide range of subject areas, including biosciences and engineering[16]. Recent technological advancements make it possible to learn more about a sample than just its topography, and properties such as chemical composition, nanomechanics, thermal conductivity, elasticity and the Young's Modulus can all be determined[1, 2, 17-23]. The aim of this PhD has been to apply more well known, and also bespoke, AFM methods to the peptide Amyloid beta 1:42 (Aβ1:42), the main pathogenic component of Alzheimer's disease (AD), with the hope of elucidating more about its nanostructure, assembly, dynamics and interaction with potential pharmaceuticals.

This first chapter focuses on the theoretical concepts and current literature relevant to the work in this thesis. The first section is devoted to the theoretical concepts which govern AFM, and the other techniques used in this work. The latter section is a review of the Aβ1:42 and its role in AD, and the biological process in which amyloid peptides gain their toxicity.

1.2 Scanning probe microscopy

Some SPM techniques, including AFM, are capable of examining the surface properties of a sample ultimately with atomic resolution, but typically of a few nanometers (nm), whilst generating 3D images of the sample in questions. In general a probe, with a tip radius of approximately 5-10 nm, is scanned across the sample surface in a raster pattern. The interaction between the tip and the sample is used to generate the 3D image map, and allow determination of topological, nanomechanical or spectroscopical data. The tip-surface interactions are an essential component of AFM, and will first be discussed in detail below.

1.2.1 Tip-surface Interactions

The tip-surface interaction can have a strong effect on cantilever deflection, as AFM gathers information on the sample by sensing the force interactions between the tip and the surface. Close to the surface of the sample, Coulomb electron repulsions and van der Waals (VDW) forces dominate, while forces such as electrostatic and magnetic are more dominate at longer distances exceeding 1-10 nm (Fig 1.1).

When the tip is far away (a few nm) from the sample surface the dominant force is attractive due to the VDW forces, and does not deflect. As the cantilever approaches this attractive VDW force increases in strength until the atoms are close enough for their electrons to interact and repel one another. As the attractive force increases, so does the total attractive force on the cantilever until dF/dz exceeds the spring constant of the cantilever and the tip snaps into contact with the sample surface. Once in contact the tip-surface interaction is governed by the repulsive regime due to Coulomb forces. Coulomb forces arise because of the electrostatic repulsion between the electron clouds of tip and sample. This repulsion becomes stronger the closer the tip is to the sample surface.

In addition to these attractive and repulsive forces, ambient AFM imaging must also contend with the thin layer of water which will cover the sample surface forming the meniscus. The meniscus gives rise to capillary forces between the sample and the tip, which is in most cases an adhesive force[24, 25].

Imaging in liquid presents a different challenge, as capillary forces are absent and VDW forces being significantly reduced[26]. Instead the tip-surface interaction is dominated by electrostatic forces. The charge of the sample being imaged is masked by that of the buffer solution being used for imaging due to the interactions between the co- and counter-ions it contains. This screening charge is known as the electric double layer and determines the resolution which can be achieved when imaging under-liquid as it determines the tip-sample distance[26]. The buffer must be finely tuned to minimise these electrostatic interactions by negating charged interactions.

On retraction the cantilever follows the same path as approach, but in reverse. Overcoming the meniscus attraction generates a notable negative deflection of the

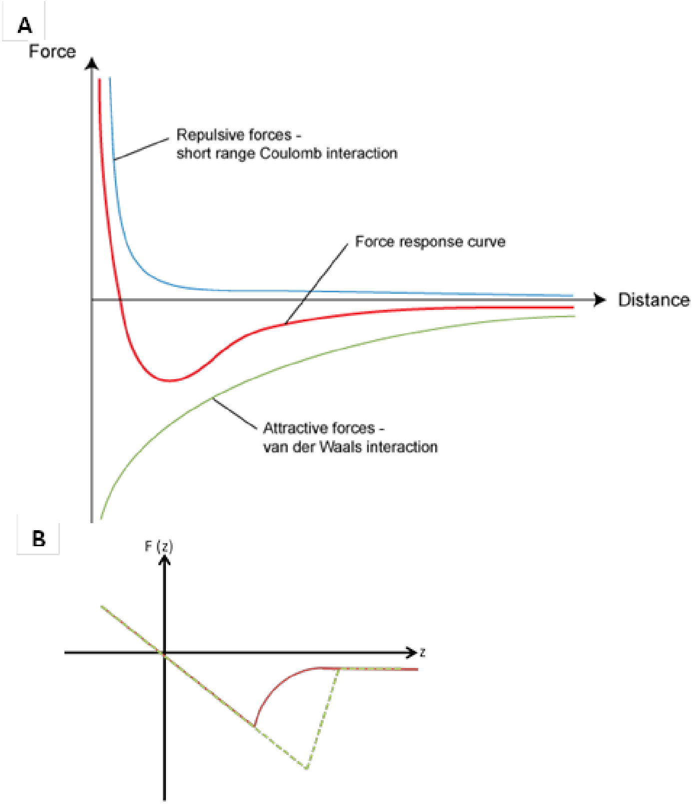

Figure 1.1. (A) Showing the tip-surface interaction between a cantilever probe and sample. The force response curve is the response of the probe to the forces acting upon it and is shown in red © DoITPoMS, University of Cambridge[8] and (B) the approach-retract curve showing the path of the cantilever when governed by repulsive and attractive forces. The approach (red) and retract (green) are both shown.

cantilever, which must be larger than the snap-in due to the initial approach, until the cantilever can overcome the attractive force and jump-off the sample surface.

Over the larger distances, longer range forces come into play to govern the interaction between the sample and the tip, and can be exploited by the use of conducting or magnetic cantilevers. A simplified equation can be used to explain the interactions between F_E, the electrostatic force, and F_M, the magnetic force:

$$F_E = -\frac{1}{2}(\Delta V)^2\frac{\partial c}{\partial s}$$

$$F_M = \nabla(m \cdot B) \ ,$$

where *C* is the tip-surface capacitances, *s* the separation between tip and surface, ΔV the potential difference between sample and tip, *m* the tip's magnetic dipole and *B* the magnetic field from the sample[27]. These simplified equations give a feel for how tip surface interactions can be used to detect sample properties, but do not take into consideration the geometry, electrical, magnetic or structural properties of either the tip or the sample.

1.2.2 AFM Detection modes

The SPM techniques covered here are all designed around the same system, in which samples are scanned in a raster pattern beneath a stationary probe with deflection of the force sensitive cantilever being continuously monitored. The sample movements are controlled by the scanner, upon which it is attached (by means of a magnetic “puck”) operating in the raster way along x-y axis. An alternative to this sample scanning method of AFM is probe scanning, where the sample is fixed and the probe is moved across the sample surface using a piezo to drive the movements as before. In sample scanning mode the mass of the sample itself must be included in the feedback loop and limiting the dimensions of the sample which can be imaged[28]. Probe scanning AFM's do not have this limitation, and are often simpler for work which needs to be conducted under-liquid as it is easier to add the necessary accessories[28]. The construction of a probe scanning AFM is considerably more complex than a sample scanning one, and is also more susceptible to the introduction of vibrations during use, while sample scanning systems are simple and less susceptible to interference while scanning[28]. The scanner itself can come with a range of capabilities linked to scan size and lateral resolution. Typically work here used a large scale scanner as biological materials were not being studied on the atomic level. The specific AFM type used here, a Multi-Mode (Bruker, USA), is capable of numerous different detection systems. Those used in this work are detail more below.

Contact mode (CM) The topography is measured by moving the probe to scan the sample surface, and generating a feedback loop using the cantilevers deflection, which then allows details of the samples topography to be generated as a 3D image map. Onto the reverse of the cantilever a laser beam is focused, which is reflected onto a 4 quadrant photo-diode. Any vertical or horizontal change in behaviour of the

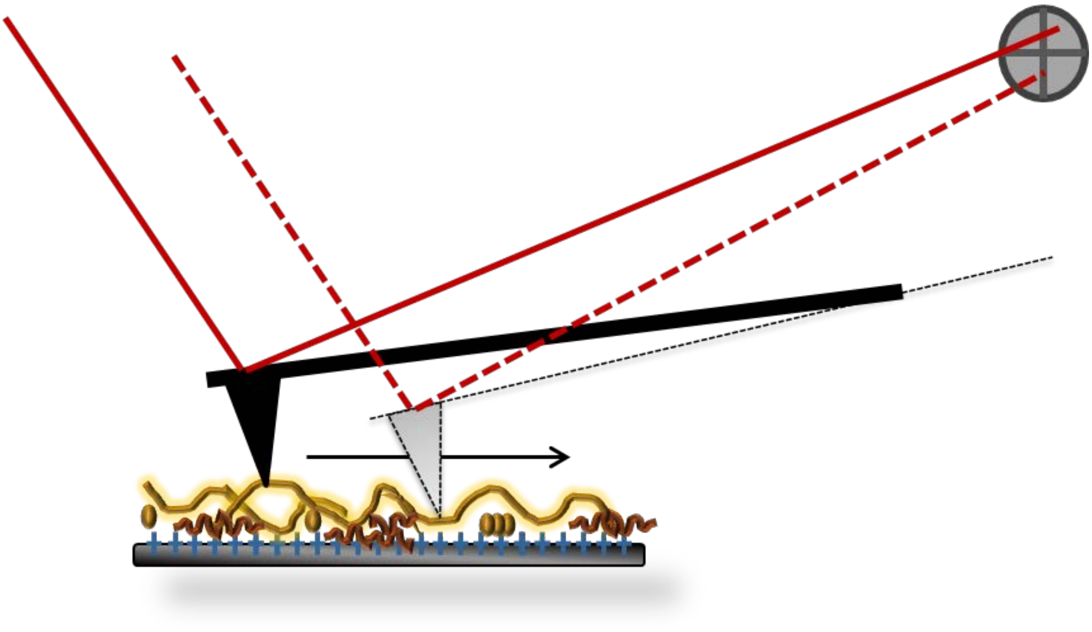

Figure 1.2. A laser is focused onto the reverse of the cantilever, and deflected onto a four-quadrant photodiode. Any changes in topography as the cantilever scans in the x-y direction lead to the movement of the sample in the z direction. This change is reflected in a change in the deflection of the laser on the photodiode. This change in laser position is fed back into the computer to generate the feedback loop which maintains a constant tip-surface distance and forms the 3D topographical maps produced.

cantilever alters the position of the laser on the photo-diode, (Fig. 1.2 and 1.3 A). Upper and lower quadrants record changes in vertical height, generated by the topology of the sample directly, while lateral quadrants reflect friction or torsion based events on the cantilevers position. In CM the cantilever must be kept within the repulsive Coulomb force dominated regime until after the initial snap-in to the sample surface. The feedback loop is used to maintain a tightly controlled position, or set point deflection, for the cantilever during scanning, using the addition of a z-axis piezo to adjust the height of the sample relative to the tip. By maintaining a constant deflection the force between the tip and the sample remains constant. Hooke's law is used to calculate the force, *F*:

$$F = -kx,$$

where *k* is the spring constant of the cantilever and *x* is the cantilever deflection. CM is ideal for imaging any stable or hard samples that are not affected by interactions with the tip.

Samples must be firmly attached to not be susceptible to the friction and torsional forces placed upon them by the cantilever tip during scanning. The force applied is usually on the order of few tens of nN but varies with spring constants, and soft, biological samples are often not compatible with this imaging mode[16]. CM does present some advantages in that it can be readily modified to gain nanomechanical information or used with chemically modified cantilevers to provide chemical contrast on the sample[16]. In addition CM is the highest resolution form of AFM as it maintains contact with the sample surface throughout scanning.

Tapping Mode (TM)

This AFM mode is also known as "dynamic" or "intermittent contact" mode to reflect the movement of the cantilever during TM. In all these modes the cantilever is vibrated, and the amplitude, frequency or phase of this vibration is monitored. TM-AFM preformed in ambient conditions involves using an oscillating cantilever near its resonance frequency, usually in order of 100-300 kHz, at an amplitude of 20-100 nm by means of the piezo built into the cantilever holder driving the oscillation (Fig 1.3

B), while work in a liquid environment typically requires a much softer cantilever, with a resonant frequency of approximately 30 kHz. With the advancement of underliquid imaging specialised cantilevers are now available which are ultra-short, and have resonant frequencies closer to that of traditional TM cantilevers[26]. The resonance frequency of the cantilever will depend on its dimensions and material properties, and is easily determined by sweeping through a range of frequencies to detect the response peak. A cantilever will usually have multiple resonance frequencies, but the strongest lowest natural frequency response is typically used for scanning. During the cantilevers oscillation it will “tap” into the sample surface, and this contact creates a change in the resonance frequency and the amplitude of the cantilever. As the cantilever is being maintained at a constant set-point amplitude by the feedback loop (the same principle as during CM) the tip-surface distance is maintained. Any shifts in the amplitude are detected and corrected by the feedback loop producing 3D image maps of the topographical features of the sample.

Phase TM imaging makes use of the specifics of tip-surface interactions which are not just topography dependent, but depend on characteristics such as elasticity, adhesion or hardness. Variations in these properties lead to a phase lag between the cantilevers oscillation and the signal being sent to the piezo driving the oscillation. The phase lag is recorded producing a 3D image map providing a qualitative map of the adhesion, and elastic moduli of the sample. Additionally, features such as sharp edges, which cannot be easily identified in the topography channel, can often be seen in phase, providing there is a difference between hardness and elasticity.

Non-contact modes like TM are particularly attractive for the imaging of biological samples due to the reduced friction placed on the sample. Data gathered in this manner will be discussed later (Chapter 4.2). TM AFM uses the cantilever in the border between attractive and repulsive regime, making use of VDWs forces, consequently a lower force (<1 pN) needs to be applied to maintain the regime.

Ultrasonic Force Microscopy (UFM)

UFM[29] was originally developed to overcome the limitations of the measuring the maximum measurable contact stiffness, which is usually determined by the cantilever's spring constant[1, 2, 17, 30]. Although an approximately spring constant is provided by the cantilevers manufacturer, should quantitative work been undertaken it is possible to accurately calculate a cantilevers spring constant using the Sader method. This method utilises the cantilever's resonant frequency and quality (*Q)* factor, (a measure of the dampening a resonator has), to determine the spring constant[31]. This variation of contact AFM allows qualitative[32, 33] and quantitative[34, 35] measurements of the elastic behaviour of a sample by oscillating the sample at frequencies f well above the cantilever resonant frequency f_0 (typically at f =2-10 MHz compared to $f_0 = 10 - 300\,\mathrm{kHz}$). This out-of-plane vibration of the sample increases the effective cantilever's spring constant due to inertia[29]. In the context of UFM it is assume the cantilever does not vibrate at ultrasonic frequencies, and thus becomes "dynamically frozen" as the ultrasonic vibration of the sample is sufficiently high to prevent the cantilever responding to the sample surface motion. The cantilever's behaviour at this point makes it almost perfectly rigid due to this inertia, and allows the cantilever to indent briefly into the sample surface and pull away, thus probing the elastic properties of the sample surface (Fig. 1.3, C[29]).The elastic indentation of the tip-sample can also be further modified by modulating the amplitude of the sample oscillation.

A vital component of UFM is the use of a piezo-transducer beneath the sample, which converts electrical energy into mechanical energy. By applying and electrical field to the piezo-ceramic disk attached to the metal stub AFM samples are held in place with an ultrasonic vibration can be applied directly to the sample in the *z* axis. The exposure of the ceramic to an AC field will cause it to cycle between expanding and contracting, at the cycling frequency of the field. By vibrating the piezo-ceramic between 2-4 MHz (close to its fundamental longitudinal frequency) its spatial movement can be controlled. The frequency of the vibration applied is controlled tightly by the thickness of the piezo-ceramic used, as thinner disks respond to higher frequencies, and shape and composition can also influence the behaviour of piezo-

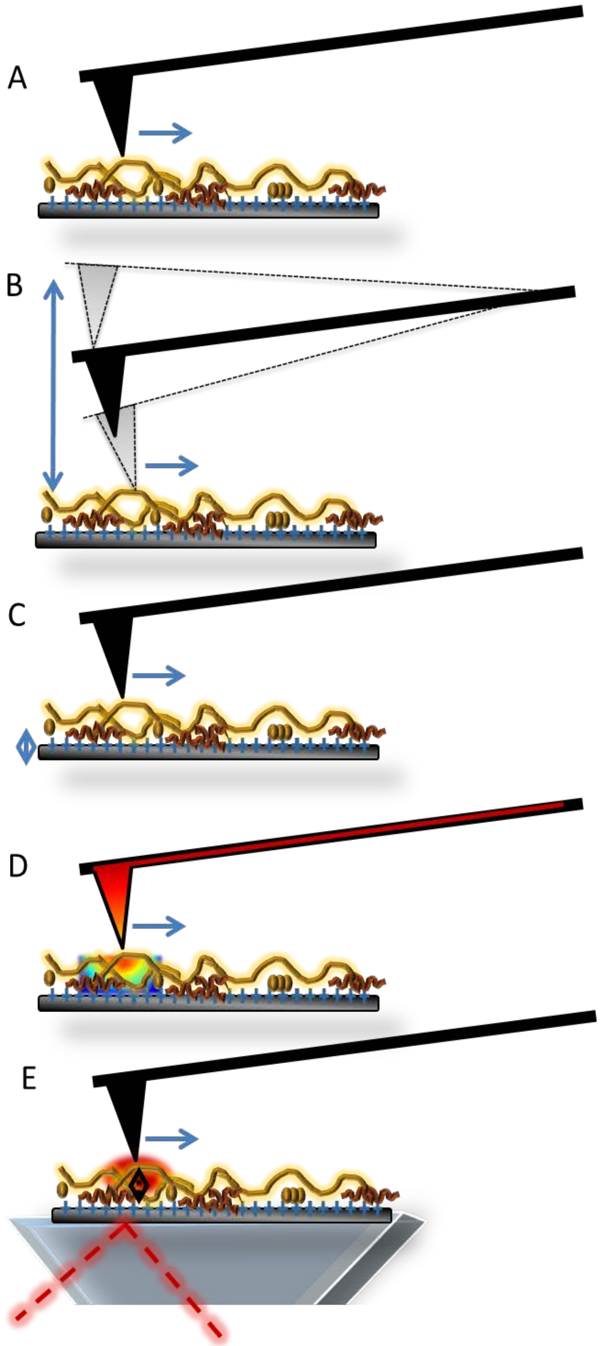

Figure 1.3. This illustration shows the main AFM modes used in this work. (A) Contact mode AFM involves holding the cantilever in the repulsive regime at a set constant height above the sample while recording data on the topology and friction, using a feedback loop. (B) Tapping mode AFM oscillates the cantilever to reduce friction and the force applied to the sample. Phase data can also be collected to show a map of changes in the samples elasticity, (C) Ultrasonic Force Microscopy and (D) SThM; the cantilever is used as a heat sensor, with heat being applied using an AC current. Heat dissipation into the sample can be measured via the cantilever tip. (E) IR-AFM; a pulsed, tunable laser is focused onto the sample, and the IR-absorption of the sample leads to photothermal expansion. This expansion "kicks" the cantilever, leading to deflection and a measureable response.

ceramics.

The tip-surface interaction can be described using the force-vs-indentation curve (Fig. 1.4). As previously mentioned, when the cantilever tip is in close proximity to the sample surface, it experiences an attractive force followed by a repulsive one. As the tip retracts, it remains adhered to the sample surface until the pull-off distance is reached. In UFM an ultrasonic vibration (a) is applied to the sample. If this amplitude, a_0, is small, the tip remains in contact with the sample surface for the full oscillation cycle, and the displacement of the sample is smaller than the initial indentation, so the average force, *F*, does not change (green line). When amplitude is increased to a_1 tip/sample contact is broken for part of the cycle, which creates additional force due to the nonlinearity of the force-vs-distance curve and hence the change in the average F_0 (grey line), which is otherwise known as the "force jump"[1, 2]. This is the threshold amplitude for the UFM, and the point at which the probe breaks free creates the "force jump" in the normal cantilever deflection.

The new force F_m can be calculated from the interaction force between sample and tip as follows:

$$F_m\,(h_1\,,\alpha) = \frac{1}{2\pi}\int_{T_{ul}} F(h_1 - \,\alpha\cos f_{ult}t)dt,$$

where *F* (*h*) is the force dependence on the indentation depth without an out-of-plane ultrasonic vibration; f_{ult} is the ultrasonic frequency; the integral is taken over a period . $T_{ult} = 1/f_{ult}$. When F_m increases due to the non-linearity, the cantilever deflection increases as well until a new equilibrium position is reached. This new stationary normal deflection is given by:

$$F_m\big(h_{eq}, a\big) = k_c\,z_{eq}\,,$$

where z_{eq} and h_{eq} are the new cantilever deflection and sample indentation depth, respectively and k_c is the cantilever stiffness constant.

This pull-off amplitude becomes the threshold amplitude for the system in use, and variations in it allow materials of different elastic properties to be contrasted as it is dependent on both elastic constant and adhesion hysteresis[17]. Adhesion hysteresis is defined as the difference between the work needed to break two surfaces apart compared to the work needed to bring them together[36, 37]. The elastic constant referred to here is the *Young's modulus*, and describes the tensile elasticity of an object, or its ability to deform along and axis when opposing force is applied. Further increases in the averaged force, F_u, leads to an increase of the average cantilever deflection z_0 by z_a, ultrasonic force deflection. As average deflection increases, it can be assumed that the equilibrium modulated indentation ($h_0 + a\cos 2\pi f t$) would decrease by the same amount of z_0.

Variations in the threshold amplitude and force jump depend on the different elastic properties of the sample being scanned, and lead to variation in the ultrasonic deflection. In order to detect the deflection of the cantilever as a response of the sample the amplitude modulation frequency must be carefully chosen. It must be

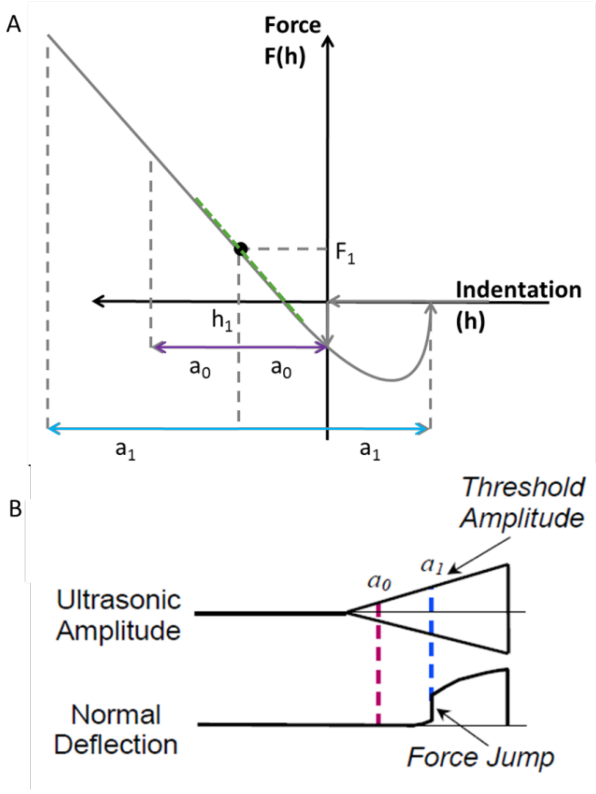

Figure 1.4. (A) typical force-vs-indentation curve. Tip –surface indentation is modulated using ultrasonic vibration at a set amplitude (*a*). A large enough amplitude (a_1) causes a force jump, seen in panel (B) as the tip leaves the sample surface. This force jump is detected as the deflection of the cantilever[1-3]

above the SPM cut-off frequency but below that of the cantilevers resonance and is usually between 0.5-3 kHz. In the case of this system the cut-off frequency was 2.3 kHz. If a value above is used, the cantilevers delay becomes comparable with the modulation period of the amplitude altering the UFM response. Below this frequency, the AFM feedback circuit modifies the ultrasonic deflection[17]. The deflection signal is fed into a lock-in using the modulation frequency signal as a reference, while the output from this lock-in amplifier becomes the UFM image. Another factor for consideration is the profile of the amplitude modulation used. A ramped (symmetrical saw toothed) profile was used throughout the work here but others have been tested. Incorrect selection can result in ambiguity in sample contrast and therefore material stiffness[1, 2]

The role of elasticity and adhesion in UFM

The force it takes to move one atom away from another, or to displace, is connected to the chemical bonds between atoms which determine the equilibrium position of one atom to another. This equilibrium position can be represented as directly proportional to the distance, $F = kx$, where F is the applied force, x is the deformation, and k the spring constant of the material in questions. This is otherwise known as Hooke's law and allows a deduction of the attractive and repulsive forces that govern atoms in an interatomic bond, and provides information about the force needed to break this bond. Hooke's law only describes a linear elastic deformation between bonds however, and caution should be taken when working with materials which have a non-linear relationship such as Silicon Carbide.

The behaviour of such force is linearly elastic and is usually the case for small displacements in most solid materials. However this is a simplified case and in reality the equilibrium position is effected by the forces imposed by neighbouring atoms and the characteristics of the sample[11].

If one atom is pulled away from another Hooke's law provides the maximum value of force required to do so. This breaking of the chemical bond is known as the cohesive strength. After the bond is broken less and less force needs to be applied to keep the atoms separate. The bonds strength is equal to the max cohesive force (Fig. 1.5).

A force displacement curve can be approximated by a portion of a sine function[11] and the region between the equilibrium position and the max force is of most interest. Here

$$F = F_{max} \sin\frac{\pi x}{2L},$$

where L is the distance from the equilibrium position at F_{max}.

For small θ values $\sin\theta \approx \theta$, the force required for small displacements *x* is

$$F = F_{max} \sin\frac{\pi x}{2L}$$

$$F = \left[\frac{F_{max}\,\pi}{2L}\right] x$$

Values L and F_{max} can be considered constant for any one particular material, therefore it becomes $F = kx$ (Hooke's law). This can be extended to a force distributed over a unit area so that

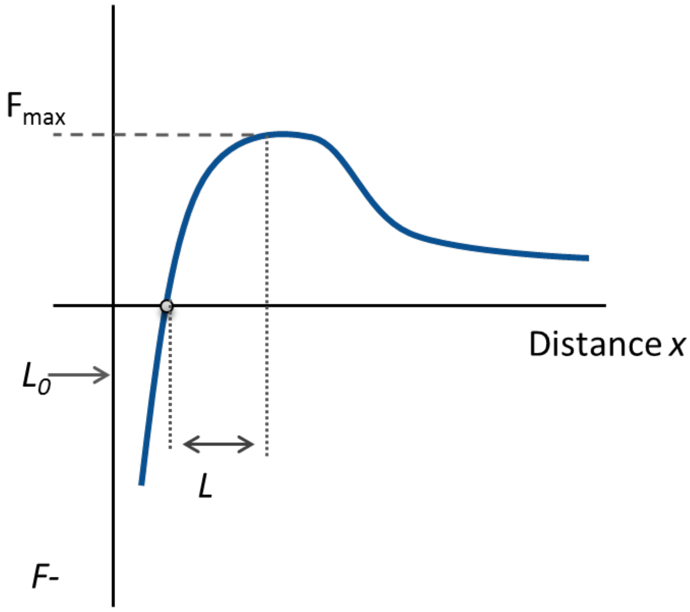

Figure 1.5. The forces between an atom as part of a solid as it is pulled away from its equilibrium position. The short range interactions are governed by repulsive forces, while attractive forces act over a larger distance. F_{max} refers to the strength of the bond and the force necessary to break it. *L* is the distance from equilibrium position.[11]

$$\sigma = \frac{\sigma_{max}\pi}{2L}x,$$

where σ_{max} is the tensile strength of the material and the units of pressure.

If L_0 is the equilibrium distance then the strain ε for a given displacement *x* is defined as

$$\varepsilon = \frac{x}{L_0}$$

$$\text{Thus } \frac{\sigma}{\varepsilon} = \left[\frac{L_o\pi\sigma_{max}}{2L}\right] = E$$

The terms in the square brackets are considered constant for any one particular material, and represent a single material property, *E*, the elastic modulus or Young's modulus of a material. This is another form of Hooke's law where stress is considered proportional to strain.

UFM can be used to discriminate between the elastic properties of materials by using this Young's modulus[2]. The Johnson-Kendal-Roberts[38] (JKR model) can be used to model the tip-surface interaction and adhesion hysteresis seen in UFM. In this model the contact area r_c between 2 spheres is given by

$$r_c^3 = \frac{3R}{4E_r}\left[F + 3\Delta\gamma\pi R + (6\Delta\gamma\pi RF + (3\Delta\gamma\pi R)^2)^{\frac{1}{2}}\right],$$

where $\Delta\gamma$ is the Dupré work of adhesions, *R* is the tip radius on a perfectly flat surface, E_r is the reduced Young's modulus and *F* is the normal force being applied in the system.

Indentation depth h of the cantilever in a system is then calculated using:

$$h = \frac{r^2}{R^*}\left[1 - \frac{2}{3}\left(\frac{r_0}{r_c}\right)\right]^{\frac{3}{2}} \text{ is normalised to}$$

$$h_0 = \left(\frac{\Delta\gamma^2\pi^2 R}{E_r^2}\right)^{\frac{1}{3}}$$

Where the contact radius at zero normal force is r_0 and is equal to:

$$r_0^3 = 6\Delta\gamma\frac{\pi^2}{R^*}E_r$$

Which is normalised to $F_0 = \Delta\gamma\pi R$.

Materials that are more compliant have higher threshold amplitudes and adhesion hysteresis. This in turn will lead to an increased discontinuity at the pull-off point and subsequently the force jump of ultrasonic deflection. A more adhesive material will also have the same consequence. Simulations of the contact mechanics of UFM have shown that the threshold amplitude increases with increasing force, and also by reducing Young's modulus or increasing adhesions, and that the latter two factors will lead to an increase in the force jump detected by the system[1, 2]. It can therefore be difficult to distinguish between higher adhesion or increased compliance of a material, without additional information, such as friction behaviour. Topographical artefacts can also interfere with the adhesion properties or a material.

Caution should be taken with the above model of UFM as it can be considered over simplified. UFM as a technique is not without limitations; it does not take into consideration phase information and is therefore unsuitable for characterising materials with high viscoelastic properties (where indentation is time dependent)[1], surface topography and adhesion can affect quantitative analysis when preformed (only the elastic properties of the sample and tip-sample interactions are considered by this model)[39], and thirdly adhesion forces are assumed to be uniform across the sample surface and contrast comes only from the change in the samples elastic properties, which can prove challenging for thin films or polymeric structures[1, 2, 17]. In addition any sharp changes in topography can affect the threshold amplitude and subsequent image contrast making the interpretation of the surface mechanical properties more challenging.

Scanning Thermal Microscopy

Scanning Thermal Microscopy (SThM) was originally developed in 1986 by combining STM with a thermal field to control the tip-sample height while probing the samples thermal properties[40, 41]. Several advances have occurred since the techniques initial development, reviewed extensively by Majumdar[42, 43]. The adaption of CM AFM used in this work allows the mapping of the local thermal properties of a sample by scanning the sample surface with a specially adapted cantilever which acts as a thermal sensor (Fig. 1.3, D). As with all AFM techniques information is gained on nanometre scale resolution. Joule heating is used to heat the tip while in contact with the sample. Heat diffuses from tip to sample due to the temperature difference between them, and is proportional to the thermal conductivity of the sample and the tip. This subsequently changes the sensor temperature which is recorded as a change in the sensors electrical resistance, measured as the current flowing into the electrical bridge. This current change is ultimately used to produce the thermal image.

The stationary diffusive heat transport equation is used to describe the heat transfer process in SThM,

$$\rho C_P \frac{\partial T}{\partial t} - \nabla(k \nabla T) = Q ,$$

Where p is the density of the material, C_p is the heat capacity, k is the thermal conductivity and Q is the heat source. In some samples there can be deviations from the diffusive heat transport model, such as at the end of the tip or in highly thermally conductive samples. In these samples the ballistic heat transport is significant and should be considered.

Heat flow into the sample is governed by the thermal resistance of the tip-sample contact, and is connected to the samples thermal conductivity, k. If the samples thermal conductivity is less than that of the probe then the measurements are dominated by the thermal conductivity of the sample[44]. Thermal conductivity is determined by the free path of phonons in the material, l, where

$$k = Cvl$$

and C is the specific heat and v the speed of sound in the sample. To calculate the temperature difference between the probe and sample ΔT and the heat flow (per unit time) ΔQ. Ultimately

$$\frac{\Delta Q}{\Delta T} = k_{sample}\pi R,$$

where R is the contact radius, which is pressure dependent.

The cantilever operation in SThM depends to a degree on the application it is being used for; thermomechanical data writing has very different needs to the nanoscale deposition of materials[45]. The application of SThM for the study of amyloid fibres is particularly useful and several studies have looked at the thermal properties of amyloid proteins during aggregation. Amyloid proteins by nature are display a high level of thermal stability, due to the thermodynamically favourable state of the aggregated form[46]. Dandurand[47] and colleagues (2014) recently showed the aggregation of a synthetic peptide, S4, could replicate that of amyloid fibres when under the correct conditions. Aggregation leads to an increase in thermal stability linked to the typical conformational change to a cross-β structure. Thermodynamic stability has also been linked to the folding and unfolding in Light Chain Amyloidosis[48]. Amyloid proteins have also been shown to undergo thermally induced melting, and unfold to their native conformations, a change which was not linked to their morphoplogy[49].

Nanoscale Infrared Spectroscopy as an extension of Contact Mode AFM

A new extension of CM AFM involves combining IR spectroscopy techniques with an AFM cantilever as the nanoscale detector of the IR light absorption. This allows the optical diffraction limit of 10-30 µm to be overcome and provide spatial resolution on the order of 10-100 nm, and also overcoming a limit of AFM: the provision of chemical characterisation of a sample. This spatial resolution is improved upon compared to typical FTIR imaging, which is limited by the fundamental limit of twice the wavelength (10-30 µm) and also Attenuated Total Reflectance (ATR) which is limited by λ/2 (3-10 µm). In comparison Scanning Near-field IR Microscopy (SNIM) is also able to produce a resolution of 10-30 nm. IR-microspectroscopy allows the mapping of samples to produce a spatially resolved map of their chemical content.

AFM-IR was one of several techniques that resulted from the development of a tuneable Free Electron Laser (FEL) at CLIO (Centre Laser Infrarouge d'Orsay, Paris)[50] and showed the most promise for development. After consideration was given to the theoretical principles behind AFM-IR[51], the first experiments were conducted using the tuneable FEL teamed with an AFM to map the local transient deformations induced by IR light at sample specific wavelengths[19, 52, 53].

The principle of AFM-IR (Fig. 1.6) is simple, instead of a traditional laser light being shone onto the cantilever for detection of movement/mechanical responses of the sample, a pulsed, tuneable IR laser is used to illuminate the sample which is sat upon a ZnSe prism. This IR radiation will locally heat the sample via vibrational excitation of the sample molecules, which leads to rapid photothermal expansion of the sample. This local expansion is the result of the absorption of the IR radiation by the sample and it’s transmission through the sample by phonons within the sample lattice as a thermal wave. This occurs in a short pulse of expansion detected by the cantilever tip, (see Fig. 1.3, E. for an overview of the cantilever detection). This pulse “kicks” the cantilever, and the ringdown of this kick can be measured, making it possible to extrapolate the amplitudes and oscillations of the ringdown for further analysis. In the case of the Nano-IR system developed by Anasys Instruments (Santa Barbara, USA) the IR absorption spectra which are obtained from the sample by measuring the photothermal expansion as a function of the wavelength of incident laser light. By tuning the laser to a specific absorption band the sample is then mapped for its photothermal response at that wavelength, but on the resolution level of the cantilever tip, not the optical diffraction limit. The sample stiffness can also be determined by studying the oscillation frequency of the cantilever ringdown. A thorough discussion of the details of the AFM-IR technique have been set out recently by Dazzi[18]. This technique is reliant on exciting molecules via local heat absorption, and the propagation of the thermal waves this induces sample thickness is vital. The Nano-IR2 system can image samples approximately 20 nm thick but is optimal for samples 100-1000 nm thick, while thicker samples can be imaged with the original Nano-IR system.. Detection of the IR induced thermal expansion is more challenging in samples whose thickness is on the order of microns.

The field of microspectroscopy is highly applicable to the study of biological samples, and the Nano-IR has proved to very popular in this respect. Selected areas of application are not limited to, but include, plants cells[54], lipids within the human cornea and hair[55, 56], pharmaceuticals[57], bone and other mineralised samples[58-60], cells[61] and also for detection of cancer biomarkers in a variety of cancers[62-65]. The

most relevant application of AFM-IR to the work shown in this thesis is that conducted by Műller and colleagues[66]. A microstamp was used to deposit droplets of monomeric and aggregated lysozyme onto a ZnSe prism, and were able to differentiate between random coiled and β-sheets, which is a typical structural transition for amyloid proteins.

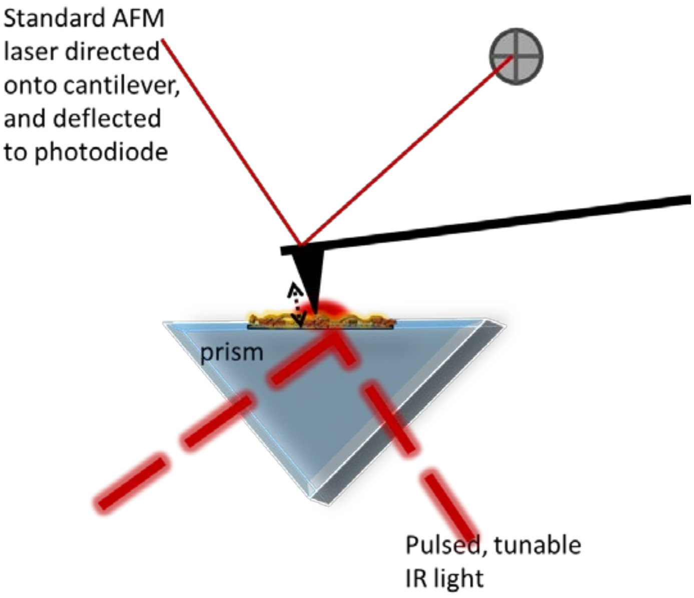

Figure 1.6. The principle of Nano-IR. A pulsed and tuneable IR source is directed though a ZneSe prism, (from underneath), and onto the sample. The photothermal expansion of the sample "kicks" the cantilever, the movement of which is detected by a standard CM setup of a laser focused onto the cantilever and its deflection monitored. The ringdown of the cantilever produces the deflection, while its amplitude and absorption as a function of the wavelength can also be extracted.

1.3 Dynamic Light Scattering (DLS)

Also sometimes referred to as Quasi-Elastic Light Scattering, DLS is an ideal technique for characterising particles in suspension in the sub-micron range. A highly sensitive technique it can readily be used to detect macromolecules such as proteins in solution.

In order to determine the size of a particle the Brownian motion of the particle can be measured. Particles such as proteins within a suspension are subject to random motion caused by interactions with the solvent molecules within the suspension. Brownian motion is linked to the size of the particle as larger particles are influenced less by the solutes within the suspension, and move slower than smaller particles which are moved more rapidly. Two other important factors in accurately measuring the Brownian motion of a particle and thus determining its size are the temperature of the solution, and its viscosity. A stable temperature during measurement is essential to prevent random movements of the particles within the suspension. The speed at which a particle moves at is known as the translational diffusion coefficient (*D*).

Using *D* the hydrodynamic radius of a particle can be calculated via the Stokes-Einstein equation;

$$d(H) = \frac{kT}{3\pi\eta D}$$

Where *d(H)* the hydrodynamic diameter, *k* the Boltzmann's constant, *T* the absolute temperature and *η* the viscosity. The Stokes-Einstein equation assumes that the particle being measured is spherical, so caution must be used when measuring larger, fibril like particles whose dimensions are not spherical. Determining the hydrodynamic radius of a particle is also influenced by any surface structures on the particle, such as charged residues, which may affect its diffusion speed.

In order to collect data on the particles size as a function of its translational diffusion, DLS, as its name suggests, involves collecting information on the scattering of light by the particles in a solution. Typically a HeNe laser is used to create this scattering by illuminating the sample. Depending on the scattering angle data is either collected using forward or back scattering light. Back-scatter has significant advantages over forward scattering, as the light does not have to completely penetrate the sample, removing any conflicting scattered light from neighboring particles. Time dependent fluctuations in the scattered light are measured using a fast photon counter[67] In addition, large contaminants like dust particles typically scatter light forwards and are therefore not likely to be detected. Larger particles will scatter light further and with greater intensity than smaller ones, and also obscure any nearby smaller particles scattered light, leading to a misrepresentation of the sample contents. Larger particles move much slower than smaller ones, due to the greater effects of Brownian motion upon them, and also scatter light further due their increased size (the scattering of light is proportional to the sixth power of its diameter from Rayleigh's approximation). Smaller particles conversely will scatter light with faster intensity fluctuations, as this is connected to the speed of the particles in motion. Factors such as sample concentration can also affect the signal detected using DLS, as more concentrated samples will behave in a manner similar to large particles, in that they will scatter more light and swamp the signal of neighboring particles.

DLS has been used to great success to study the aggregation of Aβ1:42, both alone and with potential pharmaceutical interactions[68-71]. One study has shown that Aβ1:40 samples can initially be detected at ~7 nm in size and monodispersed, indicating a uniform population structure. As aggregation persisted this population became more polydispersed as aggregates ranging from 10-52 nm in size were detected. Larger aggregates at later time points, more akin to fibrils were not detected by DLS, but detectable by Multi-angle Light Scattering[72-74]. In contrast the monomeric form of Aβ1:42 is 1-2 nm in diameter[75, 76]. Cizas et al (2010) noted that Aβ1:42 monomer size is particularly sensitive to different preparations, or deseeding techniques. Pretreatment of Aβ1:42 with HFIP produced monomers ~2 nm in size, while agitation of this sample produced monomers of 8 nm in size. This technique has also been used to monitor the effect of metal ions, and their chelators, on Aβ1:42 aggregation and for complex studies of aggregation kinetics[77]. It is therefore possible to use DLS to monitor the temporal change in aggregate sizes of Aβ1:40/2. A disadvantage of DLS is that no details of the population sizes i.e. monomer/dimer/trimer can be determined. It is for this reason DLS is best used in conjunction with other techniques, such as AFM[75, 76] or ThT[77].

1.4 Direct imaging via AFM and Electron Microscopy studies of Aβ1:42 and their findings

The pathology of AD and aggregation process of the main pathogenic component of the disease, Aβ, will be discussed in more detail in Part B of this literature review. Here we will focus purely on the information about Aβ which has been gained from the application of physical techniques, most notably cryo-EM, STM and AFM.

It has been over a decade since Aβ was first imaged using AFM; in 1999 Blackley[78] and colleagues successfully imaged Aβ1:40 and followed the aggregation of the peptide using TM AFM. Immediately after wetting the peptide was visible as small spherical aggregates, before fibrillisation commenced. Fibrillisation took the form of the spherical aggregates interacting to become short fibrillary structures which later elongated, occasionally becoming branched structures. The detection of a period twist of approximately 25 nm on some mature Aβ fibres was also an important discovery. In addition the transient nation of oligomeric units of Aβ was noted.

The first time point noted using an AFM, and most crucial for studies of pharmaceutical and neurotoxic behaviours, are the early aggregates. Several studies have confirmed the monomer has an spherical appearance and is approximately 2 nm in size[75, 76, 78, 79], which correlates well with DLS and other techniques. Dimers of Aβ are typically around 4 nm in size and maintain an elliptical state[79].

Morphological differences between the two main isoforms of Aβ can be detected at later stages of aggregation; Aβ1:40 protofibrils are smaller than Aβ1:42, (3.1 ±0.31 nm compared to 4.2±0.58 nm), however both forms of protofibrils were typically 50-200 nm long and curved in appearence[80, 81]. The difference in widths of the two protofibrillar isoforms can be attributed to the additionally amino acid residues in

Aβ1:42[80]. Later aggregates have been classified further with the aid of AFM to be either type I (~5nm high, 600 nm long[80-83]) or type II structures. Type II fibres are longer, (>1 µm), between 6-13 nm wide, and often have a branched or junctional morphology[80, 84, 85]. Type II fibrils are the mature fibres produced after several protofibrils have elongated, interacted and twisted together[84].

Aβ fibres are highly polymorphic in nature due to the stacking nature of the β-sheets, and their morphology can be surface dependent. Aβ1:42 deposited onto Highly Ordered Pyrolytic Graphene (HOPG) forms ribbon like protofibrils as opposed to cylindrical ones on mica[86] while positively and negatively charges surfaces have

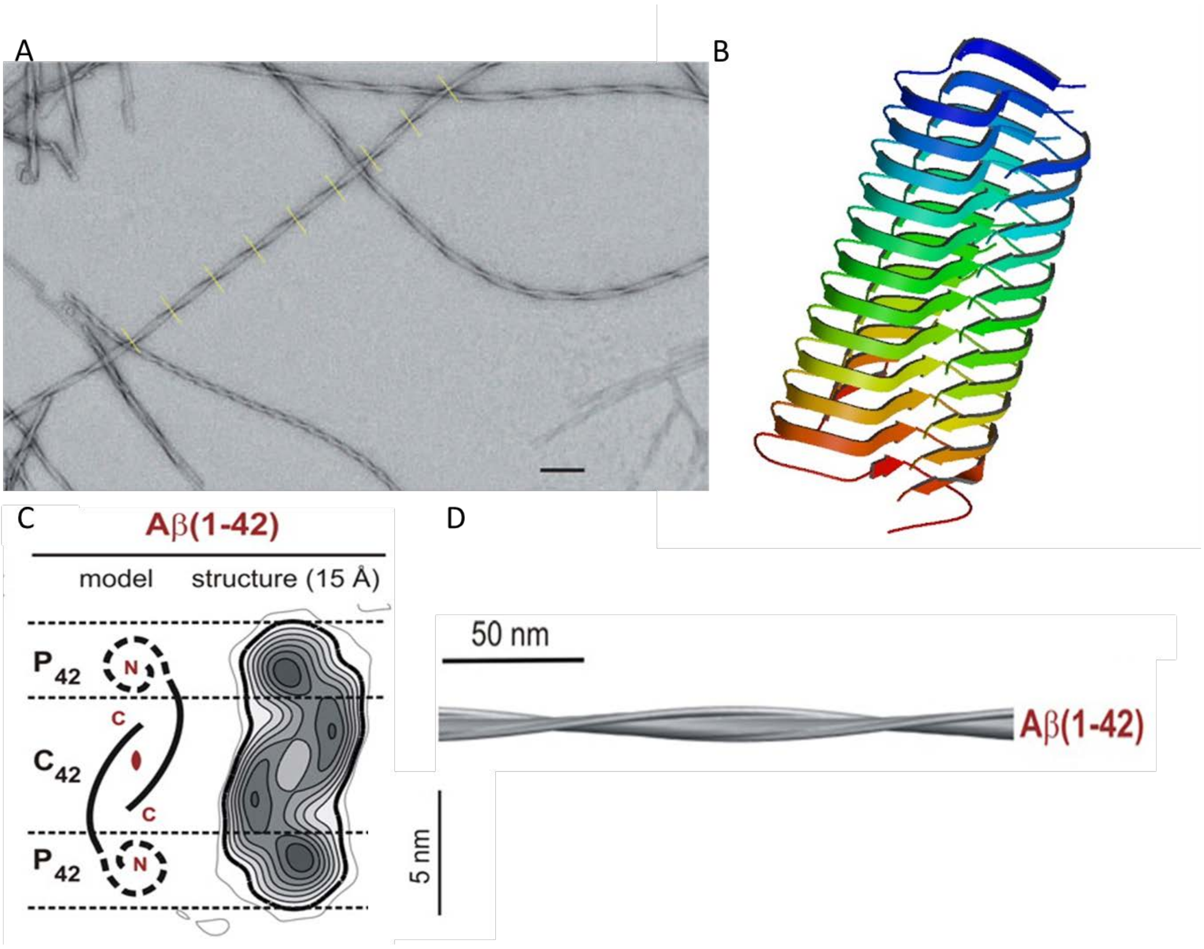

Figure 1.7 The structure of Aβ fibres. (A) EM imaging of Aβ1:40 fibres reveals a two protofilament structure periodicity, with the twist indicated by the yellow line[10]. (B) Solid State NMR data suggests Aβ1:42 has a triple β sheet motif with hairpin turns surrounding a central core[3]. (C & D) advanced cryo-EM work suggests reveals the structure of the protofilaments within a fibre: Aβ1:42 is made of of two peripheral regions surrounding a central core, which itself has a region of lower density and two higher density packed cores[10, 12].

different effects on aggregation. Adjusting the surface of the substrate to become more hydrophobic by CH_3 modification leads to the formation of spherical and amorphous aggregates which cluster together in a dense surface covering, and while surfaces modified with COOH or NH_2 also showed an initial covering of spherical aggregates ~2nm high, these elongated rapidly into mature fibres[87]. It was proposed that the hydrophobic surface promoted the formation of alpha helix dominated aggregates, while charged surfaces will interact with the charged regions within Aβ leading to the promotion of β-sheets, and therefore fibre formation[87]. The periodicity of the twist often seen on amyloid fibres can also be affected by the surface the protein is deposited onto, or aggregated on. A right handed helical periodicity has been noted for deposition on HOPG[88] while hydrophilic surfaces lead to a left handed helix forming[80, 82].

One of the most significant features of amyloid fibres for which evidence is hard to gather is that of the substructure. It is well established that mature amyloid fibres are made of multiple protofibrils, or elongated protofilaments, twisted together, but debate still exists about the exact number which occur in Aβ1:40/2 and the substructure that their interaction creates. Imaging of MF by TEM has shown that Aβ fibres have a polarity or directionality to their structure[89]. It has been suggested from STM images of MF of Aβ1:42 that these fibres are made of 1 or 2 intertwining protofilaments[12, 82, 90, 91], each of which is made of two protofibrils with its own has a cross-β structure[92, 93]. A hollow core within the MF was been detected by EM in 1986[90] and numerous times with STM, but not AFM[88, 94, 95] (Fig. 1.7). Recently it has been proposed that the internal structure of Aβ1:42 is composed of two peripheral regions surrounding a central core, which itself has a region of lower density and two higher density packed cores[12, 89, 91]. Cryo-EM techniques have so far proven to show the most detailed information about Aβ internal structure and morphology, and the higher density regions have been linked directly to the hairpin turn produced by the β-sheets[91]. More importantly differences between the morphology of Aβ1:40 and 1:42 have been noted using cryo-EM and STM. The central hollow core seen in Aβ1:42 is lacking in Aβ1:40, with the higher density region extending the whole cross section of the fibre[91]. This increased width for Aβ1:40 MF indicates that the high density regions are composed of more β-hairpins than the longer isoform, potentially indicating that Aβ1:40 is made of 2 intertwining protofilaments, each made of 2 protofibrils[89, 91] (Fig.1.7). However multiple reconstructions of the Aβ1:40 MF indicate different structures suggesting that incubation conditions, sample preparation, substrate deposition and numerous other factors could all affect the structure ultimately formed. Models have proposed anything from 2-3 protofilaments interact together to produce the MF[12, 96, 97], with multiple morphologies within the same sample possible due to differences in inter- and intra-residue interactions[97].

1.5 Conclusion

Here we have discussed the key physical techniques employed in this thesis to study Aβ1:42 during its aggregation. Multiple modes of SPM have been employed. While TM is the most commonly used AFM mode for imaging biological samples it fails to offer any insights into chemical, thermal or nanomechanical properties. These insights can be gained by employing adaptions of CM AFM to produce techniques such as UFM, SThM and AFM-IR (commercially available as the Nano-IR system). The differences between the data which can be gathered by these techniques has been discussed above. In addition mention is given to DLS, which can offer detailed analysis of particle sizes and population dynamics over the aggregation timecourse.

In order to understand more about the morphological behaviour and structural details of biological materials it is necessary to move beyond modelling their structures based on computational techniques, and study their aggregation in reality. Techniques such as EM, STM and AFM allow one to see a snapshot of the aggregation state of peptides like Aβ1:42, and make connections with the theoretical models. AFM and cryo-EM have provided a detailed image of what the MF of Aβ looks like, and how it forms. When used in conjunction with techniques such as FTIR (or other spectroscopy methods) or DLS applications commonly applied elsewhere can provide a powerful arsenal for the study of amyloid peptide aggregation.

Chapter One: Theoretical concepts and Literature review

Part B: Alzheimer's disease and the Aggregation of Amyloidβ

1.6 Introduction

The amyloidoses are a group of diseases which are characterised by the pathogenic feature accumulation of an amyloid protein[6, 98, 99]. Amyloid proteins form extracellular, fibrillar deposits which accumulate over time, and in the case of brain amyloid disorders, lead to the progressive death of neurons in different parts of the Central Nervous System (CNS), and presentation of degenerate neurological features[100]. In addition to AD Parkinson's disease, motor neuron disease, Huntington's disease and prion diseases are all categorised as amyloid disorders. All amyloid proteins share several characteristics; they undergo a hierarchy of aggregation into highly β-sheeted, insoluble fibres which can be detected by binding to dyes such as Congo red or Thioflavin T (ThT)[98, 99]. The mature amyloid fibres are typically 7-10 nm wide and made of subunits composed of a particular amyloidogenic protein or peptide.

It has been over 100 years since the first description of a patient with AD; in 1907 Alois Alzheimer published details of a 51 year old female with severe memory problems, disorientation, aggressive behaviour and hallucinations. Following her death histological examination of her cortical grey matter showed the presence of focal lesions between nerve cells and dense, fibrillar bundles within nerve cells themselves. It was this combination of senile plaques, neurofibrillary tangles and presenile dementia (i.e. with an onset of <65 years), which has become the disease Alzheimer lent his name to. More commonly AD now also includes those with plaques and tangles but also a more common senile form of dementia (>65 years onset).[4, 101]

Research in more recent years has come to universally determine that the main pathogenic factor behind the development of AD is the accumulation of the peptide

Amyloid-beta (Aβ), which exists within the brain in numerous isoforms. The accumulation of this peptide via its aggregation process is the initial and central step of disease pathogenesis[102]. Evidence for this comes from numerous sources, not least the fact that transgenic Mice which overexpress the precursor peptide for Aβ have a similar spatial and temporal pattern of amyloid plaques to human AD patients[103].

In this section of the literature the general pathology of AD will be discussed, along with details of the possible toxic mechanisms behind this disease. The biological processes which lead to some of the morphological features detected in the previous section of literature, by techniques such as AFM and DLS will also be discussed. Lastly possible treatments for AD are focused on, in line with later work carried out as part of this thesis.

1.7 Symptoms and Diagnosis

In AD it is thought that neurodegeneration begins 20-30 years before presentation of clinical symptoms[101]. Typically AD is a progressive disorder, and clinical symptoms include a loss of speech and/or word recognition, loss of voluntary movements and poor object recognition. Cognitive decline gradually occurs, which slowly advances to severe memory loss and increased behavioural problems, including confusion and aggression[99]. Ultimately this decline in cognitive function leads to dependence on nursing care, and death, typically 8 years from diagnosis[99]. Diagnosis usually involves clinical observations and cognitive assessments, however post mortem diagnosis is still the definitive method for confirming diagnosis[104]. Brain atrophy can also be measured using structural MRI scans, and it is also possible evaluate a patients bloodflow and metabolic processes to aid diagnosis[104]. The most promising line of enquiry to improve diagnosis is the move to develop a biomarker test to quickly diagnose or monitor potential cases. In the USA a panel of 8 biomarkers is used in conjunction to aid diagnosis, and includes measuring CSF levels of Aβ (1:40/42), tau, specific plasma phospholipids and phosphatides[104].

One clinical method of determining whether an individual has AD is to evaluate their cognitive abilities. Mild Cognitive Impairment (MCI) is where memory impairment is poorer than expected, but not severe enough to be defined as dementia. It has been shown that around 12% of patients with MCI will convert to AD each year, and that the development of MCI in these patients separates them as a subpopulation with preclinical AD[105, 106]. Clinical diagnosis alone is not infallible, with the "gold standard" AD cognitive function test now being thought to give numerous cases of false positives in those with borderline MCI[104].

The protocol for the most promising method of diagnosing AD is currently under development and involves the use of biomarkers in conjunction with brain imaging, well before MCI and other cognitive features can be noted[105]. There is some indication that this technique can lead to the correct diagnosis of patient's pre-MCI, making them the ideal targets for early acting AD pharmaceuticals. However more research is needed to determine whether biomarkers and imaging can successfully identify all pre-AD patients, and if so, how they will be implemented as an early detection system[105].

Numerous risk factors have been identified, and include but are not limited to; age, brain injury, vascular disease and low brain reserve capacity[99]. Although the vast majority of cases of AD are sporadic and have no known cause, a small minority (~5%) are inherited in an autosomally dominant fashion. Familial AD (fAD) is a more severe disease, with rapid and aggressive onset and progression of presenile dementia.

1.8 Pathology and physiology

At a tissue level there are three main components to the pathology of AD, extracellular senile plaques, intracellular neurofibrillary tangles and cerebrovascular amyloid deposits, mainly found in the hippocampus and fronto-temporal cortex[107], (Fig.1.7). Within the core of these senile plaques are deposits of amyloid fibres, which accumulate in the form of radiating fibres[99, 108]. The principle component of these amyloid deposits is Aβ1:39-42 [108] with a strong link between isoform length and pathogenisis.

Knauer and colleagues (1992) were among the first to note that Aβ accumulates within cells in a stable manner, and that isoforms <39 residues in length failed to accumulate, whereas the 42 residue isoform showed the highest propensity foraccumulation[109]. Only peptides 42 residues and longer are insoluble, and depending on the pH, peptide concentration and incubation time/media this insolubility and aggregation tendency can be moderated[110]. Overall it is Aβ1:42 which is the most pathogenic of all commonly found isoforms, with the most rapid aggregation process, capability of seeding the aggregation of monomeric samples of Aβ, thus stimulating their conversion to insoluble fibrils and its dominant presence within senile plaques (Fig.1.7, A)[107, 109, 110].

The other components of AD are the neurofibrillary tangles which are found inside nerve cells, occupying most of the cytoplasm and disrupting cell processes (Fig.1.8, B). They are composed of a microtubule associated protein called tau, and in AD a phosphorylated form of tau aggregates into paired helical filaments. These filaments

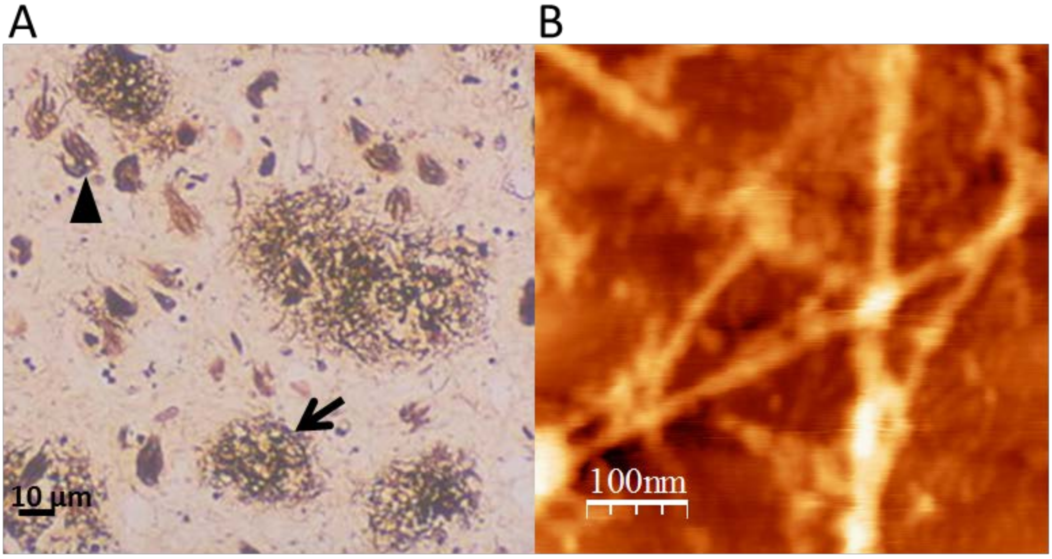

Figure 1.8. (A) Histology sample from an AD patient. Senile plaques composed of Aβ are indicated by the arrow while the arrowhead indicates a neurofibrillary tangle. This image was taken by silver staining a sample of brain cortex and provided courtesy of Prof. D.M.A Mann, University of Manchester (UK). Panel (B) shows AFM of recombinant Aβ fibres, aggregates for 72 h. It is this peptide which forms the core of the senile plaques seen in AD patients.

are composed of two individual 10 nm tau filaments wound together to create a double helix[101, 111].

The combination of amyloid deposits and neurofibrillary tangles leads to extensive neuronal and synaptic degradation, early oxidative damage, an inflammatory response from activated neighbouring glial cells and ultimately loss of function of the cholinergic neurotransmitter system[4]. Over time there is also a substantial loss of brain weight[4]. Cerebrovascular deposits of Aβ1:42 are also common, as the peptide also accumulates in cerebral blood vessels, sometimes leading to brain haemorrhage[4, 101].

1.9 Epidemiology of AD

Currently AD represents the leading cause of dementia in the elderly, with 11% of those >65 being affected, and 32% of those >85 years[112]. Overall the incidence of dementia doubles ever 5 years after the age of 65, and the >90 population is the fastest growing age group in the US alone[113]. As humans begin to live longer diseases of aging, such as AD, are set to become an increasing problem. The prevalence of AD is set to increase rapidly, from 36 million cases worldwide in 2010, and to double approximately every two decades. In the UK alone there are predicted to be 850, 000 cases in 2015[114]. By 2030 there are predicted to be 66 million cases worldwide and 115 million by 2050, suggesting that 1 in every 85 individuals would have AD by this date[115]. Equally concerning is the burden that this places on healthcare systems, as current treatments are ineffective at halting the progression of AD for long, and no cure or ability to reverse the disease has so far been found. It is estimated that 43% of current cases need high level care (nursing home), and only a modest improvement in therapeutics or delaying of disease onset could dramatically reduce the burden for future generations[115]. The total cost of dementia in the UK is estimated to be £26.3 billion, when healthcare, social care and research funding is taken into consideration, with a cost of £4.3 billion directly incurred by the NHS[114].

1.10 Genetic risk factors associated with AD

As already stated, only a small minority of cases of AD are familial (fAD), and these have been studied in detail to try and determine the causative process behind sporadic cases. Autosomally dominant fAD gene mutations are located in genes controlling the production or aggregation of Aβ, and include the gene encoding Amyloid Precursor Protein (APP), or the genes responsible for Presenilin I, and to a lesser extent Presenilin II[116]. So far 25 mutations of the APP gene have been identified, and are responsible for about 1% of all fAD cases[117] (Fig. 1.9). Mutations which affect the processing of APP can also be found in one of the enzymes (namely γ-secretase) responsible for the generation of the peptide. There are three clusters of mutations due to amino acid substitutions within the APP gene which have been identified, each located close to one of the secretase cleavage sites. These mutations have the effect of either increasing the production of Aβ1:42 over shorter isoforms (γ-secretase cleavage site mutations) or increasing the overall production of the full length Aβ peptide (α- and β-secretase cleavage site mutations)[101, 116, 118] . A fourth cluster of mutations, just downstream from the α-secretase cleavage site at residues 21-23 gives rise to the A21G (Flemish), E22Q (Dutch), E22G (Arctic), E22K (Italian), and D23N (Iowa) mutations[116]. The latter mutations all affect the aggregation of Aβ. For example, the Flemish mutation increases the amount of Aβ1:42 being produced by increasing β-secretase cleavage activity, while the others all increase the rate of fibril formation by enhancing production of the more amyloidogenic Aβ1:42.

Mutations in the Presenilin genes are responsible for the majority of fAD cases. Presenilin I and II are located on chromosome 14 and 1 respectively, and mutations in these genes also lead to increased Aβ1:42 production and alterations in the processing of APP[116]. The two Presenilin genes, PSEN1 and 2, code for the presenilin component of the catalytic complex within γ-secretase which is essential for the successful cleavage of APP[116]. The first case of AD in 1907 is most likely to have been the result of a mutation in the Presenilin 1 gene[119].

Genetic studies have also provided evidence for the confirmation that Aβ is the pathogenic factor behind AD. Individuals with Down's syndrome will frequently develop a condition similar to fAD, in that their cognitive function declines due to an increased accumulation of senile plaques and neurofibrillary tangles within their hippocampus and other regions of the brain. Trisomy 21 results in 3 copies of the APP gene, and therefore overproduction of Aβ, accelerated deposition and formation of plaques and tangles.[116] Some cases of fAD have also been caused by APP gene duplication, although very rare, while in contrast one mutation in APP (A673T) is protective from AD, by inhibiting the β-secretase cleavage and therefore Aβ production[116, 120].

Another common risk factor for consideration in pre-senile AD is the number of apolipoprotein (Apo) E4 (ε4) alleles an individual possess. ApoE is a major apolipoprotein expressed in the brain, and is a vital lipid and cholesterol transporter with a role in neuronal repair[121]. The ε4 variant is less efficient at recycling lipid membranes and facilitating neuronal repair, indicating a link between vascular disease, dietary fat intake and AD development, and possession of the allele lowers the age of AD onset by approximately 10 years[121]. Heterozygote individuals are 3 times more likely to develop AD, while homozygotes are 8 times more likely to develop AD, than individuals with no ε4 alleles. Apoε4 has also been shown to promote the aggregation of Aβ and its deposition while conversely the ε2 variant has been shown to be protective[122, 123]. This particular isoform is also less resistant to

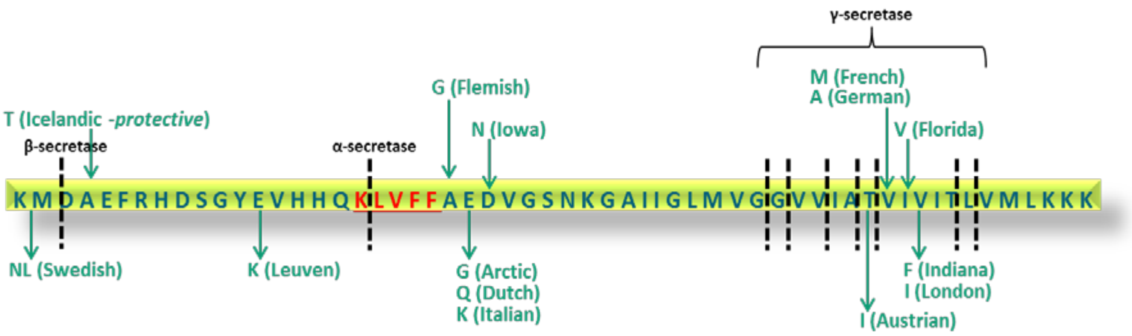

Figure 1.9. Mutations of APP are typically located close to the cleavage sites for the three secretases responsible for releasing Aβ into the cell. These mutations either increase release of Aβ by downregulated the α-secretase pathway, or increase β- and γ-secretase cleavage. Mutations also exist which increase the amount of APP which is produced and consequently the amount of peptide released from the

oxidative damage and stress, thought to be key components of the neuronal damage seen in AD patients[124]. There are also established links between ε4 and other neurodegenerative diseases, suggesting that its effect on the development of AD is both dependent and independent of its interaction with Aβ.

1.11 The Amyloid Precursor Protein

Isoforms of Aβ are released from a precursor protein during a series of regulated cleavage steps involving multiple enzymes. The Amyloid Precursor Protein (APP) is a cell surface protein with a large NH_2 extracellular sequence, a single transmembrane region and a short COOH cytoplasmic tail[5], (Fig.1.9). The precursor protein is 695-770 amino acids long, with Aβ located 99 residues from the cytoplasmic tail[6]. Its physiological role remains uncertain but several potential roles have been suggested, including intracellular calcium regulation[125], metal ion homeostasis[126] and regulation of cell growth[127]. The large extracellular domain of APP contains a metal binding domain, which has a strong affinity for copper[126]. Disruption of the APP gene produces a “fail to thrive” phenotype in mice[128], while evidence for a role in metal ion homeostasis is suggested by APP knockout mice having elevated copper levels within the brain and other organs[129].

APP has a short half-life and is metabolised rapidly[128] down one of two pathways: the amyloidogenic or non-amyloidogenic pathway. APP is cleaved in a process known as Regulated Intramembrane Proteolysis (RIP), which involves two consecutive

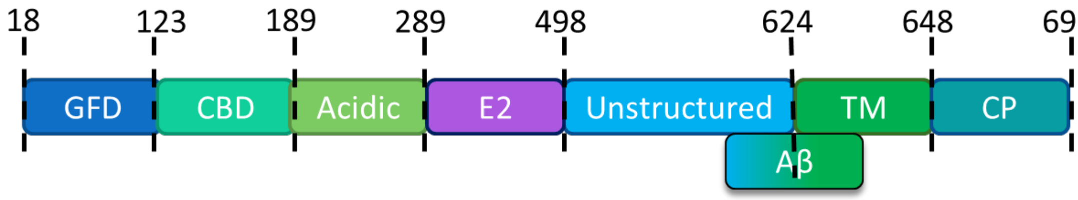

Figure 1.10. APP structure. The domains found in APP are shown above; GFD = Growth Factor Domain, CBD = Copper Binding Domain, an acidic residue rich region, E2 = glycosylated domain, TM = transmembrane domain and CP =cytoplasmic tail. The Aβ peptide is cleaved from APP via the Amyloidogenic or non-amyloidogenic cleavage pathway and spans the transmembrane (12-14 residues) and plasma membrane (28 residues) domains[4-6].

cleavages of the precursor protein[130]. The first releases or “sheds” the ectodomain while a second cleavage in the transmembrane domain of APP leads to the secretion of the peptide and an intracellular domain into the cytosol[130]. Increasing this cleavage process leads to increased levels of Aβ within the brain. The majority of all Aβ released through this RIP is Aβ1:40, while about 10% is the more pathogenic Aβ1:42[130].

Cleavage involves the actions of three enzymes, α-, β- and γ-secretase. In the amyloidogenic pathway it is the actions of β- and γ-secretases which release Aβ, while α- and γ-secretase cleave APP in the non-amyloidogenic pathway. After decades of research these secretases have finally been revealed. The α-secretase cleavage is performed by a family of sheddases called ADAMs (A Disintegrin And Metalloproteinase) and initially ADAM 10, 17 and 9 were all candidates for α-secretase. These are type I transmembrane protease between 750-900 residues long, and all have the same key features of a N-terminal signal peptide, a prodomain (which must be removed by furin-cleavage to activate the protease), a zinc binding metalloprotease domain, a cysteine rich domain, and for ADAM 9 and 17, an EGF domain[130]. All ADAMs have broad substrate specificity, and in the case of Aβ ADAM 10 is responsible for the constitutive cleavage of Aβ, while ADAM 9/17 preform regulated cleavage[131]. Cleavage favours the α-helical conformation of APP[130] and occurs in lipid raft regions of the cell membrane, and prevents the release of the full length, pathogenic Aβ[132]. The β-secretase cleavage of Aβ is carried out by a sheddase, called BACE1 (beta-site amyloid precursor protein cleaving enzyme 1). This mediates ectodomain shedding with more substrate specificity that the ADAMs proteases[133]. They are glycosylated type I membrane proteins approximately 500 amino acids long with an N-terminal signal peptide region, followed by a prodomain, a transmembrane domain and cytoplasmic region. The catalytic activity of BACE relies on 2 aspartly residues[102, 130]. The activity of BACE1 is confined to cholesterol rich lipid-rafts, and depletion of cholesterol has been shown to not only reduce the activity of BACE1 but redirect Aβ cleavage to the non-amyloidogenic pathway[132]. Both ADAM and BACE cleavage lead to the shedding of the APP ectodomain for the subsequent cleavage by the third enzyme involved in APP processing, γ-secretase.

This final secretase is a complex of proteins; Presenilin, Nicastrin, Aph-1 and Pen-2[134], with the catalytic core being within the Presenilin dimer[135]. The complex is assembled in sequential steps; Nicastrin and Aph1 form an initial complex, with Presenilin joining next (in its precursor form), before Pen2 binds[131]. Presenilin is synthesised as a precursor and once inserted into the γ-secretase complex Pen2 binds, stabilisation and maturation via cleavage of its prodomain occurrs[131, 134]. APP is cleaved by the active site which is composed of an aspartly triad which forms at the interface between the Presenilin dimer[135].

The non-amyloidogenic pathway involves cleavage between residues 687-688 of APP and then cleavage at residue 712, within the Aβ sequence[128] (Fig. 1.10). The initial ADAMs cleavage releases the neuroprotective sAPP-α ectodomain and the C-terminal C83, which remains membrane associated. C83 is then further cleaved by γ-

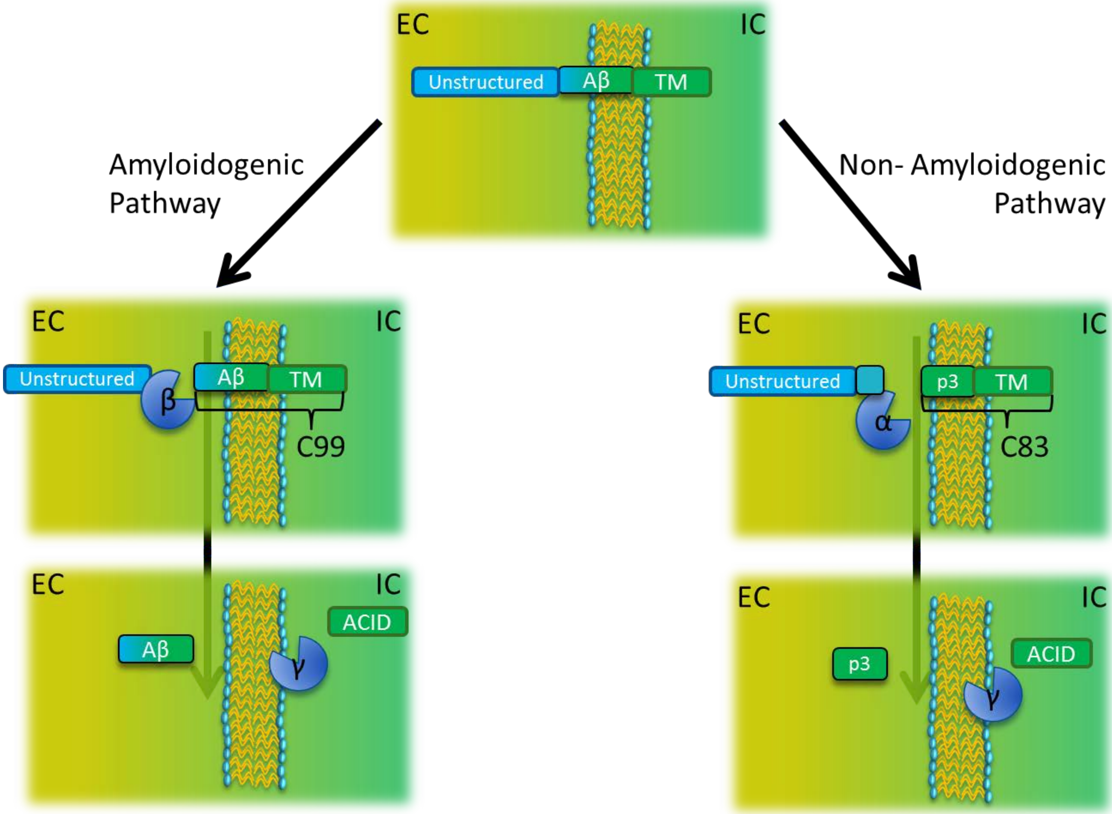

Figure 1.11. the amyloidogenic pathway involves cleavage of APP first to release the additional extracellular portion via β-secretase activity and then C99 is cleavage by γ-secretase within the transmembrane region to release Aβ and the ACID. In the non-amyloidogenic pathway α-secretase cleavage occurs in the middle of the Aβ peptide, disrupting it to release p3. The following γ-secretase cleavage again releases an ACID which is rapidly degraded.

secretase to form P3 and ACID, which are rapidly degraded[131]. The ACID is rapidly degraded rapidly and is not transcriptionally active while P3 has been suggested to be similar to a truncated form of Aβ in some studies, depositing in some AD and Down's Syndrome patients[132, 136].

The Amyloidogenic pathway (Fig.1.11) involves similar cleavage steps: BACE1 cleaves APP within its first 11 residues between 671-672 to release sAPP-β ectodomain and C99[131]. C99 is further cleaved by γ-secretase to release Aβ and ACID[131, 137]. APP is cleaved in multiple steps by γ-secretase, beginning close to the cytoplasmic membrane and occurring approximately every 3 amino acid steps along the C-terminus of APP until Aβ is released[138, 139]. The ACID has been shown to have some role in gene expression but is not strongly transcriptionally active when it results from ADAMs mediated cleavage[5].

The cleaved form of Aβ is between 39-43 residues long (Fig.1.12), with Aβ1:40 being the dominant species in normal conditions, while Aβ1:42 is a minor species outside of senile plaques, where it is found in to be highly concentrated[107, 108]. Its monomeric form is approximately 4.5 kDa in size[108] with little being known about its structure beyond the fact that it is random coiled/α-helix[83] due to the rapid aggregation of the peptide. More structural details of the Aβ fibres found deposited into senile plaques have already been discussed in Chapter one, (Part A. 1.4).

1.12 The amyloid cascade hypothesis

The leading theory into the development of AD is that Aβ1:42 plays an early and critical role in AD pathogenesis, with over production directly triggering the

Figure 1.12. The sequence of Aβ as released from APP cleavage. Important residues are indicated; blue = the Asp and His residues key for Cu(II) binding, purple = key oxygen donating Ty residue, red= key areggation sequence for Aβ which forms the β-sheets during aggregation and green = the Met residue which has metal reducing abilities.

pathogenic cascade. The deposition of Aβ1:42 into plaques is central to disease development, and that Aβ itself is neurotoxic[140, 141]. In addition to overproduction, there is evidence for reduced Aβ1:42 clearance and contact with factors which may stimulate its aggregation[142]. The cleaved form of Aβ must be generated and deposited and itself have demonstrable abilities to cause neuronal death or neurofibrillary tangle formation[140]. The aggregation of Aβ is dependent on the concentration of monomers being above a critical concentration, which differs depending on which isoform is under investigation[74]. Above the critical concentration aggregation is independent of concentration, possibly due to the presence of more rapid formation of Aβ “seeds”, while below this level aggregation is proportional to the concentration of peptide[74].

The aggregation of Aβ involves nucleation dependent oligomeristation, once the peptide concentration is above the critical level a lag phase occurs, in which peptide nuclei form, which trigger the rapid elongation of Aβ fibres[74, 107]. The production of these nuclei is the rate limiting step in aggregation[107]. In addition to the formation, or pre-existence of Aβ “seeds” within a sample, micelles may occur and represent localised areas of increased Aβ monomer concentration, in a rapid equilibrium with the free monomeric population or spontaneously forming into nuclei[74]. Fibril growth occurs by the binding of monomers to their ends, (Fig.1.13).

In addition to Aβ concentration being above a critical level in order to form nuclei to further seed aggregation, a structural transition must be undergone. The native structure of soluble Aβ is that of a random coil[83, 100] however a gradual conversion from α-helix to a β-sheet rich structure leads to the aggregation into an insoluble form of Aβ[83]. This transition is especially favoured by environments which promote H bonding and exposure of hydrophobic patches, necessary to stabilise the β-sheet structure formed[143]. The conformational change involves residues 18-23 and 28-33 forming antiparallel β-sheets, with the residues between them making the connecting turn stabilised by hydrophobic bonds between residues[144, 145]. The β-sheet-turn- β-sheet monomers aggregate together to form protofibrils by elongating into 2 neighbouring strands packed face to face to make a double layered β-sheet, with the β-sheet axis perpendicular to that of the overall fibril[146-149]. This structure is then stabilised by hydrophobic interactions, cross linking and salt bridges between critical residues[146, 150] to create a structure which has been likened to a venetian blind being pulled closed[149, 151]. This stability is the result of Columbic interactions between residues Lys28 and Glu22/Asp28, β-turn sequences and the hydrophobic side chains on Val24 and Lys28[152]. Once the β-turn between residues 24-28 has been formed the monomer folds into its pathogenic conformation to create the nucleus which seeds aggregation. Monomers bind together by hydrophobic interactions between side chains, stabilising using the aforementioned bonding and a partial unfolding to reveal Val24, which is key to the binding[152]. Resistance to degradation is provided by residues 7-11 and 21-30[152]. Monomers bind together and rapidly elongate into protofibrils. As previously described in this work, depending on the Aβ isoform, a minimum of 2 protofibrils will combine to generate a mature fibril with a central hollow core[12, 80, 90, 91]. The next section will discuss the alterations to this hypothesis and how the early aggregates, namely oligomers, are the toxic moiety of Aβ1:42[153] and the implication of this for AD.

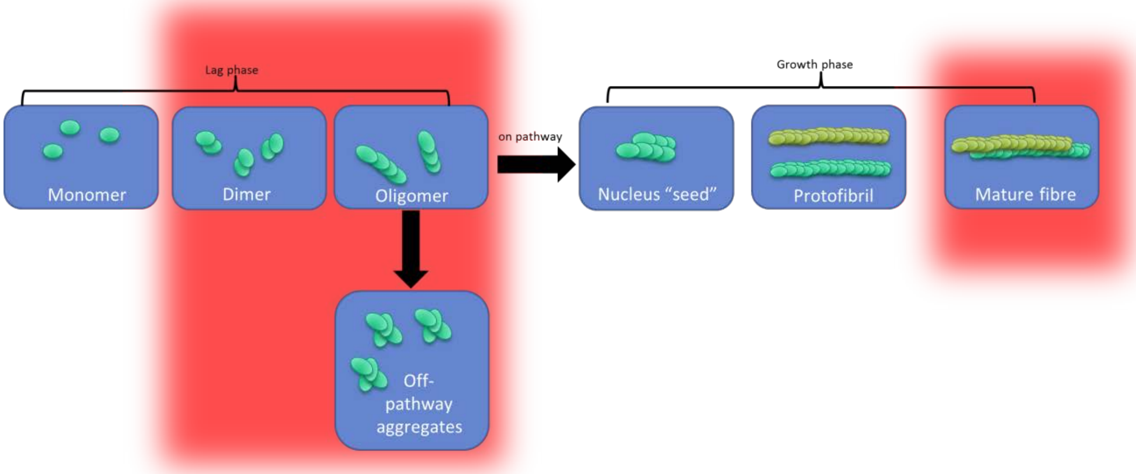

Figure 1.13. The Amyloid Cascade hypothesis. Once released from APP Aβ monomers undergo a structural transition and gain increased β-sheet content. This allows them go aggregate together into dimers/trimers then small oligomers, which act as the "seeds" for a rapid elongation phase of protofibrils growth. The final phase is the formation of mature fibres from these protofibrils. Off pathway aggregates, which may or may not, be sequestered into fibrils have also been noted to exist. Neuronal damage is thought to occur through increased ROS production during dimer/oligomer formation, while the mature fibres are still redox active and can reduce hydrogen peroxide, (possible toxic aggregates indicated in red).

1.13 Oligomers of Aβ are likely to be the cause of AD pathology

Aβ peptides are toxic to cells, mediating cell death via the necrotic not apoptotic pathway[154]. Initially it was thought that the mature fibres of Aβ were the toxic moieties, however much attention has been given to the earlier aggregates. Several early aggregates have been implicated in Aβ induced toxicity, namely protofibrils, annular protofibrils, soluble oligomers, globular structures and Aβ-derived diffusible ligands (ADDLs)[155].

Soluble oligomers of Aβ have been found to impair cognitive function in rodents by inhibition of long term potentiation in the hippocampus, create alterations of the morphology, and decrease the number of dendritic spines and create a general neuroplastic imbalance [156-164]. The neuroplastic imbalance is typically reversible, and occurs before neuronal death[160, 161, 165]. Numerous studies have shown that molecular weight species akin to dimers, trimers and slightly larger oligomers can lead to this neurotoxic behaviour, but not monomers, or later aggregates[156-158, 162, 164].

Oligomers of Aβ solubilised from cerebral plaques from subjects with AD were potent in their inhibition of long term potentiation, and in addition enhanced long term depression of rodent hippocampal neurons[157]. Moieties akin to dimers were the most potent, with the strongest effects on the learned behaviour of rodents, while no effect of insoluble material extracted from plaques was noted. It was proposed after this study that plaques represent a sink of neurotoxic dimers/oligomeric aggregates which can be released over time[157]. Similarly when water soluble AD brain extracts were injected into rats the structural plasticity essential for behavioural consolidation was compromised, indicating that oligomers of Aβ act on processes early in the long-term memory pathway[164]. Work has suggested that the toxicity of dimers results from their ability to aggregate further, and to continue to form low-n-oligomers with their own toxicity while themselves persisting over time[163].

In addition to dimers, trimers have been implicated in the progressive loss of hippocampal neurons in rodents, with a marked effect on dendritic spine and synapse function after exposure to picomolar levels[158].

Small soluble aggregates of Aβ termed ADDLs have been shown to accumulate in the brain and CSF of AD patients, acting as gain-of-function ligands to interfere with synaptic plasticity. ADDLs show specificity for binding to neurons, and with continual exposure dendritic spine morphology becomes akin to some deafferentation/prion disorders. Synaptic deterioration in this can be rescued by the use of the ADDL targeting treatment Namenda[161]. Injection of Aβ specific monoclonal antibodies following injection with Aβ oligomers can prevent the otherwise seen inhibition in long-term potentiation, and active immunisation against Aβ oligomers showed potential at reversing the damage previously caused[162].

There is increasing evidence that the possible mode of Aβ neurotoxicity could be the result of oxidative stress, an imbalance between Reactive Oxygen Species (ROS) production and the mechanisms which usually defend against this pathway. These species can include but are not limited to superoxide, hydrogen peroxide and hydroxyl radicals. In addition it is well documented that AD patients commonly have increased levels of redox-active transition metal ions, and the results of increased ROS can be detected (lipid peroxidation, DNA and protein oxidation)[155].

Aβ can generate hydrogen peroxide by interactions with redox active Cu(II) and Fe(III) using molecular oxygen. This hydrogen peroxide has then been shown to convert to the more aggressive hydroxyl radical via Fenton's chemistry. In order to detect this ROS production incubated peptides must be combined with Fe(II) and the resulting radicals must be trapped for detection. To detect the rapidly formed ROS a spin-trap method has frequently been employed. This involves using a DMPO (5,5-dimethyl-1-pyrroline*N*-oxide) to react with the hydroxyl radical produce and create a DMPO-OH adduct, which has a unique spectrum when examined by Electron Spin Resonance (ESR) spectroscopy. This technique has confirmed that Aβ is capable of generating hydroxyl radicals in a metal dependent manner, but most significantly for the toxicity of Aβ, this generation is not continuous throughout the aggregation processes[166]. The generation of hydrogen peroxide is confined to a short burst in the initial stages of aggregation, with MF being unable to generate any ROS directly[166]. It is important to note however that MF and later aggregates are still able to reduce hydrogen peroxide if it is present in the environment (i.e. produced by the aggregation of earlier aggregates)[167]. The fact that MF remain redox active in their abilities to produce hydroxyl radicals implies that plaques are not necessarily the inert tombstones they are frequently assumed to be, and can cause long term inflammation and damage once formed[167].

Crucial to this ROS generation is the ability of Aβ peptides to bind redox active metals. Oligomeric complexes have been shown to bind Cu^{2+} and subsequently generate hydrogen peroxide, an activity which can be inhibited by anti-Aβ antibodies or metal chelators [168]. By using a spin trapping technique Aβ peptides can increase the level of Cu mediated hydroxyl radical formation four-fold[169] and a other neurodegenerative peptides have been shown to produce hydroxyl radicals via the same method[166, 170].

The binding of metal ions to Aβ is pH dependent and appears to involve N-terminal Asp and three His residues in co-ordination, and with a level of protonation of the His residues during the binding[171]. The key isoforms of Aβ (1:40/1:42) and truncated proteins with no N-terminal deletions all show Cu binding abilities, while scrambled/reversed peptides do not[169].

Oxidative damage could precede Aβ deposition, and may even precipitate the event, which may explain the differences between clinical AD symptoms and Aβ plaque load[155].

1.14 Counter arguments of the Amyloid Cascade Hypothesis

One central flaw in the cascade hypothesis is the poor correlation between AD symptoms and amyloid deposition. It is well noted that Aβ deposition occurs in patients who fail to develop AD, while a proportion of AD patients fail to develop the amyloid deposits and other brain pathologies associated with the disorder[172].

However patients who are amyloid positive, regardless of whether they have normal cognitive function or suffer from mild impairment, will experience a greater and more rapid cognitive decline than individuals who are negative for amyloid[173, 174]. In fact evidence exists that suggests a variety of cognitive decline pathways can occur, with individuals displaying “amyloid-first” or “neurodegeneration-first” biomarker pathways[173]. Clarity to what is meant by the clincopathological term “Alzheimer’s disease” as opposed to the neuropathological alterations is needed[174]. The neuropathology of AD can only truly be observed during an autopsy, and can occur regardless of behavioural and clinical changes/diagnosis[174]. The relationship between pathology and clinical symptoms appears to be complex.

Extracellular deposits of Aβ induce neuroinflammation, which in turn leads to neuronal death within the affected brain regions, and may or may not trigger tau deposition[175]. McGeer and colleagues (2013) argue that toxicity *in vivo* of Aβ1:42 is within the micromolar range, yet levels in the brain are in the picomolar. They suggest that Aβ1:42 deposition stimulates an inflammatory response, and increased activation of microglial cells, which lead to neuronal damage and death[175].

The adaptive response hypothesis suggests that given the often inaccurate correlation between Aβ deposits and AD pathology it cannot be the deposition of Aβ which is the central causative factor behind the disease pathology[172]. Instead an argument is placed for oxidative stress or metabolic dysregulation in combination with inflammation causing an adaptive response of neurons, which either adapt to the increased “stressed” environment, or leads to the development of AD[172].

Formation of Aβ deposits has been proposed to be a response to brain injury, with Aβ being among several acute-phase proteins seen within amyloid plaques, and experimental lesions in rat brains lead to elevated APP synthesis and tau tangle formation[154]. Indeed, formation of neurofibrillary tangles by tau is often correlated with, but not isolated to deposition with Aβ[154].

Overall modifications to the amyloid cascade hypothesis suggests that the accumulation of Aβ deposits is, at least in the case of sporadic patients, the result of an age related decline in the loss of cellular protection systems. This leads to the accumulation and deposition of Aβ, with secondary effects on tau deposition and inflammation[154]

1.15 Therapeutic design for the treatment of AD

Current strategies for the treatment of AD focus on relieving the symptoms of the disorder, but the focus is now shifting to trying to tackle the early damage caused before clinical decline is seen. Current treatments are limited to acetylcholinesterase inhibitors (donepezil, rivastigmine and galantamine) and a NMDA receptor antagonists memantine, and only relieve the symptoms temporarily[176]. Current drug development strategies focus on modulating the activity of one of the secretases involved in cleaving APP, immunotherapy, anti-inflammatory therapy and inhibiting Aβ aggregation[175, 176].

Targeting the secretases which release Aβ from APP is not without challenges. BACE1 has aparticularly broad substrate specificity, meaning limiting any inhibition specifically to its action on Aβ would be challenging. Targeting this secretase is attractive as BACE1 KO mice fail to produce any Aβ, however given the fact that the physiological function of Aβ is still unknown, its complete blocking could be foolhardy. Similarly, γ-secretase represents an unlikely target due to its complex sub-unit structure, and involvement in the vital Notch signalling pathway.

Immunisation, either directly or passively, against Aβ, initially showed promise in rodent models, by reversing and preventing plaque formation. However in human trials the pro-inflammatory side effects were considered too adverse, with death, stroke and encephalitis[175, 176]. Given it is possible that senile plaques of Aβ can act as “sinks” for more toxic, early stage aggregates, care should be taken with any approach which releases them into the brain via the breakdown of existing plaques.

In addition the analysis of the trials 80 patients, including those who had died, showed no sign of reduction or reversal in disease progression[175].

Numerous methods also target neuronal systems within the brain. As well as cholinergic neurons, glutamatergic neurons also decline in function in AD patients. These neurons regulate synaptic plasticity, with a strong role in learning and memory[176]. Improving function and preventing loss of these neurons is also crucial. Similarly GABAergic targeting drugs are shown to have a cognitive enhancing effect. One possible mode of action is the stimulatory effect on α-secretase that some GABA modulators have, offering a potential longer term neuroprotective benefit[176].

Anti-inflammatory treatments have also been used, after it was noted that some NSAIDs treatments for rheumatoid arthritis had a neuroprotective effect. This effect is limited to certain NSAIDs, as some COX-2 inhibitors actual increased the risk of causing AD substanitially[175]. Long term doses of ibuprofen have also shown potential rescuing effects in rodent models, with the ability to decrease Aβ deposits and improve behaviour[175].

Other strategies have included modulating serotonin and histamine levels with mixed success at pre-clinical trials. Targeting strategies at the Aβ aggregation itself are also under consideration. Despite being largely insoluble once deposited into plaques, some proteases are capable of degrading them, and are found to have reduced activity in AD patients. While several protease inhibitors are currently on the market for other uses, and could be redirected, there are concerns over their controlled/targeted use specifically for the removal of Aβ plaques. Preventing aggregation, or removing the early aggregates before damage can occur is also one line of enquiry, as monocolonal antibodies targeting the monomeric form of Aβ have been shown to reduce the cognitive decline in patients if provided early enough[177]. The use of liposomes to attract oligomers, capture and retain them, thus allowing easy facilitation of their removal by existing clearance methods is now under focus[68, 70, 71, 178]. The liposomes can be readily modified to enhance their ability to attract Aβ and increase its passage across the blood brain barrier[70] making them an attractive prospect for further development.

1.16 Amyloidosis as the causative factor in a wide range of diseases

AD, prion disorders, type II diabetes, Huntington's and Parkinson's disease are all examples of amyloidosis disorders. Amyloidosis is the collective term for diseases caused by amyloid proteins; the miss-folded form of otherwise harmless proteins, and can be systemic or localised. In addition secondary amyloidosis occur, typically as a result of chronic inflammatory conditions such as rheumatoid arthritis[179]. There are approximately 30 different peptides which have been noted to form amyloids, and vary from those which are disease significant (such as Alzheimer's disease, Parkinson's) to those which aggregation only occurs through laboratory based manipulation[180, 181]. One such peptide is glucagon, which forms amyloid fibres at specific pH (2), peptide or ionic concentration and is readily available for the study of aggregation. Once aggregated this peptide is highly stable, to the point where it is the focus of some nanotechnology application, due to its high level of tensile strength[182]. Morphologically the fibres of glucagon are similar to that of amylin, α-synuclein, Aβ and other amyloid forming peptides, being 4-7 nm in height and having distinct Type I and Type II fibre populations which has been noted for Aβ[181].

All amyloid peptides form amyloid deposits in a similar manner, typically beginning with a conformational switch from an α-helix/random coiled structure to that which is predominantly β-sheeted. This miss-folded peptides aggregated together to form the fibres discussed previously, which are between 7-10 nm in height, and made up protofilaments intertwined together and stabilised by hydrogen bonds and hydrophobic interactions[183]. While AD is the most common amyloid disorder others are being defined. In 2012 Alkaptonuria was determined to be a secondary amyloidosis disorder. This condition results from a lack of homogentisic oxidase activity, leading to the accumulation of homogentisic acid in melanin associated deposits[179]. More recent research has shown that two serum amyloid proteins Serum Amyloid A and P are also present at elevated levels in the amyloid deposits found in

Alkaptonuria and analysis of deposits by EM reveals amyloid fibres present within them[184].

Amylin is one of several disease causing amyloid peptides. Secreted alongside insulin by the islets of Langerhans in the pancreas, its miss-folded form is found in deposits in type II diabetes. *In vitro* this peptide forms amyloid fibrils, and has been shown to be toxic to pancreatic cells[185]. Studying this peptide has provided evidence that amyloid fibres grow longitudinally, and elongate once the initial protofibrils have bound together[185].

Amyloid proteins were also found to be the main causative factor behind Creutzfeldt-Jakob's disease and kuru, in which increasing cerebral deposition of the amyloid peptide leads to a dramatic reduction in grey matter and overall functionality[186]. The peptide responsible, the prion protein, shows a powerful ability to convert the normal cellular form, PrP^{C} into the abnormal PrP^{SC}, becoming insoluble and protease resistant[186].

There is an extensive list of amyloidosis, which at their core share a similar pathology: a miss-folded β-sheeted peptide accumulates and can, in some cases, seed further aggregation and deposition. While the peptides themselves share similar features due to the common β-sheet structure, the pathology of the disease is determined by the location of deposition, and the tissues affected. Given some amyloid proteins are more challenging to work with *in vitro* it is only by studying a range of them that insights into the pathology of amyloidosis are possible. AD, prion disorders, type II diabetes, Huntington's

1.17 Conclusions

AD is defined by the accumulation and aggregation of the peptide Aβ, leading to a gradual decline in cognitive function which ultimately dramatically reduces quality of life and shortens life expectancy. The leading cause of dementia worldwide, it is now a desperate race to develop suitable pharmaceuticals to combat it. Like all amyloid disorders Aβ aggregates into highly β-sheeted, insoluble fibres to create local lesions or plaques. As more is understood about Aβ and its aggregation process it is which can, among other causes, produce toxic hydroxyl radicals during their aggregation with each other. These hydroxyl radicals lead to increased oxidative stress and an inflammatory response in the short term, but eventually reduce the number of active neurons within the hippocampus and cerebral cortex. This process begins decades before the clinical symptoms manifest, and slowing or eliminating this process is now the focus of pharmaceutical development.

By providing an overview of AD as a disease, along with the pathology and biology underlying this chapter has aimed to provide an understanding as to why new techniques (or the reapplication of existing ones), are needed to shed light on the disease process and aid the development of new pharmaceuticals. The methodology behind the techniques used in this thesis will now be discussed in detail, followed by a presentation of the results of this thesis.

Chapter Two: Experimental Methodology

2.1 Introduction

During this research samples of Amyloid peptide, namely Aβ1:40 and 1:42, have been prepared at Lancaster University in the Faculty of Health and Medicine laboratories, and studied using SPM and DLS techniques in the Physics department. Where samples have been provided by other researchers this has been indicated. This chapter will aim to detail the experimental methodology used during this research, both from a biological aspect of this project and a physics aspect. Alongside comparative methods of SPM for measuring the nanomechanical and spectroscopical properties of samples, classical biological techniques for studying Aβ1:42 are discussed, such as the Thioflavin T, immunoassays and DLS . Substrate design is a key component of SPM work and it was necessary as part of this project to develop a reliable, robust surface, clear of topographical and Nanomechanical defects, which could be utilized during this work. Details of the process undergone to develop this are also presented below.

2.2 Materials and general reagents

Recombinant human Aβ1:42 and Aβ1:40 were from rPeptide (Ultra-pure, HFIP, A-1163-2, >97% purity), (Georgia, USA). Both peptides were pretreated with HFIP during production. Aβ1:42 treated with TFA, HCL and NaOH salt were also tried when working underliquid. HiLyte™Fluor 647 Aβ40 was from Anaspec, (Eurogentec, Belgium). Amylin was from American Peptide Company, (California, USA).

AFM cantilevers were Tap-300-G for TM-AFM and Contact for CM-AFM from Windsor Scientific, (Berkshire, UK), unless otherwise stated.

Colloidal gold particles for DLS standards were from Anachem (Bedfordhsire, UK)

Cuvettes used in DLS measurements were low-volume quartz cuvettes (ZEN2112) and micro cuvettes (ZEN0040) for protein and liposome measurements respectively, (Malvern, Malvern, UK). Deionized water (dH_2O) was used to make up all buffers.
Unless otherwise stated all other regents were from Sigma Aldrich, (Dorset, UK).
All liquid samples were disposed of via immersion in 1:10 Tri Gene (MediMark, UK) overnight before autoclaving. Mica was reused by baking for 1 h at 60 °C before recleaving to produce a smooth surface.

2.3. Nanomechanical methods of SPM

At its simplest level SPM typically involves scanning the sample surface with a probe, and detecting the interaction of the tip with the sample surface. At the nanoscale this interaction is subject to the effect of short range forces such as van der Waals, or longer range ones such as electrostatic forces. Each of these nanomechanical responses causes deflection of the laser which is being reflected off the back of the cantilever onto a photodetector. This signal is then converted into an image map. Details of the experimental setup used for UFM and HFM are detailed below.

2.3.1 Nanomechanical mapping of peptides and proteins via Scanning Probe Microscopy

Throughout this research all SPM work was carried out on a MultiMode AFM (MM-AFM), fitted to a NanoScope IIIa controller unit, (Bruker, USA). The probe is held in a stationary position and the sample beneath is moved using a piezo-actuator scanner tube. Substrates are attached to metal disks using salol (phenyl salicylate), and held upon the top of the scanner magnetically (Fig. 2.1. MultiMode AFM[7]).

Various scanner tubes can be used with MM-AFM's, which determine the maximum scan sizes which can be taken and the amount of positioning noise seen within scans. A vertical "J" scanner was used for the research conducted in this thesis, with a lateral scan range of 125 x 125 µm, and a vertical range of 5 µm. Movement of the scanner tube is controlled by applying voltage to conductive areas, thus moving the scanner along X, Y and Z axis.

Upon the MM-AFM scanner sits the microscope head, attached by spring clips, and within this the holder for the cantilever which is clamped into place, (Fig. 2.2). The path of the 670 nm laser through the AFM head is shown in orange. The laser is guided onto the cantilever using a fixed and an adjustable tilting mirror before being

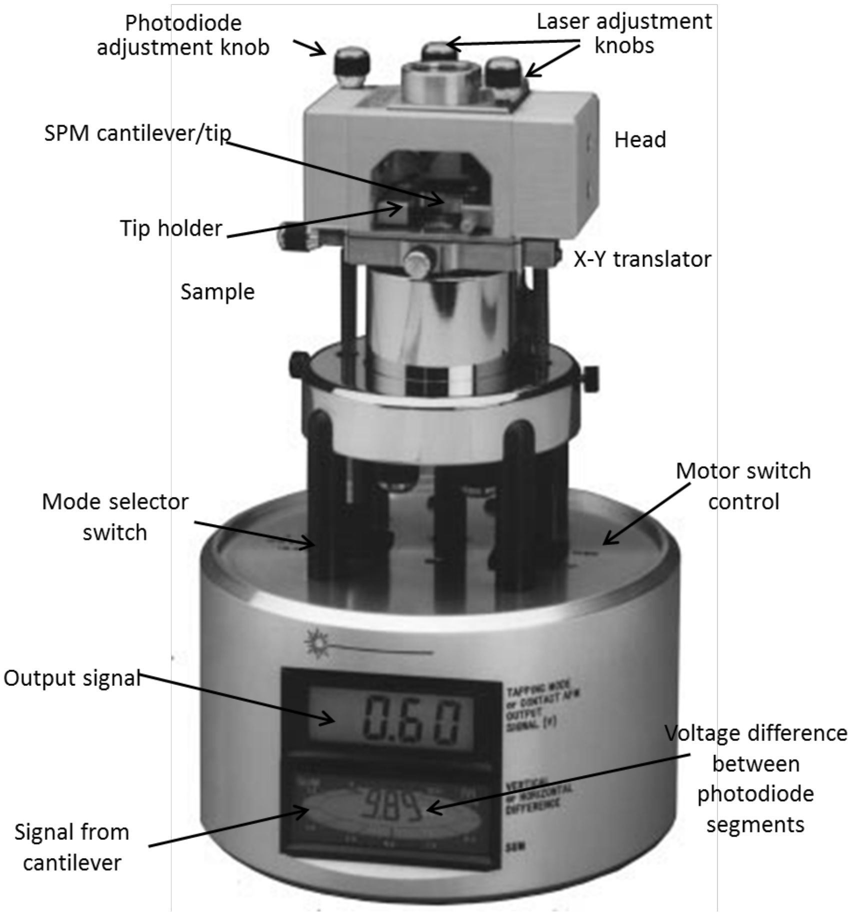

Figure 2.1. MultiMode-AFM^{7}. The physical setup of the MM-AFM used in this research is shown above, with key features indicated. Scanner used during this research was the vertical J scanner, (not shown).

reflected onto the 4 quadrant photodiode array. Laser positioning within this head is controlled by screws, along with an additional set of screws which adjust the cantilevers position with respect to the sample.

All MM-AFM's used during this work were routinely calibrated by following the manufacturers guidelines[7] using a Veeco (now Bruker, USA) Metrology Group NGR-11100 3D reference made of Pt coated Si. This reference consists of a 200 nm grid with a 5µm pitch. Orthogonality was checked and linearity in fast and slow scan settings adjusted until the AFM was calibrated to within 2% of the reference sample along all axis (*x-y-z).*

Software of the control of the MM-AFM is done via a computer using Bruker, (formerly Digital Instruments/Veeco), NanoScope v.4.43r8 software, which allows real time capturing of data and simultaneous off-line image manipulation. Scan parameters (size, rate and resolution), are set in the real time mode, along with selection of the data which is to be collected from the available channels, (topography, friction, deflection UFM etc.). The channels available are determined to a degree by which operating profile is selected within the software. For example for

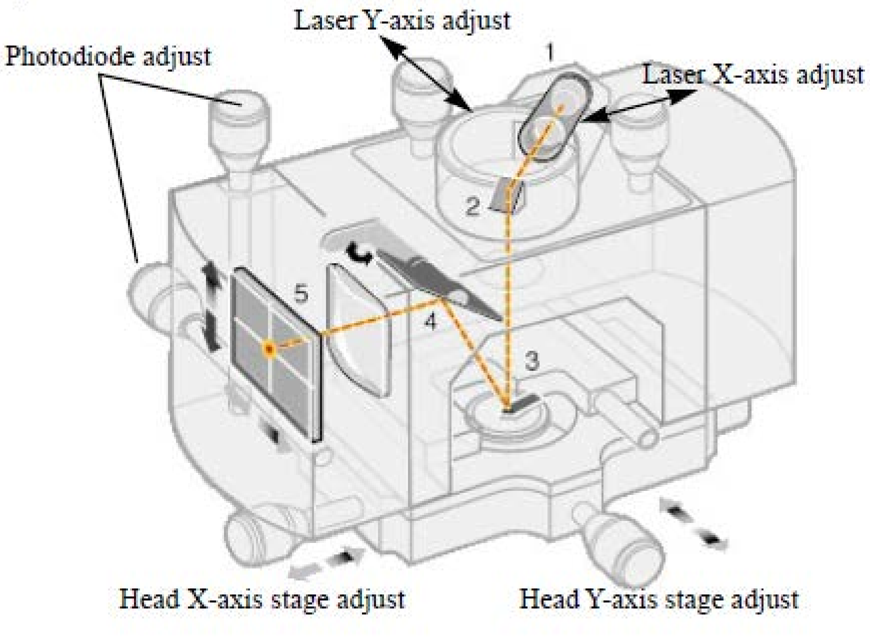

Figure 2.2. MM-AFM head with major components highlighted; 1) laser, 2) mirror, 3) cantilever, 4) tilting mirror for laser adjustment and 5) photodetector.

UFM data to be collected the MM-AFM must be running in the "Contact" profile. Data was collected and saved by selecting the "capture" option within the NanoScope software, before being processed off-line using the programs indicated later in this chapter, and examples of the data collected can be seen in Fig. 2.3. When collecting samples for AFM analysis samples were taken at each time point and imaged in triplicate (i.e. 3 samples were collected and imaged in 3 separate

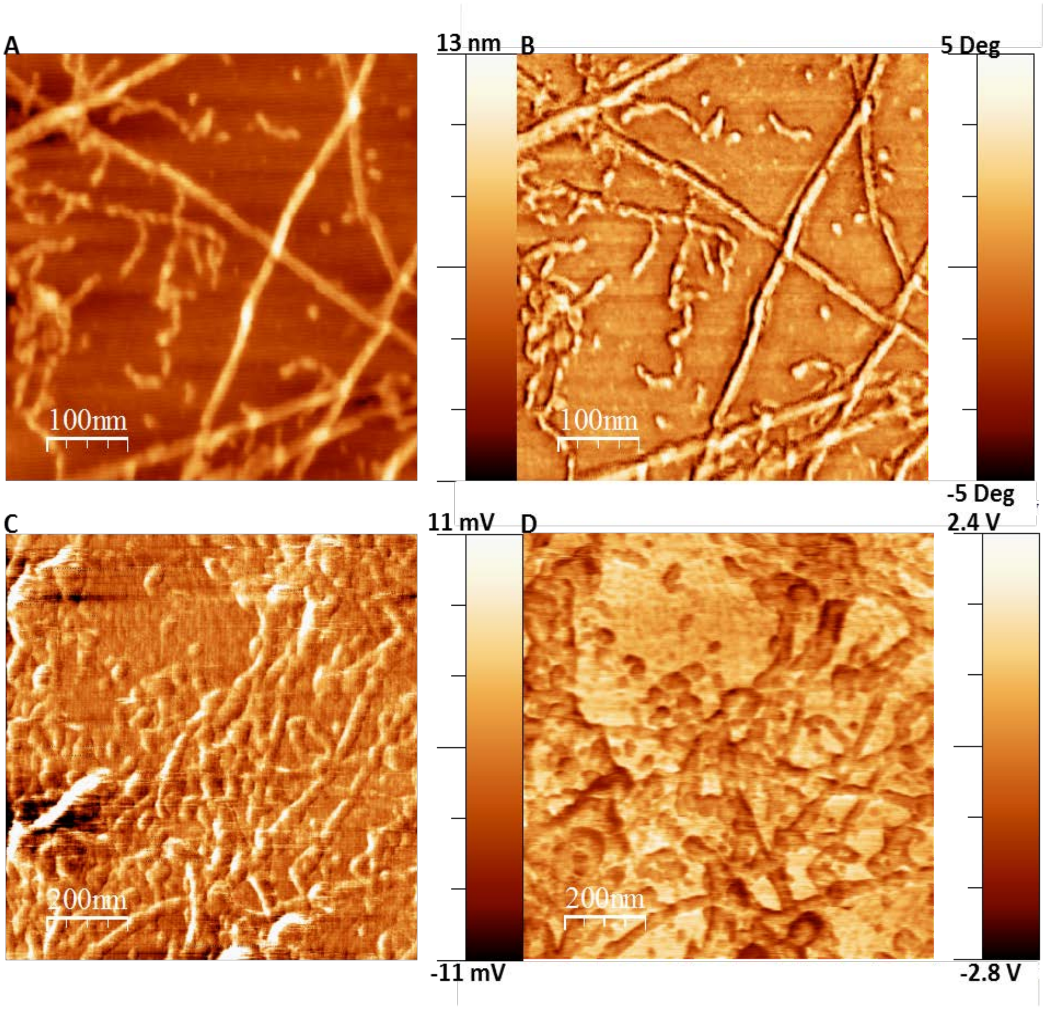

Figure 2.3. The types of AFM data gathered from during this thesis. (A) Topography is the most basic and readily available information that can be gathered on a sample, and was collected at all times. (B) TM phase, a measure of sample adhesion, is collected in Tapping Mode AFM, and is unique to TM. (C) and (D) show data which must be collected in Contact Mode AFM; Friction (C) allows the user to see the torsion and sheer forces being applied to a sample, and is particularly useful to monitor when looking at biological samples. (D) shows the UFM data which can be collected, with darker areas suggesting areas which are less rigid and more compliant than lighter areas.

locations) to be sure the samples represented the overall sample.

Tapping mode. Tapping mode AFM (TM) is frequently employed to overcome issues with sample friction and adhesion can cause, and is particularly applicable to the imaging of biological samples. Consequently this dynamic AFM mode has been employed routinely throughout this thesis. The theoretical concepts of AFM have already been discussed in Chapter 1.A, so will not be discussed in detail here. Data was collected in TM for topography and phase channels. Cantilevers used had resonant frequencies of approximately 300 kHz ±100 kHz, and force constants of 20-75 Nm^{-1}, and have an approximate tip radius of 10 nm. Unless otherwise stated, all scans were conducted with the tip vs sample speed between 0.5-1.5 µm/s.

Contact mode. The widely used mode of AFM, contact mode (CM) forms the basis of the subsequent techniques discussed below. During CM the tip is kept in direct contact with the sample, and so, if the applied force is not monitored carefully, friction and torsion can damage the sample. Where direct contact to the sample was necessary to gather data, the force was kept to a minimum of 5-10 nN.

Contact tips had resonant frequency of 13 ±kHz, with force constants between 0.007-0.4 Nm^{-1}, with a tip radius of approximately 10 nm. Scan speeds were as previously mentioned.

Ultrasonic Force Microscopy (UFM) and waveguide-UFM (w-UFM). UFM operates in contact mode and therefore requires the use of contact mode cantilevers, but uses a dedicated piezotransducer stage to vibrate the sample at higher frequency but with small amplitude. A typical UFM setup is shown in Fig.2.4. UFM samples are attached to a disk piezotransducer stage (PI piezoceramics, Germany) using salol and driven using an external AC source, (LXI Keithley, UK) at frequencies higher than that of the cantilever’s resonant frequency, typically 2-4 MHz amplitude modulated at low frequency (1-5 kHz). The cantilever at this frequency is effectively rigid and will indent briefly into the sample surface before pulling away. The non-linearity between the tip-surface interaction provides detection of the HF sample vibration with resulting readily detectable response at AM frequency that can be used to produce an image that is a measure of sample stiffness. Darker areas are softer and more compliant compared to lighter areas which are stiffer, as a brighter area refers to a higher lock-in amplifier (LIA) output as a response to a lower threshold amplitude. It is also possible with UFM to detect stiffness changes ~5 nm below the samples surface[187]. Adhesion and tip-surface interactions can also be modelled using the Young's modulus as previously discussed in Chapter 1.A 1.1.2.

The piezotransducer was driven using either a Hewlett Packard 33120A waveform generator or the aforementioned external AC source (Keighley, UK), while the amplitude was modulated at 2.3 kHz and detected using a LIA amplifier (SR830 DSP,

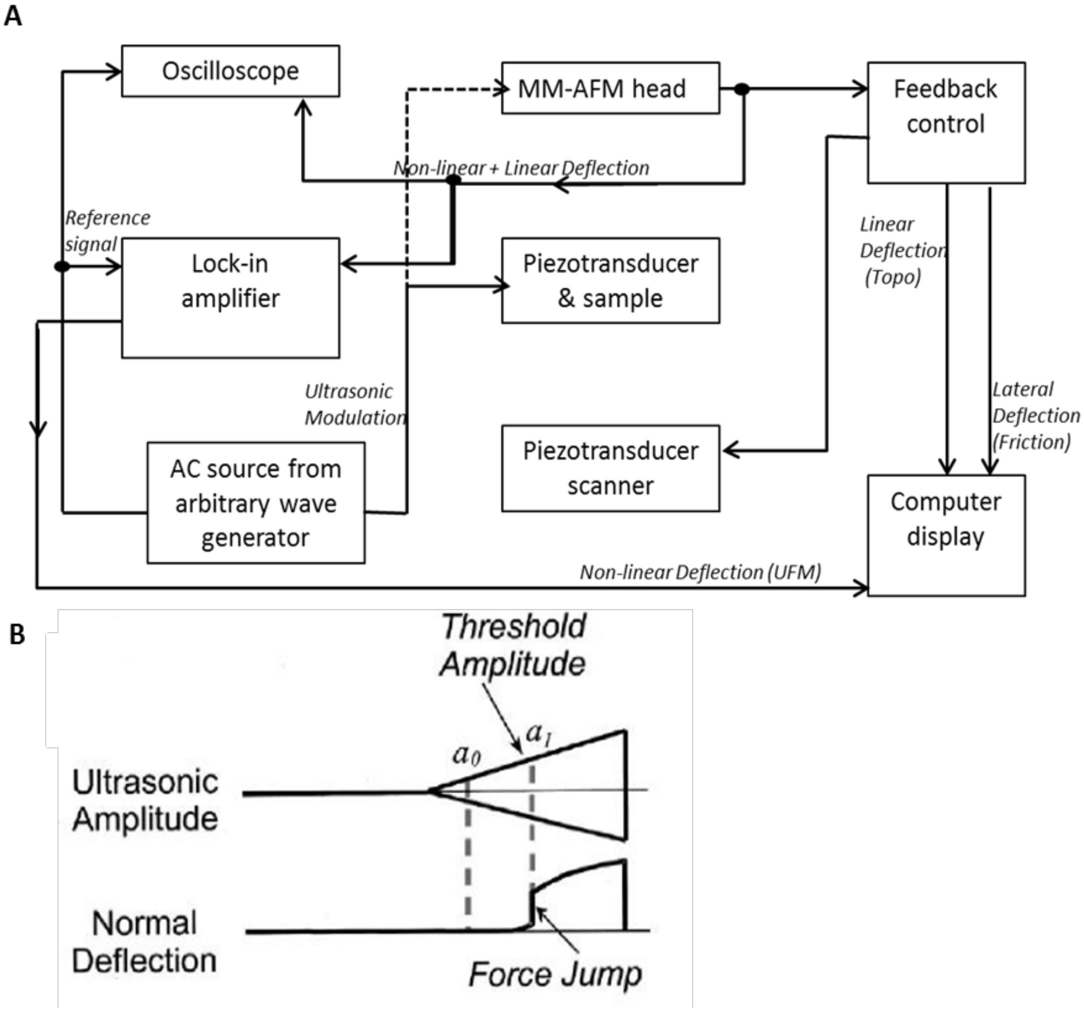

Figure 2.4. (A) Schematic and signal flow diagram of a typical UFM setup. Where w-UFM was employed the AC source is used to apply the ultrasonic vibration to the cantilever within the MM-AFM head instead of the piezo-transducer, (dashed lines). (B) Illustration of the amplitude modulation symmetrical envelope and UFM deflection signal monitored during UFM scanning. The drive amplitude (the force at which the cantilever was driven) was typically 0.2V for UFM experiments.

Stanford Research Systems). This LIA allows for the detection of the deflection of the cantilever which results from the non-linearity of the tip-sample interaction (the UFM signal). By connecting the LIA output to the auxiliary input of the Nanoscope IIIa controller the resulting UFM output is recorded as an image scan. The use of an oscilloscope to monitor and visualize the UFM signal allows for tuning up, calibration and modification of it as necessary.

For waveguide UFM (w-UFM) experiments and identical setup was used, however the ultrasonic vibration was applied directly to the cantilever itself rather than beneath the sample. It was not necessary to use a piezo-transducer stage here, however all samples were compared directly so remained on UFM stages regardless of the mode of operation.

HFM Heterodyne Force Microscopy allows for probing of local changes in the viscoelastic response of samples. In a similar manner to UFM, the HFM set up of the MM-AFM requires the application of an ultrasonic vibration, however in contrast to UFM, this vibration is applied to a transducer at the cantilever base on the MM-AFM head (Function Generator #1, Fig.2.4) and also from a transducer on the sample,

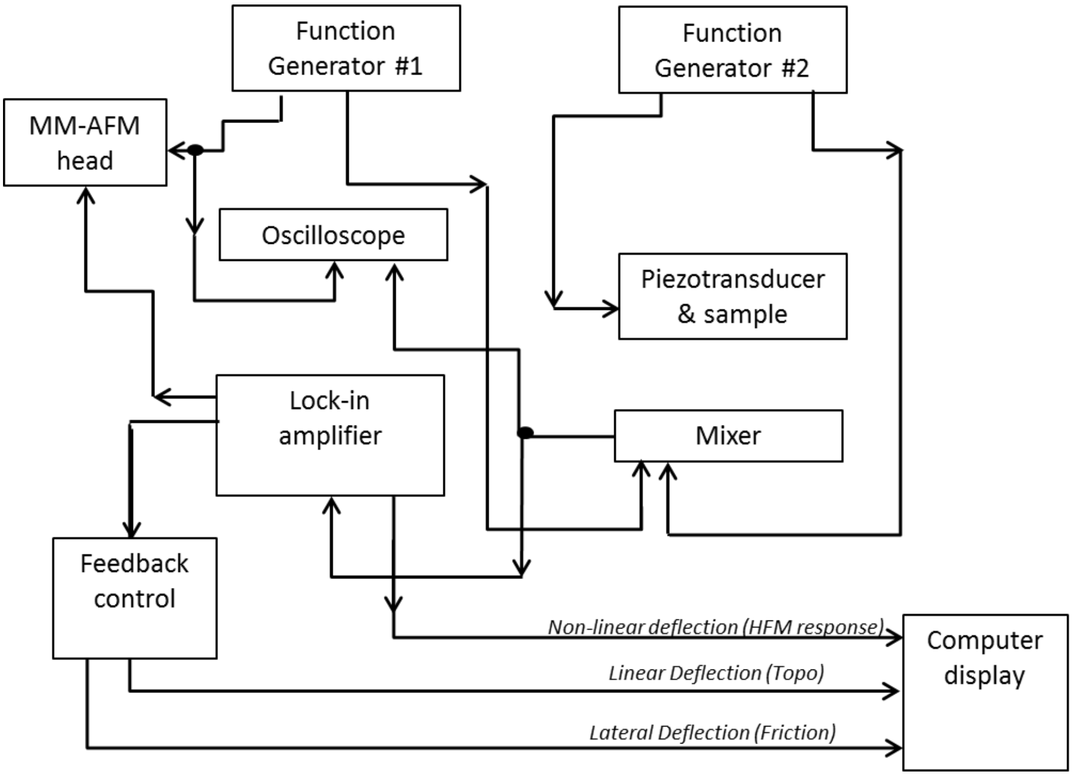

Figure 2.5. Schematic of the HFM setup.

(Function Generator #2, Fig.2.5). These two function generators are excited simultaneously and synchronously mixed to create a reference signal for the lock in. Adjacent frequencies are used, both around 4.5 MHz, with the sample piezo being excited at a frequency few kHz below or above that of the cantilever to allow for the detection of the response. The non-linear deflection of the cantilever or the samples phase response is then monitored and plotted accordingly as the HFM response.

2.4 Spectroscopic methods of SPM

In addition to the AFM methods for looking at the topography and nanomechanical properties of a biological sample, spectroscopical AFM techniques were also developed. These techniques are based upon the Scanning Thermal MM-AFM (SThM) system previously reported[188] with the view to using a tunable infrared laser to detect the change in a samples thermal response at specific wavelengths.

SThM experimental set up. For SThM work resistive SThM cantilevers (Kelvin Nanotechnology, Glasgow, UK) , were attached to a half-moon SPM probe holders (Anasys Instruments, Santa Barbara, USA), (Fig. 2.6), and calibrated between 25-80 °C on an Echo Therm IC20 Peltier plate with variable temperature control (Torrey Pines Scientific, Carlsbad, USA). This initial step allowed calculations of the probes resistance as a function of its temperature. Following this the self-heating of the probe as a function of the power applied to it was measured by applying a varying voltage and combined with the previous results. A more detailed analysis of the probes operations has been provided by Dobson *et. al.* (2007)[189]. The relationship for calibration with silicon nitride tips is a quadratic and was performed by Dr. Peter Tovee, (Department of Physics, Lancaster University, UK).

The SThM system used here is as previously reported[23, 188], (Fig.2.7 (A) and (B)). Briefly for SThM measurements an AC signal of 91 kHz was applied, with a higher DC offset self-heating the probe as part of a balanced Maxwell bridge. This bridge was balanced in the absence of the AFM 630 nm laser, using the variable resistor and variable capacitors. Probe excitation was provided using a precision function generator, (3390, Keithley Instruments, Berkshire, UK). The output from this bridge is recorded using a LIA. A band-pass filter (Stanford research systems inc, model SR650) was added just before the LIA with high pass and low pass filters at 99 kHz and 81 kHz, respectively, to reduce noise.

Following engagement of the tip the laser alignment frequently needs realigning as the application of the AC frequency to the tip causes some bending of the cantilever. This realignment was done by setting a setpoint value of -10V to remove the cantilever from direct sample contact, realigning before reducing the setpoint to 0.2-0.5V as per standard contact mode scanning corresponding to 10-25 nN force.

In SThM, on contact with the sample surface, the tip is cooled as heat flows into the sample, which changes the resistance of the tip. By combining AC-DC excitation across the Maxwell Bridge Joule heat can be generated by applying a well-defined power, measuring the resistance from the tip and creating a thermal image which shows the local thermal resistance of the sample. Darker areas in SThM image then correspond to increased sample thermal conductivity, and brighter areas to decreased thermal conductivity, (Fig.1. 7. (C) and (D)).

Thermal conductance (k_1) can be calculated using the following equation;

$$Q = k_1 \frac{(T_2 - T_1) \int A}{d}$$

Where Q is the heat source, T_1 and T_2 are the temperatures of the materials, and d is the dimension of the tip.

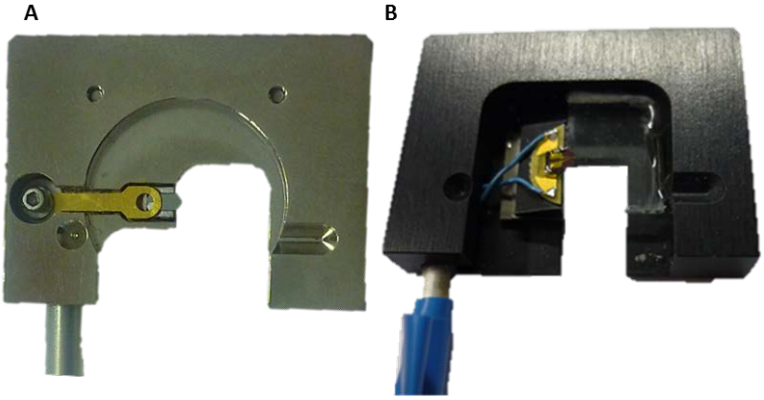

Figure 2.6. (A) A typical MM-AFM cantilever holder and (B) SThM cantilever holder. SThM cantilevers were attached to half-moon probe holders and fitted into a custom built SThM probe holder from Anasys Instruments.

Silicon as an ideal background for SThM studies. In addition to the substrates previously used, SThM studies required a background with a stronger thermal contrast. As a result single crystal silicon was tested. A 100 nm wafer (Testbourne, Basingstoke, UK) was cleaved into small 10x10 mm pieces, cleaned with Isopropanol alcohol (IPA) and dH_2O before being stored in a desiccator. This latter step was necessary for all samples on Si substrates as degradation of the sample due to the water layer occurred more rapidly. Sample deposition itself was as previously described.

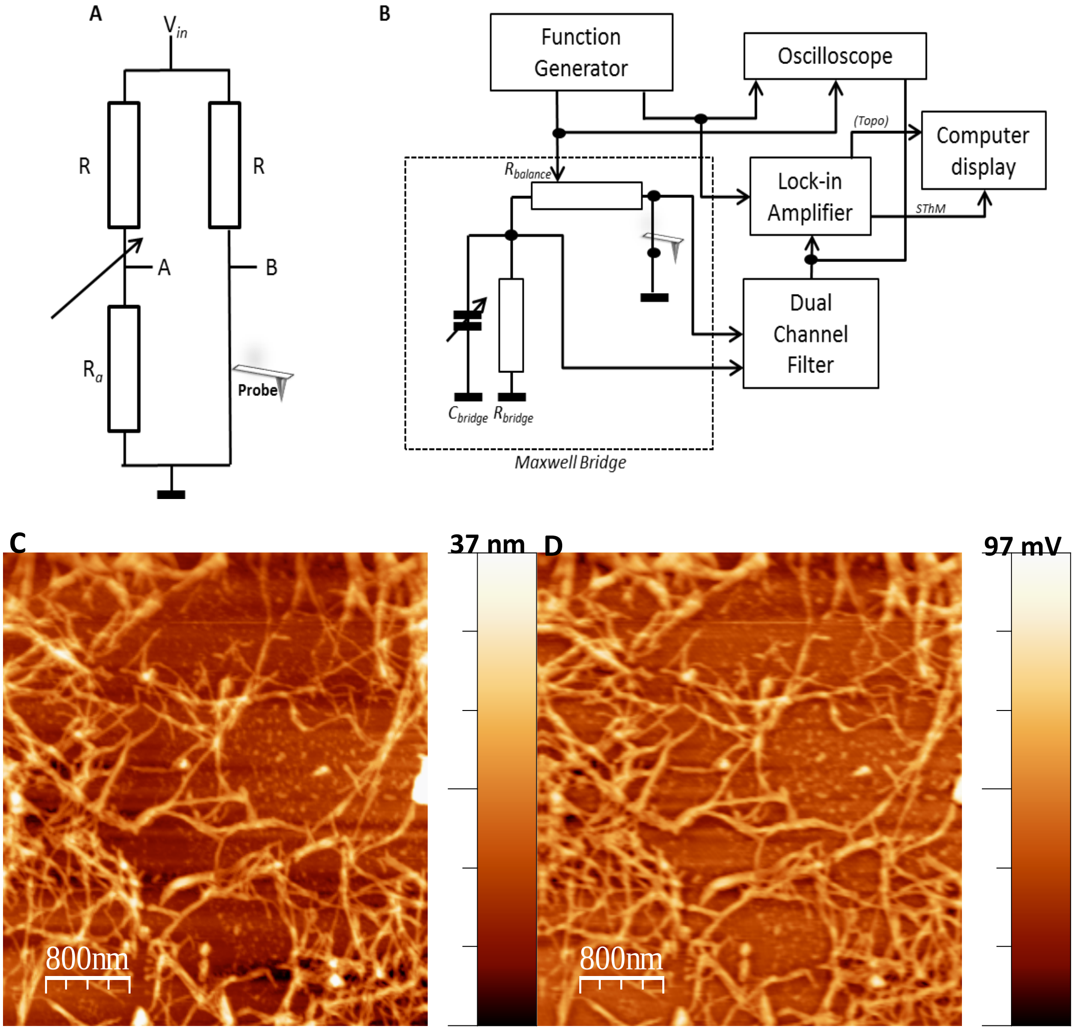

Figure 2.7. Schematic diagrams of the SThM system used in this thesis, showing (A) Maxwell bridge employed to apply the AC current to the tip, and (B) whole SThM system used, including the Maxwell bridge. Panels (C) and (D) show the topography and SThM contrast map from a typical scan of Aβ1:42 fibres.

Sample preparation for SThM-IR. Given the changes in Aβ structure during aggregation, (namely from disordered/α-helix to β-sheets), it was deemed necessary to find a method of isolating the fibrils, which are predominantly β-sheeted, from any smaller aggregates which are potentially representative of a α-helical structure. This would produce a simple, well defined sample to experiment upon. Given extensive work that has shown that the monomers/oligomers are difficult to separate by centrifugation, and work by our group that has already shown the isolation of fibrils using this technique is possible, the use of an airfuge was

A

Parameter	Value
Undulator parameter, a_u	0.877
Undulator period	2.7 cm
Number of undulator periods	40
Electron beam energy	17.3 MeV
Energy spread	0.475% rms
Bunch charge	80 pC
Bunch length	2.1 ps FWHM
Peak current	37.5 A
Micropulse repetition rate	16.25 MHz
Wavelength range	5.8-9 μm

B

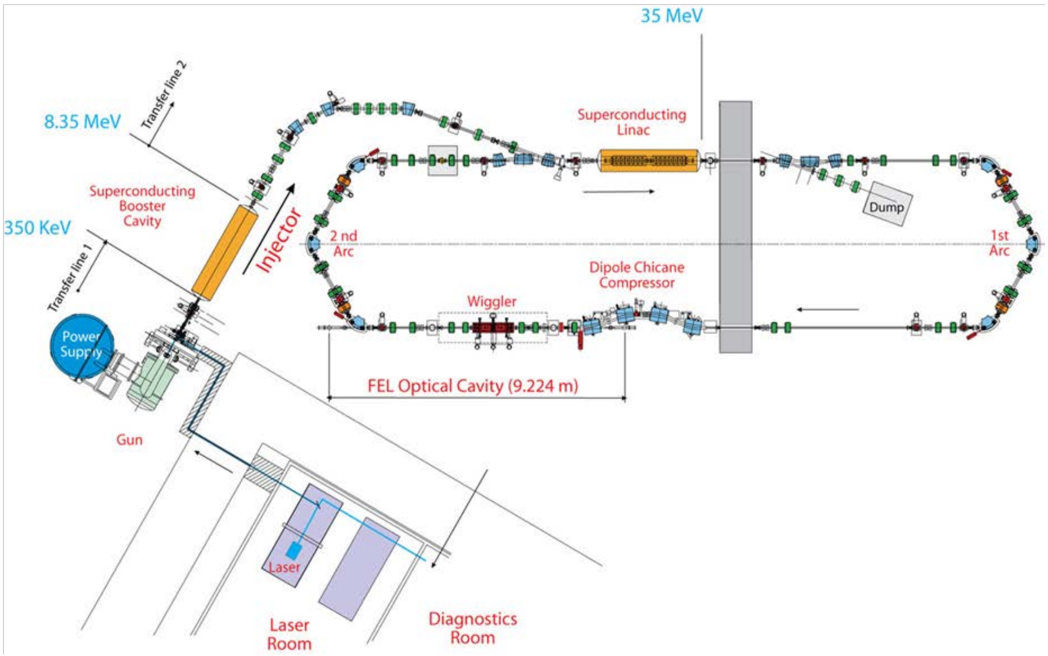

Figure 2.8. (A) Experimental operating parameters of ALICE and (B) Diagram of the ALICE accelerating hall. The FEL is accelerated round the beamline ring and steered onto the laser table in the diagnostics room where SThM-IR work was conducted.

appropriate[167]. Samples of 144 h aggregated Aβ1:42/40 peptide were spun in an airfuge (Beckman Coulter, (UK) High Wycombe, UK) for 1 h at 125,000 x *g*. The supernatant was pipetted off and tested using ThT to ensure no fibrils remained in suspension. The pellets were re-suspended in 100 µl dH_2O before being deposited onto the substrate and air dried. No subsequent washing was deemed necessary; however this protocol did produce a highly concentrated sample of fibrils, of which some further dilution as necessary. Where this has occurred the dilutions were done in dH_2O. Where work was intended to be carried out using the SThM-IR system samples were deposited onto 2 mm thick CaF_2 disks, which were IR transparent (Crystran Ltd, Poole, UK).

SThM-IR experimental set up. Work for SThM-IR was conducted using the FEL at ALICE energy recovery linear accelerator, (Daresbury Science Park, UK) in a manner analogous to that reported by Smith and collegues[190]. For SNOM work, however the FEL was guided into the SThM set up described above and by tuning the wavelength of the FEL a thermal response was possible from the sample where the sample contained particular structures.

A more detailed description of the ALICE setup can be found in Thompson *et al.* (2012)[191] and details of some important running values are listed in Fig. 2.8 (A). ALICE delivers ~60 pC electron bunches at 16.25 MHz, with long pulse trains of ~100 µs at 10 Hz using a superconducting accelerator. These pulses of IR light create an oscillating FEL which can be tuned in the mid-IR by changing the length of the undulator gap. Presently ALICE operates between 5.8-9 µm, however some loss of power is seen at either extremity of this range. IR radiation travels under vacuum through a beamline to the SThM-IR set up and an Acton SP2500 spectrometer (for diagnostic purposes). A full outline of ALICE can be seen in Fig. 2.8 (B).

In order to align the FEL pulse onto the cantilever a HeNe laser following the same path is employed. The presence of the FEL on the cantilever was detected by an increase in signal on the oscilloscope.

The adapted SThM-IR setup is shown in Fig. 9. A boxcar is used to take each FEL pulse and fix the background signal at that pulse level until the next pulse is initiated, (represented as I_0), as the power levels between pulses can vary. The FEL pulse is brought in through the beamline and into the boxcar, and also to the oscilloscope, (to determine the laser alignment and presence of the FEL). The FEL signal is converted into wavenumbers (µm) for the image processing. The thermal conductive response of the sample as a result of the heating using the FEL pulse is recorded via LIA output.

Two approaches for data collection were tried with this setup. The first involved taking image maps at fixed wavelengths, which was considered successful but did not indicate whether the wavenumber selected was the most ideal for the sample. A second approach was to sweep the range of potential ALICE wavenumbers, between 5.8-9 µm at 100 nm gaps, in order to identify any potential responses of the samples. This approach proved problematic as power levels between each increment varied greatly, affecting the signal and therefore the thermal response. This was particularly notable at the extremities of the spectrum and was therefore not continued as it was deemed too unstable to produce reliable data.

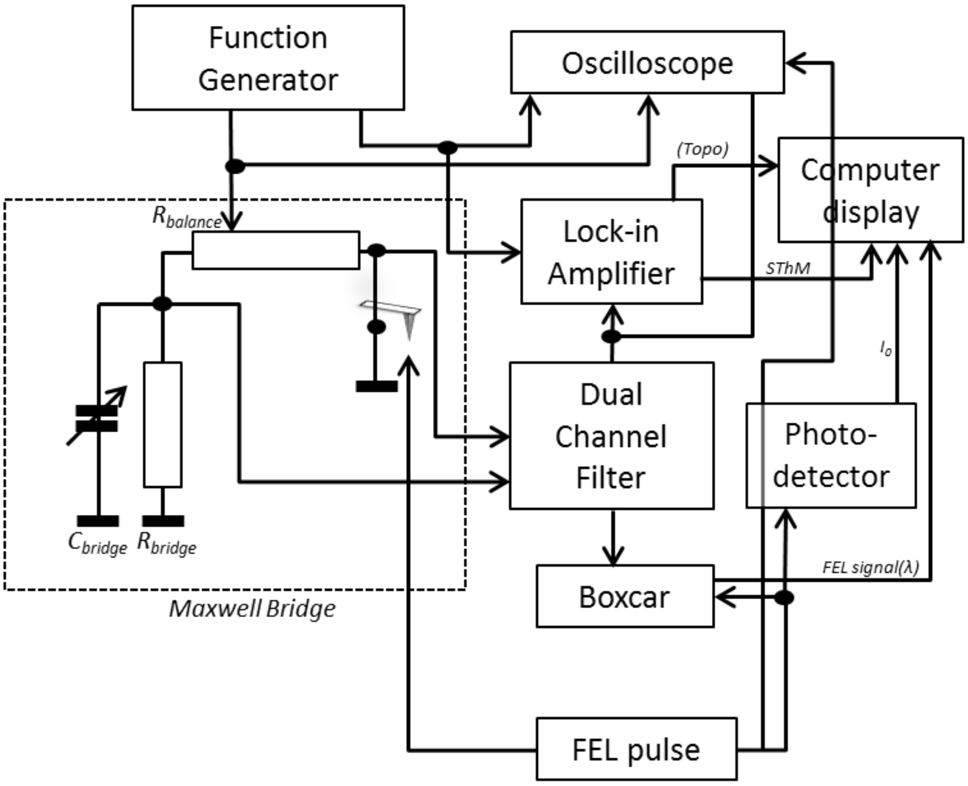

Figure 2.9. Schematic of the SThM-IR setup, incorporating the FEL from ALICE as the heat source for the cantilever.

Nano-IR (Anasys Instruments, Santa Barbara, USA). Samples of Aβ1:42 prepared as described for AFM-IR work above were deposited onto CaF_2 disks and gold coated Si substrates. Imaging was kindly performed by Kevin Kjoller using the Nano-IR2 system. Samples were imaged at fixed wavelengths and data primarily gathered at 1650 cm^{-1} (Amide I), with some additional data gathered at amyloid specific wavelengths. Image maps correspond to the photothermal expansion of the sample at set wavelengths while IR absorption spectra are obtained from the sample by measuring the photothermal expansion as a function of the wavelength of incident laser light.

2.5 SPM image processing and tip convolution

Windows Scanning x Microscopy WSxM[192] was used to view, manipulate and analyse the majority of images away from the MM-SPM system. Images were also viewed and analysed using Bruker NanoScope v6.14r1, Gwyddion and NanoScope Analysis 1.40.

As AFM topography can be affected by the convolution caused by the tip non-finite dimensions during scanning, which is more notable when imaging small, soft samples. An estimation of the real size of the structure if treated as spherical/cylindrical can be made using the following equation:

$$D = 2\left(\sqrt{R^2 + d^2/4}\right) - R$$

Where *D* is the real diameter of the object, *R* is the tip radius and *d* is the diameter measured at half the molecules height.[193]

2.6 Identification of Amyloidβ by classical biomedical techniques

2.6.1. Aggregation conditions of Amyloid peptides

The conditions for the aggregation of amyloid peptides are unique and specific to each particular peptide, each requiring different experimental conditions in order to produce reliable results. Before use Aβ must also been deseeded, a chemical process designed to remove any larger aggregates found in the initial vial of peptide. In the case of Aβ1:42 particularly, these seeds can trigger a rapid aggregation process, rather than a more controlled study desired, resulting in an inaccurate determination of aggregation state, or effect of inhibitors upon the peptide.

Deseeding of Aβ1:40 and 1:42 The peptide was deseeded using a protocol adapted from personal communication with Manzoni and colleagues[194]. Aβ1:42 was first split from 1 mg vials of initial peptide sample to 0.5 mg aliquots using 0.01% NH_4OH pH 10.6, with peptide being brought into solution by vortexing and 4 x 30 secs sonication. The 0.5 mg vials were then dried by centrifugation under a vacuum. Following this each 0.5 mg aliquot was dissolved in trifluoroacetic acid (TFA) containing 4.5% thioanisol at 1 mg/ml, sonicated and vortex as before, and dried gently under a nitrogen stream. Finally the deseeded protein was then treated again at 1 mg/ml with 1,1,1,3,3,3-hexafluoro-2-propanol (HFIP) and briefly vortexed and sonicated as before. This peptide was then split into working aliquots and dried by centrifugation under a vacuum, to give a final protein mass of 22.5 µg per sample. All working aliquots of peptide were stored at -20ºC until future use.

For testing the potential of underliquid AFM work Aβ1:42 was purchased from rPeptide, (Georgia, USA), with 4 pretreatments. These peptides underwent no further exposure to strong solvents except being split into working aliquots with 0.01% NH_4OH pH 10.6.

Aβ1:40 required significantly less deseeding than Aβ1:40, due to the less frequent presence of pre-existing seeds within the peptide sample. Instead the peptide was split directly into working aliquots using 0.01% NH_4OH pH 10.6. Once wetted the peptide was vortexed and sonicated as before to solubilize it before splitting and storing. HiLyte™Fluor 647 Aβ40 was treated as unlabelled Aβ1:40, with working aliquots being stored with minimal light exposure. Amylin samples were also treated in this manner.

Amyloidβ aggregation conditions. All Aβ peptides were aggregated in 10 mM Phosphate buffer (PB), unless otherwise stated. Stored samples were brought into solution by wetting, vortexting and sonicating 4 x 30 secs as before.

As part of the development of an artefact free protocol for AFM imaging, Aβ1:42 was incubated in a number of volatile buffers namely Trimethylammonium acetate and bicarbonate buffers and Trimethylammonium formate solution, (pH6-8.5). Aggregation in these buffers was again performed using a 10 mM solution.

For samples including metal ions, Copper (II) (Cu(II)) solution was made up to the appropriate concentration in 10 mM PB, before being added to the peptide sample. Samples were incubated at 50 µM peptide for 144h, at ratios of 0:1, 1:4 and 1:1 Cu(II):Aβ.

2.6.2. Monitoring of aggregation state using Thioflavin T assay

A 1 mM Thioflavin T (ThT) stock was made using dH_2O. At all points solutions containing ThT were kept wrapped in foil to prevent exposure to light. A second buffer of 100 mM glycine, with 2.5 MNa OH added to pH 8.5 was prepared. Glycine-NaOH buffer was then used to produce a 15 µM ThT in 50 mM glycine-NaOH working solution, which was stored at 4ºC, in the dark, for 1 week.

The ThT solution was allowed to reach room temperature before use and first used to prime the Synergy 2 multilabel plate reader (Biotek) reader before reading samples.

For the assay, 10 µl samples were taken in triplicate were taken at the desired time points throughout the experiment period and added to the wells of a black 96 well microtitre plate. The samples were then injected with 50 µl 15 µM ThT in 50mM glycine-NaOH buffer, pH 8.5, mixed and read 10 times over 2 mins at Ex λ=450nm and Em λ=482nm[195]. Average fluorescence was calculated over the course of the 2 mins together with standards deviations and plotted as relative fluorescence units (RFU), and example data is presented in Fig. 2.10. For experiments conducted with liposomes ThT data is presented as a percentage of aggregation, with the control peptide being taken as 100% aggregation.

2.7. Dynamic Light Scattering

All Dynamic Light Scattering data was collected on a Zetasizer Nano system from Malvern (Malvern, UK). For work with Aβ1:40/42 all measurements were carried out using the low volume quartz cuvette (ZEN2112) with a 12 µl sample volume, and for all other work disposable micro cuvettes (ZEN0040) of 40 µl sample volume or glass cuvettes (PCS8501) of 1 ml volume were used. All measurements were taken at 25˚C unless otherwise stated. All cuvettes used are shown in Fig.2.11 (A-C).

Following use low volume quartz cuvettes were cleaned for reuse in the following manner. Cuvettes were sonicated for 1 h in 1:10 MicroSol3+ (Anachem, Bedfordshire, UK), rinsed x 10 in dH_2O, and left overnight on 69% dilute nitric acid. Following the overnight incubation cuvettes were rinsed in dH_2O as before, and allowed to dry upside down before reuse.

Data presented is an average of at least 3 separate system runs, each containing ~30 individual measurements, and taken from at least 3 experimental repeats. The hydrodynamic radius (H) of each particle was calculated from the translational diffusion coefficient by using the Stokes-Einstein equation;

$$d(H) = \frac{kT}{3\pi\eta D}$$

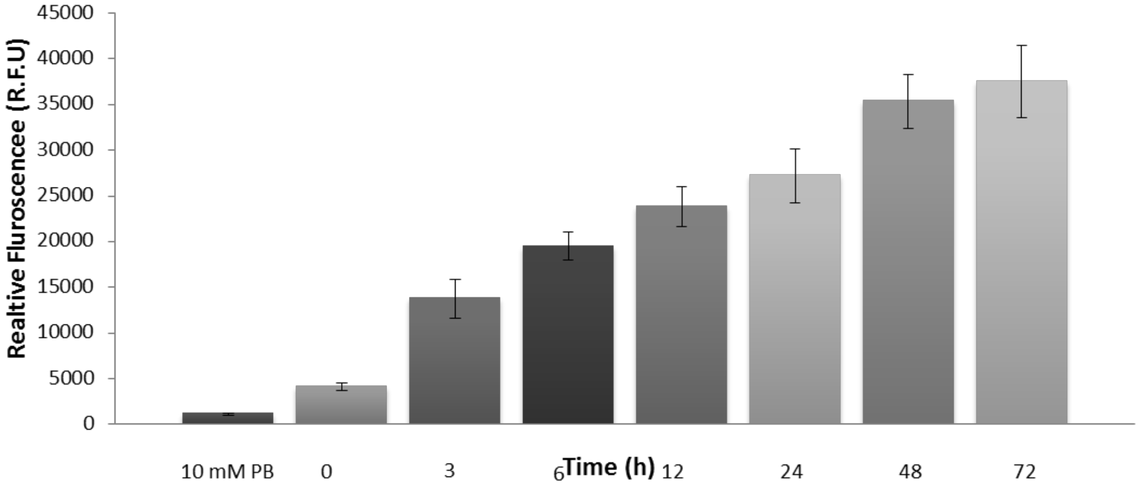

Figure 2.10. Example ThT data for Aβ1:42. Due to the rapid aggregation of this isoform the lag phase seen with Aβ1:40 is absent from this graph. Instead growth into fibrils, (represented by the increased ThT fluorescence read), is rapid and exponential for the first 24-48 h before plateauing at 72 h. The data presented here is an average of multiple experiments, each with data taken in triplicate.

Where D is the translational diffusion coefficient, *k* the Boltzmann's constant, T the temperature and *η* the sample viscosity.

2.7.1. Calibration of DLS system using Gold nanoparticles

Zetasizer Nano data were calibrated and tested using gold nanoparticles of predetermined sizes. For these experiments particles of 2, 10, 20 and 100 nm were used, and diluted 1:50 (2 nm) and 1:10 (10, 20 and 100 nm) in dH_2O, (Fig. 2.11 (D)). Particles of a wide range in sizes can be detected, with 2 – 100 nm readily detected by the system, however smaller particles require significantly more dilution in order to be detected without interference from light being scattered by neighbouring particles.

2.7.2. Experimental setup for temperature dependent measurements of LCST compounds

2D micelle compounds provided by Prof. Martin Bryce, Durham University, (Durham, UK) and were diluted 1:5 in dH_2O before measuring across a defined temperature range at 5˚C temperature steps, with further measurements taken at 1˚C steps around the predicted LCST point.

2.7.3. Characterization of Peptide Inhibitor NanoParticle liposomes using DLS

Before studies with peptide were conducted Peptide Inhibitor NanoParticle's PINPs liposomes, supplied by Maria Gregori, (University of Milano-Bicocca, Italy), were characterized by DLS, both here and at University of Milano-Bicocca. Liposomes

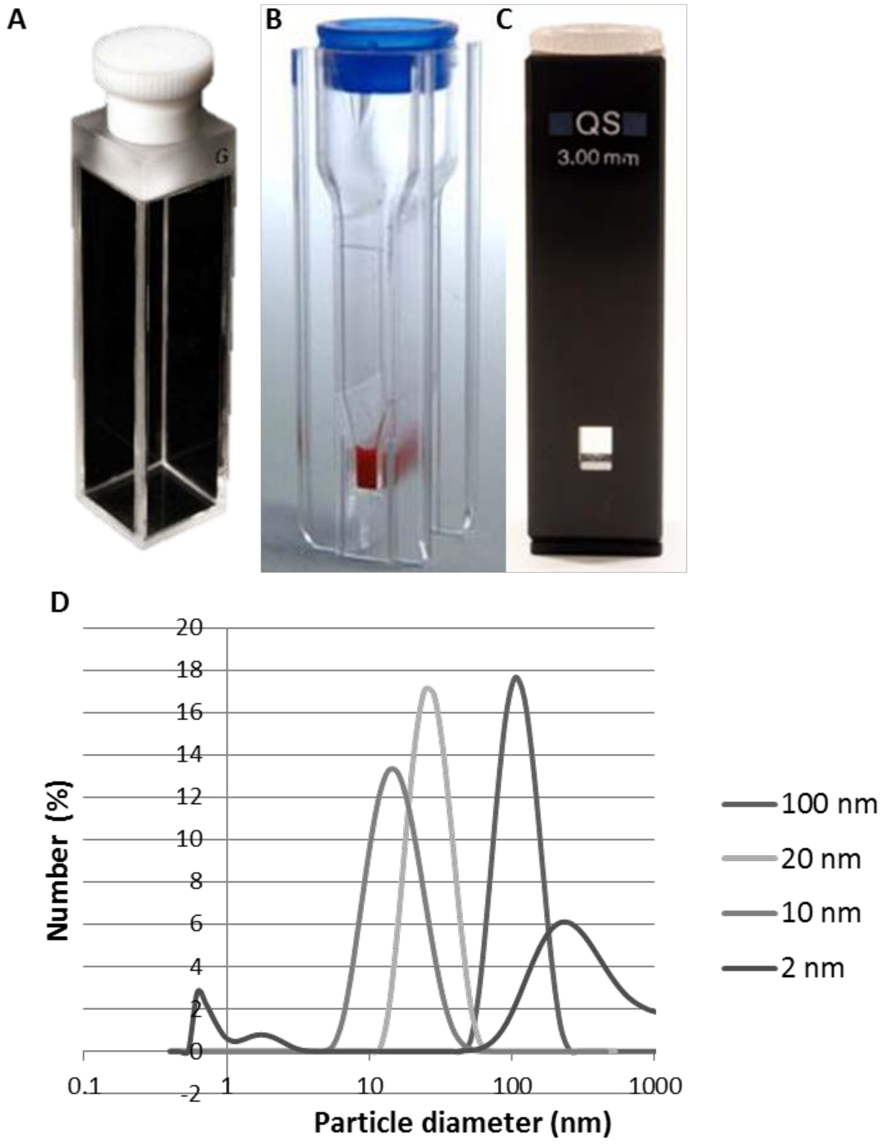

Figure 2.11. Showing (A-C) the differences between cuvettes used in this experiment; (A) 1 ml high temperature resistant glass cuvette (PCS8501), (B) low volume disposable cuvette (ZEN0040) and (C) low volume quartz cuvette (ZEN2112). (D) shows the experimental data gathered when gold standards were analysed using DLS.

were measured for stability at 37˚C for one week, and were also measured by dilution in 10 mM PB.

2.7.4. Detection of Aβ1:40 and 1:42 using DLS

Samples of Aβ1:40/42 were initially collected without diluting the peptide sample. However it became clear that due to the nature of DLS larger aggregates, or "seeds" which may remain in the sample even after deseeding, may interfere with the detection of the monomer/small oligomers, which have a predicted hydrodynamic radius of ~1-2 nm[75, 76]. A dilution series was performed using the 40 µl cuvettes, by diluting the sample in 10 mM PB until the monomeric population could be seen, demonstrated as a peak around 1 nm. In order to visualise this population all samples were diluted 1:30 10mM PB and measured in the 12 µl cuvette.

2.8 Substrate modification for the attachment of Amyloid proteins

Deposition onto mica. Initial tests of deposition of Aβ was performed by diluting samples of peptide 1:10 in dH_2O and depositing 2 µl directly onto the surface of freshly cleaved mica. Samples were then allowed to air dry before being imaged with and without subsequent washing with x2 200 µl dH_2O. This initial dilution and deposition remained standard for all substrates unless otherwise stated.

Use of divalent ions. Freshly cleaved mica was incubated for 30 minutes in 150 µM CaCl, room temperature with constant agitation and subsequently washed vigorously to remove excess CaCl before drying. Peptide samples were deposited as described above before being imaged.

Poly Prep slides. These slides were standard glass microscope slides coated with HMW Poly-L-Lysine solution (~150 kDa) and traditionally used for cell studies. Slides were cleaved into small *ca.* 1 x 1 cm pieces, before the diluted protein sample was placed on.

PLL-mica. Poly-L-Lysine (PLL) coated mica was prepared by incubating freshly cleaved mica with 0.01% 70-300 kDa MW Poly-L-Lysine solution, diluted 1:10 in dH_2O for 5 min before baking for 1 h at 60˚C.

2.8.1 Confirmation of Aβ attachment to the substrate.

Immunogold ELISA. Samples of peptide were prepared on PLL-mica and placed in 12-well microtitre plates, (Fig.2.12 (A), and first blocked with PBS plus 0.05% Tween-20 (PBST), for 15 mins. Samples were then coated with 6E10, (Fig.2.12 (B), diluted 1:1000 in 10 mM PBS, pH 7.4, for 1 h at 25ºC. The plates were incubated for 1 h at 37ºC and then washed with PBST. For the secondary antibody a 1:1000 dilution of the 6 nm gold nanoparticle tagged IgG, (Fig. 2.12(C), Aurion, Netherlands) was then added to each well, left for 1 h at 25ºC, and the plates were washed with PBS, and

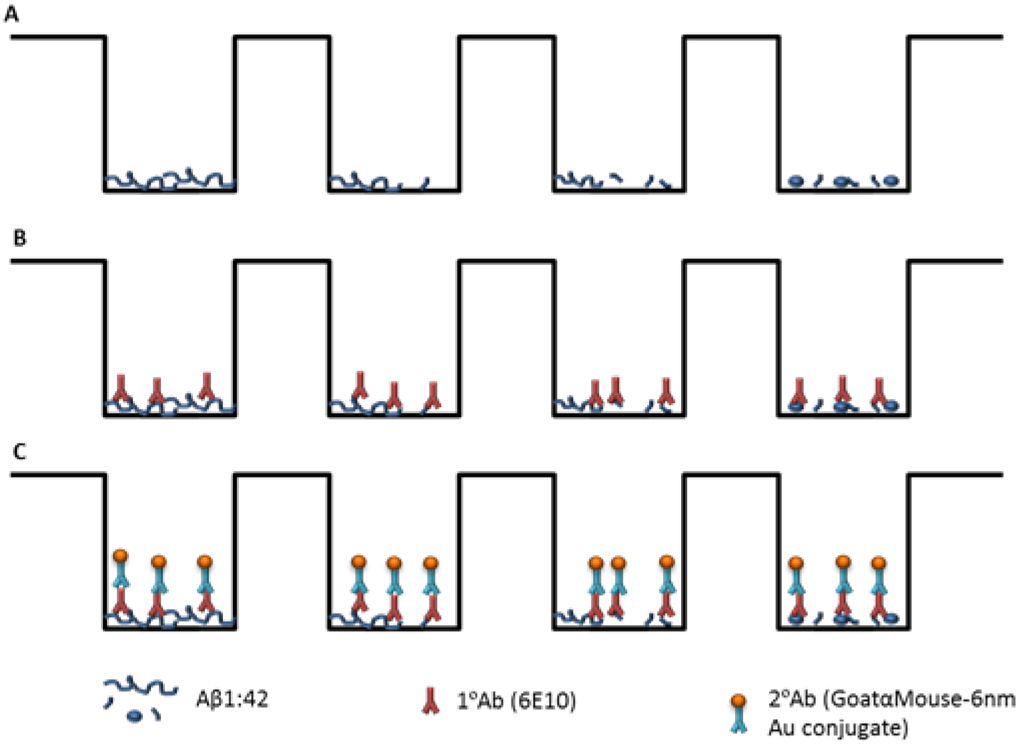

Figure 2.12. Immunogold staining of Aβ1:42 peptide was conducted in a clear bottomed 12 well plate. (A) Samples of peptide were examined at different time points. (B) After the sample had dried none specific binding was blocked with PBST and then coated with the 6E10 primary antibody. (C) after being blocked and washed the samples were then treated with a Goat-anti-Mouse secondary antibody with a 6 nm Au conjugate.

further washed with dH_2O. Samples were imaged once dry as using TM AFM.

Confocal microscopy with HiLyte™Fluor 647 Aβ40. HiLyte™Fluor 647 Aβ40 was aggregated for 144h at 25 µM in 10 mM PB, before being deposited onto PLL-mica as previously described. These samples, along with blank PLL-mica were imaged with a Zeiss LSM 510 Meta laser scanning confocal using a 633 HeNe laser at 3 mW (Zeiss UK, Cambridge, UK).

2.9 Conclusion

This chapter has reviewed the experimental techniques used throughout this research, covering the preparation of samples and substrates to their analysis with SPM techniques and DLS. Details of each of the different SPM methods have been given with regards to their setups, particularly where differences beyond the MM-AFM profile necessary to run them are found.

While commonly used to characterize the size of particles and study population dynamics it is not apparent whether DLS is a sensitive enough technique to detect the early aggregates of Aβ and their changing populations. The technique was tested against samples which are of more standard size and predicted behaviours as well as more unpredictable, polydispersed samples such as Aβ timepoints.

While SPM has already shed light on numerous morphological details of Aβ aggregates any information from this family of techniques into the nanomechanical, thermal, or chemical properties of the peptide are lacking. The techniques detailed here all offer additional information, should it be found they are compatible with imaging biological samples. Once a substrate system has been designed and tested using TM AFM it can be expanded upon to techniques which can better probe Aβ structure and chemical properties.

The chapter which follows details the results of the processes unnecessary to design a substrate system which was considered suitable for deposition of Aβ, and its subsequent imaging by TM AFM. Care is taken to produce a reliable, robust surface which was artefact free and also did not interfere with the aggregation process of Aβ.

Chapter Three: Substrate development of the imaging of amyloid proteins with SPM methods

3.1 Introduction

Following on from the previous chapter which detailed the experimental techniques used in this thesis this chapter will focus on the work which was undertaken to overcome the first barrier to successful AFM imaging, substrate design and the attachment of samples to it. In order to effectively use the nano-characterisation methods described previously it was necessary to test a variety of substrates and test their suitability, along with modifications of those substrates.

Presented in this chapter is the development of a reliable artefact free substrate in PLL-mica, and its suitability for the imaging of amyloid proteins, namely Aβ1:42. Care was taken when modifying the substrate that increased attachment by the peptide did not come at a cost of altering the native structure or substructure of Aβ1:42. Once a reliable substrate had been selected it was analysed for any nanomechanical properties or surface roughness that would obscure smaller aggregates. The attachment of Aβ1:42 was confirmed using both an adapted immunogold ELISA and confocal microscopy utilising a fluorescently tagged form of Aβ1:40.

3.2 Muscovite mica as a standard SPM substrate

In addition to careful sample preparation it is essential for any SPM work that the substrate used is compatible with the work being undertaken. In the case of AFM work, all modes of microscopy require the substrate to be flat on the nanoscale, with minimal nanomechanical background contrast. Muscovite mica is frequently employed in AFM imaging as a substrate because in addition to producing layers which are atomically flat to a few angstroms, it is cheap, readily modified in a variety of ways and can be cleaved to open pristine uncontaminated surface.

Throughout this study Aβ1:42 aggregation was monitored using the ThT assay[167, 195] with the example of ThT in Chapter 2, (Fig. 2.10) showing that the peptide follows a reliable pathway of aggregation, including a brief lag phase and rapid aggregation before plateauing out. The kinetics of Aβ aggregation have already been discussed in the literature review chapter and will not be discussed further here beyond noting

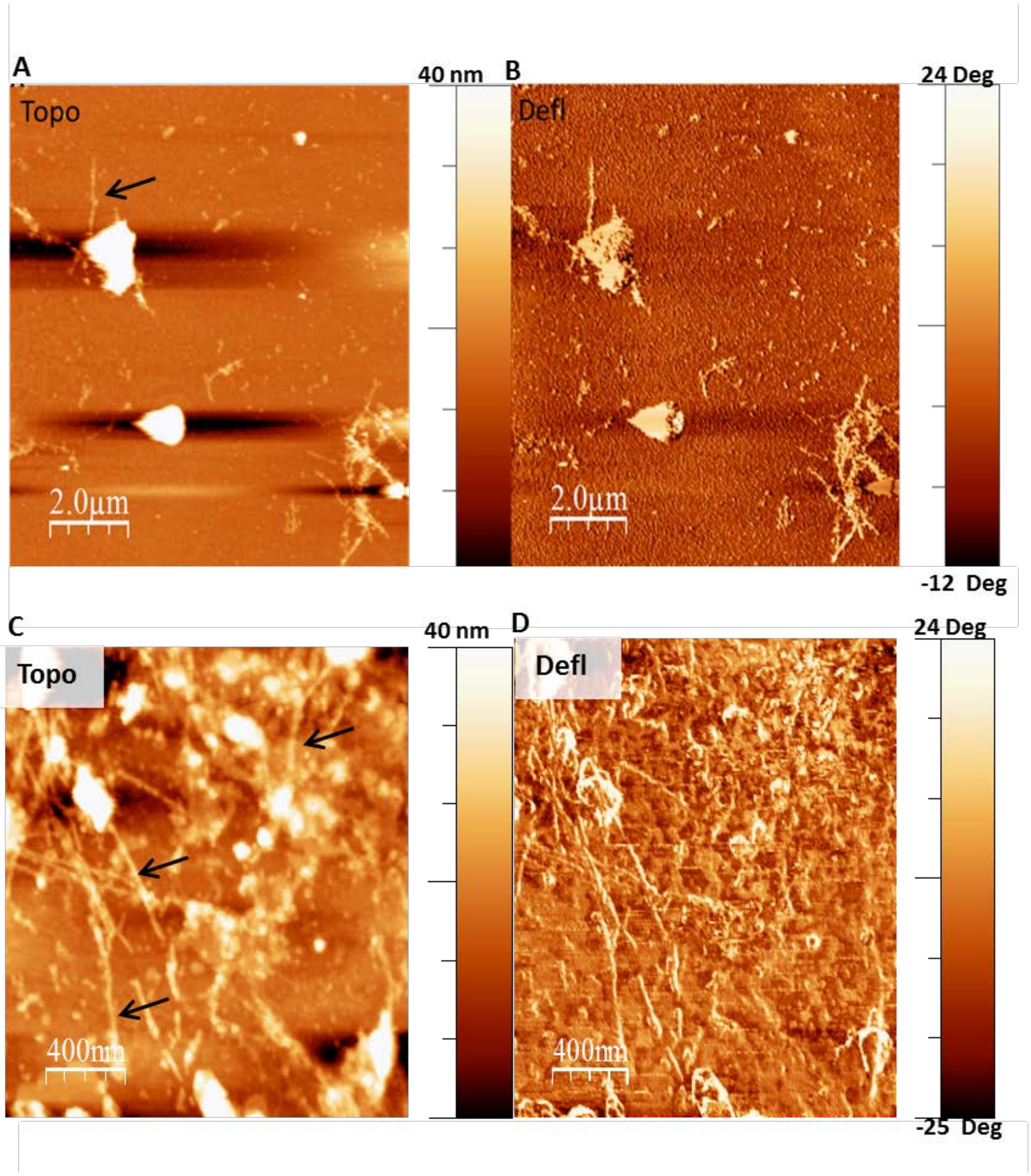

Figure 3.1. (A-D) showing TM AFM of 72 h aggregated Aβ1:42 deposited onto freshly cleaved mica. While some fibres can be seen the presence of salt clearly disrupts imaging and leads to damage to the cantilever tip. Panels A and B show the sample after it has been dried and washed gently with x 2 200 ul dH$_2$0, while C and D show the result of imaging without any additional washing of the sample. Solid arrows indicate MF of Aβ1:42.

that the peptide used in this study behaves as predicted and in a reproducible manner. Aβ1:42 was incubated, and deposited onto freshly cleaved mica, (Fig. 3.1), and although other groups have had success with this strategy[196] it was not deemed to be particularly successful in the case of this work due to rather week attachment of the fibres. While Fig. 3.1, (B) and (C) shows the presence of fibres (solid arrows) after gentle washing, both on the topography and deflection panels, they are sparse in number, and a great deal of time must be spent to locate them. Given that the aggregation pathway of Aβ contains numerous stages, one can assume that fibres are not the only aggregate that can be seen by AFM[86, 98]. Work has already shown that batch-to-batch variation, and indeed differences between suppliers can make this initially straightforward strategy more challenging[197]. The attachment and adherence of a sample to a surface depends on numerous factors, one of which is the relative charges of the two components. However, due to the similar isoelectric points of mica and Aβ1:42 with both being negatively charged at neutral pH[198, 199], the attachment of this peptide to mica is likely to be problematic. Due to the kinetics of Aβ1:42 aggregation it is not possible to merely adjust the pH in which incubation occurs, and below pH4 the α-helix is the dominant structural component while β-sheets are favored between pH 4 to 7 [145, 200-202].

A secondary problem is the presence of salt within the buffer solution, which is

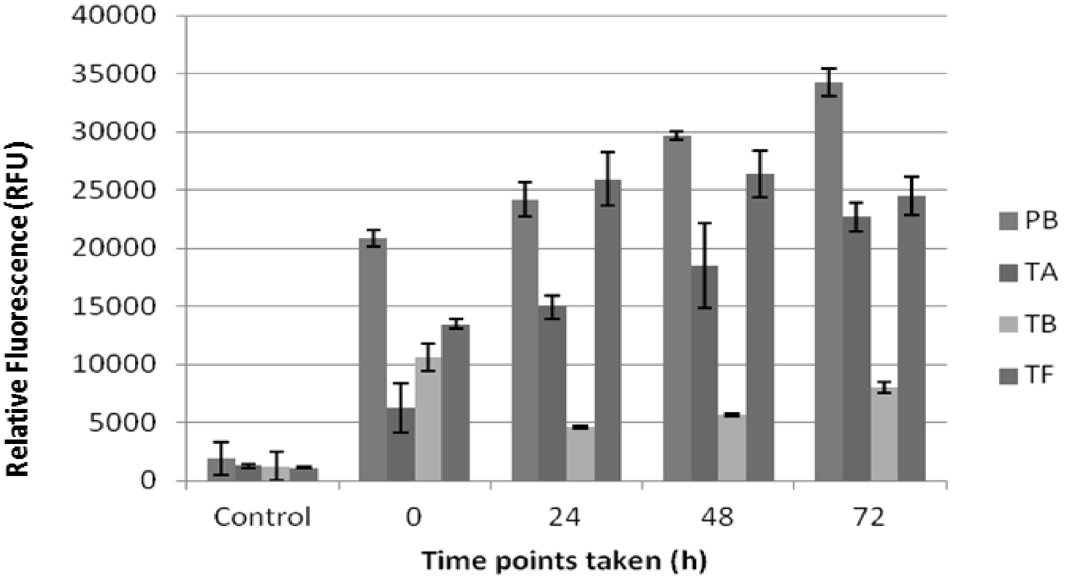

Figure 3.2. Incubation of Aβ1:42 in volatile buffers. Sample was monitored at the above timepoints using a ThT assay. Data is representative of least n=3 experiments.

necessary for biologically relevant aggregation of Aβ1:42[75, 82, 86]. In all panels of Fig.3.1 phosphate crystals can be clearly seen, which result from drying of the sample. Indeed if the sample is not washed, (Fig. 3.1 (D) and (E)), smaller aggregates are present but imaging is greatly interfered with by salt residue. These crystals not only obscure fibers but also lead to increased wear and tear on the delicate cantilever, destroying the tip and increasing the chances of tip-induced artefacts alongside buffer induced ones.

3.3 Incubation of Aβ1:42 in volatile buffers

Although it was unlikely to be successful Aβ1:42 was aggregated in three volatile buffers, in addition to the 10 mM PB usually used for aggregation. Volatile solutions readily evaporate without additional assistance (i.e. N_2 stream) and theoretically should leave behind no residue which would create artefacts or interact with the AFM cantilever in a detrimental way during scanning. Thriethylammonium acetate or bicarbonate buffers (TA/B) and Triethylammonium formate (TF) solution, all at 10 mM, were trialled for buffer media. As can be seen in Fig.3.2 when ThT data is compared both TA and TF buffers showed potential as useful aggregation buffer, TB did not. The most likely reason for this is the pH of the three buffers, TA and TF are pH6-7, and therefore within the small window at which aggregation occurs in the most controlled manner[145, 200, 202], while TB which has a pH of 8.5 is too alkali a buffer for aggregation to occur within. High pH solutions have been shown to be unfavourable for aggregation by creating a kink in the peptide and thus disrupting its secondary strutcure[202], and indeed high pH solutions are used to prevent aggregation during deseeding and splitting of the peptide into working aliquots. Although TA and TF buffers showed promise with initial ThT tests, deposition and imaging on mica was no more successful compared to standard buffers. Given the differences between TA/TF and a physiologically relevant system it was decided to modify the substrate rather than the aggregation conditions.

3.4 Chemical modification of the mica substrate

It was decided at that a more reliable substrate was needed and the process of surface modification began. Protein absorption is mediated by several forces; hydrophobic, van der Waals and the electrostatic double layer. Water, when deposited onto mica, causes the dissociation of K^+ ions from hydroxyl groups within the mica, thus generating a negatively charged surface which equally negatively charge molecules are repelled from[199, 203]. Simple surface modification of mica for attachment of different substrates is a common process; DNA attachment has been modified using glutaraldehyde, or other salinizing agents like aminoproplytriethoxysilane (APTES)[204], and divalent ions have been employed by several groups to increase attachment[205, 206].

3.4.1 Incubation of cleaved mica with divalent ions

The repulsive force present between Aβ1:42 and the cleaved mica surface can be altered by incubation of the mica with divalent ions. Divalent cations such as Ni^{2+} or Ca^{2+} have been shown to increase the attachment of extracellular matrix proteins and DNA[203, 205, 206] and it therefore seemed possible to apply this process to our experiments. Sherratt and colleagues[206] looked at the absorption of microfibrils to

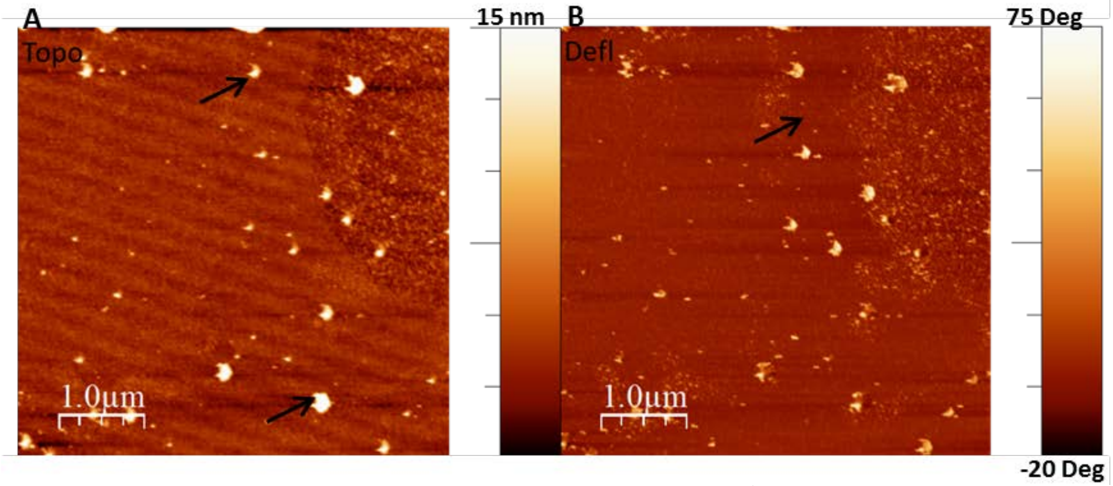

Figure 3.3. Freshly cleaved mica was incubated with 150 µM Ca^{2+} and protein was deposited as normal. Despite subsequent washing an increased number of salt crystals (indicated by arrows) remained on the mica surface and no improvement of protein attachment was seen.

mica across a physiologically relevant concentration range of 31-1000µM of Ca^{2+} ions, a biologically significant cation. Maximal absorption was seen 125-250 µM. Based on this study, freshly cleaved mica was incubated with 150 µM Ca^{2+} for 30 mins, washed with dH_2O before drying with a nitrogen stream. AFM imaging was then conducted, on substrates with and without peptide, (Fig. 3.3). Unfortunately no greater protein attachment was seen compared to bare mica, while an increase in the number of salt crystal artefacts were noted. Concern that divalent ion modification of the substrate may alter the morphology of the deposited fibres was also noted, as Ca^{2+} can disrupt the morphology of Type VI collagen during deposition[206].

3.4.2 Poly prep slides

Another method of altering the surface charge of an AFM substrate is to use Poly-L-Lysine to create a more hydrophobic charge across the surface. Two approaches were tried, using “Poly-Prep” glass slides, and also developing in-house protocol of coating mica with diluted PLL solution.

Poly-prep slides were purchased from Sigma-Aldrich, and immediately showed that by altering the surface to increase its hydrophobicity more effective protein attachment could be achieved. Fibres of Aβ1:42 remained attached to the slides even after gentle washing, (Fig.3.4 (C) and (D)). However these samples are coated with a layer of Poly-L-Lysine strong enough to maintain cell attachment, and on examination were found to be far from atomically flat. Topography of 1.6 nm ±0.9 nm was noted across the slide, (Fig. 3.4 (A) and (B)). The monomer of Aβ1:42 has been noted to be 1-2 nm [75, 76, 87, 207] and therefore had an uneven background topography which could not be discerned from small Aβ aggregates.

3.4.3 PLL-mica

Another approach to using PLL for substrate modification is coating mica with a dilute solution, and has been shown to be very successful with a variety of biological samples.[196, 206, 208-210]. Caution is advised when using PLL, as the conformation of the peptide is pH dependent: at a neutral pH the lysine side chain residues have a high net charge and the molecule has a random coil conformation. Above pH 10.6 PLL has an α-helix conformation due to a reduction of the charges due to being above the lysine side chain pKa[211, 212]. This α-helix structure can be converted to a β-sheet by heating PLL in a highly alkali buffer and cooling it[212]. These β-sheeted structures are capable of aggregating into chains and forming large aggregates however this does

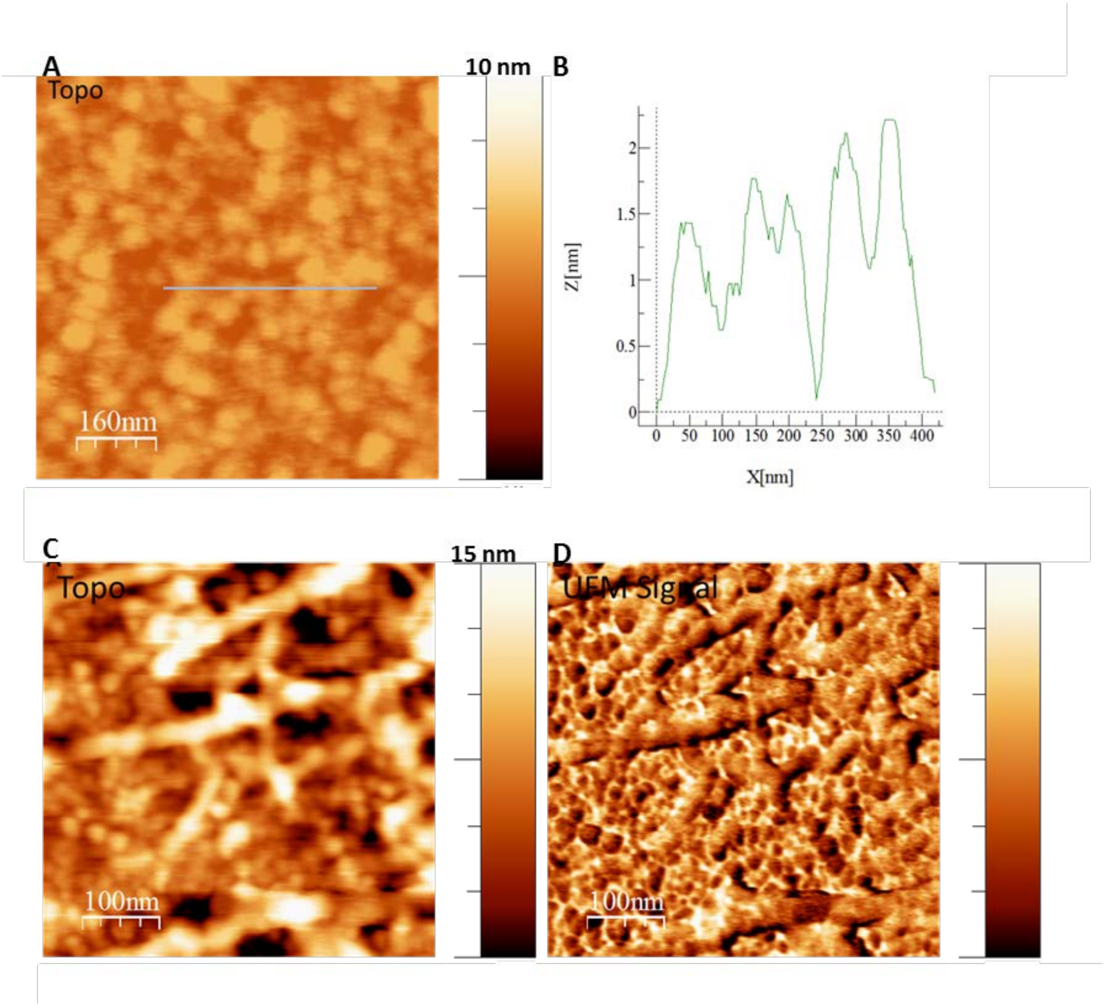

Figure 3.4. Poly Prep slides as an AFM substrate. The surface roughness of the slides was found to be 1.6 ±0.9 nm (Panels A and B), and while attachment of Aβ1:42 was possible, even after washing, it was impossible to discern smaller aggregates from background topography.

not occur at a basic/acidic pH[211]. All experimental conditions used when working with PLL were at a neutral pH, and therefore this conformational shift was not found to be problematic.

When scanned with both CM and TM AFM the surface was found to be clean, and flat to the nanoscale roughness. After coating with PLL the surface roughness of the mica was approximately 4.5 ±1.5 Å, (Fig. 3.5 (A) and (B)). When this PLL-mica surface was exposed to 10 mM PB it was not found to retain salt crystals in great numbers after drying and washing, (Fig. 3.5 (C)), while fibres and other aggregates attached in large numbers without the need for arduous scanning providing one looked with the area deposition had occurred (Fig. 3.5 (D)).

The PLL layer was investigated further, to test it for thickness and nanomechanical background contrast, (Fig. 3.5 (E) and (F)). High force stiffness cantilevers ($k = 3\ Nm^{-1}$, CSC11/Cr-AU, MikroMasch, Bulgaria, Europe) were used at elevated force of 100 nN to scratch the surface of PLL in contact mode AFM with no ultrasound over the 500x500 nm^2 square area, in order to determine the thickness of the PLL layer. Measurements indicated that the PLL layer was typically 0.36 ± 0.1 nm thick. When UFM was employed no nanomechanical contrast was seen, indicating the substrate made ideal conditions for studying biological materials.

3.5 Confirmation that PLL does not interfere with fibre morphology

Although PLL is frequently used to modify substrates for attachment of peptides, Aβ is a particularly sensitive protein, and some substrate modifications can affect the structure of the sample being deposited. Sherrat and colleagues[206] noted a negative correlation between fibrillin microfibril height and Ca^{2+} concentration. Between 1000 – 31 µM Ca^{2+} the microfibril height decreased from 90 to 17 nm, although no other structural features (such as periodicity) were affected. One report of PLL affecting Aβ fibre formation was found[213] and a brief investigation was carried out. Nguygen *et al.* briefly incubated Aβ1:40 with PLL solution at a concentration of 12.5 mg/ml, and found that this lead to instant disaggregation of 5 day old fibrillar aggregates. Once diluted the mica in our experiments was coated with a 0.01 mg/ml solution, and then

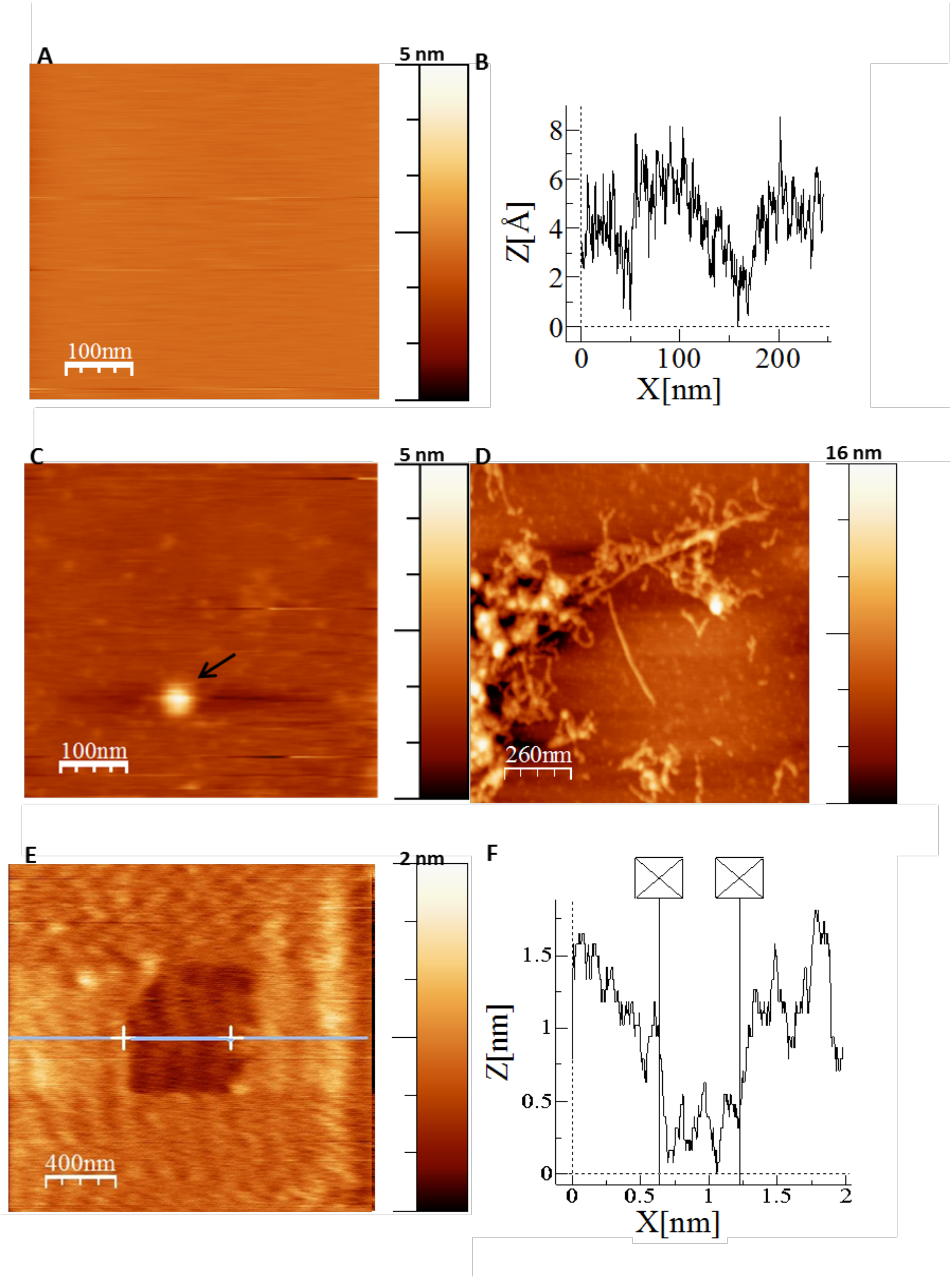

Figure 3.5. PLL coated mica as an AFM substrate. Panels A and B show the smooth, almost atomically flat surface of mica coated with a dilute PLL solution. C and D show the effect of deposition of 10 mM PB and 72 h aggregated Aβ1:42 followed by gentle washing (remaining buffer indicated by arrow). E and F show the calculation of the approximate thickness of the PLL coating. Thickness was calculated by measuring multiple line scans across the scratched area to calculate a thickness of approximately 0.7 ±1 nm.

baked dry, which would presumably render any mode of action void due to the denaturation of the poly-L-Lysine. Our protocol does not involve combining Aβ and PLL in solution, at any stage of aggregation. Although this concentration is >100-fold lower than that used by Nguyen and colleagues, we endeavoured to ensure it did not interfere with aggregation when deposition occurred.

Comparative ThT analysis of samples incubated over 72h and exposed to PLL-mica was performed, with readings being taken before and after exposure (Fig.3.6). Although a small decrease in fluorescence is detected following a 30 min incubation period, this is not a statistically significant difference and could be accounted for by attachment of protein to the PLL-mica surface. No dramatic alteration in fibre structure was seen to be detected by the ThT or by AFM. Samples of Aβ1:42 were deposited onto freshly cleaved mica and PLL-mica and compared for differences in height and width, and no gross morphological differences were found. The details of fibre sizes will be discussed further in Chapter 5. Time of exposure was chosen as this is the approximate time a sample taken at a much smaller volume for AFM analysis would have taken to become dry for imaging. Nguyen et al. saw a complete dissolution of β-sheeted aggregates, and if this were found at a concentration of 0.01 mg/ml in our system one could expect a dramatic shift in the level of ThT

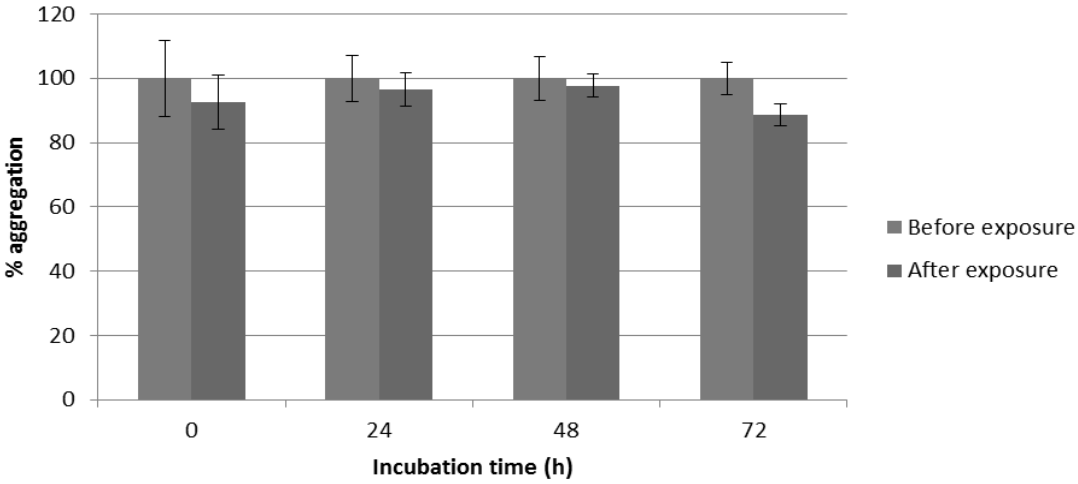

Figure 3.6. Exposure of Aβ to PLL-mica does not disrupt fibre morphology during attachment. ThT is presented as a percentage of aggregation and is a triplicate or three independent experiments

fluorescence detected.

3.6 Confirmation of attachment of Aβ1:42 to PLL coated mica.

Immunogold staining. In order to ensure that the protein attached to the PLL-mica is indeed Aβ1-42 immunogold staining of the sample was carried out. By adapting a sandwich ELISA containing AuIgG antibodies detection of small and large aggregates of Aβ is possible. Fig. 3.7 (A) shows PLL mica which has not been exposed to protein but has been treated with the full ELISA protocol, and is therefore a representative control. Panel (B) shows the sample before staining, and (C) confirms the attachment as fibres and oligomers well decorated with Au particles. An appearance of a coating

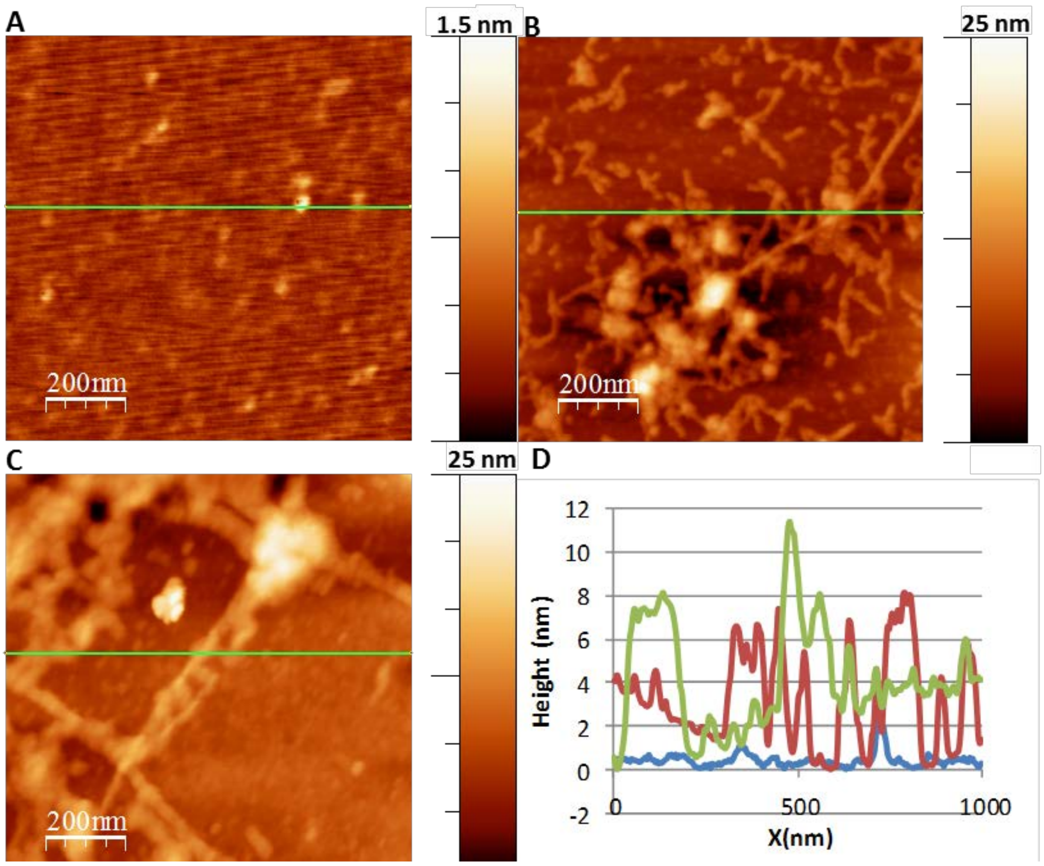

Figure 3.7. The standard 6E10 ELISA protocol was adapted to use 6 nm tagged AU antibodies to detect Aβ aggregates bound to the PLL-mica surface. TM AFM topography for (A) PLL-mica incubated as a control, (B) Aβ1:42 before staining and (C) after staining. Panel (D) shows the increase in height following incubation with the 6E10 primary and AuIgG; control (blue), before staining (red) and after staining (green). Data presented is from a single line scan, but is representative of multiple line scans.

across the sample would suggest the presence of many small aggregates of Aβ. This is indicated by the increased width observed between fibres and aggregates in panels (B) and (C). An increase in height is also noted in the roughness profiles in panel (D), showing control (blue), before staining (red) and after staining (green).

Confocal microscopy. In addition to the use of the AuIgG to detect Aβ aggregates attached to the PLL-mica surface a fluorescently tagged form of Aβ1:40 was used. HiLyte™Fluor 647 Aβ40 was aggregated at 25 μM as normal before being deposited onto PLL-mica, (with and without subsequent washing). Part of the characteristics of this peptide is that upon wetting with buffer the peptide solution is blue in colour (compared the transparent for all other peptides used in this study). This meant aggregation could not be monitored using ThT or any other measure of fluorescence as normal, (Fig.3.8 (A)), however no problems with aggregation were noted when examining the peptide with AFM, (Fig.3.8 (D) and (E)).

Initially, excitation and emission were checked using a Tecan Infinite Pro 200 plate reader, and found to be within suppliers predictions of 649 and 674 nm respectively (Switzerland, Europe).

To confirm that the aggregates seen with AFM on PLL-mica substrate were peptide confocal microscopy was used to check attachment. When a washed PLL-mica substrate was examined at 674 nm wavelength no background contrast was seen, (Fig.3.8 (B)), while large amounts of peptide "clouds" were visible on a PLL-mica substrate deposited with peptide, (Fig.8. (C)). Given the lack of background fluorescence seen for PLL-mica alone one can attribute the fluorescence on Fig.8. (C) solely to that of the HiLyte™Fluor 647 Aβ40. Unsurprisingly untagged Aβ did not show any fluorescence.

From these results, combined with the immunogold assay, it is possible to determine that aggregates of Aβ would successfully attach to PLL coated mica.

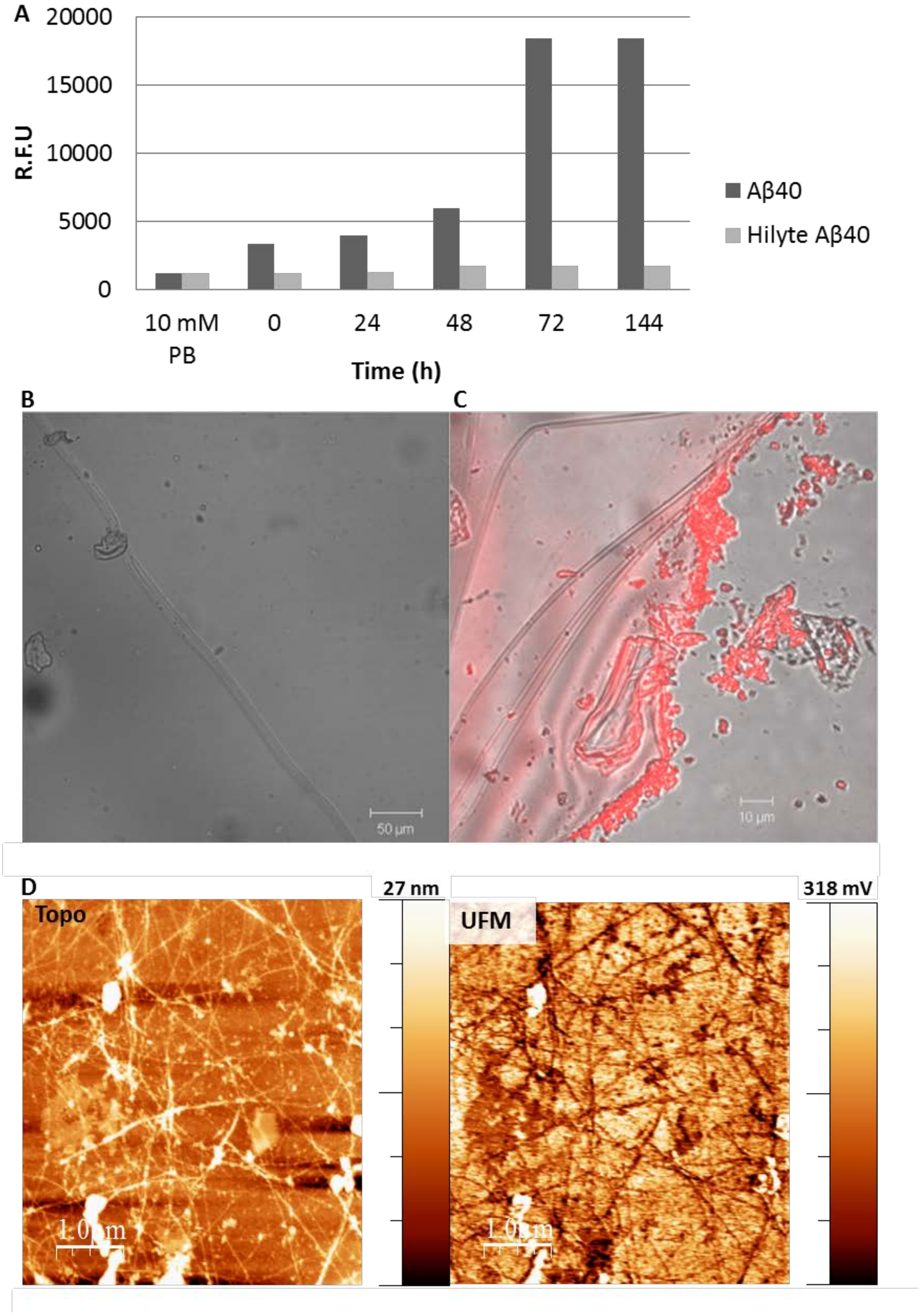

Figure 3.8. HiLyte™Fluor 647 Aβ40 was incubated for 144 h before depositing on PLL-mica. Incubation was monitored with ThT (Panel A) but due to the colour of the peptide it was not possible to monitor aggregation. Confocal microscopy was used to determine whether peptide had remained attached. Panel B shows washed PLL-mica while C shows HiLyte™Fluor 647 Aβ40 deposited onto the PLL-mica substrate and washed. UFM was used to confirm that fibres had indeed formed and that aggregation occurred as expected, showing (A) topography and (B) UFM.

3.7 Conclusion

This chapter has examined the process by which an anatomically flat, robust substrate for the AFM imaging of Aβ peptides was generated. The challenges of designing a substrate to which the peptide would attach, while providing no background contrast, either topographical or nanomechanical, have been overcome in the use of PLL coated mica, making it a preferential substrate for future imaging. Furthermore, this substrate has been shown to have no detrimental effects on aggregation or alter the type of aggregates seen. Attachment of the peptide has been verified using an immunogold ELISA and fluorescent labelling in addition to visual confirmation using the AFM. Looking forward this substrate will be used to study aggregates of Aβ using a variety of AFM techniques, where it is applicable as a substrate and no other requirements need to be met, (for example, IR transparency).
For substrates with other requirements alternatives will be investigated, such as Si or Au coated substrates. Evaporated gold coated substrates have been used to great success for the development of an atomically flat imaging substrate for other β-sheeted molecules such as Titin[214]. More recently ultra-stable Au substrates for cryo-EM have been developed which is able to resist deformation provides a high resolution substrate[215]. Ultimately although PLL-mica is an idea substrate care must be given to other imaging factors.

In the next chapter the substrate designed here, PLL-mica, will be used extensively to allow for the nanomechanical imaging of Aβ1:42 in order to determine more about its nanostructure in addition to testing the compatibility of UFM as a imaging mode for biological samples. UFM itself will also be compared with other AFM modes which characterise the elastic and stiffness properties of the sample being imaged.

Chapter Four: Scanning Probe Microscopy methods of imaging Amyloid Peptides during the aggregation process

4.1 Introduction

Following on from the development of a robust, anatomically flat substrate lacking in nanomechanical contrast, samples of Aβ1:42 were incubated and deposited onto PLL-mica before being imaged using TM, UFM and HFM AFM modes. As TM AFM is the most frequently employed AFM mode for the studying of biological samples[27, 98], due to its reduction in shear forces and friction placed upon the sample, it is the logical starting point for imaging Aβ1:42. However TM seem to be inefficient in providing the user any information beyond topographical properties of the sample being imaged, and, unlike UFM and HFM, could not easily differentiate between Ab and the PLL substrate, as may have a reduced resolution compared to CM. This chapter details the information which could be gathered on samples of Aβ1:42 across a range of time points, and the differences between the details of nanomechanical variations within the sample these techniques can provide.

4.2 Tapping Mode imaging of Aβ1:42 – detection of metal ions induced alterations in morphology.

As with all modes of AFM, TM captures the topography of the sample, but in addition to this, the phase is also captured. The phase provides an indicator of local sample adhesion, and variations within this feature across the sample, (Fig. 4.1 (B)). Following 72 h aggregated samples of Aβ1:42 were imaged using TM and showed the presence of elongated mature fibres (MF), often greater than 1 µm in length, although shorter fragments were present, (indicated in Fig. 4.1 (A and B)). A few smaller aggregates can also be seen. When the profile of these fibres is drawn, and tip convolution is taken into consideration, MF are 4.15 ±1.3 nm high and 17.72 ±8.8

nm wide, (n = 32). The width vs height difference is seen in all modes of AFM, and is linked to the tip convolution, and tip-sample forces interacting[98, 216], leading to an increase in fibre width. In addition the z resolution of an AFM is limited by the scanner being used, and the z-limit imposed by the scanner. Higher resolution scanners are able to take finer steps in the z axis and thus produce a higher resolution image. Aβ fibres diameters are typically reported based on their heights, and measured to be between 5 to 13 nm, however this does vary depending on the incubation conditions being used[81, 82, 98, 99]. The stacking nature of β-sheets suggests that the fibril morphology represents a flattened cylinder shape[12, 91, 217, 218]. If this is the case, height is not necessarily an accurate reflection of diameter. Any dimensions reported in this thesis will endeavour to take tip convolution into consideration. Ultimately, one can be assured that the samples of Aβ1:42 are consistent with those within the literature, if batch to batch variations are taken into account[197].

As a further study of TM being used to study the morphology of Aβ1:42 fibres, samples of peptide were exposed to specific metal ions, Cu(II) and Zn(II), which have previously been shown to bind to Aβ[219, 220], and that Aβ can subsequently reduce these metal ions via the Fenton’s reaction, leading to the production of hydroxyl radicals[155, 166, 170], (for more discussion of this please refer to Chapter 1.B 1.13). Peptide was incubated at 0, 1:4 and 1:1 molar ratios of Cu(II)/Zn(II): Aβ and examined for changes in morphology. It was noted that profound changes in aggregate size and morphology can be seen with increasing levels of Cu(II) presence in the buffer medium, (Fig. 4.2). Where no Cu(II) was present individual fibres were measured at 3.71 ±0.7 nm high and 9.19 ±0.1 nm wide, (n =19), while some larger fibres were also present, at almost double the dimensions, 6.88 ±0.5 nm and 18.45±0.5 nm wide, (n =13). This latter population is indicative of two thinner fibres (protofibrils) having intertwined during aggregation, such as those seen at 24 h in Fig 4.4 (E). Over the increase in Cu(II): Aβ ratio an additional category of aggregate, smaller non-fibrillar aggregates appear, in addition to fibres. Finally at a 1:1 ratio of Cu: Aβ the sample consisted entirely of shorter, amorphous aggregates with no fibres present at all. In terms of dimensions this population reflects that of the fibres, in that its height (3.96 ±1. nm) and width (7.91 ±0.1 nm, n = 14) are similar but the aggregates are much shorter and clearly non-fibrillar, (Fig. 4.2 (C)). These images also highlight common features seen when imaging amyloid fibres: a periodic twist along the fibres axis as a result of the β-sheet stacking and fibres unwinding at their ends to reveal their protofibril substructure. When examined using both the topographical information and elastic profiles (UFM) the periodicity of the fibres studied here was found to be 25.7 ±3.9 nm, in agreement with other studies of Aβ[78, 221].

It was also noted that the morphology of Aβ1:42 as determined by TM AFM could be further modified by the addition of Zn(II) to the buffer, and that its ratio with Cu(II) was also vital for any influence on morphology, as shown in Fig. 4.3. When Zn(II) is present in the buffer at a 1:1 ratio with Aβ1:42, but Cu(II) is absent there is a dramatic alteration in Aβ1:42 morphology, from fibillar aggregates to small, amorphous almost spherical aggregates which are clearly non-fibrillar. These small aggregates are 5.97 ±1.4 nm high and 27.50 ±2.73 nm wide (n = 16). However the fibril morphology is rescued when Cu(II) is added at the same 1:1:1 ratio, with fibres being seen which are4.62 ±0.8 nm high and 14.68 ±0.9 nm wide.

The production of small, amorphous aggregates when Aβ1:42 is incubated with Cu(II) have been reported elsewhere[222, 223], but the effect of Cu(II) on Aβ1:42 aggregation is highly sensitive to changes in pH, temperature and other experimental conditions[224, 225]. It is generally thought that Cu(II) has a promoting effect on Aβ aggregation[226, 227] but the extent to which is alters peptide morphology, particularly that of the fibres,

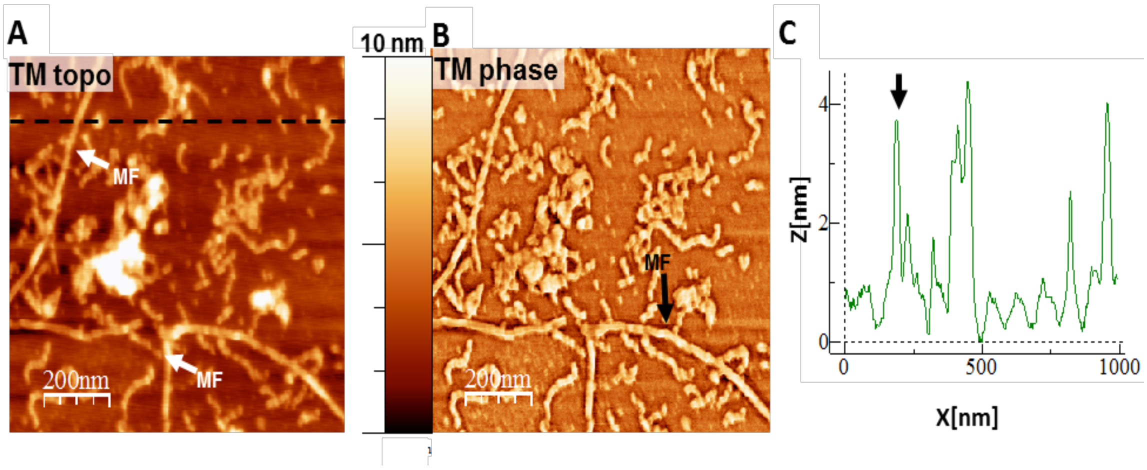

Figure 4.1. TM images of 72 h aggregated Aβ1:42 showing (A) topography (B) phase and (C) fibre profile generated from the topography channel. MF = mature fibre and indicated by the solid arrow.

remains unclear. It appears that Zn(II) affects the morphology by leading to the formation of non-fibrillary aggregates, but with the effect depending on the concentration of Zn(II)[228, 229]. Cu(II) on the other hand, also stimulates Aβ aggregation, but when present alongside Zn(II) prevents the Zn(II) induced aggregation[230]. This is in line with the results seen here, that when Cu(II):Zn(II): Aβ1:42 are present at a 1:1:1 ratio the sample contains a mix of fibrillar and non-fibrillar aggregates, whereas when Cu(II) is removed from the ratio only non-fibrillar aggregates can be seen. That Aβ1:42 aggregates into non-fibrillar aggregates as the ratio of Cu(II) increases is also comparable with what has been seen by others[222].

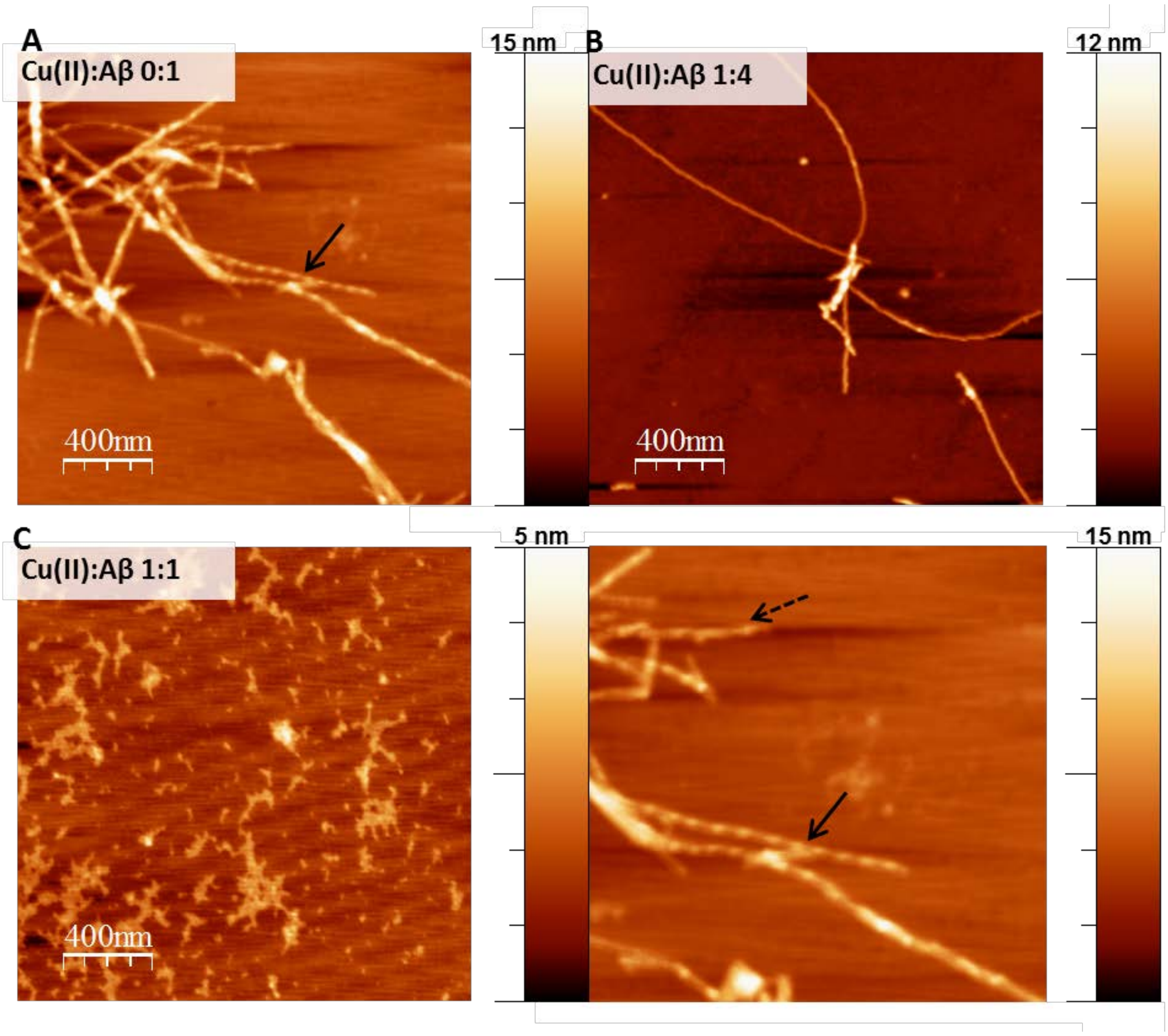

Figure 4.2. Increasing levels of Cu(II) lead to alterations to fibre morphology. Panel (A) also shows the common characteristics of amyloid fibres and has been enlarged in (D) to highlight the periodic twist (solid arrow) and a MF unwinding (dashed arrow).

4.3 UFM of Aβ1:42

UFM has already been shown to be superior to other techniques for the nanomechanical mapping of stiff sample properties[1] as well as proteins[2] and shows promise for its application to biological materials. By applying a vibration frequency in the low MHz region alongside a sub-nm to nm range amplitude to a sample, the tip-surface contact is broken, thus reducing shear forces which are introduced in CM AFM. When samples of Aβ1:42 are imaged using UFM, the topography produces comparable morphological detail to that of TM, (Fig. 4.1 (A) compared with Fig. 4.4 (A)), and no difference in size dimensions of the MF is noted between the imaging modes, (Profile (C) Fig. 4.4). What is interesting is the presence of smaller aggregates in the UFM stiffness profile, (Fig. 4.4 (B) and (E)), which are not visible on topographical imaging of either TM or UFM, or the phase channel of TM, (Fig. 4.1(B)). These smaller aggregates are similar in size to what can be predicted to be protofibrils or small oligomeric aggregates.

This population of smaller aggregates has been studied further. By taking samples of Aβ1-42 at various time points it was possible to monitor the changes in populations seen throughout aggregation. Immediately after a working aliquot of Aβ1-42 is solubilized samples were taken, dried and imaged, (Fig. 4.5 (A) and (D)), revealing a layer of globulomers across the PLL-mica surface. These globulomers were again more identifiable on the UFM profile, and this was used to locate them on the topography profile. Measurements indicated they were 1.52 ±0.6 nm (n =892) in height, which is comparable with the values proposed to be monomers and dimers, and therefore typical for an oligomeric population[75, 76, 87, 207]. Several larger features of approximately 6 nm in height are also seen, and suggested to be conglomerates of monomers and dimers, a feature of Aβ1-42 oligomers that was also noted by Lin and colleagues[207]. After 24 h incubation short flexible chains could be identified, and given their morphological and topographical features, were determined to be PF, (Fig. 4.5 (B) and (E)). Individual PF at 24 h were approximately 0.74 nm ±0.5 nm high and 1.75 ±0.9 nm wide (n = 30). Lengths of PF ranged from 50 -200nm as previously reported[86, 231].

One interesting discovery from the use of UFM for mapping the surface stiffness of samples was the ever present population of oligomers and PF, regardless of the timepoint being studied. As can be seen in Fig. 4.5 (C) and (F), alongside MF, at 72 h incubation, a large number of oligomers, > 80 per 1 μm^2, are still detectable. In addition aggregates of a similar size to those determined to be PF are present, with heights of 0.59 ±0.3 nm and a width of 4.82 ±2.1 nm (n = 30). These latter PF are not visible on their corresponding topography data so must be measured using UFM. These aggregates are thought to appear within the earlier stages of aggregation as a transient population which is sequestered into MF over time. While these earlier stages are far less stable, with binding being readily reversible and unstable, MFs are typically considered to be more stable, with dissociation of oligomers and monomers not occurring at appreciable levels[73, 74, 98, 231]. Given the complex nature of Aβ1-42 aggregation it would be naïve to assume that monomer → protofibril → mature fibre is the only viable pathway of aggregation. The hierarchy of amyloid aggregation has already been discussed in Chapter 1: Part B (1.12) and begins with the miss-folding of the Aβ monomer into a β-sheeted conformation[74, 107]. Monomers will gradually aggregated by binding together using key peptide sequences stabilised with hydrogen bonding and salt bridges to produce small aggregates such as dimers/trimmers[144, 145]. These are further able to aggregate and elongate into protofibrils, which ultimately associate to stack in such a way that their β-sheet

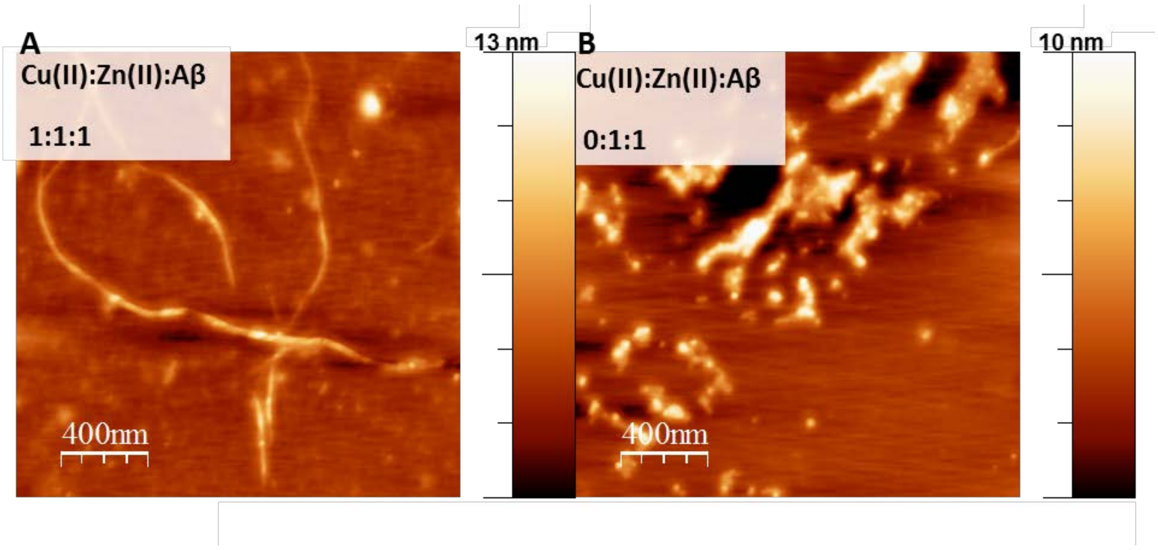

Figure 4.3. The presence of Zn(II) within the sample disrupts fibre morphology in the absence of Cu(II), however when both metal ions are present at a 1:1 ratio with Aβ1:42 fibre morphology is restored.

component is perpendicular to the MF axis[183]. The MF themselves can be made of multiple protofibrils, with some debate about the actual number[12, 80, 90, 91]. Evidence suggests that off-pathway aggregation does occur via the presence[232] of oligomers and PF which may fail to aggregate further. Early aggregates are considered to be the most neurotoxic form of Aβ1-42, so the presence of this possible off-pathway population of oligomers could have implications for disease progression and the damage which occurs in AD[122, 157, 158, 165, 233], and off-pathway aggregates could potentially alter their conformation to release toxic oligomers over a longer timespan than those which end up rapidly sequestered into MF. Alternatively this surviving population of PF could represent a linear colloidal dispersion susceptible to the laws of Brownian motion[72]. For monomers/oligomers to aggregate they must undergo favourable collisions with one another and PF/MF already forming. As more, smaller

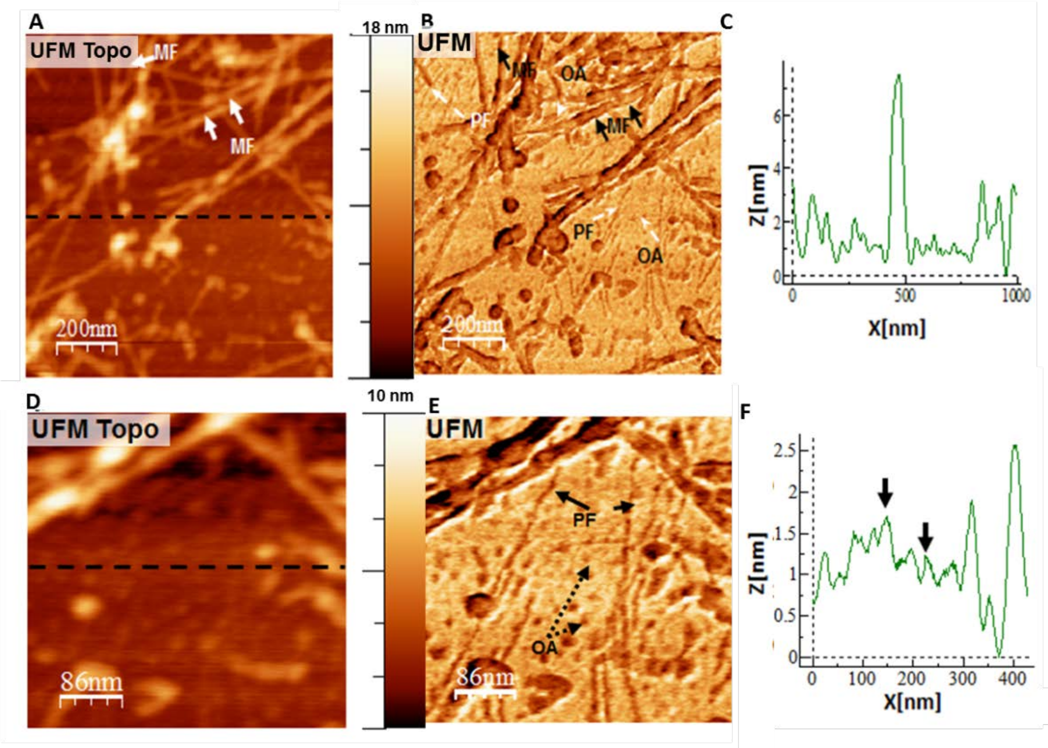

Figure 4.4. UFM of Aβ1:42 samples aggregated for 72 h. while the topography panels (A) and (D) show similar detail to that seen in the topography panels from TM, the UFM image map (B) and (E) shows enhanced detail, including smaller aggregates and protofibrils still present within the sample at this later time point, (indicated by PF (protofibril) and OA (oligomeric aggregate). These smaller aggregates are much smaller in height and width dimensions than the MF (C) and (F).

aggregates are sequestered into MF the likelihood of a successful collision decreases, and the longer the aggregate persists. Although UFM allows the ready detection and confirmation of the persistence of an oligomeric population within samples of Aβ1-42, it unfortunately does not provide an explanation for it.

4.5 Determination of fine structural details of Aβ1-42 with UFM

By overlaying the topography profile with UFM data simultaneously collected a correlation between changes in sample stiffness and height can be seen. Analysis of the UFM profile of the whole fibre width indicates that its elastic properties are not uniform across it, (Fig. 4.6, (C)). In the case of the MF of Aβ1-42 an internal structure can be seen, with a softer region approximately 1 nm (full width at half maximum) across in the centre of the fibre being apparent, flanked by 2 stiffer regions. This suggests that 2 PF intertwine to produce an individual MF, as previously described elsewhere[100]. It has already been established that Aβ1-42 fibrils have a domain architecture caused by packing of the β-sheets and H-bonding between PF[217, 218]. It has been suggested that Aβ1-42 MF would have a hollow core to their structure, with 2 peripheral regions surrounding one central hollow core[88, 90, 94, 95]. This core

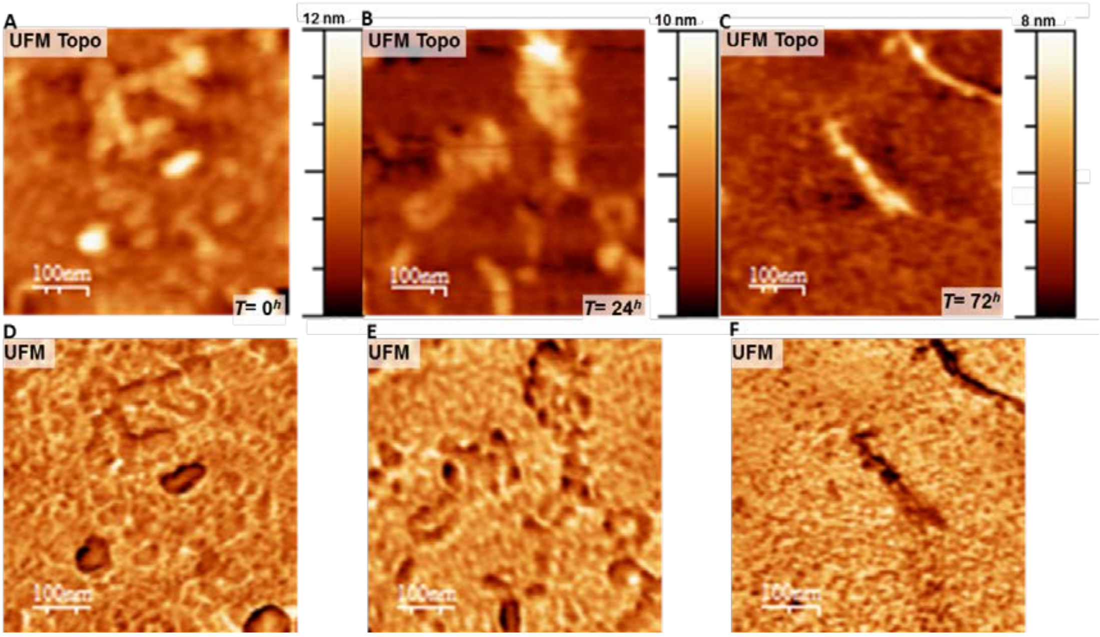

Figure 4.5. Timepoints of Aβ1-42 were taken and imaged to follow the changes in aggregate size during incubation.

itself has recently been shown to have regions of lower density and 2 small, higher density packed regions[12, 89]. Although there is still debate about the actual number of PF which interact to make up an individual MF, a factor which is possibly determined by aggregation conditions, what becomes clear from these images is that UFM can provide more evidence for the complicated nanostructure of Aβ1-42, which supports previously published cryo-EM work[89, 222]. Equally important from a methodology perspective is that UFM can apparently provide a resolution in the region of ~ 5nm, whilst providing nanomechanical details which is ideal for imaging biological molecules, with a certain sub-surface imaging possibility as already shown with graphene based nanostructures[29, 33, 234].

Another criterion regularly seen in Aβ1-42 MF is a periodic twist, again due to the nature of interactions between β-sheets which stabilize its structure[100, 231, 235, 236]. Although frequently reported, it is not always found in topographical images, this feature nevertheless is much more readily available in UFM data. In Fig. 4.7 (B) the periodicity of Aβ1-42 MF can clearly been seen as a variation in elastic properties along the fibre length, and was determined to be approximately 25.7 ±3.9 nm. The corresponding topography shows a slight decrease in height (Fig. 4.7 (A)), but does not show the level of detail that is seen with UFM. The periodicity does affect the

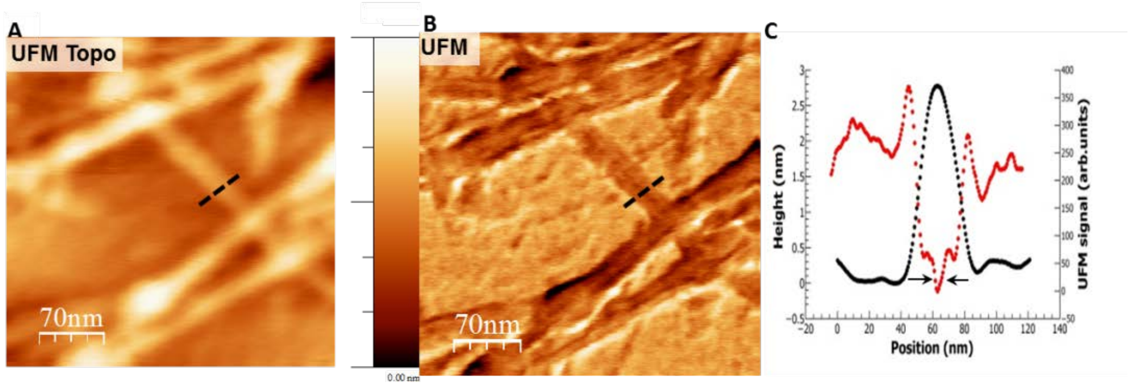

Figure 4.6. (A) topography and (B) UFM image of Aβ1-42 after 72 h incubation. (C) When the UFM profile is overlaid with its corresponding topography the internal structure of a MF is revealed. Corresponding UFM stiffness profile (red dots) across the MF (dashed lines in (a) and (b) reveals internal structure invisible neither in the topography image nor in the topography profile (c), black dots) with the width of the softer region in the fibre centre being approximately 5 nm (c), arrows in UFM profile).

measured fibre width, however, as each MF's distinct UFM profile is not affected by this twisting nature of the Aβ1-42 MF – the feature described above.

A hollow core in β-sheeted amyloid fibres is a common structural feature[93, 237, 238] and has been noted in numerous techniques, including cryo-EM, solid-state NMR spectroscopy, x-ray diffraction and circular dichroism. Although the hollow core in Aβ has been noted in numerous studies[91, 94, 95] the use of UFM to detect the potential hollow core within Aβ1-42 could be further validated by the study of well-defined peptide fibres which are known to have this structural feature. There are numerous proteins which could be studied, including transthyretin, which has been shown to make fibres consisting of numerous numbers of protofilaments. Regardless of the number of protofilaments within the MF a hollow core can be detected within the centre of transthyretin[93, 239]. Microtubules also make ideal proteins to study if trying to identify a hollow core. Between 8 and 17 protofilaments made of tubulin heterodimers associate to form a microtubule[240]. At 7–10 nm in diameter for transthyretin fibrils and approximately 25 nm for microtubules both make an ideal comparison[93, 241].

4.6 Reducing friction forces and sample damage artefacts via UFM

A key feature of UFM is the significant reduction in shear (friction) forces acting on

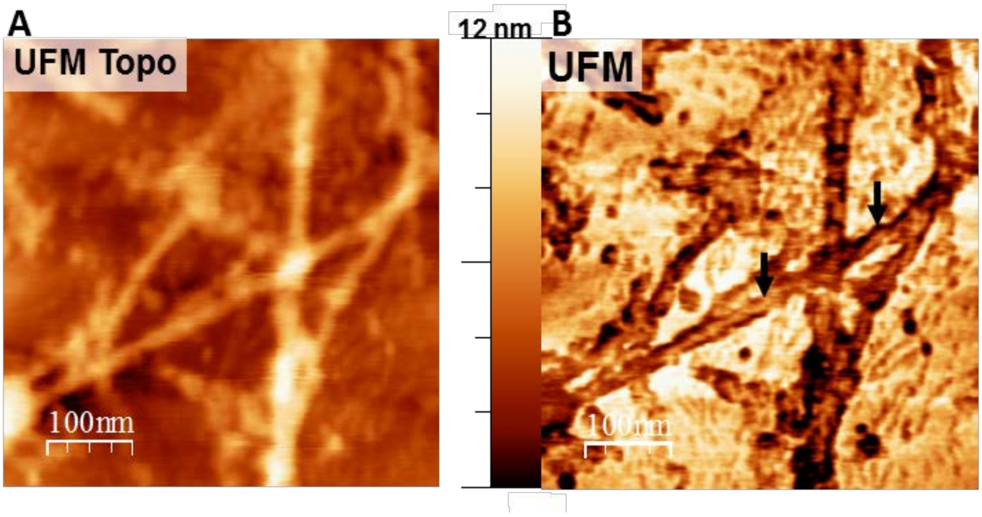

Figure 4.7. UFM (B) can readily detect the periodicity of Aβ1-42 during imaging, a feature which can be difficult to detect by topography (A).

the sample in CM AFM, thus allowing the user to have the enhanced resolution and reduced damage even in comparison to TM. In UFM it has been shown that when the tip-surface contact is broken due to the out-of-plane vibration friction vanishes, as well as being reduced before the contact is broken[30]. One must also be aware that fibres formed at earlier timepoints were more susceptible to tearing and manipulation by the cantilever, suggesting a less rigid morphology than those seen at *t* > 72 h. Care was therefore taken with early timepoints to minimise the force being applied to the sample regardless of the AFM mode being used.

The damage to samples of Aβ1-42 when CM is used can be seen in Fig. 4.8 (B). An area of Aβ1-42 was scanned first using UFM, (Fig. 4.8 (A)), before the ultrasonic vibration was removed by simply turning off the AC source. The set-force being applied to the sample remained the same (0.2V) while the same area was then rescanned (Fig. 4.8 (D)), showing a less clear image and evidence of streaking which is a result of increased friction and torsion on the cantilever as it scans across the

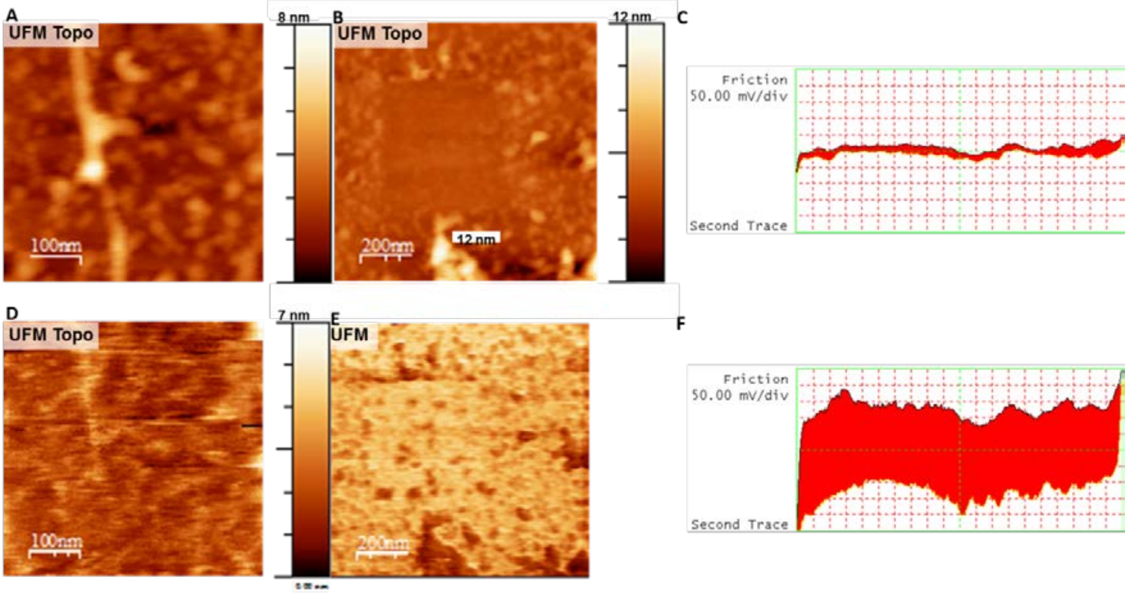

Figure 4.8. (A) Topographical image of amyloid fibrils and oligomer aggregates in the presence of ultrasonic vibration (UFM mode). (B) UFM scans of a wider area showing the damage caused when imaging in CM alone, without ultrasonic vibration. (C) raw friction data showing the reduction when the ultrasonic vibration is switched on. (D) subsequent topographical image of the same area without ultrasound (CM) with the image being lower in quality without UFM (compared to (A). (E) corresponding UFM channel data to (B). (F) the increased friction seen in CM, without the ultrasonic vibration being applied.

sample surface. Following this scan the UFM was turned on, and a larger area encompassing the previous one was imaged. As can clearly be seen in (Fig. 4. 8 (B) and (E)), the morphology of the fibres within the area imaged without UFM has been grossly and irreversibly damaged. Despite the low set-force applied to the sample, without the applied ultrasonic vibration of UFM, any CM imaging is almost useless if repeat scanning of an area is needed, and also reducing the resolution of the topography. When the friction channel itself is studied, (Fig. 4.8 (C) and (F)), on can clearly see the huge jump between UFM on, (C) and off (F) in the level of friction detected.

4.7 Application of UFM underliquid

The aim of the under-liquid results presented here was to produce a reliable under-liquid imaging method for Aβ1-42 at an improved resolution to what has been seen before which could be used both *in* and *ex-situ*. By employing the use of a liquid cell in the AFM setup, UFM can easily be applied underliquid[32], providing the ideal imaging environment for any biological sample is to image them in their native environment. The application of AFM underliquid is challenging, and even more so when working with Aβ1-42. Although some groups have had some success with Aβ1-42 under-liquid the results in the literature are mixed. Innocenti and colleagues[223] were able to follow the aggregation of Aβ1-42 for 48 h after injection in the liquid cell, monitoring fibril growth and the effect of metal ions upon the aggregates. However the concentration of peptide was considerably higher than that which we choose to work with, (100 µM compared to 25-50 µM), and surprisingly no aggregates were detected by this group until 24h had elapsed. As can clearly be seen from our samples taken on PLL-mica at this time point and at earlier timepoints , small aggregates we suggest to be oligomers/monomers, protofibrils and even some fibres are present <24 h (Fig. 4.5). However other groups have had more success at imaging smaller aggregates *in situ*[86, 148], with both fibrils and aggregates of various sizes being imaged. In most of these studies however, the attachment of Aβ1-42 is poor, leading to increased friction and damage to the fibres/aggregates as the sample is scanned, thus reducing the resolution of the data collected.

Initial efforts with under-liquid imaging of Aβ1-42 involved the application of UFM using the liquid cell for samples of already dried peptide (deposited onto PLL-mica). Unfortunately the results were not promising. Imaging in an aqueous environment appears to result in a loss of UFM signal and therefore a reduction in sensitivity (Fig. 4.9). Alterations were made to the peptide used, with the removal of excess fluorinated deseeding treatments and different re-treated forms of the peptide being used. While these peptides showed aggregation potential when monitored by ThT, no improved attachment was seen when used *in-situ*.

An alternative approach was to rehydrate samples previously imaged and image these *ex-situ*. As noted with previous studies[9], rehydration of a sample appears to cause instability within the protein structure, resulting in the gradual appearance of globules (C, D) within 30 mins and the complete disintegration of fibres by 80 mins (E, F). Maurstad and collegues[9] have previously noted this was the case with imaging of Aβ1-42 fibres. They found, similar to our observations, that initial drying of fibres on its own does not affect their morphology or indeed their stability, whereas the following rehydration does lead to the deterioration. They suggested that dehydration causes an internal change to the peptide, which further weakens once rehydrated.

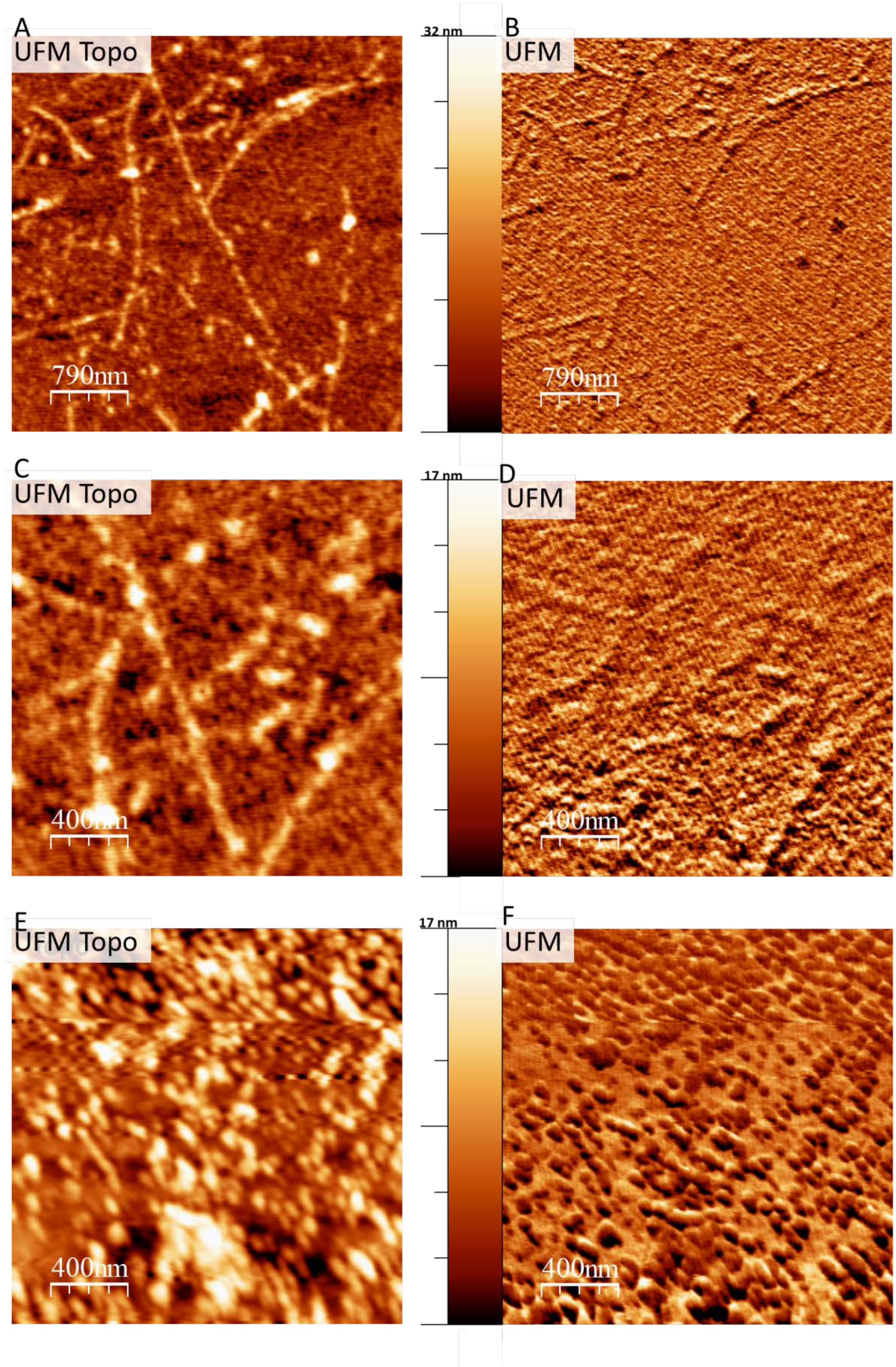

Figure 4.9. The under-liquid imaging of Aβ1-42 proved challenging. Although it was possible to image in a liquid environment, Aβ1-42 fibres proved to be unstable and deteriorated over time, as noted with previous studies[9]. Rehydration of a sample appears to cause instability within the protein structure, resulting in the gradual appearance of globules (C, D) within 30 min and the complete disintegration of fibres by 80 min (E, F).

4.8 Tip only ultrasonic excitation - waveguide-UFM; further enhancement of the technique.

The application of UFM has already been shown to be an ideal technique for studying Aβ1-42, with enhanced sensitivity over TM and also other CM techniques. Standard UFM protocol involves applying an ultrasonic vibration to the sample by the utilisation of a piezo crystal stage, requiring that the sample to be mounted on a suitable thin, ultrasonically transparent substrate. In contrast, this ultrasonic vibration can be applied directly to the cantilever by use of a modified holder,

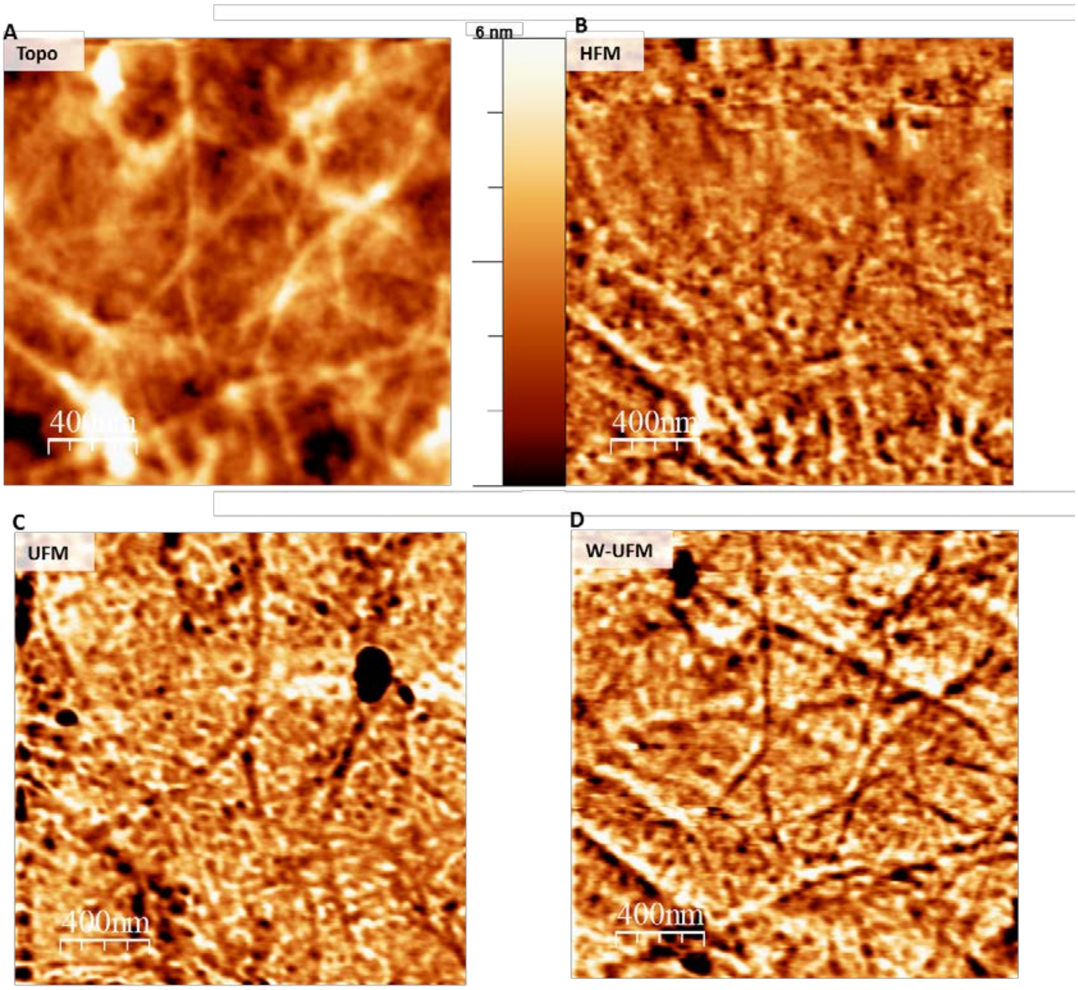

Figure 4.10. w-UFM delivers the ultrasonic vibration to the cantilever directly (D) compared to a piezo transducer placed beneath the sample (C). An alternative method of measuring sample stiffness is HFM (B).

exciting the cantilever at a frequency in the MHz range, allowing realisation of the nano-mechanical imaging on any substrate. The mode is called the Waveguide UFM (W-UFM) as the cantilever acts as an ultrasonic waveguide in this case[242]. The principle is identical, with the cantilever becoming infinitely rigid, and briefly indenting into the sample surface before pulling away. The high frequency modulated vibration is also detected in this mode via force-vs-distance non-linearity, and a contrast image map of the samples stiffness is produced. In order to compare the detail available from each technique the same sample area was imaged with both. This was made possible by briefly placing the cantilever out of contact with the sample surface (by using of a reduced set-point amplitude) and the adjustment of the ultrasonic vibration amplitude. This ensured an identical area could be re-imaged and the data could therefore be directly compared. While Fig. 4.10 shows that it is possible to identify Aβ1-42 aggregates of all sizes using UFM (C) and w-UFM (D) but imaging conducted with w-UFM is sharper, and features are more readily identifiable. When compared to the topography (A) there is better definition between topographical details and the w-UFM image than with sample UFM.

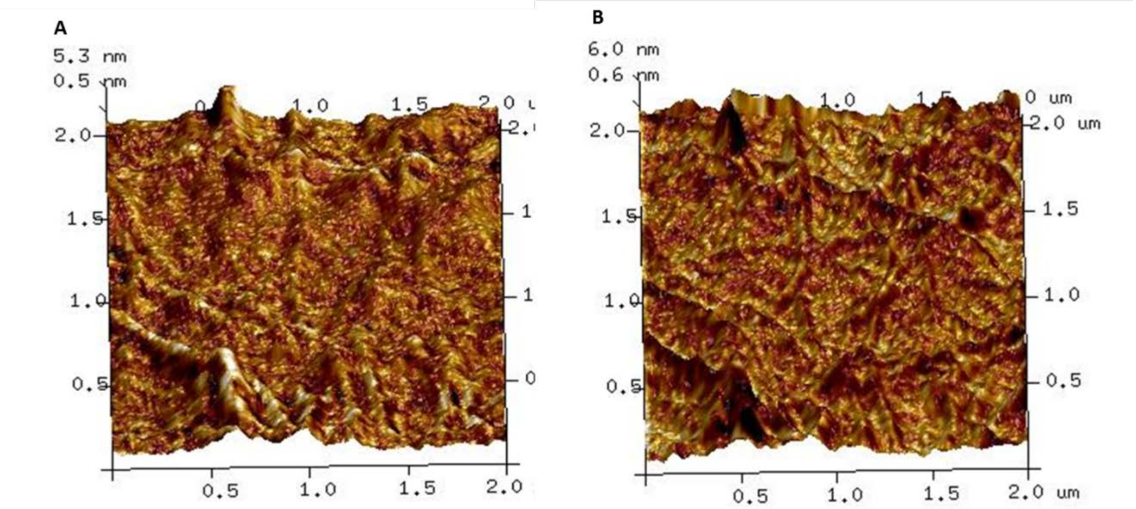

Figure 4.11. When topography is overlaid with the nanomechanics channel better contrast and a better spatial resolution is provided by w-UFM (B) than HFM (A).

An additional method of identifying variations in nanomechanical properties of the substrate is HFM, a method stemming from the UFM approach[243]. In a manner which combines both UFM and w-UFM the ultrasonic vibration is applied to both the base of the cantilever and a transducer beneath the sample simultaneously, with a 3 kHz difference between these frequencies to allow for detection of a response, the non-linear deflection of the cantilever. HFM of Aβ1-42 can be seen in Fig. 4.11(B) and was also collected on an identical area to UFM/w-UFM. Of the three techniques for identifying changes in the elastic properties of a sample surface HFM data is less clear and detailed compared to the UFM/w-UFM data. Although the image (B) map shows the presence of fibres, smaller aggregates present around them are much less clear and areas with a lack of overall clarity are present. When the HFM and w-UFM channels are overlaid with the topographical channel the difference between the level of detail captured is obvious. While both techniques are capable of identifying differences in nanomechanical responses across the sample surface, UFM, in particular w-UFM provides the greatest detail without damaging the delicate Aβ1-42 aggregates.

It is possible to extract information about the nanomechanical properties of samples using the UFM data gathered during scanning. Friction can be quantified by analysing the lateral force and lateral amplitude during scanning[244]. The Young's modulus, and therefore the elasticity of the sample, can be determined from the UFM signal itself by calculating the load dependent indentation of the tip into the sample using the JKR model. Indentation of the cantilever in IFM is determined by the adhesion properties of the sample, the tip curvature, the Young's modulus of the tip-sample interaction and the load placed on the sample[245]. The load on the cantilever is controlled by the setpoint value used during scanning. A simple quantitative analysis of local sample stiffness can also be performed by averaging the UFM response of the material over the representative force interval[35]. To quantify the UFM response of Aβ1:42 fibres, and others, at varying stages of aggregation would be the next step for this work.

4.9 Conclusion

The widely used AFM mode for imaging biological samples - TM[27, 98] seem to limit the contact with the sample surface, and therefore any potentially destructive friction forces applied to the sample. The imaging of Aβ1:42 aggregates at different timepoints using TM was successful, with both smaller aggregates (at earlier timepoints) and MF (> 24 h), being readily identifiable. Our samples of Aβ1:42 aggregated into fibres with morphologies that are in agreement with previous studies[82, 98], with typical dimensions being 4.15 ±1.3 nm high and 17.72 ±8.8 nm wide, (n = 32). It was also possible to determine alternations in fibre morphology as a result of incubation with AD relevant metal ions. It was noted that following incubation with increasing concentrations of Cu(II) that Aβ1:42 aggregates became non-fibrillar in appearance. In addition a similar effect was seen with Zn(II) concentrations. To add further dimension to this when Aβ1:42:Zn(II):Cu(II) were present at a 1:1:1 ratio the non-fibrillar morphology seen at 1:1 Aβ1:42:Zn(II) was rescued by the presence of the Cu(II) suggesting a complex interplay between AD relevant metal ions. It is clear that while TM AFM studies can shed light on the sensitive and flexible nature of Aβ1:42 aggregated morphology, more work is needed to clarify how metal ions influence it.

While TM is an ideal method of AFM study for biological materials it is limited by being unable to offer any additional information on the sample, e.g. nanomechanical properties of the sample. In contrast, UFM, whether standard or waveguide, and HFM allows the mapping the stiffness of a sample using ultrasonic vibrations. This ultrasonic vibration, particularly well documented here in the case of UFM, reduces friction being placed on Aβ1:42 and prevents damage to it that would otherwise be seen in contact mode, (Fig. 5). No differences in aggregate sizes were noted with UFM compared to TM, however it UFM is able to detect the presence of small aggregates comparable to monomers and dimers, which is undetectable on the topography channel. This discovery has led to the identification of a persistent population of oligomeric aggregates, which are present at least as late as 72 h after aggregation first begins.

In addition to the identification of the persistent oligomeric population, UFM was able to identify finer structural features such as a periodic twist, which is often difficult to identify via the topography channel. Furthermore it was possible to use the elastic profile details gained by scanning with UFM to infer details of the MF substructure. While HFM also allows details of the samples stiffness to be mapped when compared to UFM/w-UFM it was not found to be as efficient at mapping. In conclusion UFM can be considered to be an ideal technique for studying biological molecules, and has proven very effective at detecting aggregates <5 nm while allowing details of the internal MF structure to be detected. The success of UFM in providing new information on Aβ1:42 in addition to details about its topography prompted the exploration of other physical parameters, which may reveal new contrast and nanoscale properties, including thermal conductivity and spectrally selective optical absorption. Data in the following chapter was collected utilising techniques which allow this, including the development of novel methods of SPM.

Chapter Five

Spectroscopy and Thermal SPM Methods of studying Aβ1:42

5.1 Introduction

This chapter builds on the previous work into the imaging of Aβ with SPM techniques. Previously it has been shown that with careful substrate design is it possible to capture a variety of aggregate sizes and study their nanomechanics in detail. The SPM methods in this chapter move forward to focus on exploring Aβ beyond these nanomechanical properties. SThM maps thermal conductivity of the sample using a Joule heated cantilever[42, 43], and can also be modified using an IR laser pulse to provide the heat to detect a cantilever response which is wavelength (and therefore chemical feature) specific. Chemical features of biological samples have for years been identified using techniques such as FT-IR, particularly in the mid-IR range. However these techniques are typically limited by the spatial resolution ~5µm due to the diffraction limit of IR light[20], and as such tip-enhanced techniques have been developed[246-249]. Recently work has been done to combine the nanoscale resolution of AFM with spectroscopy data which can be collected in the IR range. One such system, the Nano-IR designed by Anasys Instruments (Santa Barbra, USA), has used a tuneable, pulsed IR laser focussed onto the sample, but near an AFM cantilever to deliver IR information with a resolution of ~100nm[20, 55-57, 250, 251]. The Nano-IR examines the nanoscale thermal properties of the sample under investigation, a pulsed, tuneable IR laser excites the molecular bonds within the sample, causing it to vibrate and expand via a phonon thermal wave. This transient dilation of the sample then excites resonant oscillations within the cantilever, the amplitude of which is directly proportional to the samples absorption coefficient[52]. Over time the oscillations naturally reduce, until the next pulse and this is known as the cantilever ring down. By extracting information from the subsequent cantilever ring-down (between IR pulses) details of local absorption spectra can be generated, alongside topography and sample stiffness, all at the nanoscale.

In this chapter work on the Free Electron Laser (FEL) at ALICE is detailed, a tuneable mid-IR facility, which was utilised to further develop the technique of SThM-IR, a technique similar to AFM-IR[19]. Currently this technique provides details on samples with ~100nm resolution; however the aim of this project was to create a system which could improve this resolution to closer to that of traditional AFM (5-10 nm). Work detailed here is from the early stages of establishing such a system, and was limited by time constraints and system challenges beyond our control, but does show the promise a SThM-IR technique with true nanoscale resolution has. All SThM-IR work was carried out in conjunction with Dr. Peter Tovee, (Department of Physics, Lancaster University, UK), who was also responsible for calculating the time decays, (the heating and cooling of the cantilever until the response to the thermal expansion has passes), for the SThM-IR thermal and deflection signals. These values provide information on the thermal conductivity of the sample and its behaviour during thermal expansion.

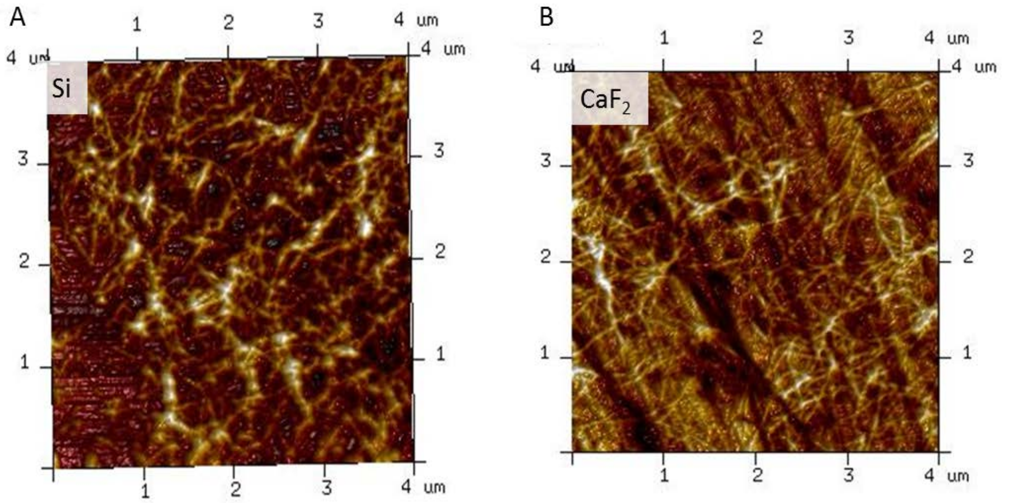

Figure 5.1. SThM data gather on Aβ1:42 samples on (A) silicon and (B) CaF$_2$ disks. In order to compare the substrates the topography data has been converted into 3D, and the thermal data overlaid. This was achieved using Bruker NanoScope v6.14r1 software.

5.2 Scanning Thermal Microscopy nanoscale mapping of thermal conductivity of Aβ1:42

The SThM AFM system previously used at Lancaster University[22, 23, 35, 188, 252], employs a Joule heated cantilever. During scanning the AFM probe is kept at a constant voltage, and thus the heating to the probe remains constant. As the probe moves across the sample surface, heat dissipates from the tip into the sample, based on the samples thermal resistance, which changes the sensor temperature. This temperature change quadratic relationship between the probe and the sample and is detectable by a change in the probe's electrical resistance, measured through an electrical bridge configuration. On a SThM image darker areas are those of increased thermal conductivity while brighter areas have lower thermal conductivity.

Samples of Aβ1:42 were aggregated for 144 h before being spun down to sediment fibres. The buffer and any remaining monomers were then pipetted off to create a pellet containing β-sheeted MF. The supernatant was tested via ThT to ensure it did not give a response above background levels meaning that one could assume all β-sheet structures remained in the pellet. This sample was then resuspended in dH_2O and deposited onto substrates.

The thermal response of the sample can depend on the substrate on which it sits as some substrates have a greater thermal contrast than others, due to their thermal conductive properties and potential to act as a heat sink during experiments. The MF from Aβ1:42 were deposited onto both silicon and CaF_2 substrates. Silicon and silicon dioxide can make ideal substrates for SThM based on their atomic flatness, low cost and good thermal contrast properties due to their relativity high thermal conductivity compared to the amyloid fibres. Aβ1:42 MF were readily attached to the sample surface, and were found to be stable during imaging. The fibres show a lower level of thermal conductivity than the surrounding silicon, but the contrast is clear between peptide and substrate (Fig. 5.1 (B)). Calcium fluoride, while considerably more expensive than Si, makes an ideal substrate for later AFM-IR work as it is transparent in the whole mid-IR range, while Si is not. However, as can be seen from Fig. 5.1 (B), it does not provide the strongest thermal contrast for the fibres. Fibres and substrate both show low thermal contrast in comparison to Si substrates, and it can be difficult on CaF_2 disks to differentiate one from another. In addition, because the individual disks are produced by cleaving a larger cylinder of CaF_2 multiple trenches can be seen across the sample surface increasing roughness. As with other surface sensitive microscopies[253] thermal microscopy is susceptible to topographical features and therefore more care must be taken when making determinations from these results as the higher the sensor is from the substrate, the higher the temperature and resulting signal (reflected as brighter contrast in the images). SThM imaging is also affected by the size of the contact area, increased roughness and contact of the sample along the side of the cantilever (thus leading to a higher contact area) and therefore increased heat flow and a lower signal.

5.3 SThM-IR imaging at fixed wavelength of Aβ1:42

For SThM-IR measurements, the tuneable laser from the ALICE FEL was used, as previously done with Scanning Near-field Optical Microscopy (SNOM)[190]. A guiding

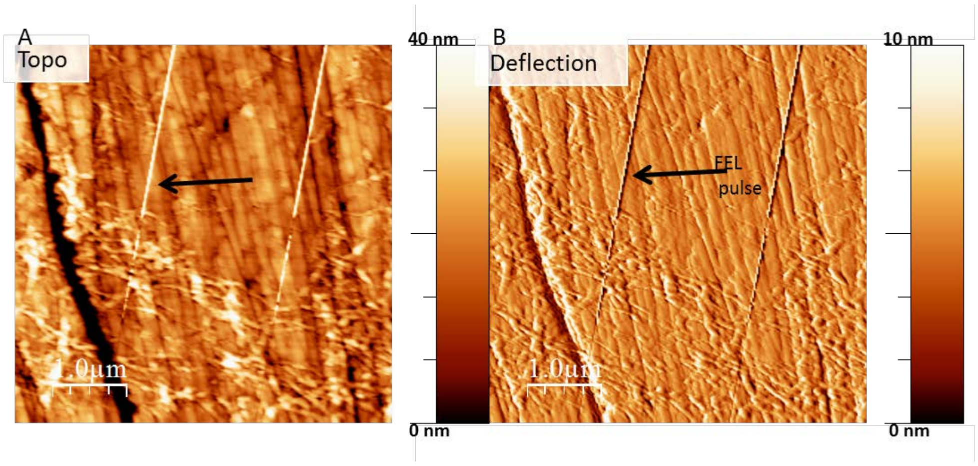

Figure 5.2. Standard contact imaging of Aβ1:42 fibres on CaF_2 substrates (A) Topography and (B) Deflection. The FEL trigger pulse received from the boxcar can be seen as a repeating diagonal line across the image map, and is due to the FEL pulse “kicking” the cantilever. The FEL lines were not processed from the image as evidence that the signal seen (i.e. topography and deflection) was indeed as a result of the FEL being focussed onto the cantilever in the correct position. If the FEL was not focussed onto the cantilever so signal, and therefore not image, would be recorded, (in a manner analogous to a standard 670 nm AFM laser not being correctly aligned with the cantilever).

HeNe laser along with some gold mirrors and a CaF_2 lens was used to focus the FEL onto the thermal cantilever, and when in contact the FEL could be confirmed in one of two ways. The particular FEL in operation for these experiments delivers short pulses every 10 Hz of 5-9µm, which can show itself as diagonal lines across an AFM scan topography and deflection (Fig. 5.2). These represent the FEL pulse heating the sample, and the subsequent thermal expansion “kicking” the cantilever. Contact is not lost with the sample surface during these “kicks” due to the cantilever acting as a spring. The FEL pulse can also be detected by monitoring the thermal response of the cantilever. When the FEL is focused onto the cantilever, the IR light causes it to heat, which is detected by the sensor, (Fig. 5.3 “out of contact”, pale grey line). This heating of the cantilever causes it to bend as well as oscillate, leading to a ring down that ceases well before the next pulse of IR light. Due to its metal coating and increased width, SThM cantilevers are also susceptible to more torsional excitation than standard cantilevers. The use of metallic substrates and cantilevers, i.e. a gold coating can be used to further enhance the thermal expansion of the sample as metallic surfaces are highly reflective with regards to thermal radiation.[254] The use of gold substrates can generate both propagating and evanescent waves from the initial IR induced thermal expansion, which reflect and amplify between the two metallic surfaces until they are absorbed by whichever surface is coolest[254].

The signal strength both in and out of contact was highly variable, due to the FEL having an irregular spatial structure modulating the beam intensity. The FEL is focused both longitudinally and transversely by the DC photoelectron gun before the main linac within ALICE. Analysis of the beam structure following the first experimental period at ALICE has shown than the FEL has a distinct substructure, made of 2 beams at the head and the tail of each electron bunch accelerated through the system[255]. This is likely to be the result of the low energy dynamics of the beam injector and is considered to be a likely feature of all beams produced in this manner. The result is even the slightest change in laser position could dramatically affect the signal, and the results of SThM-IR measurements. The majority of the signal seen from the cantilever in SThM-IR mode is the result of the FEL heating the metal backed cantilever and it bending, creating deflection (Fig. 5.3).

This results in a high signal overall, but actually only a small proportionate of it is the result of the samples response to the pulsed IR source. The signal from the cantilever is lower when in contact due to the dissipation of heat from the cantilever into the sample.

Once it had been established that the FEL provides sufficient signal for the AFM cantilever, it was tested on samples of Aβ1:42 MF on IR transparent disks, (as seen in Fig. 5.1 (B)). Scans were taken in CM until a suitable area was found. Once this had occurred, the slow scan feature of the SPM software was disabled, meaning the same line was being scanned continually allowing efficient averaging of the data. Care was taken here to not apply too much set force to the sample, as CM scanning can be destructive for biological samples. Continuous 3D line scans were collected while ALICE was tuned to fixed wavelengths of 1650 cm^{-1}, 1610 cm^{-1} and 1660 cm^{-1} which correspond to absorptions of Amide I, β-sheet and α-helix respectively. After data collection some processing of the data was needed with MATLAB: 250 line scans

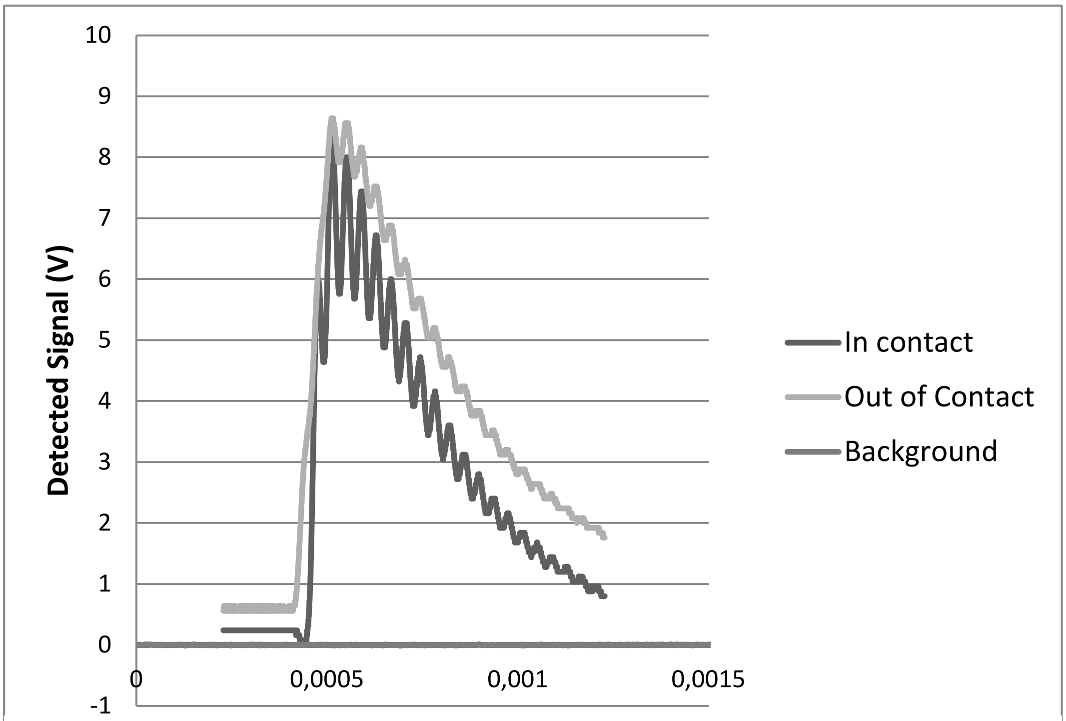

Figure 5.3. Detection of the SThM signal from the cantilever using the FEL pulse. The cantilever response can be seen both in and out of contact. Data collected is the sum of at least 3 line scans.

(each of the same line) were summed, averaged and normalised with respect to the I0 (background) signal collected from the boxcar averager. This processed data is presented in Fig. 5.4 along with AFM topography and deflection of the scanned area. It was possible to collect two types of data from the SThM-IR system. The first was the thermal response through the electrical bridge and SThM cantilever, (corresponding to the sample conductivity) and the second was the deflection caused by the photothermal expansion of the sample. This expansion leads to a temporary knock of the cantilever, which itself, and the ringdown, can be recorded and analysed. The thermal response of the sample (heating and cooling of the

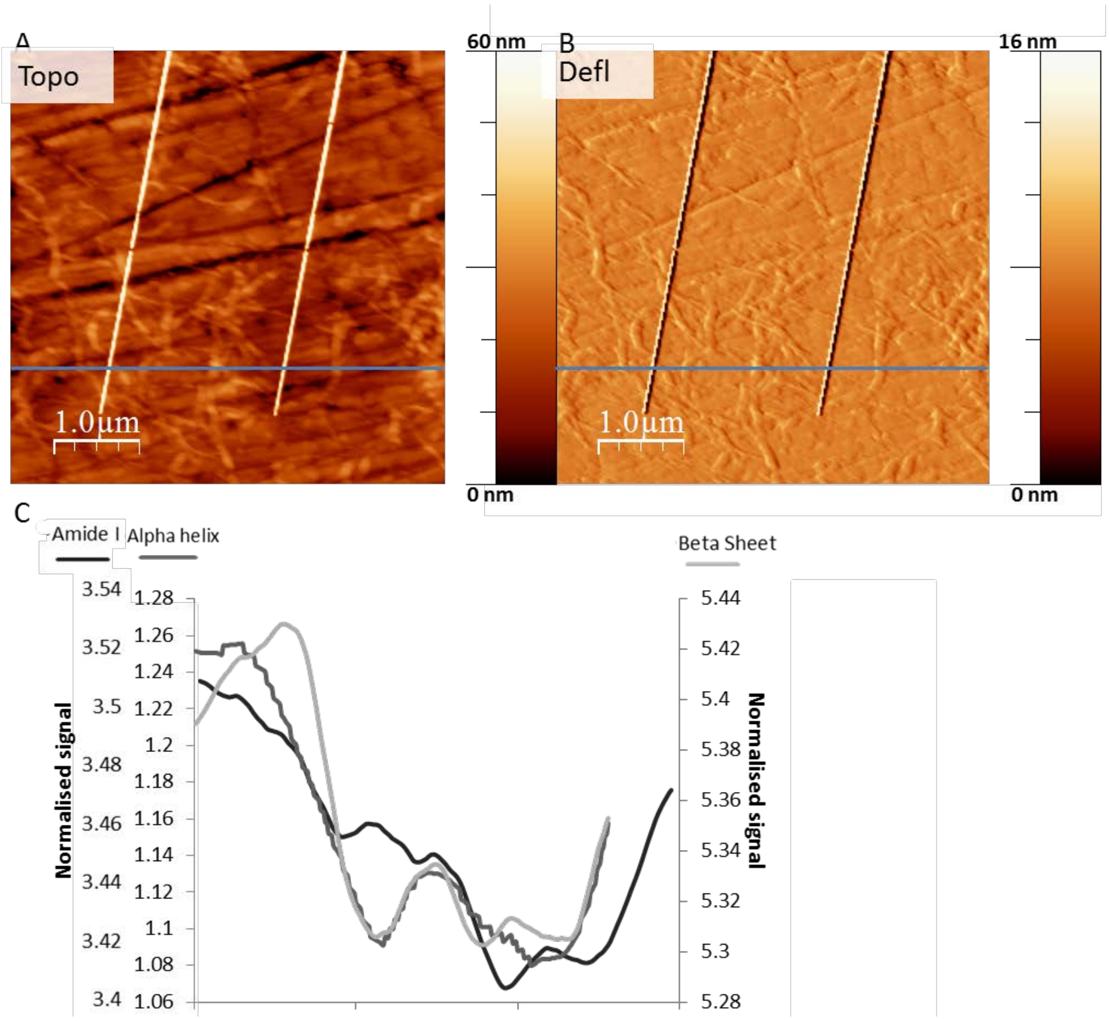

Figure 5.4. SThM-IR data collected on samples of Aβ1:42 (A) and (B) show the topography and deflection from preliminary scans before data collected from the cantilever response was collected while (C) shows the resulting photothermal data. Data was collected by fixing ALICE at Amide I (1650 cm^{-1}), β-sheet (1610 cm^{-1}) and α-helix (1660 cm^{-1}). The approximate position of the line scan is indicated in blue on topography (A) and deflection (B) panels, and is an example of the overall dataset collected.

cantilever), and the ringdown of the deflection follow a similar pattern, however have different time constants; SThM-IR thermal time decay was 2.074 x10^{-4} ± 8 x10^{-7} s while the SThM-IR cantilever deflection ringdown was 4.28 x10^{-4} ± 1.6 x10^{-5}. As is seen in Fig. 5.4 it is possible to detect the deflection of the cantilever resulting from the IR laser focused onto the sample near it, however reproducibility of the ALICE system meant data collection was limited.

The spatial resolution of ALICE in mid-IR wavelengths is estimated to be 100 nm[190], and the wavelengths of interest were sufficiently far apart to provide spectrally significant information. The most commonly used IR wavelengths used to study proteins are the amide bands, and the absorption features within them, which are specific to the structural properties and components of the sample[256]. Amide I is the result of C=O stretching vibrations, determined by the protein backbone and located typically between 1690-1600 cm^{-1} (~5.91 μm). When Aβ has been analysed for structural features previously with a similar technique, by attenuated total reflectance Fourier transform infrared spectroscopy (ATR−FTIR) key structural components of Aβ peptides have been located. The component most commonly found in the monomeric form, the α-helix is located between 1654-1660 cm^{-1}(6.02-04 μm) [249, 256, 257] while β-sheets have been detected between 1628-1630 cm^{-1} (6.13-14 μm) [256-259]. Amyloid aggregates are noted to have a specific maximum between 1910-1630 cm^{-1} [256] and it is possible to detect a difference between parallel and anti-parallel β-sheets[258, 259]. The slight variations between wavelengths is possibly the result of system specifics, differing techniques and different sample preparations of amyloid proteins (including different suppliers and deseeding techniques), as each will affect the final protein secondary structure in unique ways, with the gross structure still being α-helix versus β-sheet[197, 260]. Given the wavelength resolution is estimated to be 100 nm broad peaks to reflect the three key structural components were chosen (1650 cm^{-1} (6.06 μm), 1610 cm^{-1} (6.21 μm) and 1660 cm^{-1} (6.02 μm); Amide I, β-sheet and α-helix respectively). The processed data from ALICE is rather difficult to interpret due to relatively poor reproducibility and strong fluctuations in FEL power throughout the experimental period; however it is possible to determine that where fibres are present there is a variation in the strength of the SThM response from the cantilever. While there is clearly a strong β-sheet signal, (Fig. 5.4 (C)), the signal from the cantilever at an α-helix specific wavelength is almost as intense. The sample preparation involved an extended aggregation period of produce fibres, which were then isolated and have been shown to be wholly β-sheeted in content[167] so this possible detection of an α-helix content is conflicting. There is a possibility that some of this conflict is the result of power fluctuations, sample thickness (amyloid peptides are thin in comparison to other materials imaged with SThM) or poor signal conductivity between the cantilever and sample. However this small signal from such a thin sample has still made imaging challenging and more work is needed to improve the sample design.

5.4 Measurements of Aβ on Anasys "Nano-IR" system

One of the most promising advances of the AFM-IR field is the development of the Nano-IR by Anasys Instruments, (Santa Barbara, USA) [18-20, 51-53]. This system has a comparable spatial resolution to ALICE (100 nm) and in a manner similar to the AFM-IR system described above uses an gold coated AFM cantilever in conjunction with a pulsed tuneable IR laser source to detect the photothermal absorption of the sample[18-20, 51-53]. Success with this system and amyloid proteins has already been seen. Mű̈ller and colleagues successfully identified differences between aggregated and monomeric lysozyme using this system[256]. Samples of Aβ1:42 prepared as for SThM-IR experiments were studied by Anasys Instruments using the Nano-IR, for AFM-IR experiments. Initial experiments on CaF_2 disks proved to have too limited a signal for the system. In order to enhance the signal the sample was then deposited onto gold coated silicon wafers. The sample was then analysed at 1650 cm^{-1} (Amide I) both on the peptide sample and on the gold substrate and gold coated tip. This background can then be compared to that of a freshly cleaved gold slide, and that of the peptide (Fig. 5.5). Some substrate signal is always present due to absorption of the signal from the probe itself, (Fig. 5.5 (C) grey line), while a much lower signal can be detected on the surface of the gold slide onto which peptide was deposited (Fig. 5.5 (C), blue line). This reduced signal could potentially be the result of the probe

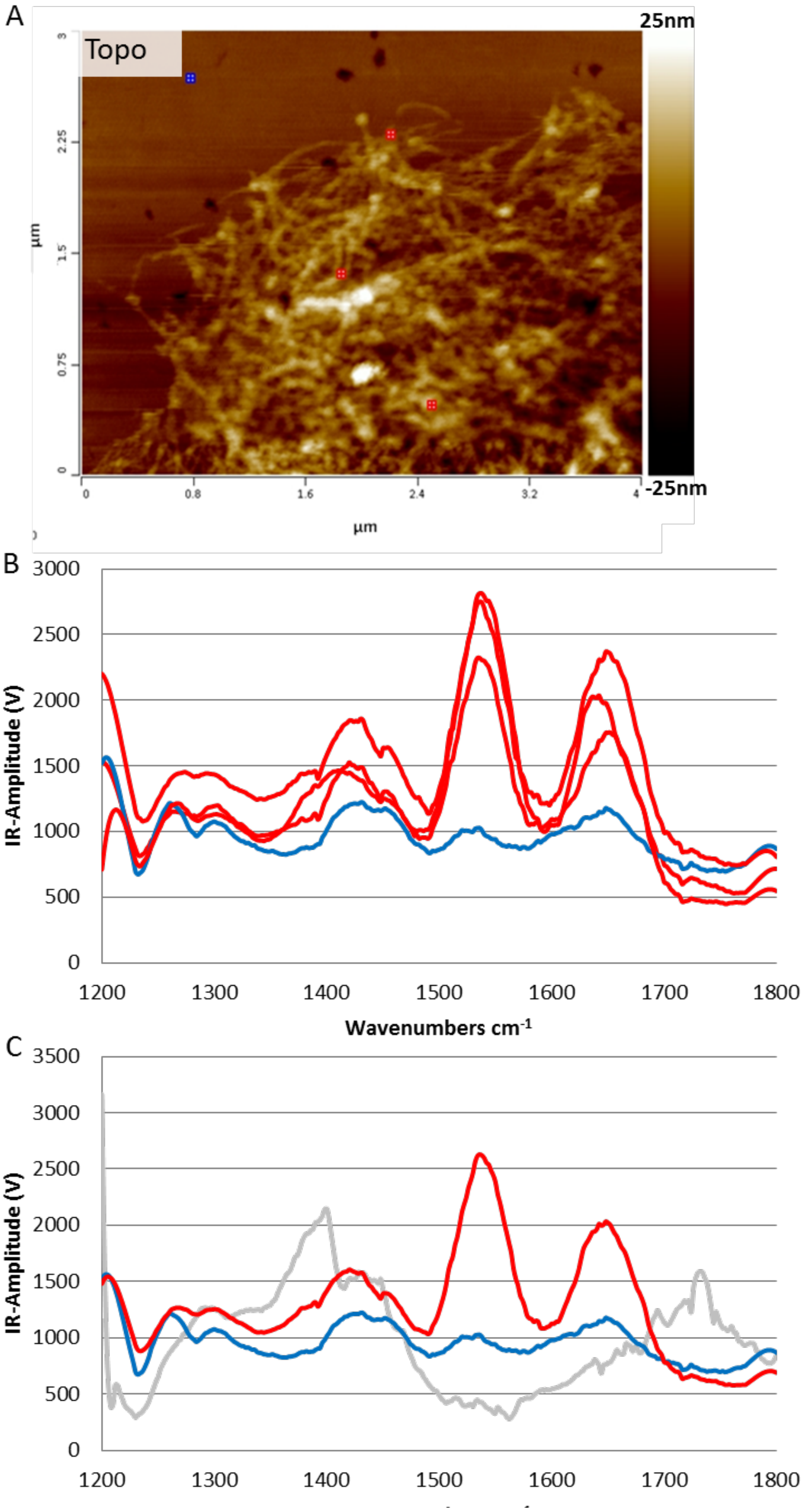

Figure 5.5 Shows the response of wavelength sweeps on samples of Aβ1:42 conducted on the Nano-IR. (A) standard AFM topography of the area imaged. (B) the red pointers from panel (A) correspond to spectra taken on amyloid, while blue corresponds to the Au-Si substrate. (C) data for the averaged Aβ1:42 response at Amide I (red), the exposed AU substrate response (blue) and the background signal detected when freshly cleaved Au substrates are imaged (grey). Data is curtsy of Kevin Kjoller, Anasys Instruments.

initial contact with the sample required to locate the sample surface. SThM-IR is a modification of CM-AFM, which typically involves higher forces being placed upon the sample. The Aβ1:42 fibres are likely to detach if too much force is applied and be dragged across the sample surface, detaching in another location, and subsequently causing a false (reduced) signal. A similar effect was seen when bacteria cells were mapped using AFM-IR by its creator, Dazzi (2007)[52] where small pieces of the bacteria cell wall were found to be dragged across the sample surface during scanning. A strong signal was seen at approximately 1640-50 cm^{-1} which correlates well with the detection of Amide I from the protein sample[256, 261]. A second strong peak is seen at 1540 cm^{-1} which correlates with Amide II, which is generated by the out of phase NH bending and CN stretching[261]. There is some evidence from the repeat spectra, before scanning (Fig. 5.6, B), that the sample has been affected by

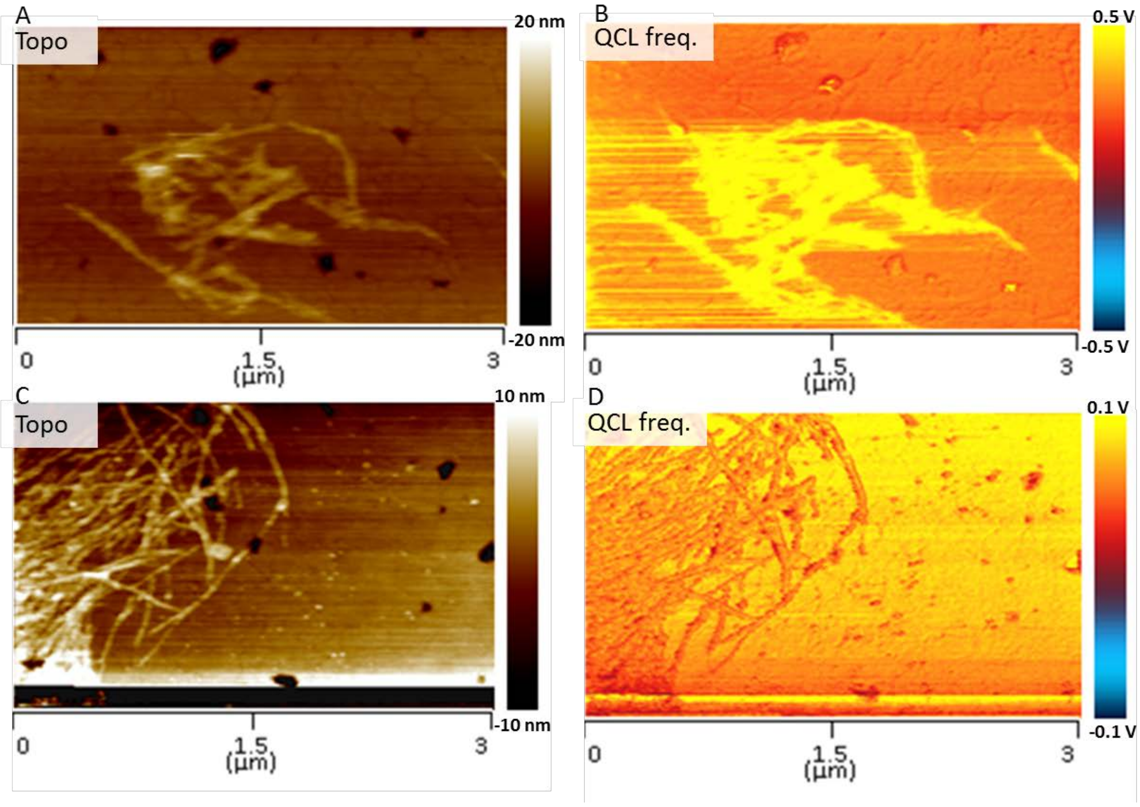

Figure 5.6. Data collected on the Nano-IR system on samples of Aβ1:42 deposited onto Au-Si substrate. While the topography panels (A) and (C) do not indicate any issues with scanning a multitude of issues were found when imaging at fixed wavelengths. Poor contrast and thermal drift can be clearly seen in (B) while the friction and subsequent contamination of the tip is evident in (D). Data shown was collected at 1628 cm^{-1} (β sheet). Data is curtsy of Kevin Kjoller, Anasys Instruments.

the presence of water molecules within the peptide film. Although not obvious a slight double-peak can be seen in Amide I could be attributed to a response by water molecules, which responds strongly between 1640-50 cm^{-1}, thus affecting the resolution of true structural components within the sample[261, 262]. The detecting of a small peak at 1640 cm^{-1} could indicate the Amide I response as a result of a strong β-sheet component, as noted when immunoglobulin G was studied under hydrated conditions[262]. This protein is 70% β-sheeted with almost no α-helix components and comparable to that of the MF of Aβ1:42[262]. It is possible to deconvolute the Amide I band to remove the water bands presence, a fact which should be considered for future work with any IR spectroscopy and Aβ1:42, as it will be almost impossible to remove, and prevent the reabsorption of water molecules into the peptide film.

In addition to the data collected at Amide I, further information was gathered at further wavelengths ideal of determining the structure of Aβ1:42 and successfully testing the technique of AFM-IR. Scans were taken at 1610, 1628, 1630 (parallel β-sheets), and 1696 cm^{-1} (anti-parallel β-sheets) which are all indicated to represent amyloid aggregates or β-sheets by similar IR based techniques[256-259]. However it was proved to be difficult to detect spectra with reliability and reproducibility at these wavelengths, (Fig. 5.6). Numerous factors could affect the data collection; rapid and unavoidable contamination of the probe (Fig. 5.6, (D)), variations in sample thickness due to the deposition of the peptide, and a strong effect of thermal drift have all hampered collecting results on more specific wavelengths within the time frame of this thesis. It is possible that with refinement of the technique i.e. generating a more uniform, thicker layer of Aβ MF which is more permanently attached to the sample surface could reduce probe contamination, and unreliability due to sample thickness and also provide a stronger response from the sample.

5.5 Conclusion

The work in this chapter largely details the attempt to advance the existing technique of SThM and AFM into a technique which is able to provide information on the chemical composition of samples. First samples were examined using SThM, and it was found that providing an appropriate substrate was used, they produced a strong enough thermal response to be detected, and that no immediate destruction of the sample (or obvious, gross morphological alterations) were seen. At this point SThM was used in conjunction with a pulsed tuneable IR source from the FEL at ALICE to measure the photothermal response of Aβ MF. While the data are preliminary, due to unavoidable variations in IR intensity, and reliability issues, it was nevertheless possible to detect a sample dependent photothermal response using an AFM cantilever designed for SThM. The same samples were then examined using the Nano-IR for comparison. What has been shown by the Nano-IR is that it is possible to resolve at least some structural details of Aβ on the nanoscale, and that with continued improvements SThM-IR could rival if not better the current Nano-IR system. Ideally, in the future, it would be possible to collect IR data on the spatial resolution of a typical AFM cantilever (~10 nm). This could prove essential for detection and understanding of the pathology of AD. Analysis of plaques from AD patient's brains has used FTIR to detect their composition, finding that in addition to the predictable amyloid core the plaque itself and its surrounding regions shows high levels of lipid peroxidation, which lends evidence to the method of possible cell death and neuronal damage seen in AD[155, 263].

The next chapter will move away from SPM methods of analysing Aβ, focussing on the detection of aggregate sizes and populations with DLS. It is discussed whether this technique can assist in the determining the effect of Aβ-aggregation inhibitors alongside classical biological methods and SPM.

Chapter Six

The application of biophysical techniques to the study of the inhibition of aggregation of Aβ using PINPs liposomes

6.1 Introduction

Although one of the key pathological factors of AD is the occurrence of senile plaques of Aβ peptide and neurofibrillary tangles made of the phosphorylated peptide tau, there is increasing evidence that early aggregates of Aβ are the most toxic form of the peptide[122, 157, 158, 160, 264-266]. Preventing oligomer formation is therefore an ideal therapeutic strategy. Given current treatments of AD include the use of drugs such as donepezil hydrochloride, rivastigmine, galantamine and memantine which are only able to provide temporary relief from the symptoms and cannot halt the disease progression, more therapeutics, particularly those which target the early aggregates, are desperately needed on the market. Promising therapeutics designed to target the monomeric form include Solanezumab, a humanised monocolonal antibody which targets the key aggregation sequence of Aβ[177, 267, 268] This chapter focuses on work to further the development a potential therapeutic to target the monomeric form of Aβ, RI-OR2-TAT PINPs. In order to better understand how the drug interacts with Aβ1:42 aggregates, AFM and DLS work have been employed. To better understand the data given by the DLS system it was first tested on standard sized particles, or those which have been modelled and therefore their size and behaviour is more readily predictable. This chapter will briefly discuss the development of RI-OR2-TAT PINPs to its current state before moving on to discuss how AFM and DLS have been useful in understanding the drug's action.

6.2 Development of the RI-OR2-TAT PINP inhibitor

We have previously shown that a small peptide known as OR2, (H_2N-RGKLVFFGR-NH_2, Fig. 6.1 (B)), is capable of inhibiting Aβ aggregation[269]. This peptide has undergone several modifications before it is the peptide-PINP conjugate presented here. Firstly its stability was greatly improved by replacing the L-amino acids with D-amino acids, and reversing the peptide's sequence thus rendering it resistant to proteolysis. This retro-inverted peptide is known as RI-OR2, (Ac-rGffvlkGr-NH_2 Fig. 6.1 (C)) [270]. A further modification was made with the aim of improving the peptide's ability to cross the blood-brain barrier, (BBB) by the addition of a retro-inverted cell-penetrating TAT sequence from the HIV virus, (RI-OR2-TAT, Fig. 6.1 (D))[271]. This final modification has produced a peptide which when tested at 100 nM/kg on 10 month old APP/PS1 mice is able to reduce soluble Aβ oligomer levels in the brain by 25%

A **D A E F R H D S G Y E V H H Q K L V F F A E D V G S N K G A I I G L M V G G V V I A**

B **H_2N-R GK L V F F GR-NH_2**

C **H_2N- G k l v f f G r-Ac**

D **H_2N- cy G r k k r r q r r r r G k l v f f Gr-Ac**

E

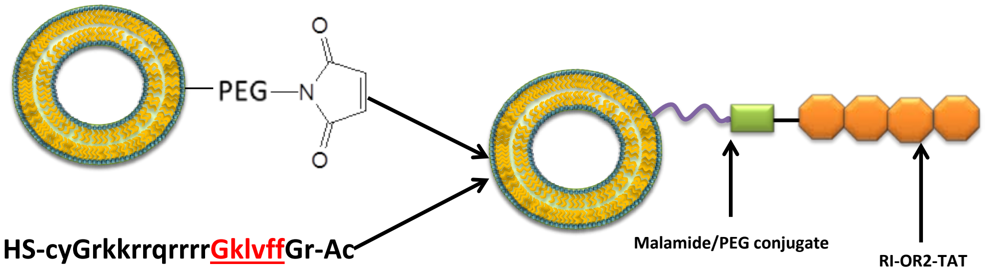

Figure 6.1. Development of the RI-OR2-TAT-PINP liposome inhibitor A) the native peptide sequence of Aβ1:42. B) OR2; residues 16-20 of the native sequence were selected, with Arg-Gly spacers to prevent self-aggregation of the inhibitor. C) RI-OR2; retro-inverso peptide sequence. Natural L-amino acids are replaced with D-amino acids, along with a reversal of the peptide bonds. This allows the tertiary structure of the peptide fragment to be maintained and therefore full biological activity. D) RI-OR2-TAT; in order to improve BBB penetration a retro-inverso TAT sequence was added to RI-OR2. L-Amino acids are in uppercase and D-amino acids in lowercase, with the direction of peptide bonds indicated by arrows. There are no separate enantiomers of glycine, which is represented in uppercase. E) RI-OR2-TAT-PINPs liposomes; the RI-OR2-TAT peptide is attached to a cholesterol/sphyingomyelin liposome using a malamide-PEG conjugate.

(p<0.01) and reduce cortical Aβ plaque load after 21 days of daily injections, while also showing a reduction in levels of inflammation and oxidation markers. However the in-vitro potential of the peptide was somewhat limited, with RI-OR2-TAT needing to be present at relatively high ratios, 1:5 inhibitor: peptide and therefore work has been undertaken to improve its potency further.

One current popular method of delivering therapeutics is the use of nanoparticles constructed of amphipathic lipids, known as liposomes. These are attractive for several reasons, including biocompatibility, biodegradability, and stability, with several liposome based systems already in use by clinicians[68]. Readily multi-functionalised at the surface, drug delivery systems with multi-ligand decorated surfaces have already been shown to be efficient at recognising their specific molecular targets. A PEG molecule acts as a steric stabiliser when added to the surface of the liposome by protecting it from immediate clearance by cells and therefore increasing its half-life[68]. In order to add functionalization onto the liposome surface a malamide group is used to conjugate the desired peptide or antibody onto the liposome-PEG surface[68].

It is possible to design nanoliposomes covalently attached to which is RI-OR2-TAT, using “click chemistry” (Fig. 6.1 (E)). “Click chemistry” refers to a group of high yield,

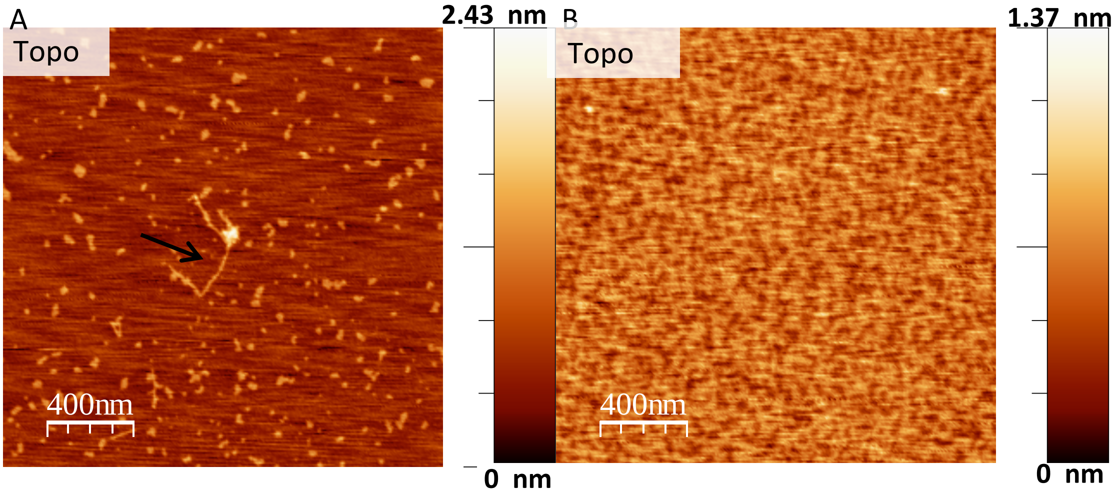

Figure 6.2. Inhibition of Aβ:42 aggregation using the inhibitor RI-OR2-TAT. Panels A and B show the height profiles when samples were imaged in Tapping Mode using AFM. Samples were incubated in the absence (B) and presence (A) of 12.5 µM inhibitor. While samples incubated with the inhibitor show only small aggregates (B) fibres can be detected (arrow) when they are not present.

stereospecific reactions that produce no harmful byproducts.[272] Reaction conditions are typical simple and utilise readily available ingredients coupled with chromatographic methods for purification of the desired products and since it's development in 2009 it has become a common method for polymer scientists to employ. "Click chemistry" employs a series of linking reactions alongside a catalyst to produce the high yield associated with the technique[272]. In this case the technique was used to conjugate a nanoliposome to the RI-OR2-TAT sequence using a malemide-PEG conjugate. The nanoliposomes are composed of cholesterol and sphingomyelin in a 1:1 ratio, and 2.5% malemide-PEG to allow for the attachment of the peptide sequence. RI-OR2-TAT was modified slightly by the incorporation of a cysteine residue at one end, to give the peptide sequence Ac-rGffvlkGrrrrqrrGyc-NH_2. It is expected that the liposomes will interact with the monomeric form of Aβ via the positive charge of the TAT sequence and the KLVFF binding sequence on the RI-OR2-TAT inhibitory peptide attached to the liposome. In addition it is possible for the long PEG molecules to have multiple interactions with oligomeric forms of Aβ. A third possible interaction is for multimeric Aβ to insert into the lipid bilayer of the liposome, as previously seen elsewhere[273, 274]. Experiments conducted within this chapter utilise PINPs liposomes donated by Maria Gregori, (University of Milano-Bicocca, Italy), to study the inhibition of Aβ1:40 and Aβ1:42 aggregation.

6.3 Use of TM-AFM to confirm the inhibition of Aβ1:42 using RI-TAT.

As previously discussed it was necessary to attach a sequence to the original RI-OR2 inhibitor sequence to improve penetration of the inhibitor across the BBB. This was done by attaching the TAT sequence from the HIV virus onto OR2[271]. Alongside cell penetration and toxicity experiments, and more conventional methods of monitoring the effects on an inhibitor on Aβ1:42 aggregation, such as ThT, AFM was used to confirm that RI-OR2-TAT did indeed prevent the aggregation of Aβ1:42. After 24 h samples were taken and examined and it was noted that in samples where the inhibitor was present much smaller aggregates were present, in comparison to the sample incubated without inhibitor, in which small fibres could be seen, (see Fig. 6.2). The results from AFM imaging of Aβ1:42 agree with the findings of other researchers working on this project who found that RI-OR2-TAT was able to reduce Aβ1:42 oligomer levels, plaque load and oxidative damage[271] and able to inhibit the aggregation of the peptide.

6.4 Test study of non-biological samples of well-defined behaviours using DLS.

The next stage in the design of RI-OR2-TAT PINPs was the attachment of the RI-OR2-TAT peptide to a sphingomyelin-cholesterol liposome by click chemistry. It was vital to have a method of measuring the size of these liposomes to ensure their size was consistent and that they were stable over the period of time the experiment was conducted and they were exposed to Aβ1:42. DLS is an ideal technique to do just this as it uses the Brownian motion of a particle to determine their size[69-71]. To achieve this, the DLS system used in this work (Zetasizer Nano, Malvern, UK) capable of producing accurate results the system was tested with non-biological samples of known size and behaviour.

Gold Nanoparticle Standards. These were tested over a scale of 2 to 100 nm and treated as a reference sample. These particles are more predictable in size, than, say, aggregates of Aβ1:42, and were therefore an ideal sample to develop a method for data capture with the DLS system. From Fig. 6.3 it can clearly be identified that while the gold nanoparticles were of distinct size populations, there is a large range of sizes seen within the sample. The number of particles present within the solutions varied with the size of the gold colloid, from 1.5×10^{14} to 5.6×10^{2}, with there being more particles present the smaller in size they were. As it was possible that neighbouring particles would interfere with the light scattering from the individual particles being measured, the gold colloid suspensions were diluted 1:50 in PB. This reduced the population distribution present, and additional dilution was likely to have reduced it further. It was noted that the 2 nm gold colloids had a tendency to "aggregate" or clump together, regardless of the dilution. The measurements of these colloids suggested that interference from neighbouring particles was a problem which was likely to be encountered when using Aβ1:42 samples and that dilution of the samples may be necessary to collect representative data, in particular for smaller aggregates. It was considered that DLS was a potentially appropriate technique for studying Aβ1:42 aggregates based on the range of sizes regularly identifiable by the system.

Confirmation of DLS sensitivity to the size variations - 2D micelles temperature-dependent behaviour via DLS. Surfactants designed to form self-assembled 2D 'starfish' micelles at predictable and tuneable temperatures were studied using DLS. These micelles were produced with varying lengths of oligoethylene glycol bridges attached to hydrophobic or hydrophilic pyrene based moieties to create a surfactant with specific and predictable dynamics and shape in the presence of water. Modelling predicted that each of these individual surfactant molecules would be approximately 2 nm in size, which is comparable to that of the Aβ1:42 monomer[75, 76]. At a specific Lower Critical Solution Temperature (LCST) the surfactants were predicted to arrange into micelles that collapse once the temperature exceeds this LCST. It is possible to collect multiple data sets over a range of temperatures using the DLS system and this feature was employed to test some of the samples to determine whether their predicted LCST was comparable to their measured LSCT.

As can be seen from Fig. 6.4 (D) the predicted LCST point for the three compounds studied here correlates well with the actual LSCT point recorded using DLS to detect

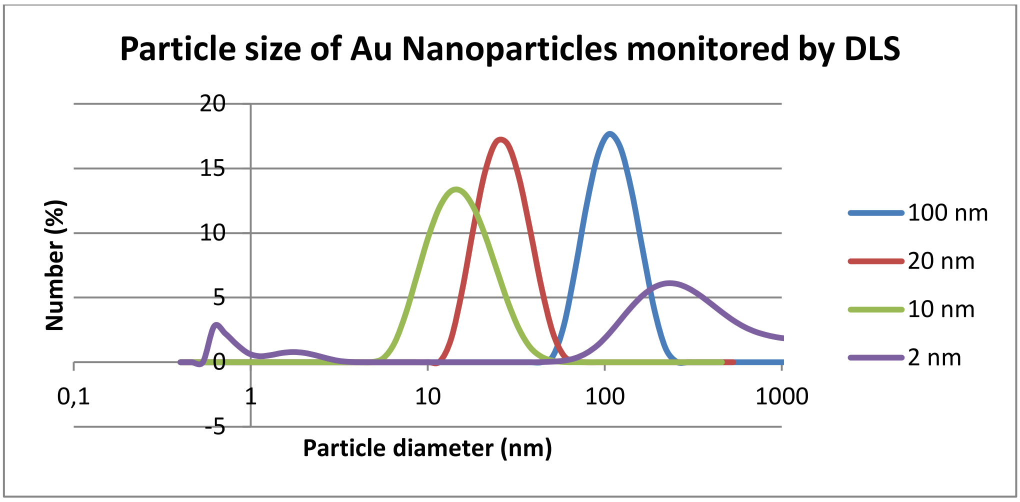

Figure 6.3. Running of standard gold colloids from Agar Scientific (Essex, UK), and is representative of 30 runs of the DLS system, taken in triplicate.

the change in particle size. Measurements were taken over a range of 1 °C temperature steps, and once the LCST transition temperature was reached the average particle diameter detected by the DLS changed from ~2-5 nm to >1000 nm. Above the transition temperature the size of the particles gradually reduced as the micelles collapsed. Not only does this study show the accuracy to which the

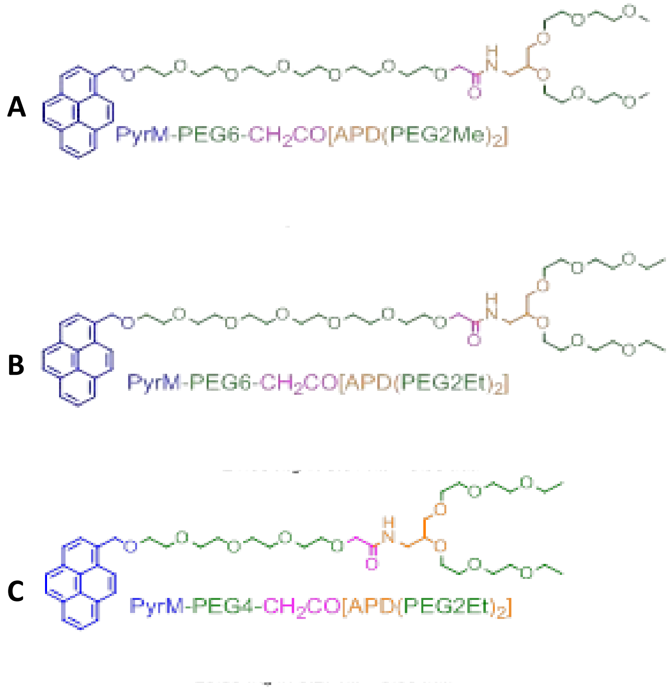

D

Surfactant	Predicted LCST (°C)	DLS LCST (°C)
A	77	77
B	48	48
C	42	42

E

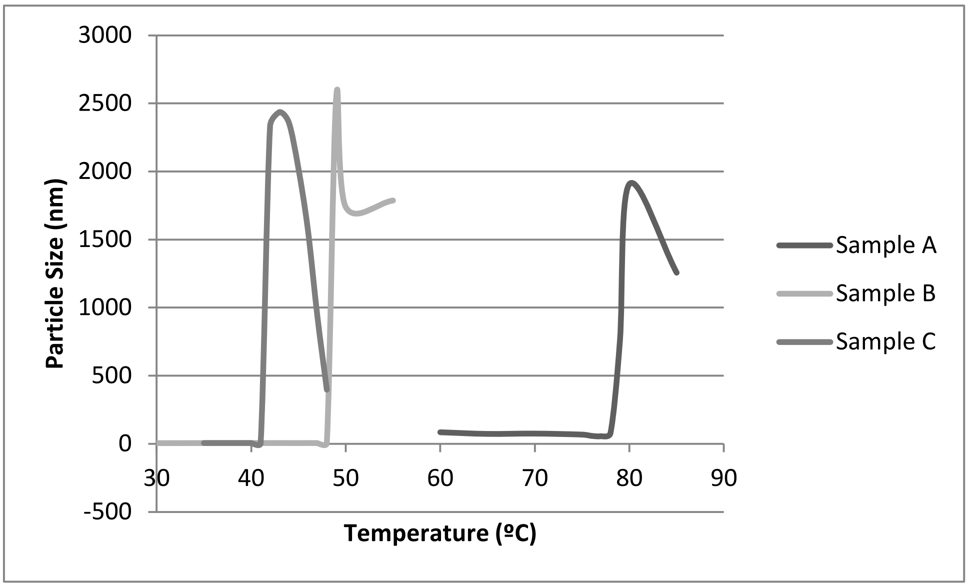

Figure 6.4. (A-C) Chemical structure of the 2D ‘starfish’ micelles studied for determination of their LCST via DLS. (D) Predicted and actual LCST of the compounds. (E) Data on particle size and detection of the transition temperature using DLS.

compounds were modelled but also the sensitivity to which that DLS can detect real-time fluctuations in the size of the population being studied. This shows promise as a means of detecting Aβ1:42 aggregation, during which, as already identified by AFM, comprises of a variety of sizes and size populations depending on the stage of aggregation.

6.5 Characterisation of the morphology and sizes of PINPs liposomes

Characterisation by DLS. Before DLS could be applied to studying the aggregation of Aβ1:42 the RI-OR2-TAT PINPs themselves had to be characterised. Samples in PBS were taken and analysed, both with the DLS here and also on production of the PINPs in Italy. Both decorated PINPs and undecorated (UD) PINPs (liposomes lacking the attachment of the RI-OR2-TAT peptide by "click chemistry") have been analysed. When measured at 37°C RI-OR2-TAT-PINPs were found to be 139.72 ±4.1 nm, while UD-PINPs are 126.15 ±2.2 nm in size. This difference in size can be attributed to the attachment of RI-OR2-TAT to the liposome via the MAL-PEG sequence.

Multiple batches of PINPs have been produced for the purpose of this study, and were initially measured at the University of Milano-Bicocca, (Department of Experimental Medicine), using a ZetaPlus DLS system (Brookhaven Instruments Corporation, Holtsville, NY, USA). The functional PINPs (i.e. those with the peptide inhibitor sequence attached), were found to be 143 ±1 nm in size. Again the slight difference in size can be attributed to the number of OR-RI2-TAT molecules attached to the outside of the liposome. A critical size for the liposome functionality was noted, as liposomes of ~30 nm were made inadvertently and found to be ineffective at preventing the aggregation of Aβ1:42. All liposomes studied here were also checked for stability, with no change in size at 37°C for 7 days, (the duration of the experiment). Liposomes of similar composition have been measured for zeta potential in other studies and found to be strongly negative, with a high zeta potential, indicating that they are also stable in solution[70, 71]

Sample polydispersity was also monitored, with RI-OR2-TAT PINPs being slightly more polydispersed than UD-PINPs, (0.123 ±0.03 compared to 0.042 ±0.01 respectively). The slight increased variation in size is likely to be the result of a variation in the number of inhibitor peptide fragments attached to the liposome. Samples are considered monodispersed as a result.

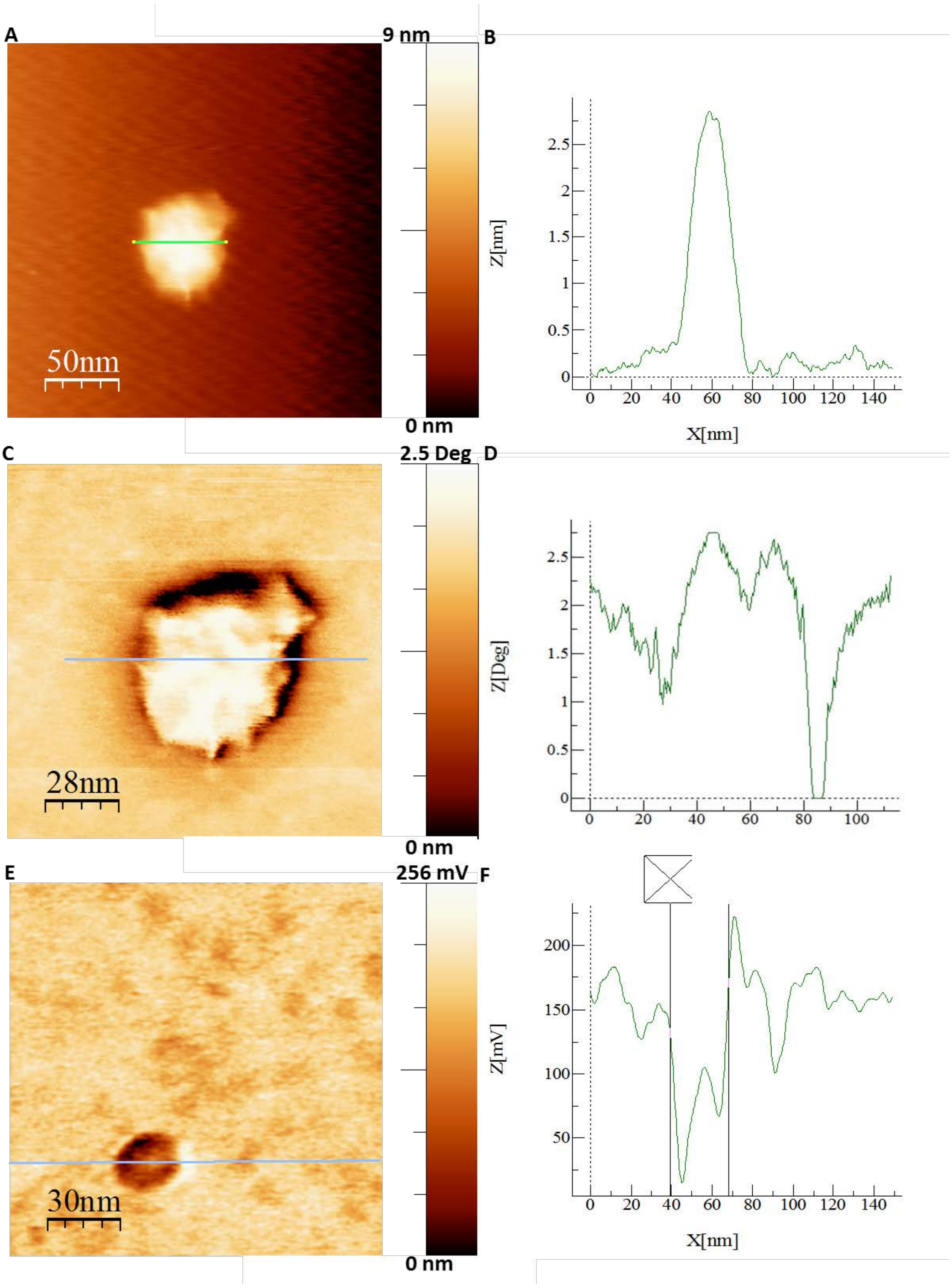

Figure 6.5. AFM characterisation of RI-OR2-TAT PINPs. Panels (A) and (B) show the smooth topography detected by the AFM tip, while panels (C-F) show the variation in the surface phase (C and D) and UFM (E and F) detects.

AFM characterisation of PINPs. RI-OR2-TAT PINPs were also studied in ex-situ using various AFM techniques, including TM and UFM after incubation with Aβ1:42 for 24 h. Standard topography TM imaging (Fig. 6.5 (A)) of RI-OR2-TAT PINPs revealed that the liposomes, dehydrated once, as work was conducted *ex-situ*, collapse to approximately 100 nm in size, and have a smooth topography which does not imply any change in surface stiffness on contact of the cantilever tip (Fig. 6.5 (B)). However both TM Phase imaging and UFM imaging suggest otherwise (Fig. 6.5 (C-F). The nanomechanical stiffness profile of the liposome measured across a central region becomes apparently softer regardless of the nanomechanical method being applied. In TM Phase images (Fig. 6.5 (D)) a region of lower phase response is located in the centre of the liposome. Phase imaging of soft materials is particularly sensitive to changes in adhesion and viscoelastic properties[275] as well as general alterations in topography. UFM imaging also shows a less stiff, more elastic region at the periphery of the PINP (Fig. 6.5 (F)), which combined with the Phase data would suggest that the RI-OR2-TAT peptide and the aggregates they collected are located on the periphery of the liposome, and not sequestered internally.

6.6 AFM of Aβ1:42 exposed to RI-OR2-TAT PINPs

In order to confirm that Aβ1:42 aggregation could be inhibited by RI-OR2-TAT PINPs and that this prevention could be detected with AFM, a 25 µM Aβ1:42 was incubated a 1:20 ratio for 144 h. In Fig. 6.6 (A) shows the peptide immediately after wetting and is therefore representative for T= 0 for all samples, and small aggregates which are comparable with monomers and small oligomers are present across the substrate surface. After 144 h incubation Aβ1:42 alone and then incubation with UD-PINPs they aggregated into MF covering the PLL-mica surface (solid arrow, Fig. 6 .6 (B)) regardless of the presence of UD-PINPs. Conversely, panel (C) shows Aβ1:42 incubated with RI-OR2-TAT PINPs, indicating the clear absence of fibres after the same incubation period. Smaller aggregates are still present, and also what can be identified as the PINPs themselves as indicated by the dashed arrow. It is therefore clear by the results of AFM imaging that this technique can be used alongside classical methods of monitoring Aβ1:42 aggregation when testing the effects of aggregation inhibitors, as they clearly show that while UD-PINPs do not interfere with Aβ1:42 aggregation the decorated ones prevent the formation of fibres and appear to reduce the number of aggregates generated.

6.7 Monitoring aggregation of Aβ1:42 using DLS

Firstly it was necessary to determine a suitable concentration of RI-OR2-TAT PINPs to

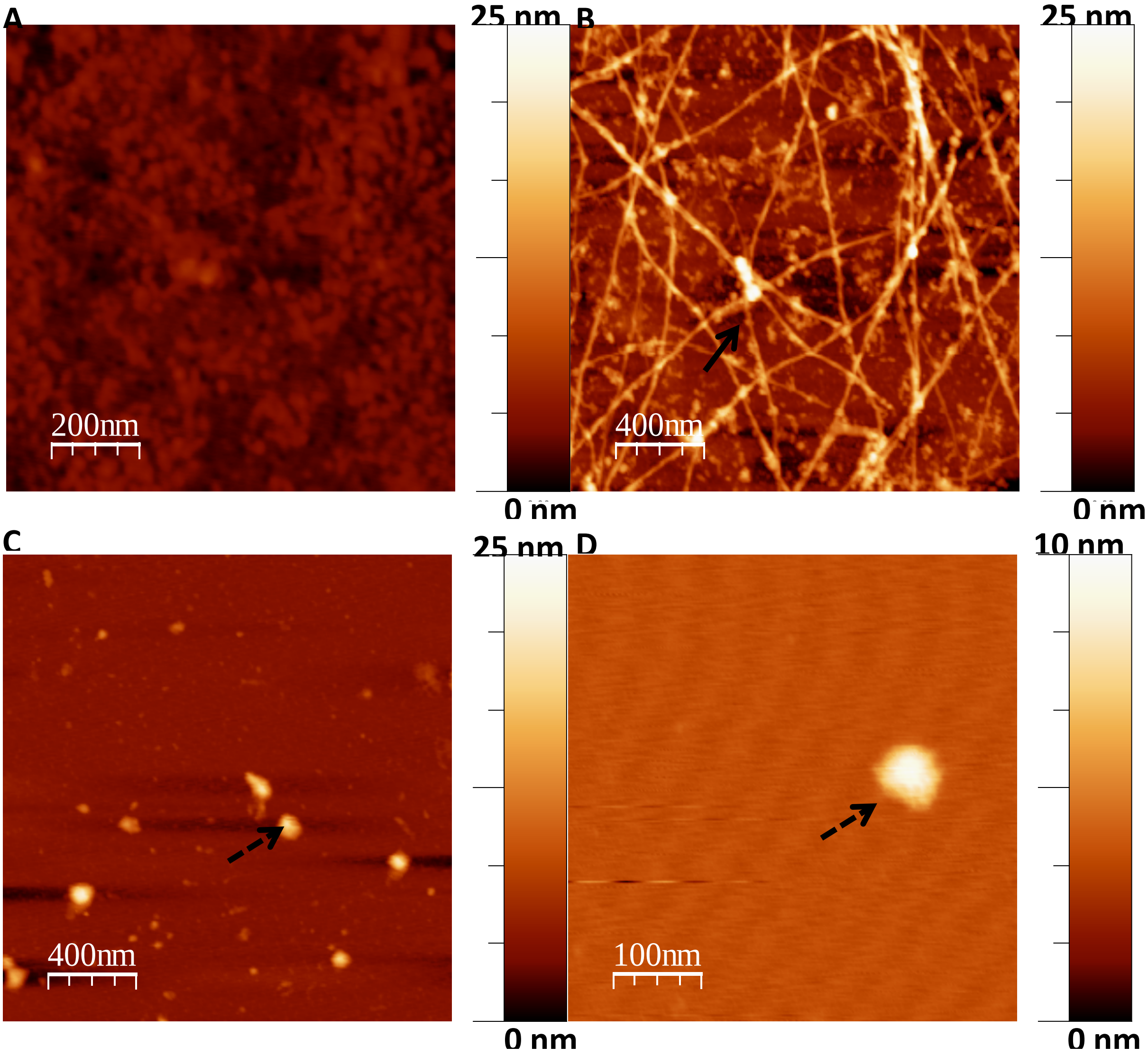

Figure 6.6. AFM detection of the inhibition of Aβ1:42 aggregation over 7 144 h. (A) 25 µM Aβ1:42 alone at T=0, (B) 25 µM Aβ1:42 ± UD-PINPs at a 20:1 ratio after 144 h, (C) 25 µM Aβ1:42 plus RI-OR2-TAT PINPs at 20:1 ratio after 144 h and (D) RI-OR2-TAT PINPs alone. PINPs are indicated by dashed arrows in panels C and D, while solid arrows indicate MF (A).

use in this pilot study, and then the conditions under which a wide range of aggregates could be detected.

Determination of RI-OR2-TAT PINPs concentration for inhibitor experiments. It was necessary to determine an inhibitor concentration at which the liposomes were effective at inhibiting Aβ1:42 but ensure this was due to their mode of action, not merely the liposome acting as a lipid sink[274, 276-278]. Due to a supplier issue these experiments were conducted with Aβ1:40, which is the shorter isoform of the peptide but just as biologically significant. When Aβ1:40 was incubated with PINPs over a range of ratios with they were found to be able to inhibit aggregation at least as far as 1:50 peptide: lipid, with higher concentrations of inhibitor being more effective as aggregation was reduced by 30-80% depending on the ratio of PINPs used (Fig. 6.7 (A)). This is evidenced further by the incubation of Aβ1:40 with UD-PINPs (Fig. 6.7 (B)). After 7 days incubation little difference between peptide incubated ± UD-PINPs can be seen. At higher ratios, (1:2 and 1:10 Aβ1:40:UD-PINP), the PINPs appear to slow or impede aggregation. Again this is likely to be due to them acting as a "sink" for Aβ1:40 monomers and oligomers. It has been well documented that Aβ is capable of interacting with lipid bilayers and inserting within them. At a sufficiently high concentration they are therefore able to slow but not halt aggregation, while at low concentrations (1:50) the UD-PINPs have a contrasting effect of increasing aggregation by ~10% compared to the control.

As previously mentioned Aβ oligomers have a tendency to insert themselves into lipid bilayers, so at high enough concentrations liposomes are capable or acting as sink for the peptide and lipids have been shown to interact with Aβ aggregates to enhance fibrillisation[274, 276-278]. A ratio of inhibitor within the centre of this scale was therefore chosen for further experiments with Aβ1:42 (1:20) and representative data can be seen in Fig. 6.7 (C). Although a slight increase in Aβ1:42 aggregation is seen over the first 48 h compared to where no RI-OR2-TAT PINPs are present there is a 55-60% reduction in detected levels of aggregation after 72 h, indicating that the decorated PINPs are, even at a low concentration, capable of reducing aggregation significantly. As with UD-PINPs for Aβ1:40, when Aβ1:42 was incubated with UD-

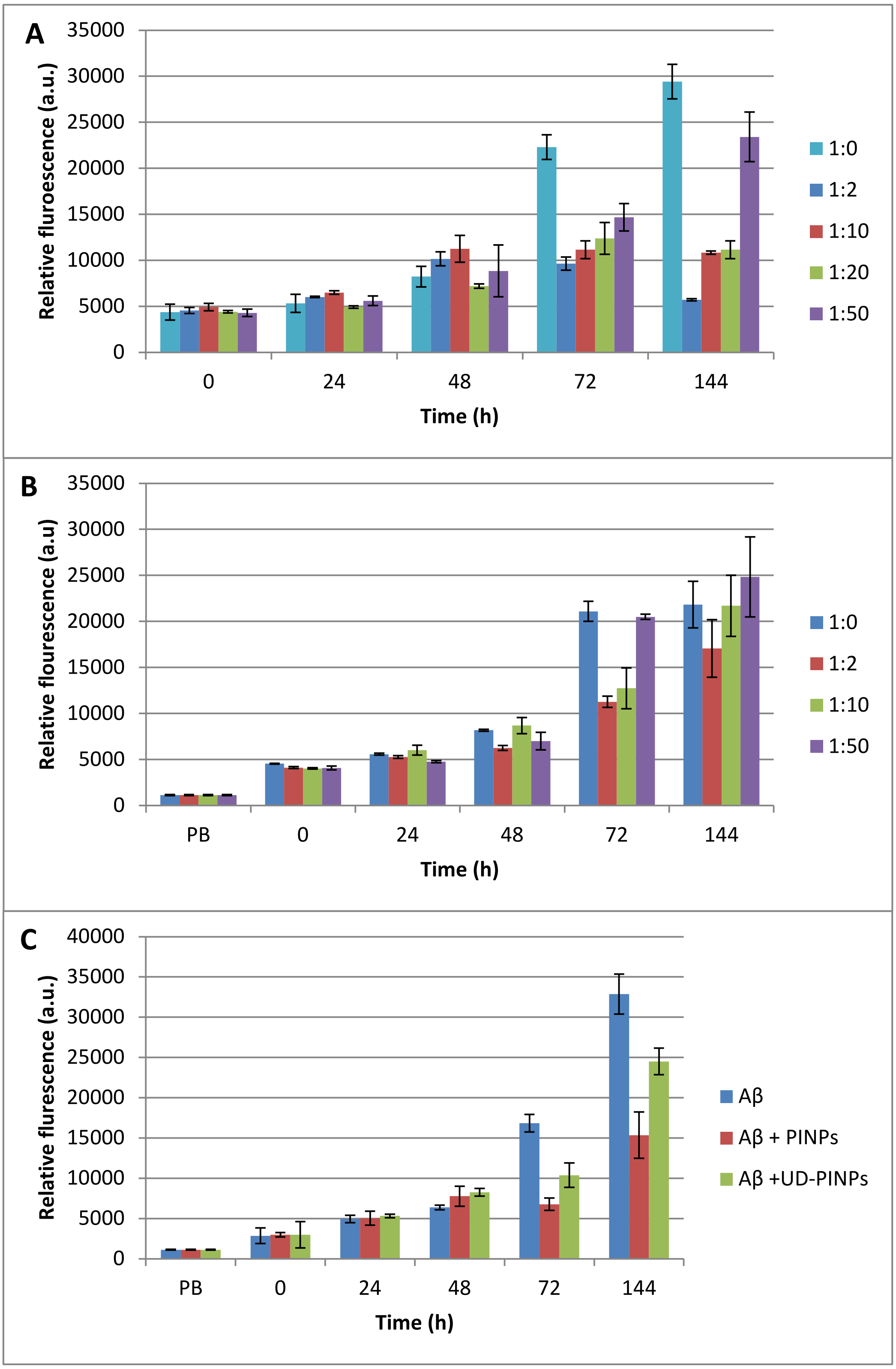

Figure 6.7. ThT monitoring of Aβ incubation with decorated and UD-PINPs (A) Aβ1:40 was incubated with a range of concentrations of RI-OR2-TAT PINPs before a concentration was decided upon for work with Aβ1:42. (B) Aβ1:40 aggregation with UD-PINPs was also monitored to ensure they did not prevent aggregation. (C) Aβ1:42 incubated at 1:20 with RI-OR2-TAT PINPs shows they prevent aggregation at this concentration. Data was taken in triplicate and is representative of at least three experiments.

PINPs 1:20 as a control it was noted that after 24 h the UD-PINPs decreased aggregation by as much as 26% (144 h Fig. 6.7 (C)). This suggests that simply by being able to attract Aβ early aggregates liposomes may have effective therapeutic potential, particularly when coupled with inhibitory peptides to further enhance their potency.

Determination of a strategy for DLS data collection. As was seen with the gold colloidal particles, dilution can be necessary for the detection of small aggregates due to the DLS feature that larger particles being capable of obscuring smaller ones during the process of data collection. As the laser hits the particle, it scatters the light, with larger particles scattering the light with greater intensity than smaller ones. The Zetasizer records this scattered light and its intensity and produces the data seen using the Stokes-Einstein equation. Given the hydrodynamic radius of the Aβ monomer is predicted to be 1-2 nm[75, 76], and that "seeds" may still be present within the sample it was essential that a suitable dilution of Aβ1:40 was found.

An aliquot of Aβ1:40 was freshly wetted and then diluted in 10 mM PB from a 1:1

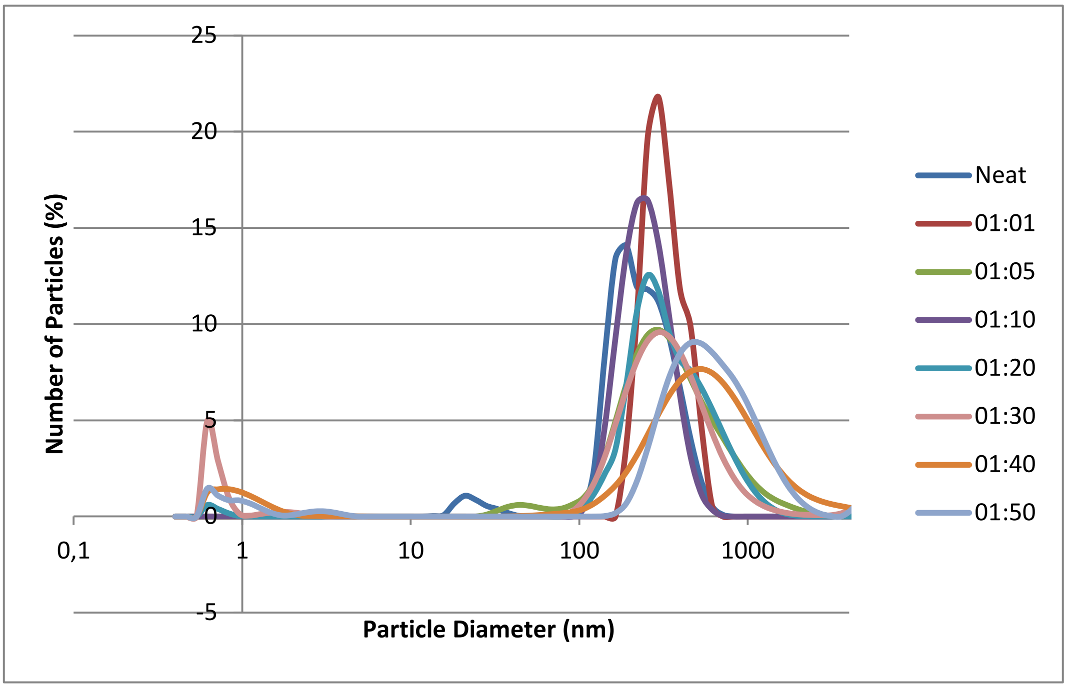

Figure 6.8. In order to detect Aβ1:40 monomers it was necessary to dilute the initial timepoint sample further with 10 mM PB. By 1:30 dilution the monomer was detectable while other populations were readily seen also.

ratio to a 1:50 (Fig. 6.8). The more concentrated dilutions of peptide:PB show that larger aggregates >100 nm are present in a significant enough population to obscure detection of smaller aggregates at dilutions <1:20. A significant population of aggregates <10 nm is present within the sample but the peptide must be diluted 1:30 or greater before this population can be observed in a consistent manner. When the PINPs were diluted 1:30 in PB they became unstable due to insufficient salt concentrations. However the transient population seen in this dilution was not in conflict with any detectable population size seen when Aβ1:40/2 was incubated with RI-OR2-TAT PINPs directly, suggesting that perhaps the liposomes are more stable once aggregates have become attached. When the liposomes (both decorated and undecorated) were tested for stability this was done in comparable conditions to an experiment with peptide present.

6.8 Inhibition of Aβ1:42 aggregation using RI-OR2-TAT PINPs as detected by DLS.

The aggregation of Aβ1:42 was monitored alone, and with both decorated and undecorated PINPs (Fig. 6.9). On initial wetting of the peptide three distinct populations could be identified, one approximately 1-2 nm large, a population which varied between 30-100 nm and in the case of Aβ1:42 alone, a population around 1000 nm, which was likely to be a "seed" which resisted the deseeding process.

No other populations of this size were detected by the DLS, most likely due to their rapid sedimentation from the sample bulk[83]. As aggregation proceeds the population of small aggregates approximately ~2 nm cannot be detected and the population becomes more uniform in size, with detectable aggregates between 10-100 nm readily detected between 24-48 h, and a larger population >100 nm detected thereafter. Aggregates greater than 1000 nm in size were not readily detected and thought to sediment out of the solution too rapidly to be detected. Currently it is not possible to agitate the sample as measurements are being taken and therefore impossible to detect the size of rapidly sedimenting particles. Separation of MF of Aβ using sedimentation has already been shown to occur[167,279] so this phenomena was

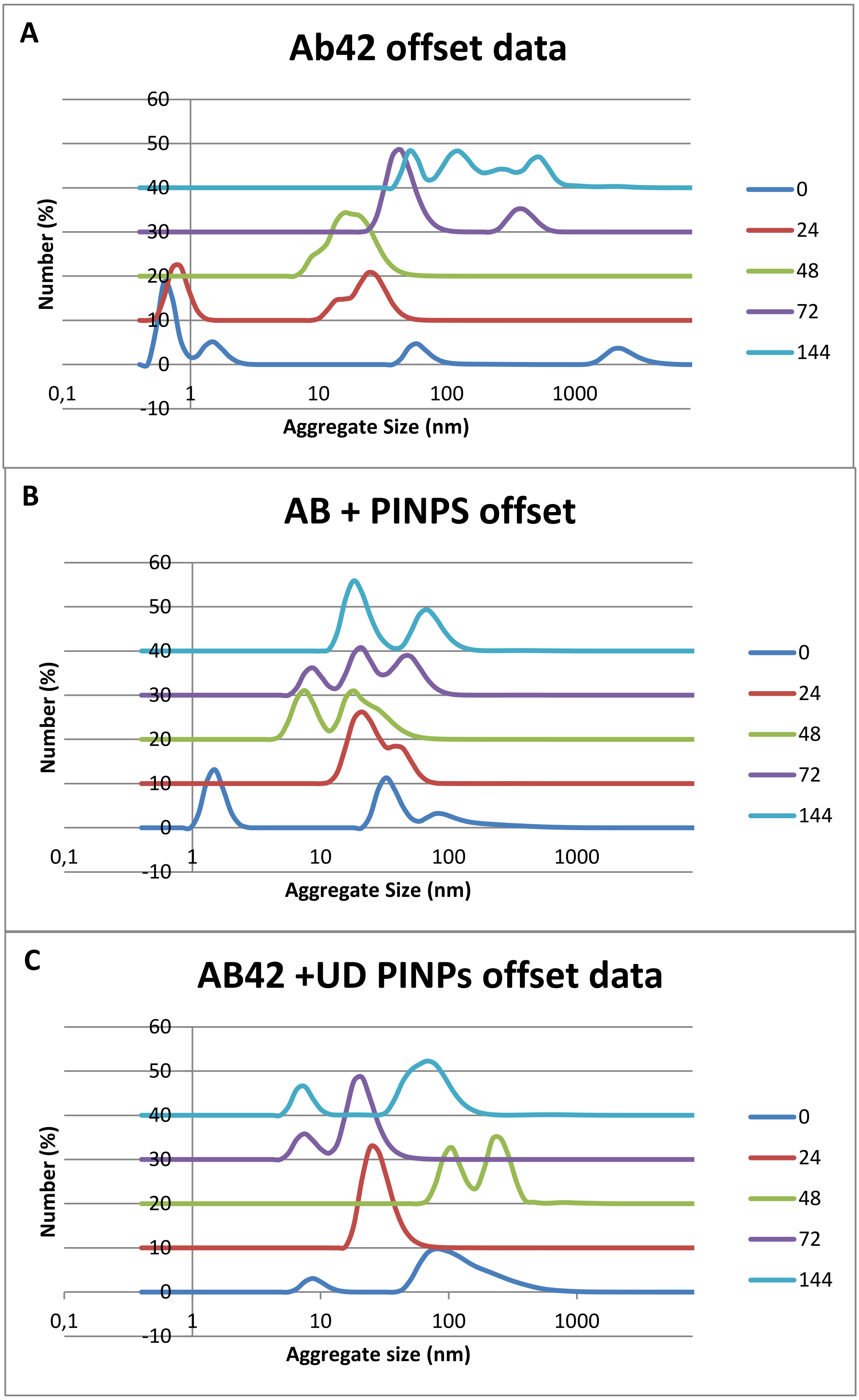

Figure 6.9. Using DLS to monitor the aggregation of Aβ1:42 (A) alone, (B) with 1:20 RI-OR2-TAT PINPs and (C) with UD-PINPs. In order to present the data in a more digestible format it has been offset by 10% (24 h), 20% (48 h), 30% (72 h) and 40% for 144 h.

not considered new. A similar situation can be seen when Aβ1:42 is incubated with UD-PINPs, (Fig. 6.9 (C)), with the smaller aggregate population being replaced by detectable populations around 100 nm. Conversely the population remains <100 nm after 144 h when RI-OR2-TAT PINPs are incubated with Aβ1:42, suggesting larger aggregates are prevented from forming (Fig. 6.9 (B)). This correlates well with visual evidence provided by AFM imaging of these samples (Fig. 4.6), and ThT results which is a more standard method of monitoring the aggregation of amyloid peptides (Fig. 6.7).

6.9 Conclusion

There is emerging evidence that early aggregates, such as small oligomers, are the most toxic form of Aβ1:42[122, 157, 158, 160, 264-266], and new therapeutics are designed with this in mind. The drug discussed in this chapter has been previously shown to be effective at inhibiting the aggregation of Aβ1:42 and reducing the effect of increased Aβ1:42 within neurons[269-271] and now is one of many liposome based drug delivery systems currently being developed for preventing the aggregation of Aβ[68-71, 280-282]. This chapter has focused on the concept that physical techniques such as AFM and DLS can be applied alongside classical biological methods for the monitoring of Aβ1:42 aggregation, or prevention of this, by its incubation with RI-OR2-TAT PINPs.

Dynamic Light Scattering is often applied to the development of liposomes as a method of determining size and stability[68-70, 281, 282] but it is possible to apply the capabilities of DLS to monitor the aggregation process of Aβ1:42. A wide range of particle sizes have been shown to be readily detectable with the DLS system (Zetasizer Nano, Malvern, UK) used here. Particles of ~2 nm (gold colloids and 2D starfish micelles) were easily detected with the system, suggesting it had promise as a method of detecting the monomeric form of Aβ. Particles of >1000 nm were also detectable, along with temperature sensitive measurements. With careful attention to dilutions to prevent larger particles obscuring smaller ones DLS was found to be capable of detecting Aβ1:40/2 molecules as small as 1-2 nm, which presumably indicates detection of the monomeric form[75, 76, 83] and also the disappearance of this population as aggregation progresses. DLS was able to detect differences in populations when RI-OR2-TAT-PINPs were present compared to incubation in their absence, suggesting it may be ideal to use alongside methods such as ThT for monitoring aggregation by the particle size. Again AFM was also considered an ideal methods of providing a visual representation of the effects of RI-OR2-TAT PINPs on Aβ1:42 aggregation, showing that in their presence at a 1:20 ratio the PINPs prevented the formation of any MF of Aβ1:42 and thus prevented aggregation. Work continues with this drug, and also the involvement of DLS in the production of PINPs liposomes in-house and the subsequent monitoring of Aβ1:42 aggregation with this technique.

Chapter 7: Conclusion and future perspectives

7.1 Conclusions

Typical AFM substrates are usually atomically flat muscovite mica, which is inexpensive and can be readily reusable by cleaving the uppermost layers. It was initially considered the ideal starting point in developing an attachment protocol for deposition of Aβ onto, as it has proven successful for other groups. However Aβ is noted for its inconsistency among suppliers, and for batch-to-batch variations. As a result, despite extensive deposition and imaging trials a freshly cleaved muscovite mica was not found to be a suitable substrate. In addition to poor attachment due to similarities between the charge of Aβ and mica (both are negatively charged at neutral pH[198, 199]) a secondary problem was noted in the presence of salt crystals of buffer residues on the sample surface. These obscured any fibres which had attached, damaged AFM tips during imaging and also created image artefacts due to their increased charge as AFM imaging is dependent on tip-surface interactions. Washing the sample was only reducing the presence of both Aβ aggregates and salt crystals and was therefore not deemed to be helpful.

Following the decision that cleaved mica would not be a suitable surface two lines of enquiry were followed; one involving adapting the incubation buffer Aβ was aggregated in and the other modification of the mica surface. The former line of enquiry was quickly ruled out; Aβ is highly sensitive to alterations in pH, salt concentration and other buffer conditions[145, 200-202]. Reducing the salt concentration to reduce artefacts would have presented an incubation system which lacked physiological relevance. It was more promising to modify the mica surface to alter its charge and thus increase attachment, as a variety of modifications are published and indicated as ideal for biological samples. DNA attachment has been mediated by the addition of glutaraldehyde or ATPES, while divalent ions have proven successful at increasing attachment in a variety of protein based samples[203-206]. For advanced cyro-

EM work of the protein Titin ultrastable Au evaporated substrates have been produced[214, 215].

Ultimately it was concluded that the most successful method of substrate modification was to coat freshly cleaved mica with a dilute solution of PLL, and bake it to create a coating of PLL 0.3 ± 0.1 nm thick. This produced a robust, anatomically flat surface with a positive charge that allowed the attachment of Aβ aggregates. When analysed further it was found that not only did this concentration of PLL not interfere with Aβ aggregation, but it was capable of attracting the attachment of aggregates over a wide range of sizes, most importantly aggregates which correlate well with that on the monomer (~1-2 nm)[75, 76]. Confirmation of attachment by Aβ came from a variety of methods, including confocal microscopy, immunogold assay and AFM. The use of PLL to coat substrates for further analysis is well established, and it has been used to image supercoiled DNA in a liquid environment[209] and amyloid proteins such as apolipoprotein C-II circularisation and surface catalysed amyloid fibril formation in amyloid protien[196, 210].

AFM was also found to be well suited for studying the effect of additional factors on Aβ aggregation. Metal ions exist in the brains of AD patients at elevated levels, and Aβ itself has metal binding capabilities[155, 166, 219, 220, 226]. In addition it had been shown that Aβ, in conjunction with redox active metal ions, can reduce hydrogen peroxide via Fenton's chemistry to the more toxic and damaging hydroxyl radical[166, 167]. Considerable interest has therefore been given to the effect incubation with metal ions have on the morphology of Aβ. As part of a study into the effect metal ions have on Aβ samples incubated with Cu(II) and Zn(II), and AFM samples imaged in conjunction with further analysis on their redox active nature. Increasing levels of Cu(II) produced profound changes in fibre morphology, from a population consisting in the majority of MF where no Cu(II) was present to a population dominated by small amorphous aggregates lacking in MF at a 1:1 ratio. When Aβ was incubated with Zn(II) is also disrupted fibre morphology to the same amorphous aggregates, however co-incubation of Cu(II) and Zn(II) at a 1:1:1 ratio resulted in rescuing of the fibre appearance to a degree.

The contribution of AFM to detect morphology changes as a result of incubation with metal ions shows the emerging importance of physical techniques for studying aggregation. Both Zn(II) and Cu(II) have shown to have dramatic effects of the aggregation of Aβ, with reports indicating these metals are capable of both enhancing or inhibiting aggregation, presumably due to other interplaying factors which can affect Aβ aggregation[224, 225, 230]. It is of general consensus that Cu(II) stimulates aggregation, to produce the rapid production of aggregates[226, 227]. Detailed analysis has shown that Cu(II) hinders the formation of the β-sheet while still promoting the aggregation of the peptide[283], and in addition AFM and EM have shown that Cu(II) has a similar effect on other amyloid peptides. When human islet amyloid polypeptide is incubated with Cu(II) fibrillisation is suppressed but the population of aggregates is smaller, and increased ROS over-production and mitochondrial dysfunction are noted[283]. AFM has also shown the concentration dependent effect of Zn(II) on Aβ aggregation to be stimulated in the direction of formation of non-fibrillar aggregates[228, 229], and that this can be rescued by the presence of Cu(II) in the incubation environment[167, 230]. Imaging with AFM is therefore a complimentary technique when establishing the effect of additional factors on the aggregation of amyloid peptides in a manner which less visual techniques such as ThT do not allow.

One main goal of the work undertaken in this thesis was to apply new, novel methods of AFM to biological samples, namely Aβ peptides. Following confirmation that PLL-mica was an ideal substrate for attachment it was imaged using UFM. This adaption of CM AFM allows for frictionless and nondestructive sample imaging to map the elastic and contact stiffness behaviour of the sample surface. The technique was found to be ideal for imaging fragile biological samples such as Aβ, which limited destruction or disruption of the sample surface while the ultrasonic frequency was being applied. In addition the technique was vastly more sensitive than imaging with TM for biological samples. It was noted that small aggregates could readily be identified on the UFM image map which were absent, or hard to detect on the topographical map. This population of aggregates could be identified by size to be akin to monomers/early oligomeric aggregates and persisted across all time points.

This lends weight to the theory that MF of Aβ are able to act as sinks for Aβ monomers, a sub-population of which are off-pathway and do not aggregate. AFM was also used to confirm the presence or absence of MF following incubation with developing therapeutics, which was found to be a complementary technique to the typical method of monitoring the contribution of MF via β-sheets (ThT). Given the likely toxic nature of oligomeric aggregates the detection by UFM of a persistent population adds weight to the argument that therapeutics targeting them could be ideal for reducing neuronal death. Studies of the interaction of early stage aggregates with liposome based inhibitors using the KVLFF sequence from Aβ to attract monomers are particularly timely given the promising news reanalysis of the drug Solanezumab shows. This humanised monocolonal antibody is designed to use the same sequence from Aβ to target the monomeric form as the PINPs liposomes reported here[267, 268]. Although initial phase III studies into the use of Solanezumab showed that it was not effective at alleviating the symptoms of mild to moderate AD, reanalysis has lead to another phase III trial focusing on the effect of Solanezumab when given earlier in the disease progression[177, 284]. This trial showed that early delivery of Solanezumab resulted in reduced cognitive decline and delayed functional decline when compared to control patients, or those receiving delayed treatment, suggesting that early treatment is most effective when given early by reducing the cognitive decline, and may make Solanezumab and ideal treatment for early stage patients. Solanezumab appears to reduce the overall Aβ1:40/42 cerebral load by promoting its efflux from the CNS to the peripheral circulatory systems[284]. Techniques which allow the detection of early stage aggregates and their interactions with potential therapeutics *in vitro* will allow further development of potential therapeutics which focus on this aggregation stage such as the RI-OR2-PINPs liposomes studied in this work.

UFM also allowed the detection of finer structural details to the MF of Aβ through its nanomechanical mapping abilities. Each MF of Aβ has an internal structure which is composed of a softer region flanked by regions of increased stiffness, indicative of a hollow core. This has been proposed by numerous studies, including those using advanced cryo-EM, and the structure detected by UFM is in agreement with experimental data which indicates the structure of Aβ1:42 MF consists of 2 intertwined protofibrils, and the stacking of the β-sheets produces the domain structure seen here[12, 89]. Miller *et. al.* (2010) showed that Aβ1:42 fibres are composed of 2 interwinding protofilaments surrounding a tubular hollow core at both acid and physiologically pH, although this conformation requires the C-terminus of the peptide facing the exterior and the core is reduced in size at physiological pH[94]. The hollow core is frequently difficult to detect, and these studies found evidence that although no less stable than its acid counterpart, only 8% Aβ1:42 fibres incubated at physiological pH showed signs of a hollow core[94]. Conflictingly an alternative study has found that Aβ1:42 is composed of only 1 protofilament based on the mapping of its hollow core structure and analysis of the number of molecules in each β-cross[12]. The structure of Aβ1:40 has been shown to differ to that of Aβ1:42, with this isomer having a triangular cavity along its length made[95]. Multiple conformations of Aβ1:40 have been studied by cryo-EM, one which has a 2 protofilament structure and a wider, single protofilament conformation[12]. The former structure shares similarities with that of Aβ1:42 in that it has an identical number of molecules per β-cross and similar size dimensions, while the wider one contains a larger number of molecules across the β-turn[12]. Amyloid fibres are notorious for having a high level of inter- and intra- sample heterogeneity resulting from structural polymorphism, deformation due to flexibility, as well as being sensitive to incubation conditions and deseeding treatments[89, 224, 225]. To reliably deduce details about the sample structure multiple techniques must be applied, including AFM and EM.

In addition to an interest in the nanomechanical mapping of a sample it is also desirable to map the thermal or chemical features of it. Amyloid proteins make ideal samples for testing the detection of chemical changes due to the structural transition they undergo during aggregation. The aim of one line of work reported in this thesis was to develop the technique of spectroscopical SThM, as an extension of Photothermal Microspectrosopy to true nanoscale resolution. This would require attention to the sample protocol and substrate again. Samples being images for thermal conductivity ideally require a substrate which has a good thermal contrast, while any work being conducted in the mid-IR range requires a sample substrate which is transparent in this region. It would be necessary to compromise between the features of an ideal AFM substrate for these experiments. The most suitable substrate which Aβ readily attaches to is silicon, while CaF_2 is ideal for work in the mid-IR yet due to its production suffers from a rough, trenched topography. SThM is highly sensitive to topographical affects during scanning, making deductions about thermal properties harder to determine. The sample protocol was refined to allow production of samples containing only the MF, which theoretically represented a completely β-sheeted peptide for simplicity of data collection.

Samples of Aβ were initially imaged using SThM to test their compatibility with the technique, and while their small size meant thermal conductivity was limited they were not found to be destroyed by the imaging method. This technique was then combined with a FEL from the ALICE energy recovery accelerator to focus a pulsed, tunable mid-IR laser onto the cantilever. This would produce a local photothermal expansion of the sample at wavelengths to which it would be excited by. The transient expansion of the sample would induce a “kick” in the cantilever which could be detected. This experimental period provide highly challenging due to inconsistencies and fluctuations with the ALICE FEL[255], making the collection of enough data to determine its reliability impossible within the time frame of this thesis. However some early conclusions can be taken on from this work. It was possible to successfully focus the laser onto the cantilever, and detect the photothermal response of the cantilever and its subsequent ringdown as the heat dissipated. Some variation in sample response was seen when imaged a key wavelengths for amyloid samples, include Amide I which has the strongest response in biological materials however it was not possible to gather enough data to confirm differences. Numerous spectroscopical studies of Aβ have been able to detect the differences between aggregation stages, and structural transitions[259, 285]. ATR-FTIR has been shown to detect oligomeric and fibril populations within the same samples of Aβ and it is hoped that the same identification could be made using SThM-IR, given UFM has also detected this heterogeneity within later stage samples[259, 286] .

In order to elucidate whether Aβ could be imaged using a mid-IR laser in conjunction with and AFM samples were tested on the Nano-IR system, (Anasys Instruments). One of the most advanced systems in use, the Nano-IR uses an Au coated cantilever in conjunction with a pulsed, tunable IR source to detect the photothermal absorption of the sample[18-20, 51-53]. These were deposited onto gold substrates which were found to be more anatomically flat than CaF_2 however they have not been analysed for thermal contrast at this time. Imaging with this commercially available system was also semi-successful, with a clear distinction between sample and substrate at Amide I being possible. However more detailed analysis at amyloid specific wavelengths was hampered by tip contamination, variations in sample height and increased thermal drift, problems already associated with the Nano-IR, as it operates in CM[52]. When Dazzi and colleagues combined topographical and nano-chemical mapping during the imaging of Escherichia coli they noted that initial scans to locate the cells were enough to damage the cell wall and contaminate the surrounding area with it, thus producing a weaker signal around the cells location[52]. More recently nano-IR spectroscopy has been applied to detect structural changes in the amyloid protein ataxin-3, the missfolding and aggregation of which is implicated in spinocerebellar ataxia-3[285]. This research utilised the Nano-IR2 system to characterise the conformation rearrangements that occur during the α- helix - β-sheet transition of ataxin-3 as it aggregates. Both oligomeric and fibre conformations of the peptide were characterised. This research opens the door to the study of more disease related amyloid proteins and provides a method of studying the structural transitions on the nanoscale.

Taking a different approach Muller and colleagues sought to develop a high-throughput method of screening samples for their chemical signatures, and have developed a sophisticated “lab on a chip” method[256]. This allows hundreds of microdroplets from a sample to be analysed by IR spectroscopy on a sub-micron spatial resolution. They were able to resolve the structural differences between monomeric and aggregated lysozyme within the amide bands of the chemical spectra gathered from the microdrolets, presenting promising results of nano-IR techniques[256]. The possibility of expanding such a technique to study pathogenic amyloid proteins interactions with potential therapeutics makes this particular branch of IR spectroscopy very appealing. By combining the experiences with both the in-house AFM-IR system and the Nano-IR it is possible to see where further modifications and attention needs to lie to enhance this technique.

Conclusions in brief;

- PLL-mica is an ideal substrate for the imaging of Aβ. It is anatomically flat, lacking in either topographical or nanomechnical features and capable of capturing aggregates ranging from 1-2 nm (monomeric) to larger MF, making it ideal for the study of amyloid aggregation.
- Imaging with AFM is capable of offering support to biological and biochemical tests into the effect of additional factors, such as metal ions and developing therapeutics on the aggregation of Aβ.
- UFM is a highly sensitive technique, and is greatly effective when applied to biological molecules. It provides non-destructive nanomechanical mapping of the sample surface, with a resolution of ~5nm. This technique was able to highlight the presence of a persistent population of small aggregates, which are otherwise not detected by TM imaging, and also provide fine structural details for the MF morphology.
- Samples of biological materials offer new challenges to thermal and spectroscopical methods of AFM. Their thicknesses, increased propensity to contaminate cantilever tips and poor contrast with respect to their substrate are all challenges to be overcome even if this technique is successful.

7.2 Future perspectives

The work in this thesis covers the application of multiple modes of AFM to the study the aggregation of the peptide Aβ, which is implicated in the pathology of AD, and effect of metal ions and developing therapeutics in the aggregation process.

UFM was developed to overcome the limitations previously found in imaging the nanomechanical properties of a sample. During scanning of the sample surface the sample is oscillated at an ultrasonic frequency above that of the cantilevers resonance, creating an rigid cantilever which briefly indents into the sample surface thus probing its elastic properties. UFM was successfully applied to the imaging of Aβ1:42 and in addition to various nanostructure details for the MF it enabled the identification of a population of early aggregates detectable at a variety of time points. UFM does not provide an explanation for this clearly present but persistent monomeric/oligomeric population. This should be investigated further in conjunction with separation techniques to attempt to isolate this population. It is already possible to separate the MF from the bulk solution via centrifugation; however no work has been done to confirm that these MF do not release smaller aggregates over time. MF are typically thought to be stable structures, however it is possible that early aggregates remain associated with them which could be released over time. Identification and isolation of specific aggregate populations is complex but possible thanks to advances in size-exclusion chromatography protocols[287]. In addition to further work to better identify this population of Aβ aggregates it would be ideal to image other amyloid peptides. Amylin, α-synuclein and ABri would all require the same attention to detail with regards to substrate development and imaging conditions due to each having their own specific incubation environment, but it would be interesting to compare the nanostructure as identified by UFM and discover potentially common structures in regions of elasticity and stiffness.

Another key area for further development is that of UFM applied underliquid. Samples of individual peptides were found to attach too poorly to image, and therefore a method of increasing this attachment or more permanent fixation need to be considered. Additionally biomembranes are an area of increasing interest and membranes made of collagen or similar would be inherently more stable, and therefore open to imaging than poorly attached individual protein moieties and offer an interesting opportunity. AFM techniques have been used in a liquid environment to image Aβ previously, with particular attention given to its interactions with lipid membranes. Liposomes reconstituted in the presence of Aβ show increased permeability to calcium, while deterioration of an intact lipid bilayer following exposure to Aβ has been observed using underliquid-AFM[207, 288, 289]. Furthermore the cholesterol content of the lipid bilayer has been noted to correlate with Aβ1:42 fibrillisation and modulate the rate of aggregation[289]. Parbhu *et al.* (2002) preformed a comprehensive study of the real time monitoring of Aβ1:42 aggregation, studying the effect of buffers and peptide concentration on aggregation, and found that imaging with higher concentrations (100 µM) was ideal, with PBS being a successful buffer for incubation compared to water alone. This study also monitored the real time effects of Zn upon aggregation and noted the enhancement of fibrillisation in its presence[75]. Ultimately it appears that to move towards the successful adaption of UFM to monitor Aβ aggregation under liquid imaging and aggregation must be conducted in a buffer with a higher salt level, such as PBS, at a higher peptide levels, than used within this work[75, 288, 289]. The monitoring of DNA and lipid membrane interactions with high-speed AFM is becoming increasingly common. This technique utilises ultra-short cantilevers in a liquid environtment to follow biological events in real time. During a high-speed study of DNA: protein interactions quantification of the forces acting upon the DNA noted that a significant amount of the overall force results from the AFM cantilever tip[290]. In addition the levels of Ni^{2+} within the buffer could be tuned to control the level of DNA mobility. Caution should be taken when manipulating the attachment of Aβ with metal ions, given the tendency of them to alter the aggregation process[223]. Imaging Aβ in real time would be an ideal method of following the aggregation process given the instability seen when the peptide is rehydrated[9], and has already been done with TM and nano-IR spectroscopy[285, 288, 289], while UFM itself has been shown to work in the liquid regime[32, 34] . However successful studies of biological molecules using high-speed AFM offers lessons which can be adapted for the use of UFM underliquid.

Moving beyond UFM the technique of SThM-IR requires further development. The first line on enquiry would be to test and develop additional substrates for SThM-IR to find one that offers a better thermal contrast, is transparent in the mid-IR region while has a more anatomically flat surface, beginning with Au coated Si, as per experiments with the Nano-IR. This would hopefully reduce the contamination seen when imaging with commercial systems such as the Nano-IR. The topographical effects of such a thin sample may also need some care and consideration.

Preliminary work conducted with stained cells indicates that a larger, more robust sample may be a more ideal starting point for this work.

It is also important to address the stability and reliability issues seen at ALICE using a mid-IR laser generated by a FEL. One alternative which has been proposed is the use of a Quantum Cascade Laser (QCL) to generate the tuneable mid-IR source. Excitation of a sample with this method requires care in order to separate the effect of the shift in resonance frequency due to the samples elastic response with that of a wavelength specific IR absorption of the sample. Alternatively, adjustment of the cantilver used, or the resonant frequency of the cantilever could be made, as fluctuations in signal intensity have been linked to the resonant frequency the cantilever is tuned to[52]. Ideally one would seek to combine independent nanomechanical measurements with spectroscopical data taken from a mid-IR source, taking reference from Ruggeri *et al.* (2015) who combined the IR-spectroscopical study of ataxin-3 with characterisation of its Young's Modulus during aggregation[285]. This combination of advanced SPM techniques allowed the team to not only monitor the structural changes seen during aggregation but also to identify that the Young's Modulus of a peptide increases along the aggregation process, indicating and increased stiffness and structural stability in MF compared to monomers[285].

A final area of development is the application of DLS to the aggregation of amyloid peptides in conjunction with drug development. This technique has shown to be highly sensitive when different time points of Aβ1:40/1:42 were analysed, and was able to detect differences between samples incubated with and without inhibitors. Ideally this technique would continue with the addition of analysing populations for molecular weight, and alterations in charge in addition to particle size. Liposomes of different sizes, with different functional modifications could also bet tested using this method in addition to that of ThT or immunoassays.

In conclusion the work presented in this thesis lays the groundwork for the advancements of developing techniques such as AFM-IR, as well as confirming the application of pre-existing ones such as DLS and UFM. The application of physical methods to samples such as proteins has been shown to be highly applicable and offer great potential to shed light on their formation and interaction with other factors.

Academic Publications

Amyloid-β fibrils in Alzheimer's Disease are not inert when bound to copper ions but can degrade hydrogen peroxide and generate reactive oxygen species

Mayes, J., Tinker-Mill, C., Kolosov, O., Zhang, H., Tabner, B. & Allsop, D.

Journal of Biological Chemistry. 289, p. 12052-12062 11 p. 25/04/2014

Ultrasonic force microscopy for nanomechanical characterization of early and late-stage amyloid-β peptide aggregation

Tinker-Mill, C., Mayes, J., Allsop, D. & Kolosov, O.

Scientific Reports. 4, 7 p.4004, 2014

A novel retro-inverso peptide inhibitor reduces amyloid deposition, oxidation and inflammation and stimulates neurogenesis in the APPswe/PS1ΔE9 mouse model of Alzheimer's Disease

Parthsarathy, V., McClean, P. L., Hölscher, C., Taylor, M., Tinker, C., Jones, G., Kolosov, O., Salvati, E., Gregori, M., Masserini, M. & Allsop, D.

PloS ONE. 8, 1, 11 p.e54769, 2013

Also in preparation

Retro-inverso peptide inhibitory nanoparticles (PINPs) as potent inhibitors of aggregation of the Alzheimer's Aβ peptide

Gregori, M., Taylor, M., Tinker-Mill, C., Michael, M., Kolosov, O., Salvati, E, Re, F., Minniti, S., Zambelli, V., Masserini, M. & Allsop, D.

Comparison of photothermal and opto-acoustic response of nanoscale probes for Mid-IR photothermal microspectroscopy (PTMS) of nanostructured biological materials

Tovee, P.D., Tinker-Mill, C., Kjoller, K., Allsop, D., Weightman, P., Surman,' M., Siggel-King, M., Wolski, A. & Kolosov, O.V.

Scanning thermal microscopy imaging of Amyloid-β

Tovee, P.D., Tinker-Mill, C., Allsop, D.,. & Kolosov, O.V.

Presentations at Conferences

Nanoscale SPM Characterisation of Nacre Aragonite Plates and Synthetic *Human Amyloid Fibres.*

Grishin, I., Tinker, C., Allsop, D., Robson, A & O.V. Kolosov.

Nanotech 2012 Santa Clara, California.

Proceedings of Nanotech - 2012, TechConnect World 2012, pages 2,940 ISBN: 978-1-4665-6278-3, NSTI, CRC press, Santa Clara, USA **(2012).**

Nanoscale morphology and nanomechanical characterisation of recombinant human Amyloid-β 1-42 via tapping mode and ultrasonic force microscopies.

Tinker, C., Allsop D. & Kolosov, O.

Seeing at the Nanoscale, July 2012, Bristol University.

Nanoscale morphology and nanomechanical characterisation of recombinant human Amyloid-β 1-42 via tapping mode and ultrasonic force microscopies.

Tinker, C., Allsop D. & Kolosov, O.

European Microscopy Conference, September 2012, Manchester.

Nanoscale dynamics of Amyloid-β fibres on poly-L-Lysine substrate in air and liquid environments via atomic force and ultrasonic force microscopy

Tinker, C., Allsop, D., Kolosova,K., Dinelli, F & Kolosov, O

Multifrequency Conference, October 2012, Madrid.

Nanoscale imaging of Alzheimer's Disease: Getting to the core of it

Tinker, C., Allsop, D., Robson, A. & Kolosov, O

Lancaster University Sci-Tech Christmas Conference, 17th December 2012, Lancaster.

Ultrasonic force microscopy studies of the nanoscale structure of Amyloid-β fibres in a liquid environment

Tinker C., Allsop, D., Kolosova, K., Dinelli, F. & Kolosov O.

Bristol University Nanomaterial Futures Conference, 17th February 2013, Bristol.

Nanostructure of Amyloid Fibres using Ultrasonic Force Microscopy

Tinker, C., Allsop D. & Kolosov, O.

Waterloo University talk as a visiting student, September 2013, Waterloo, Canada.

Nanomechanical and nanothermal mapping of initial stages of amyloid fibres formation

Kolosov, O., Tovee, P., Tinker-Mill, C. & Allsop, D.

Bristol Nanoscience Symposium 15/09/2014, Bristol

Press articles

http://www.labnews.co.uk/news/sewing-machine-inspires-imaging-tool-for-alzheimers/

21/04/14: (Lab News)

Tinker-Mill, C., Mayes, J., Allsop, D. & Kolosov, O.

Imaging tool gives insight into origins of Alzheimer's

2/04/14: (Medical Express)

Tinker-Mill, C., Mayes, J., Allsop, D. & Kolosov, O.

New imaging tool provides fresh insight into origins of Alzheimer's, Parkinson's disease

2/04/14: (News medical)

Tinker-Mill, C., Mayes, J., Allsop, D. & Kolosov, O.

Sewing machine' idea gives insight into origins of Alzheimer's

1/04/14: (USA Daily news) (Science daily) (Deccan chronicle) (Business Standard)

Tinker-Mill, C., Mayes, J., Allsop, D. & Kolosov, O.

Tools of the Trade

26/02/14: (BioTechniques - The International Journal of Life Science Methods)

Tinker-Mill, C., Mayes, J., Allsop, D. & Kolosov, O.

Awards

Juno Award for Research Excellence 2014

Juno Award for Research Excellence 2012

References

1. Dinelli, F., Biswas, S.K., Briggs, G.A.D. & Kolosov, O.V. Measurements of stiff-material compliance on the nanoscale using ultrasonic force microscopy. *Physical Review B* **61**, 13995-14006 (2000).
2. Dinelli, F. et al. Mapping surface elastic properties of stiff and compliant materials on the nanoscale using ultrasonic force microscopy. *Philosophical Magazine a-Physics of Condensed Matter Structure Defects and Mechanical Properties* **80**, 2299-2323 (2000).
3. Xiao, Y. & Ma, B. Abeta(1-42) fibril structure illuminates self-recognition and replication of amyloid in Alzheimer's disease. (2015).
4. Blennow, K., de Leon, M.J. & Zetterberg, H. Alzheimer's disease. *Lancet* **368**, 387-403 (2006).
5. Cao, X.W. & Sudhof, T.C. A transcriptively active complex of APP with Fe65 and histone acetyltransferase Tip60. *Science* **293**, 115-120 (2001).
6. Shoji, M. et al. Production Of The Alzheimer Amyloid-Beta Protein By Normal Proteolytic Processing. *Science* **258**, 126-129 (1992).
7. Digital Insturments MultiMode SPM Manual (1999).
8. DoITPoMS. in University of Cambridge, Teaching and Learning Package, (http://www.doitpoms.ac.uk/tlplib/afm/tip_surface_interaction.php Accessed 24/02/15, 2013).
9. Maurstad, G., Prass, M., Serpell, L.C. & Sikorski, P. Dehydration stability of amyloid fibrils studied by AFM. *European Biophysics Journal with Biophysics Letters* **38**, 1135-1140 (2009).
10. Fändrich, M., Schmidt, M. & Grigorieff, N. Recent progress in understanding Alzheimer's β-amyloid structures. *Trends in Biochemical Sciences* **36**, 338-345 (2011).
11. Fischer-Cripps, A.C. Introduction to contact mechanics (Springer, New York, 2007).
12. Schmidt, M. et al. Comparison of Alzheimer Aβ(1-40) and Aβ(1-42) Amyloid Fibrils Reveals Similar Protofilament Structures. *Proceedings of the National Academy of Sciences of the United States of America* **106**, 19813-19818 (2009).
13. Binnig, G., Quate, C.F. & Gerber, C. ATOMIC FORCE MICROSCOPE. *Physical Review Letters* **56**, 930-933 (1986).
14. Binnig, G. & Rohrer, H. Scanning Tunneling Microscopy. *Helvetica Physica Acta* **55**, 726-735 (1982).
15. Binnig, G., Rohrer, H., Gerber, C. & Weibel, E. TUNNELING THROUGH A CONTROLLABLE VACUUM GAP. *Applied Physics Letters* **40**, 178-180 (1982).
16. Jandt, K.D. Atomic force microscopy of biomaterials surfaces and interfaces. *Surface Science* **491**, 303-332 (2001).
17. Dinelli, F., Assender, H.E., Takeda, N., Briggs, G.A.D. & Kolosov, O.V. Elastic mapping of heterogeneous nanostructures with ultrasonic force microscopy (UFM). *Surface and Interface Analysis* **27**, 562-567 (1999).
18. Dazzi, A. et al. AFM-IR: Combining Atomic Force Microscopy and Infrared Spectroscopy for Nanoscale Chemical Characterization. *Applied Spectroscopy* **66**, 1365-1384 (2012).
19. Dazzi, A., Prazeres, R., Glotin, E. & Ortega, J.M. Local infrared microspectroscopy with subwavelength spatial resolution with an atomic force microscope tip used as a photothermal sensor. *Optics Letters* **30**, 2388-2390 (2005).

20. Marcott, C. et al. Nanoscale IR Spectroscopy: AFM-IR - A New Technique. *Spectroscopy* **27**, 60-65 (2012).
21. Tovee, P.D. & Kolosov, O.V. Mapping nanoscale thermal transfer in-liquid environment-immersion scanning thermal microscopy. *Nanotechnology* **24** (2013).
22. Tovee, P.D. et al. Nanoscale resolution scanning thermal microscopy using carbon nanotube tipped thermal probes. *Physical Chemistry Chemical Physics* **16**, 1174-1181 (2014).
23. Tovee, P., Pumarol, M., Zeze, D., Kjoller, K. & Kolosov, O. Nanoscale spatial resolution probes for scanning thermal microscopy of solid state materials. *Journal of Applied Physics* **112**, - (2012).
24. Gandyra, D., Walheim, S., Gorb, S., Barthlott, W. & Schimmel, T. The capillary adhesion technique: a versatile method for determining the liquid adhesion force and sample stiffness. *Beilstein Journal of Nanotechnology* **6**, 11-18 (2015).
25. Weisenhorn, A.L., Hansma, P.K., Albrecht, T.R. & Quate, C.F. FORCES IN ATOMIC FORCE MICROSCOPY IN AIR AND WATER. *Applied Physics Letters* **54**, 2651-2653 (1989).
26. (ed. Baro, A.M.R., R. G.) (Wiley-VCH, 2012).
27. Bonnell, D. Scanning Probe Microscopy and Spectroscopy: Theory, Techniques, and Applications (Wiley-Blackwell, New York, USA, 2001).
28. Eaton, P.W., P. Atomic Force Microscopy (Oxford University Press, 2010).
29. Kolosov, O.V. & Yamanaka, K. Nonlinear detection of ultrasonic vibrations in an atomic force microscope. *Japanese Journal of Applied Physics Part 2-Letters* **32**, L1095-L1098 (1993).
30. Dinelli, F., Biswas, S.K., Briggs, G.A.D. & Kolosov, O.V. Ultrasound induced lubricity in microscopic contact. *Applied Physics Letters* **71**, 1177-1179 (1997).
31. Sader, J.E., Chon, J.W.M. & Mulvaney, P. Calibration of rectangular atomic force microscope cantilevers. *Review of Scientific Instruments* **70**, 3967-3969 (1999).
32. Robinson, B.J., Kay, N.D. & Kolosov, O.V. Nanoscale Interfacial Interactions of Graphene with Polar and Nonpolar Liquids. *Langmuir* **29**, 7735-7742 (2013).
33. Robinson, B.J. et al. Nanomechanical mapping of graphene layers and interfaces in suspended graphene nanostructures grown via carbon diffusion. *Thin Solid Films* **550**, 472-479 (2014).
34. Robinson, B.J. & Kolosov, O.V. Probing nanoscale graphene-liquid interfacial interactions via ultrasonic force spectroscopy. *Nanoscale* **6**, 10806-10816 (2014).
35. Bosse, J.L., Tovee, P.D., Huey, B.D. & Kolosov, O.V. Physical mechanisms of megahertz vibrations and nonlinear detection in ultrasonic force and related microscopies. *Journal of Applied Physics* **115** (2014).
36. Chaudhury, M.K. & Owen, M.J. Adhesion hysteresis and friction. *Langmuir* **9**, 29-31 (1993).
37. Wei, Z., He, M.-F. & Zhao, Y.-P. The Effects of Roughness on Adhesion Hysteresis. *Journal of Adhesion Science and Technology* **24**, 1045-1054 (2010).
38. Johnson, K.L., Kendall, K. & Roberts, A.D. SURFACE ENERGY AND CONTACT OF ELASTIC SOLIDS. *Proceedings of the Royal Society of London Series a-Mathematical and Physical Sciences* **324**, 301-& (1971).
39. Rabe, U., Janser, K. & Arnold, W. Vibrations of free and surface-coupled atomic force microscope cantilevers: Theory and experiment. *Review of Scientific Instruments* **67**, 3281-3293 (1996).
40. Rajakarunanayake, Y.N. & Wickramasinghe, H.K. Nonlinear Photothermal Imaging. *Applied Physics Letters* **48**, 218-220 (1986).
41. Williams, C.C. & Wickramasinghe, H.K. Scanning Thermal Profiler. *Applied Physics Letters* **49**, 1587-1589 (1986).

42. Igeta, M., Inoue, T., Varesi, J. & Majumdar, A. Thermal expansion and temperature measurement in a microscopic scale by using the Atomic Force Microscope. *Jsme International Journal Series B-Fluids and Thermal Engineering* **42**, 723-730 (1999).
43. Majumdar, A., Carrejo, J.P. & Lai, J. Thermal Imaging Using The Atomic Force Microscope. *Applied Physics Letters* **62**, 2501-2503 (1993).
44. Fischer, H. Quantitative determination of heat conductivities by scanning thermal microscopy. *Thermochimica Acta* **425**, 69-74 (2005).
45. Lee, J. et al. Electrical, thermal, and mechanical characterization of silicon microcantilever heaters. *Journal of Microelectromechanical Systems* **15**, 1644-1655 (2006).
46. Gazit, E. The "Correctly folded" state of proteins: Is it a metastable state. *Angewandte Chemie-International Edition* **41**, 257-+ (2002).
47. Dandurand, J. et al. Conformational and thermal characterization of a synthetic peptidic fragment inspired from human tropoelastin: Signature of the amyloid fibers. *Pathologie Biologie* **62**, 100-107 (2014).
48. Blancas-Mejia, L.M. et al. Kinetic Control in Protein Folding for Light Chain Amyloidosis and the Differential Effects of Somatic Mutations. *Journal of Molecular Biology* **426**, 347-361 (2014).
49. Morel, B., Varela, L. & Conejero-Lara, F. The Thermodynamic Stability of Amyloid Fibrils Studied by Differential Scanning Calorimetry. *Journal of Physical Chemistry B* **114**, 4010-4019 (2010).
50. Ortega, J.M., Glotin, F. & Prazeres, R. Extension in far-infrared of the CLIO free-electron laser. *Infrared Physics & Technology* **49**, 133-138 (2006).
51. Dazzi, A., Goumri-Said, S. & Salomon, L. Theoretical study of an absorbing sample in infrared near-field spectromicroscopy. *Optics Communications* **235**, 351-360 (2004).
52. Dazzi, A., Prazeres, R., Glotin, F. & Ortega, J.M. Analysis of nano-chemical mapping performed by an AFM-based ("AFMIR") acousto-optic technique. *Ultramicroscopy* **107**, 1194-1200 (2007).
53. Dazzi, A., Prazeres, R., Glotin, F. & Ortega, J.M. Subwavelength infrared spectromicroscopy using an AFM as a local absorption sensor. *Infrared Physics & Technology* **49**, 113-121 (2006).
54. Wolkers, W.F., Oldenhof, H., Alberda, M. & Hoekstra, F.A. A Fourier transform infrared microspectroscopy study of sugar glasses: application to anhydrobiotic higher plant cells. *Biochimica Et Biophysica Acta-General Subjects* **1379**, 83-96 (1998).
55. Marcott, C. et al. Nanoscale infrared (IR) spectroscopy and imaging of structural lipids in human stratum corneum using an atomic force microscope to directly detect absorbed light from a tunable IR laser source. *Experimental Dermatology* **22**, 419-421 (2013).
56. Marcott, C. et al. Localization of Human Hair Structural Lipids Using Nanoscale Infrared Spectroscopy and Imaging. *Applied Spectroscopy* **68**, 564-569 (2014).
57. Van Eerdenbrugh, B., Lo, M., Kjoller, K., Marcott, C. & Taylor, L.S. Nanoscale mid-infrared imaging of phase separation in a drug-polymer blend. *Journal of Pharmaceutical Sciences* **101**, 2066-2073 (2012).
58. Paschalis, E.P., Betts, F., DiCarlo, E., Mendelsohn, R. & Boskey, A.L. FTIR microspectroscopic analysis of normal human cortical and trabecular bone. *Calcified Tissue International* **61**, 480-486 (1997).
59. Paschalis, E.P., Betts, F., DiCarlo, E., Mendelsohn, R. & Boskey, A.L. FTIR microspectroscopic analysis of human iliac crest biopsies from untreated osteoporotic bone. *Calcified Tissue International* **61**, 487-492 (1997).

60. Mendelsohn, R., Paschalis, E.P. & Boskey, A.L. Infrared spectroscopy, microscopy, and microscopic imaging of mineralizing tissues: Spectra-structure correlations from human iliac crest biopsies. *Journal of Biomedical Optics* **4**, 14-21 (1999).
61. Lasch, P., Boese, M., Pacifico, A. & Diem, M. FT-IR spectroscopic investigations of single cells on the subcellular level. *Vibrational Spectroscopy* **28**, 147-157 (2002).
62. Wood, B.R. et al. FTIR microspectroscopic study of cell types and potential confounding variables in screening for cervical malignancies. *Biospectroscopy* **4**, 75-91 (1998).
63. Lasch, P., Haensch, W., Lewis, E.N., Kidder, L.H. & Naumann, D. Characterization of colorectal adenocarcinoma sections by spatially resolved FT-IR microspectroscopy. *Applied Spectroscopy* **56**, 1-9 (2002).
64. Lasch, P., Haensch, W., Naumann, D. & Diem, M. Imaging of colorectal adenocarcinoma using FT-IR microspectroscopy and cluster analysis. *Biochimica Et Biophysica Acta-Molecular Basis of Disease* **1688**, 176-186 (2004).
65. Mordechai, S. et al. Possible common biomarkers from FTIR microspectroscopy of cervical cancer and melanoma. *Journal of Microscopy-Oxford* **215**, 86-91 (2004).
66. Mueller, T. et al. Nanoscale spatially resolved infrared spectra from single microdroplets. *Lab on a Chip* **14**, 1315-1319 (2014).
67. Pryor, N.E., Moss, M.A. & Hestekin, C.N. Unraveling the Early Events of Amyloid-beta Protein (A beta) Aggregation: Techniques for the Determination of A beta Aggregate Size. *International Journal of Molecular Sciences* **13**, 3038-3072 (2012).
68. Loureiro, J.A., Gomes, B., Coelho, M.A.N., Pereira, M.D. & Rocha, S. Targeting nanoparticles across the blood-brain barrier with monoclonal antibodies. *Nanomedicine* **9**, 709-722 (2014).
69. Yang, Z.Z. et al. Enhanced brain distribution and pharmacodynamics of rivastigmine by liposomes following intranasal administration. *International Journal of Pharmaceutics* **452**, 344-354 (2013).
70. Salvati, E. et al. Liposomes functionalized to overcome the blood-brain barrier and to target amyloid-beta peptide: the chemical design affects the permeability across an in vitro model. *International Journal of Nanomedicine* **8** (2013).
71. Gobbi, M. et al. Lipid-based nanoparticles with high binding affinity for amyloid-beta(1-42) peptide. *Biomaterials* **31**, 6519-6529 (2010).
72. Carrotta, R., Manno, M., Bulone, D., Martorana, V. & San Biagio, P.L. Protofibril formation of amyloid beta-protein at low pH via a non-cooperative elongation mechanism. *Journal of Biological Chemistry* **280**, 30001-30008 (2005).
73. Lomakin, A., Chung, D.S., Benedek, G.B., Kirschner, D.A. & Teplow, D.B. On the nucleation and growth of amyloid beta-protein fibrils: Detection of nuclei and quantitation of rate constants. *Proceedings of the National Academy of Sciences of the United States of America* **93**, 1125-1129 (1996).
74. Lomakin, A., Teplow, D.B., Kirschner, D.A. & Benedek, G.B. Kinetic theory of fibrillogenesis of amyloid beta-protein. *Proceedings of the National Academy of Sciences of the United States of America* **94**, 7942-7947 (1997).
75. Parbhu, A., Lin, H., Thimm, J. & Lal, R. Imaging real-time aggregation of amyloid beta protein (1-42) by atomic force microscopy. *Peptides* **23**, 1265-1270 (2002).
76. Cizas, P. et al. Size-dependent neurotoxicity of beta-amyloid oligomers. *Archives of Biochemistry and Biophysics* **496**, 84-92 (2010).
77. Streets, A.M., Sourigues, Y., Kopito, R.R., Melki, R. & Quake, S.R. Simultaneous Measurement of Amyloid Fibril Formation by Dynamic Light Scattering and Fluorescence Reveals Complex Aggregation Kinetics. *Plos One* **8** (2013).
78. Blackley, H.K.L. et al. Morphological development of beta(1-40) amyloid fibrils. *Experimental Neurology* **158**, 437-443 (1999).

79. Roher, A.E. et al. Oligomerization and fibril assembly of the amyloid-beta protein. *Biochimica Et Biophysica Acta-Molecular Basis of Disease* **1502**, 31-43 (2000).
80. Harper, J.D., Wong, S.S., Lieber, C.M. & Lansbury, P.T. Observation of metastable A beta amyloid protofibrils by atomic force microscopy. *Chemistry & Biology* **4**, 119-125 (1997).
81. Walsh, D.M., Lomakin, A., Benedek, G.B., Condron, M.M. & Teplow, D.B. Amyloid beta-protein fibrillogenesis - Detection of a protofibrillar intermediate. *Journal of Biological Chemistry* **272**, 22364-22372 (1997).
82. Harper, J.D., Wong, S.S., Lieber, C.M. & Lansbury, P.T. Assembly of A beta amyloid protofibrils: An in vitro model for a possible early event in Alzheimer's disease. *Biochemistry* **38**, 8972-8980 (1999).
83. Walsh, D.M. et al. Amyloid beta-protein fibrillogenesis - Structure and biological activity of protofibrillar intermediates. *Journal of Biological Chemistry* **274**, 25945-25952 (1999).
84. Serem, W.K., Bett, C.K., Ngunjiri, J.N. & Garno, J.C. Studies of the Growth, Evolution, and Self-Aggregation of beta-Amyloid Fibrils Using Tapping-Mode Atomic Force Microscopy. *Microscopy Research and Technique* **74**, 699-708 (2011).
85. Gosal, W.S., Clark, A.H. & Ross-Murphy, S.B. Fibrillar beta-lactoglobulin gels: Part 1. Fibril formation and structure. *Biomacromolecules* **5**, 2408-2419 (2004).
86. Arimon, M. et al. Fine structure study of A beta(1-42) fibrillogenesis with atomic force microscopy. *Faseb Journal* **19**, 1344-+ (2005).
87. Moores, B., Drolle, E., Attwood, S.J., Simons, J. & Leonenko, Z. Effect of Surfaces on Amyloid Fibril Formation. *Plos One* **6**, 8 (2011).
88. Wang, Z.G. et al. AFM and STM study of beta-amyloid aggregation on graphite. *Ultramicroscopy* **97**, 73-79 (2003).
89. Fändrich, M., Schmidt, M. & Grigorieff, N. Recent progress in understanding Alzheimer's β- amyloid structures. *Trends in Biochemical Sciences* **36**, 338-345 (2011).
90. Miyakawa, T., Watanabe, K. & Katsuragi, S. Ultrastructure of amyloid fibrils in Alzheimers-Disease and Downs-Syndrome. *Virchows Archiv B-Cell Pathology Including Molecular Pathology* **52**, 99-106 (1986).
91. Zhang, R. et al. Interprotofilament interactions between Alzheimer's A beta(1-42) peptides in amyloid fibrils revealed by cryoEM. *Proceedings of the National Academy of Sciences of the United States of America* **106**, 4653-4658 (2009).
92. Serpell, L.C. Alzheimer's amyloid fibrils: structure and assembly. *Biochimica Et Biophysica Acta-Molecular Basis of Disease* **1502**, 16-30 (2000).
93. Serpell, L.C. et al. Examination Of The Structure Of The Transthyretin Amyloid Fibril By Image-Reconstruction From Electron-Micrographs. *Journal of Molecular Biology* **254**, 113-118 (1995).
94. Miller, Y., Ma, B.Y., Tsai, C.J. & Nussinov, R. Hollow core of Alzheimer's A beta(42) amyloid observed by cryoEM is relevant at physiological pH. *Proceedings of the National Academy of Sciences of the United States of America* **107**, 14128-14133 (2010).
95. Miller, Y., Ma, B.Y. & Nussinov, R. The Unique Alzheimer's beta-Amyloid Triangular Fibril Has a Cavity along the Fibril Axis under Physiological Conditions. *Journal of the American Chemical Society* **133**, 2742-2748 (2011).
96. Sachse, C. et al. Quaternary structure of a mature amyloid fibril from Alzheimer's a beta(1-40) peptide. *Journal of Molecular Biology* **362**, 347-354 (2006).
97. Meinhardt, J., Sachse, C., Hortschansky, P., Grigorieff, N. & Fandrich, M. A beta(1-40) Fibril Polymorphism Implies Diverse Interaction Patterns in Amyloid Fibrils. *Journal of Molecular Biology* **386**, 869-877 (2009).

98. Gosal, W.S., Myers, S.L., Radford, S.E. & Thomson, N.H. Amyloid under the atomic force microscope. *Protein and Peptide Letters* **13**, 261-270 (2006).
99. Soto, C. Unfolding the role of protein misfolding in neurodegenerative diseases. *Nat Rev Neurosci* **4**, 49-60 (2003).
100. Rochet, J.C. & Lansbury, P.T. Amyloid fibrillogenesis: themes and variations. *Current Opinion in Structural Biology* **10**, 60-68 (2000).
101. Selkoe, D.J. Alzheimer's disease: genes, proteins, and therapy. *Physiol Rev* **81**, 741-66 (2001).
102. Citron, M. beta-secretase as a target for the treatment of Alzheimer's disease. *Journal of Neuroscience Research* **70**, 373-379 (2002).
103. Games, D. et al. Alzheimer-Type Neuropathology In Transgenic Mice Overexpressing V717f Beta-Amyloid Precursor Protein. *Nature* **373**, 523-527 (1995).
104. Wurtman, R. Biomarkers in the diagnosis and management of Alzheimer’s disease. *Metabolism* **64**, S47-S50 (2015).
105. Eckerstrom, C. et al. A combination of neuropsychological, neuroimaging, and cerebrospinal fluid markers predicts conversion from mild cognitive impairment to dementia. *J Alzheimers Dis* **36**, 421-31 (2013).
106. Petersen, R.C. Mild cognitive impairment as a diagnostic entity. *Journal of Internal Medicine* **256**, 183-194 (2004).
107. Harper, J.D. & Lansbury, P.T. Models of amyloid seeding in Alzheimier's disease and scrapie: Mechanistic truths and physiological consequences of the time-dependent solubility of amyloid proteins. *Annual Review of Biochemistry* **66**, 385-407 (1997).
108. Glenner, G.G. & Wong, C.W. Alzheimer's disease: initial report of the purification and characterization of a novel cerebrovascular amyloid protein. *Biochem Biophys Res Commun* **120**, 885-90 (1984).
109. Knauer, M.F., Soreghan, B., Burdick, D., Kosmoski, J. & Glabe, C.G. Intracellular Accumulation And Resistance To Degradation Of The Alzheimer Amyloid A4/Beta-Protein. *Proceedings of the National Academy of Sciences of the United States of America* **89**, 7437-7441 (1992).
110. Burdick, D. et al. ASSEMBLY AND AGGREGATION PROPERTIES OF SYNTHETIC ALZHEIMERS A4/BETA AMYLOID PEPTIDE ANALOGS. *Journal of Biological Chemistry* **267**, 546-554 (1992).
111. Kidd, M. Paired helical filaments in electron microscopy of Alzheimer's disease. *Nature* **197**, 192-3 (1963).
112. Thies, W. & Bleiler, L. 2013 Alzheimer's disease facts and figures. *Alzheimers Dement* **9**, 208-45 (2013).
113. Corrada, M.M., Brookmeyer, R., Paganini-Hill, A., Berlau, D. & Kawas, C.H. Dementia Incidence Continues to Increase with Age in the Oldest Old The 90+Study. *Annals of Neurology* **67**, 114-121 (2010).
114. Prince, M., Knapp, M, Guerchet,, M, M., P, Prina, M, Comas-Herrera, A, Wittenberg, R, & Adelaja, B., Hu, B, King, D, Rehill, A and Salimkumar, D. in Alzheimer’s Society (2014).
115. Brookmeyer, R., Johnson, E., Ziegler-Graham, K. & Arrighi, H.M. Forecasting the global burden of Alzheimer's disease. *Alzheimers & Dementia* **3**, 186-191 (2007).
116. Schellenberg, G.D. & Montine, T.J. The genetics and neuropathology of Alzheimer's disease. *Acta Neuropathol* **124**, 305-23 (2012).
117. Lambert, J.C. & Amouyel, P. Genetic heterogeneity of Alzheimer's disease: complexity and advances. *Psychoneuroendocrinology* **32 Suppl 1**, S62-70 (2007).
118. Tang, T.-C. et al. Conformational Changes Induced by the A21G Flemish Mutation in the Amyloid Precursor Protein Lead to Increased A beta Production. *Structure* **22**, 387-396 (2014).

119. Muller, U., Winter, P. & Graeber, M.B. A presenilin 1 mutation in the first case of Alzheimer's disease. *Lancet Neurol* **12**, 129-30 (2013).

120. Jonsson, T. et al. A mutation in APP protects against Alzheimer's disease and age-related cognitive decline. *Nature* **488**, 96-9 (2012).

121. Corder, E.H. et al. Gene dose of apolipoprotein E type 4 allele and the risk of Alzheimer's disease in late onset families. *Science* **261**, 921-3 (1993).

122. Walsh, D.M. & Selkoe, D.J. A beta Oligomers - a decade of discovery. *Journal of Neurochemistry* **101**, 1172-1184 (2007).

123. Holtzman, D.M. et al. Apolipoprotein E isoform-dependent amyloid deposition and neuritic degeneration in a mouse model of Alzheimer's disease. *Proc Natl Acad Sci U S A* **97**, 2892-7 (2000).

124. Lauderback, C.M. et al. Apolipoprotein E modulates Alzheimer's Abeta(1-42)-induced oxidative damage to synaptosomes in an allele-specific manner. *Brain Res* **924**, 90-7 (2002).

125. Mattson, M.P. et al. Evidence for excitoprotective and intraneuronal calcium-regulating roles for secreted forms of the beta-amyloid precursor protein. *Neuron* **10**, 243-54 (1993).

126. Barnham, K.J. et al. Structure of the Alzheimer's disease amyloid precursor protein copper binding domain. A regulator of neuronal copper homeostasis. *J Biol Chem* **278**, 17401-7 (2003).

127. Small, D.H. et al. A heparin-binding domain in the amyloid protein precursor of Alzheimer's disease is involved in the regulation of neurite outgrowth. *J Neurosci* **14**, 2117-27 (1994).

128. Hardy, J. The 'amyloid cascade hypothesis' of AD: decoy or real McCoy? Reply. *Trends in Neurosciences* **20**, 559-559 (1997).

129. White, A.R. et al. Copper levels are increased in the cerebral cortex and liver of APP and APLP2 knockout mice. *Brain Res* **842**, 439-44 (1999).

130. Lichtenthaler, S.F., Haass, C. & Steiner, H. Regulated intramembrane proteolysis - lessons from amyloid precursor protein processing. *Journal of Neurochemistry* **117**, 779-796 (2011).

131. Zhang, H., Ma, Q.L., Zhang, Y.W. & Xu, H.X. Proteolytic processing of Alzheimer's ss-amyloid precursor protein. *Journal of Neurochemistry* **120**, 9-21 (2012).

132. Grimm, M.O.W., Rothhaar, T.L. & Hartmann, T. The role of APP proteolytic processing in lipid metabolism. *Experimental Brain Research* **217**, 365-375 (2012).

133. Citron, M., Teplow, D.B. & Selkoe, D.J. Generation Of Amyloid-Beta Protein From Its Precursor Is Sequence-Specific. *Neuron* **14**, 661-670 (1995).

134. De Strooper, B. Aph-1, Pen-2, and nicastrin with presenilin generate an active gamma-secretase complex. *Neuron* **38**, 9-12 (2003).

135. Schroeter, E.H. et al. A presenilin dimer at the core of the gamma-secretase enzyme: Insights from parallel analysis of Notch 1 and APP proteolysis. *Proceedings of the National Academy of Sciences of the United States of America* **100**, 13075-13080 (2003).

136. Zheng, H. & Koo, E.H. Biology and pathophysiology of the amyloid precursor protein. *Molecular Neurodegeneration* **6** (2011).

137. Farzan, M., Schnitzler, C.E., Vasilieva, N., Leung, D. & Choe, H. BACE2, a beta-secretase homolog, cleaves at the beta site and within the amyloid-beta region of the amyloid-beta precursor protein. *Proceedings of the National Academy of Sciences of the United States of America* **97**, 9712-9717 (2000).

138. Yagishita, S., Morishima-Kawashima, M., Ishiura, S. & Ihara, Y. A beta 46 is processed to A beta 40 and A beta 43, but not to A beta 42, in the low density membrane domains. *Journal of Biological Chemistry* **283**, 733-738 (2008).

139. Qi-Takahara, Y. et al. Longer forms of amyloid beta protein: Implications for the mechanism of intramembrane cleavage by gamma-secretase. *Journal of Neuroscience* **25**, 436-445 (2005).
140. Hardy, J.A. & Higgins, G.A. Alzheimers-Disease - The Amyloid Cascade HypothesiS. *Science* **256**, 184-185 (1992).
141. Hardy, J. & Allsop, D. Amyloid Deposition As The Central Event In The Etiology Of Alzheimers-Disease. *Trends in Pharmacological Sciences* **12**, 383-388 (1991).
142. Selkoe, D.J. Proteolysis of integral membrane proteins and the mechanism of Alzheimer's disease. *Molecular Biology of the Cell* **10**, 351A-351A (1999).
143. Chiti, F. et al. Designing conditions for in vitro formation of amyloid protofilaments and fibrils. *Proceedings of the National Academy of Sciences of the United States of America* **96**, 3590-3594 (1999).
144. Nelson, R. et al. Structure of the cross-beta spine of amyloid-like fibrils. *Nature* **435**, 773-778 (2005).
145. Zagorski, M.G. & Barrow, C.J. NMR-Studies Of Amyloid Beta-Peptides - Proton Assignments, Secondary Structure, And Mechanism Of An Alpha-Helix- Beta-Sheet Conversion For A Homologous, 28-Residue, N-Terminal Fragment. *Biochemistry* **31**, 5621-5631 (1992).
146. Petkova, A.T. et al. A structural model for Alzheimer's beta-amyloid fibrils based on experimental constraints from solid state NMR. *Proceedings of the National Academy of Sciences of the United States of America* **99**, 16742-16747 (2002).
147. Di Carlo, M. Beta amyloid peptide: from different aggregation forms to the activation of different biochemical pathways. *European Biophysics Journal with Biophysics Letters* **39**, 877-888 (2010).
148. Karsai, A. et al. Mechanical manipulation of Alzheimer's amyloid beta 1-42 fibrils. *Journal of Structural Biology* **155**, 316-326 (2006).
149. Hoyer, W. & Hard, T. Interaction of Alzheimer's A beta peptide with an engineered binding protein - Thermodynamics and kinetics of coupled folding-binding. *Journal of Molecular Biology* **378**, 398-411 (2008).
150. Guo, M., Gorman, P.M., Rico, M., Chakrabartty, A. & Laurents, D.V. Charge substitution shows that repulsive electrostatic interactions impede the oligomerization of Alzheimer amyloid peptides. *Febs Letters* **579**, 3574-3578 (2005).
151. Bitan, G. et al. Amyloid beta-protein (A beta) assembly: A beta 40 and A beta 42 oligomerize through distinct pathways. *Proceedings of the National Academy of Sciences of the United States of America* **100**, 330-335 (2003).
152. Lazo, N.D., Grant, M.A., Condron, M.C., Rigby, A.C. & Teplow, D.B. On the nucleation of amyloid β-protein monomer folding. *Protein Science* **14**, 1581-1596 (2005).
153. Hardy, J. & Selkoe, D.J. The amyloid hypothesis of Alzheimer's disease: progress and problems on the road to therapeutics. *Science* **297**, 353-356 (2002).
154. Armstrong, R.A. A critical analysis of the 'amyloid cascade hypothesis'. *Folia Neuropathologica* **52**, 211-225 (2014).
155. Tabner, B.J., El-Agnaf, O.M.A., German, M.J., Fullwood, N.J. & Allsop, D. Protein aggregation, metals and oxidative stress in neurodegenerative diseases. *Biochemical Society Transactions* **33**, 1082-1086 (2005).
156. Shankar, G.M. & Walsh, D.M. Alzheimer's disease: synaptic dysfunction and A beta. *Molecular Neurodegeneration* **4** (2009).
157. Shankar, G.M. et al. Amyloid-beta protein dimers isolated directly from Alzheimer's brains impair synaptic plasticity and memory. *Nature Medicine* **14**, 837-842 (2008).
158. Shankar, G.M. et al. Natural oligomers of the Alzheimer amyloid-beta protein induce reversible synapse loss by modulating an NMDA-type glutamate receptor-dependent signaling pathway. *Journal of Neuroscience* **27**, 2866-2875 (2007).

159. Welzel, A.T. et al. Secreted Amyloid beta-Proteins in a Cell Culture Model Include N-Terminally Extended Peptides That Impair Synaptic Plasticity. *Biochemistry* **53**, 3908-3921 (2014).
160. Walsh, D.M. et al. Naturally secreted oligomers of amyloid beta protein potently inhibit hippocampal long-term potentiation in vivo. *Nature* **416**, 535-539 (2002).
161. Lacor, P.N. et al. A beta oligomer-induced aberrations in synapse composition, shape, and density provide a molecular basis for loss of connectivity in Alzheimer's disease. *Journal of Neuroscience* **27**, 796-807 (2007).
162. Klyubin, I. et al. Amyloid beta protein immunotherapy neutralizes A beta oligomers that disrupt synaptic plasticity in vivo. *Nature Medicine* **11**, 556-561 (2005).
163. O'Malley, T.T. et al. A beta dimers differ from monomers in structural propensity, aggregation paths and population of synaptotoxic assemblies. *Biochemical Journal* **461**, 413-426 (2014).
164. Borlikova, G.G. et al. Alzheimer brain-derived amyloid beta-protein impairs synaptic remodeling and memory consolidation. *Neurobiology of Aging* **34**, 1315-1327 (2013).
165. Shrestha, B.R. et al. Amyloid beta peptide adversely affects spine number and motility in hippocampal neurons. *Molecular and Cellular Neuroscience* **33**, 274-282 (2006).
166. Tabner, B.J. et al. Hydrogen peroxide is generated during the very early stages of aggregation of the amyloid peptides implicated in Alzheimer disease and familial British dementia. *Journal of Biological Chemistry* **280**, 35789-35792 (2005).
167. Mayes, J. et al. beta-Amyloid Fibrils in Alzheimer Disease Are Not Inert When Bound to Copper Ions but Can Degrade Hydrogen Peroxide and Generate Reactive Oxygen Species. *Journal of Biological Chemistry* **289**, 12052-12062 (2014).
168. Opazo, C. et al. Metalloenzyme-like activity of Alzheimer's disease beta-amyloid - Cu-dependent catalytic conversion of dopamine, cholesterol, and biological reducing agents to neurotoxic H2O2. *Journal of Biological Chemistry* **277**, 40302-40308 (2002).
169. Dikalov, S.I., Vitek, M.P. & Mason, R.P. Cupric-amyloid beta peptide complex stimulates oxidation of ascorbate and generation of hydroxyl radical. *Free Radical Biology and Medicine* **36**, 340-347 (2004).
170. Turnbull, S. et al. alpha-Synuclein implicated in Parkinson's disease catalyses the formation of hydrogen peroxide in vitro. *Free Radical Biology and Medicine* **30**, 1163-1170 (2001).
171. El Khoury, Y., Dorlet, P., Faller, P. & Hellwig, P. New Insights into the Coordination of Cu(II) by the Amyloid-B 16 Peptide from Fourier Transform IR Spectroscopy and Isotopic Labeling. *The Journal of Physical Chemistry B* **115**, 14812-14821 (2011).
172. Castello, M.A., Jeppson, J.D. & Soriano, S. Moving beyond anti-amyloid therapy for the prevention and treatment of Alzheimer's disease. *Bmc Neurology* **14** (2014).
173. Jack, C.R., Jr. et al. Amyloid-first and neurodegeneration-first profiles characterize incident amyloid PET positivity. *Neurology* **81**, 1732-1740 (2013).
174. Hyman, B.T. et al. National Institute on Aging-Alzheimer's Association guidelines for the neuropathologic assessment of Alzheimer's disease. *Alzheimers & Dementia* **8**, 1-13 (2012).
175. McGeer, P.L. & McGeer, E.G. The amyloid cascade-inflammatory hypothesis of Alzheimer disease: implications for therapy. *Acta Neuropathologica* **126**, 479-497 (2013).
176. Anand, R., Gill, K.D. & Mahdi, A.A. Therapeutics of Alzheimer's disease: Past, present and future. *Neuropharmacology* **76**, 27-50 (2014).
177. Liu-Seifert, H. et al. Cognitive and Functional Decline and Their Relationship in Patients with Mild Alzheimer's Dementia. *Journal of Alzheimers Disease* **43**, 949-955 (2015).

178. Bereczki, E., Re, F., Masserini, M.E., Winblad, B. & Pei, J.J. Liposomes functionalized with acidic lipids rescue A beta-induced toxicity in murine neuroblastoma cells. *Nanomedicine-Nanotechnology Biology and Medicine* **7**, 560-571 (2011).
179. Millucci, L. et al. Alkaptonuria is a novel human secondary amyloidogenic disease. *Biochimica Et Biophysica Acta-Molecular Basis of Disease* **1822**, 1682-1691 (2012).
180. Huang, L., Liu, X., Cheng, B. & Huang, K. How our bodies fight amyloidosis: Effects of physiological factors on pathogenic aggregation of amyloidogenic proteins. *Archives of Biochemistry and Biophysics* **568**, 46-55 (2015).
181. De Jong, K.L., Incledon, B., Yip, C.M. & DeFelippis, M.R. Amyloid Fibrils of Glucagon Characterized by High-Resolution Atomic Force Microscopy. *Biophysical Journal* **91**, 1905-1914.
182. Dong, M.D. et al. AFM-based force spectroscopy measurements of mature amyloid fibrils of the peptide glucagon. *Nanotechnology* **19**, 7 (2008).
183. Shammas, S.L. et al. Perturbation of the Stability of Amyloid Fibrils through Alteration of Electrostatic Interactions. *Biophysical Journal* **100**, 2783-2791 (2011).
184. Millucci, L. et al. Amyloidosis in alkaptonuria. *Journal of inherited metabolic disease* **38**, 797-805 (2015).
185. Green, J.D., Goldsbury, C., Kistler, J., Cooper, G.J.S. & Aebi, U. Human amylin oligomer growth and fibril elongation define two distinct phases in amyloid formation. *The Journal of biological chemistry* **279**, 12206 (2004).
186. Ganchev, D.N., Cobb, N.J., Surewicz, K. & Surewicz, W.K. Nanomechanical properties of human prion protein amyloid as probed by force spectroscopy. *Biophysical Journal* **95**, 2909-2915 (2008).
187. Yamanaka, K., Ogiso, H. & Kolosov, O. Analysis Of Subsurface Imaging And Effect Of Contact Elasticity In The Ultrasonic Force Microscope. *Japanese Journal of Applied Physics Part 1-Regular Papers Short Notes & Review Papers* **33**, 3197-3203 (1994).
188. Tovee, P.D. & Kolosov, O.V. Mapping nanoscale thermal transfer in-liquid environment-immersion scanning thermal microscopy. *Nanotechnology* **24**, 8 (2013).
189. Dobson, P.S., Weaver, J. M. R., Mills, G. . New methods for calibrated Scanning Thermal Microscopy (SThM). *Ieee Sensors,* (2007).
190. Smith, A.D. et al. Near-field optical microscopy with an infra-red free electron laser applied to cancer diagnosis. *Applied Physics Letters* **102** (2013).
191. Thompson, N.R. et al. First lasing of the ALICE infra-red Free-Electron Laser. *Nuclear Instruments & Methods in Physics Research Section a-Accelerators Spectrometers Detectors and Associated Equipment* **680**, 117-123 (2012).
192. Horcas, I. et al. WSXM: A software for scanning probe microscopy and a tool for nanotechnology. *Review of Scientific Instruments* **78**, 013705 (2007).
193. Kiselyova, O. & Yaminsky, I. in Atomic Force Microscopy (eds. Braga, P. & Ricci, D.) 217-230 (Humana Press, 2004).
194. Manzoni, C. et al. Overcoming synthetic A beta peptide aging: a new approach to an age-old problem. *Amyloid-Journal of Protein Folding Disorders* **16**, 71-80 (2009).
195. Levine, H. Thioflavine-T Interaction With Synthetic Alzheimers-Disease Beta-Amyloid Peptides - Detection Of Amyloid Aggregation In Solution. *Protein Science* **2**, 404-410 (1993).
196. Zhu, M., Souillac, P.O., Ionescu-Zanetti, C., Carter, S.A. & Fink, A.L. Surface-catalyzed amyloid fibril formation. *Journal of Biological Chemistry* **277**, 50914-50922 (2002).
197. May, P.C. et al. β-amyloid peptide in vitro toxicity: Lot-to-lot variability. *Neurobiology of Aging* **13**, 605-607 (1992).
198. Arimon, M., Sanz, F., Giralt, E. & Carulla, N. Template-Assisted Lateral Growth of Amyloid-beta 42 Fibrils Studied by Differential Labeling with Gold Nanoparticles. *Bioconjugate Chemistry* **23**, 27-32 (2012).

199. Gaines, G.L. & Tabor, D. Surface adhesion and elastic properties of mica. *Nature* **178**, 1304-1305 (1956).

200. Zagorski, M.G. et al. Methodological and chemical factors affecting amyloid beta peptide amyloidogenicity. *Amyloid, Prions, and Other Protein Aggregates* **309**, 189-204 (1999).

201. Orlando, R., Kenny, P.T.M. & Zagorski, M.G. Covalent modification of Alzheimer's amyloid β-peptide in formic acid solutions. *Biochemical and Biophysical Research Communications* **184**, 686-691 (1992).

202. Kirshenbaum, K. & Daggett, V. PH-Dependent Conformations Of The Amyloid Beta(1-28) Peptide Fragment Explored Using Molecular-Dynamics. *Biochemistry* **34**, 7629-7639 (1995).

203. Bezanilla, M., Manne, S., Laney, D.E., Lyubchenko, Y.L. & Hansma, H.G. Adsorption Of Dna To Mica, Silylated Mice, And Minerals - Characterization By Atomic-Force Microscopy. *Langmuir* **11**, 655-659 (1995).

204. Wang, H.D. et al. Glutaraldehyde modified mica: A new surface for atomic force microscopy of chromatin. *Biophysical Journal* **83**, 3619-3625 (2002).

205. Hansma, H.G. & Laney, D.E. DNA binding to mica correlates with cationic radius: Assay by atomic force microscopy. *Biophysical Journal* **70**, 1933-1939 (1996).

206. Sherratt, M.J., Baldock, C., Morgan, A. & Kielty, C.M. The morphology of adsorbed extracellular matrix assemblies is critically dependent on solution calcium concentration. *Matrix Biology* **26**, 156-166 (2007).

207. Lin, H., Zhu, Y.W.J. & Lal, R. Amyloid beta protein (1-40) forms calcium-permeable, Zn2+-sensitive channel in reconstituted lipid vesicles. *Biochemistry* **38**, 11189-11196 (1999).

208. Sherratt, M.J. et al. Fibrillin microfibrils are stiff reinforcing fibres in compliant tissues. *Journal of Molecular Biology* **332**, 183-193 (2003).

209. Bussiek, M., Mucke, N. & Langowski, J. Polylysine-coated mica can be used to observe systematic changes in the supercoiled DNA conformation by scanning force microscopy in solution. *Nucleic Acids Research* **31** (2003).

210. Hatters, D.M. et al. The circularization of amyloid fibrils formed by apolipoprotein C-II. *Biophysical Journal* **85**, 3979-3990 (2003).

211. van Bommel, K.J.C., Jung, J.H. & Shinkai, S. Poly(L-lysine) aggregates as templates for the formation of hollow silica spheres. *Advanced Materials* **13**, 1472-+ (2001).

212. Greenfield, N.J. & Fasman, G.D. Computed circular dichroism spectra for the evaluation of protein conformation. *Biochemistry* **8**, 4108-4116 (1969).

213. Nguyen, K.V., Gendrault, J.-L. & Wolff, C.-M. Poly-l-lysine Dissolves Fibrillar Aggregation of the Alzheimer β-Amyloid Peptide in Vitro. *Biochemical and Biophysical Research Communications* **291**, 764-768 (2002).

214. Fowler, S.B. et al. Mechanical unfolding of a titin Ig domain: Structure of unfolding intermediate revealed by combining AFM, molecular dynamics simulations, NMR and protein engineering. *Journal of Molecular Biology* **322**, 841-849 (2002).

215. Russo, C.J. & Passmore, L.A. Ultrastable gold substrates for electron cryomicroscopy. *Science* **346**, 1377-1380 (2014).

216. Dinelli, F., Albonetti, C. & Kolosov, O.V. Ultrasonic force microscopy: Detection and imaging of ultra-thin molecular domains. *Ultramicroscopy* **111**, 267-272 (2011).

217. Tsai, H.-H., Gunasekaran, K. & Nussinov, R. Sequence and Structure Analysis of Parallel β Helices: Implication for Constructing Amyloid Structural Models. *Structure* **14**, 1059-1072 (2006).

218. Richardson, J.S. & Richardson, D.C. Natural β-sheet proteins use negative design to avoid edge-to-edge aggregation. *Proceedings of the National Academy of Sciences* **99**, 2754-2759 (2002).

219. Huang, X.D. et al. The A beta peptide of Alzheimer's disease directly produces hydrogen peroxide through metal ion reduction. *Biochemistry* **38**, 7609-7616 (1999).
220. Huang, X.D. et al. Cu(II) potentiation of Alzheimer A beta neurotoxicity - Correlation with cell-free hydrogen peroxide production and metal reduction. *Journal of Biological Chemistry* **274**, 37111-37116 (1999).
221. Harper, J.D., Lieber, C.M. & Lansbury, P.T. Atomic force microscopic imaging of seeded fibril formation and fibril branching by the Alzheimer's disease amyloid-beta protein. *Chemistry & Biology* **4**, 951-959 (1997).
222. Smith, D.P. et al. Concentration dependent Cu2+ induced aggregation and dityrosine formation of the Alzheimer's disease amyloid-beta peptide. *Biochemistry* **46**, 2881-2891 (2007).
223. Innocenti, M. et al. Trace Copper(II) or Zinc(II) Ions Drastically Modify the Aggregation Behavior of Amyloid-beta(1-42): An AFM Study. *Journal of Alzheimers Disease* **19**, 1323-1329 (2010).
224. Klug, G. et al. beta-amyloid protein oligomers induced by metal ions and acid pH are distinct from those generated by slow spontaneous ageing at neutral pH. *European Journal of Biochemistry* **270**, 4282-4293 (2003).
225. Olubiyi, O.O. & Strodel, B. Structures of the Amyloid beta-Peptides A beta(1-40) and A beta(1-42) as Influenced by pH and a D-Peptide. *Journal of Physical Chemistry B* **116**, 3280-3291 (2012).
226. Lin, C.-J., Huang, H.-C. & Jiang, Z.-F. Cu(II) interaction with amyloid-beta peptide: A review of neuroactive mechanisms in AD brains. *Brain Research Bulletin* **82**, 235-242 (2010).
227. Faller, P. Copper and Zinc Binding to Amyloid-beta: Coordination, Dynamics, Aggregation, Reactivity and Metal-Ion Transfer. *Chembiochem* **10**, 2837-2845 (2009).
228. Garai, K., Sahoo, B., Kaushalya, S.K., Desai, R. & Maiti, S. Zinc lowers amyloid-beta toxicity by selectively precipitating aggregation intermediates. *Biochemistry* **46**, 10655-10663 (2007).
229. Garai, K., Sengupta, P., Sahoo, B. & Maiti, S. Selective destabilization of soluble amyloid beta oligomers by divalent metal ions. *Biochemical and Biophysical Research Communications* **345**, 210-215 (2006).
230. Tougu, V., Tiiman, A. & Palumaa, P. Interactions of Zn(II) and Cu(II) ions with Alzheimer's amyloid-beta peptide. Metal ion binding, contribution to fibrillization and toxicity. *Metallomics* **3**, 250-261 (2011).
231. Blackley, H.K.L. et al. High resolution investigations of beta-amyloid fibrillization by atomic force microscopy. *Faseb Journal* **13**, A1574 (1999).
232. Powers, E.T. & Powers, D.L. Mechanisms of protein fibril formation: Nucleated polymerization with competing off-pathway aggregation. *Biophysical Journal* **94**, 379-391 (2008).
233. Walsh, D.M. et al. Certain inhibitors of synthetic amyloid beta-peptide (A beta) fibrillogenesis block oligomerization of natural A beta and thereby rescue long-term potentiation. *Journal of Neuroscience* **25**, 2455-2462 (2005).
234. Trabelsi, A.B. et al. Charged nano-domes and bubbles in epitaxial graphene. *Nanotechnology* **25**, 16 (2014).
235. Goldsbury, C. et al. Amyloid structure and assembly: Insights from scanning transmission electron microscopy. *Journal of Structural Biology* **173**, 1-13 (2011).
236. Blackley, H.K.L. et al. In-situ atomic force microscopy study of beta-amyloid fibrillization. *Journal of Molecular Biology* **298**, 833-840 (2000).
237. Sunde, M. et al. Common core structure of amyloid fibrils by synchrotron X-ray diffraction. *Journal of Molecular Biology* **273**, 729-739 (1997).
238. Jimenez, J.L. et al. Cryo-electron microscopy structure of an SH3 amyloid fibril and model of the molecular packing. *Embo Journal* **18**, 815-821 (1999).

239. Fitzpatrick, A.W.P. et al. Atomic structure and hierarchical assembly of a cross-beta amyloid fibril. *Proceedings of the National Academy of Sciences of the United States of America* **110**, 5468-5473 (2013).
240. Donhauser, Z.J., Jobs, W.B. & Binka, E.C. Mechanics of Microtubules: Effects of Protofilament Orientation. *Biophysical Journal* **99**, 1668-1675 (2010).
241. Vinckier, A. et al. Immobilizing And Imaging Microtubules By Atomic-Force Microscopy. *Ultramicroscopy* **57**, 337-343 (1995).
242. Inagaki, K., Kolosov, O.V., Briggs, G.A.D. & Wright, O.B. Waveguide ultrasonic force microscopy at 60 MHz. *Applied Physics Letters* **76**, 1836-1838 (2000).
243. Cuberes, M.T., Assender, H.E., Briggs, G.A.D. & Kolosov, O.V. Heterodyne force microscopy of PMMA/rubber nanocomposites: nanomapping of viscoelastic response at ultrasonic frequencies. *Journal of Physics D-Applied Physics* **33**, 2347-2355 (2000).
244. Skilbeck, M.S. et al. Multimodal microscopy using 'half and half' contact mode and ultrasonic force microscopy. *Nanotechnology* **25** (2014).
245. Kraatz, M., Geisler, H. & Zschech, E. in Characterization and Metrology for Ulsi Technology (eds. Seiler, D.G. et al.) 343-347 (2003).
246. Moran, S.D. & Zanni, M.T. How to Get Insight into Amyloid Structure and Formation from Infrared Spectroscopy. *Journal of Physical Chemistry Letters* **5**, 1984-1993 (2014).
247. Benseny-Cases, N., Klementieva, O., Cotte, M., Ferrer, I. & Cladera, J. Microspectroscopy (mu FTIR) Reveals Co-localization of Lipid Oxidation and Amyloid Plaques in Human Alzheimer Disease Brains. *Analytical Chemistry* **86**, 12047-12054 (2014).
248. Xue, L. et al. High-Resolution Chemical Identification of Polymer Blend Thin Films Using Tip-Enhanced Raman Mapping. *Macromolecules* **44**, 2852-2858 (2011).
249. Amenabar, I. et al. Structural analysis and mapping of individual protein complexes by infrared nanospectroscopy. *Nature Communications* **4** (2013).
250. Marcott, C. et al. Using 2D correlation analysis to enhance spectral information available from highly spatially resolved AFM-IR spectra. *Journal of Molecular Structure* **1069**, 284-289 (2014).
251. Van Eerdenbrugh, B., Lo, M., Kjoller, K., Marcott, C. & Taylor, L.S. Nanoscale Mid-Infrared Evaluation of the Miscibility Behavior of Blends of Dextran or Maltodextrin with Poly(vinylpyrrolidone). *Molecular Pharmaceutics* **9**, 1459-1469 (2012).
252. Bosse, J.L. et al. Nanothermal characterization of amorphous and crystalline phases in chalcogenide thin films with scanning thermal microscopy. *Journal of Applied Physics* **116** (2014).
253. Sadewasser, S., Leendertz, C., Streicher, F. & Lux-Steiner, M.C. The influence of surface topography on Kelvin probe force microscopy. *Nanotechnology* **20** (2009).
254. Shen, S., Mavrokefalos, A., Sambegoro, P. & Chen, G. Nanoscale thermal radiation between two gold surfaces. *Applied Physics Letters* **100**, 233114 (2012).
255. Saveliev, Y.M., Jackson, F., Jones, J., McKenzie, J. in International Particle Accelerator Conference (New Orleans, USA, 2012).
256. Muller, T. et al. Nanoscale spatially resolved infrared spectra from single microdroplets. *Lab on a Chip* **14**, 1315-1319 (2014).
257. Shivu, B. et al. Distinct beta-Sheet Structure in Protein Aggregates Determined by ATR-FTIR Spectroscopy. *Biochemistry* **52**, 5176-5183 (2013).
258. Stroud, J.C., Liu, C., Teng, P.K. & Eisenberg, D. Toxic fibrillar oligomers of amyloid-β have cross-β structure. *Proceedings of the National Academy of Sciences* (2012).
259. Cerf, E., Ruysschaert, J.-M., Goormaghtigh, E. & Raussens, V. ATR-FTIR, a new tool to analyze the oligomeric content of A beta samples in the presence of apolipoprotein E isoforms. *Spectroscopy-an International Journal* **24**, 245-249 (2010).

260. Olofsson, A., Lindhagen-Persson, M., Sauer-Eriksson, A.E. & Ohman, A. Amide solvent protection analysis demonstrates that amyloid-beta(1-40) and amyloid-beta(1-42) form different fibrillar structures under identical conditions. *Biochemical Journal* **404**, 63-70 (2007).
261. Barth, A. Infrared spectroscopy of proteins. *Biochimica et Biophysica Acta (BBA) - Bioenergetics* **1767**, 1073-1101 (2007).
262. Kong, J. & Yu, S. Fourier transform infrared spectroscopic analysis of protein secondary structures. *Acta Biochimica Et Biophysica Sinica* **39**, 549-559 (2007).
263. Benseny-Cases, N., Cocera, M. & Cladera, J. Conversion of non-fibrillar beta-sheet oligomers into amyloid fibrils in Alzheimer's disease amyloid peptide aggregation. *Biochemical and Biophysical Research Communications* **361**, 916-921 (2007).
264. Bieschke, J. et al. Small-molecule conversion of toxic oligomers to nontoxic beta-sheet-rich amyloid fibrils. *Nature Chemical Biology* **8**, 93-101 (2012).
265. Cleary, J.P. et al. Natural oligomers of the amyloid-protein specifically disrupt cognitive function. *Nature Neuroscience* **8**, 79-84 (2005).
266. Freir, D.B. et al. A beta oligomers inhibit synapse remodelling necessary for memory consolidation. *Neurobiology of Aging* **32**, 2211-2218 (2011).
267. Farlow, M. et al. Safety and biomarker effects of solanezumab in patients with Alzheimer’s disease. *Alzheimer's & Dementia: The Journal of the Alzheimer's Association* **8**, 261-271.
268. Dodart, J.-C. et al. Immunization reverses memory deficits without reducing brain Aβ burden in Alzheimer's disease model. *Nature Neuroscience* **5**, 452 (2002).
269. Austen, B.M. et al. Designing peptide inhibitors for oligomerization and toxicity of Alzheimer's beta-amyloid peptide. *Biochemistry* **47**, 1984-1992 (2008).
270. Taylor, M. et al. Development of a Proteolytically Stable Retro-Inverso Peptide Inhibitor of beta-Amyloid Oligomerization as a Potential Novel Treatment for Alzheimer's Disease. *Biochemistry* **49**, 3261-3272 (2010).
271. Parthsarathy, V. et al. A Novel Retro-Inverso Peptide Inhibitor Reduces Amyloid Deposition, Oxidation and Inflammation and Stimulates Neurogenesis in the APPswe/PS1 Delta E9 Mouse Model of Alzheimer's Disease. *Plos One* **8** (2013).
272. Hein, C.D., Liu, X.M. & Wang, D. Click chemistry, a powerful tool for pharmaceutical sciences. *Pharm Res* **25**, 2216-30 (2008).
273. Davis, C.H. & Berkowitz, M.L. Interaction Between Amyloid-β (1–42) Peptide and Phospholipid Bilayers: A Molecular Dynamics Study. *Biophysical Journal* **96**, 785-797 (2009).
274. Qiang, W., Yau, W.-M. & Schulte, J. Fibrillation of beta amyloid peptides in the presence of phospholipid bilayers and the consequent membrane disruption. *Biochimica et biophysica acta* **1848**, 266-76 (2015).
275. Tamayo, J. & Garcia, R. Deformation, contact time, and phase contrast in tapping mode scanning force microscopy. *Langmuir* **12**, 4430-4435 (1996).
276. Poojari, C. & Strodel, B. Stability of Transmembrane Amyloid beta-Peptide and Membrane Integrity Tested by Molecular Modeling of Site-Specific A beta 42 Mutations. *Plos One* **8**, 12 (2013).
277. Ambroggio, E.E. et al. Surface Behavior and Lipid Interaction of Alzheimer β-Amyloid Peptide 1–42: A Membrane-Disrupting Peptide. *Biophysical Journal* **88**, 2706-2713 (2005).
278. Sublimi Saponetti, M. et al. Aggregation of Aß(25-35) on DOPC and DOPC/DHA Bilayers: An Atomic Force Microscopy Study. *PLoS ONE* **9**, e115780 (2014).
279. Kumar, A. et al. Specific Soluble Oligomers of Amyloid-beta Peptide Undergo Replication and Form Non-fibrillar Aggregates in Interfacial Environments. *Journal of Biological Chemistry* **287**, 21253-21264 (2012).

280. Kuo, Y.C. & Wang, C.T. Protection of SK-N-MC cells against beta-amyloid peptide-induced degeneration using neuron growth factor-loaded liposomes with surface lactoferrin. *Biomaterials* **35**, 5954-5964 (2014).

281. Theunis, C. et al. Efficacy and Safety of A Liposome-Based Vaccine against Protein Tau, Assessed in Tau.P301L Mice That Model Tauopathy. *Plos One* **8** (2013).

282. Vu, H.T. et al. Effect of liposome membranes on disaggregation of amyloid beta fibrils by dopamine. *Biochemical Engineering Journal* **71**, 118-126 (2013).

283. Bin, Y., Li, X., He, Y., Chen, S. & Xiang, J. Amyloid- peptide (142) aggregation induced by copper ions under acidic conditions. *Acta Biochimica Et Biophysica Sinica* **45**, 570-577 (2013).

284. Doody, R.S. et al. Phase 3 Trials of Solanezumab for Mild-to-Moderate Alzheimer's Disease. *New England Journal of Medicine* **370**, 311-321 (2014).

285. Ruggeri, F.S. et al. Infrared nanospectroscopy characterization of oligomeric and fibrillar aggregates during amyloid formation. *Nat Commun* **6** (2015).

286. Tinker-Mill, C., Mayes, J., Allsop, D. & Kolosov, O.V. Ultrasonic force microscopy for nanomechanical characterization of early and late-stage amyloid-β peptide aggregation. *Sci. Rep.* **4** (2014).

287. Jan, A., Hartley, D.M. & Lashuel, H.A. Preparation and characterization of toxic A beta aggregates for structural and functional studies in Alzheimer's disease research. *Nature Protocols* **5**, 1186-1209 (2010).

288. Yip, C.M. & McLaurin, J. Amyloid-beta peptide assembly: A critical step in fibrillogenesis and membrane disruption. *Biophysical Journal* **80**, 1359-1371 (2001).

289. Yip, C.M., Darabie, A.A. & McLaurin, J. A beta 42-peptide assembly on lipid Bilayers. *Journal of Molecular Biology* **318**, 97-107 (2002).

290. Lee, A.J., Szymonik, M., Hobbs, J.K. & Walti, C. Tuning the translational freedom of DNA for high speed AFM. *Nano Research* **8**, 1811-1821 (2015).